

Friction-induced Vibration
in
Lead Screw Systems

by

Orang Vahid Araghi

A thesis
presented to the University of Waterloo
in fulfillment of the
thesis requirement for the degree of
Doctor of Philosophy
in
Mechanical Engineering

Waterloo, Ontario, Canada, 2009

© Orang Vahid Araghi 2009

Author's Declaration

I hereby declare that I am the sole author of this thesis. This is a true copy of the thesis, including any required final revisions, as accepted by my examiners.

I understand that my thesis may be made electronically available to the public.

Abstract

Lead screw drives are used in various motion delivery systems ranging from manufacturing to high precision medical devices. Lead screws come in many different shapes and sizes; they may be big enough to move a 140 tons theatre stage or small enough to be used in a 10ml liquid dispensing micro-pump. Disproportionate to the popularity of lead screws and their wide range of applications, very little attention has been paid to their dynamical behavior. Only a few works can be found in the literature that touch on the subject of lead screw dynamics and the instabilities caused by friction. The current work aims to fill this gap by presenting a comprehensive study of lead screw dynamics focusing on the friction-induced instability in such systems.

In this thesis, a number of mathematical models are developed for lead screw drive systems. Starting from the basic kinematic model of lead screw and nut, dynamic models are developed with varying number of degrees of freedom to reflect different components of a real lead screw drive from the rotary driver (motor) to the translating payload. In these models, velocity-dependent friction between meshing lead screw and nut threads constitute the main source nonlinearity.

A practical case study is presented where friction-induced vibration in a lead screw drive is the cause of excessive audible noise. Using a complete dynamical model of this drive, a two-stage system parameter identification and fine-tuning method is developed to estimate parameters of the velocity-dependent coefficient of friction. In this approach the coupling stiffness and damping in the lead screw supports are also estimated. The numerical simulation results using the identified parameters show the applicability of the developed method in reproducing the actual systems behavior when compared with the measurements. The verified mathematical model is then used to study the role of various system parameters on the stability of the system and the amplitude of vibrations. These studies lead to possible design modifications that solve the system's excessive noise problem.

Friction can cause instability in a dynamical system through different mechanisms. In this work, the three mechanisms relevant to the lead screw systems are considered. These mechanisms are: 1. negative damping; 2. kinematic constraint, and; 3. mode coupling.

The negative damping instability, which is caused by the negative gradient of friction with respect to sliding velocity, is studied thorough linear eigenvalue analysis of a 1-DOF lead screw drive model. The first order averaging method is applied to this model to gain deeper insight into the role of velocity-dependent coefficient of friction and to analyze the stability of possible periodic solutions. This analysis also is extended to a 2-DOF model. It is also shown that higher order averaging

methods can be used to predict the amplitude of vibrations with improved accuracy.

Unlike the negative damping instability mechanism, kinematic constraint and mode coupling instability mechanisms can affect a system even when the coefficient of friction is constant. Parametric conditions for these instability mechanisms are found through linear eigenvalue analysis. It is shown that kinematic constraint and mode coupling instability mechanisms can only occur in self-locking lead screws.

The experimental case study presented in this work demonstrates the need for active vibration control when eliminating vibration by design fails or when it is not feasible. Using the sliding mode control method, two speed regulators are developed for 1-DOF and 2-DOF lead screw drive system models where torque generated by the motor is the controlled input. In these robust controllers, no knowledge of the actual value of any of the system parameters is required and only the upper and lower bounds of parameters are assumed to be available. Simulation results show the applicability and performance of these controllers.

The current work provides a detailed treatment of the dynamics of lead screw drives and the topic of friction-induced vibration in such systems. The reported findings regarding the three instability mechanisms and the friction parameters identification approach can improve the design process of lead screw drives. Furthermore, the developed robust vibration controllers can be used to extend the applicability of lead screws to cases where persistent vibrations caused by negative damping cannot be eliminated by design modifications due to constraints.

Acknowledgements

I wish to express my gratitude to my supervisor, Dr. Golnaraghi. I have benefited greatly from his guidance and insightful suggestions throughout my research.

The experimental part of this work would not have been possible by without the generous support of Dr. Erkorkmaz and his team in the Precision Control Laboratory. I am especially thankful to Amin Kamalzadeh and Wilson Wong for their helps in the preparation of the hardware and software used in the tests.

I would like to express my thanks to my colleague and friend Nima Eslaminasab for his help in the preparation of the test setups and for his assistance during many hours of testing. I am also grateful to him for letting me bounce ideas off him whenever I needed.

I am forever indebted to my wife, Maryam. Without her undying support and encouragement, this journey would not have been possible.

To Maryam

Table of Contents

List of Figures.....	xi
List of Tables	xix
Chapter 1 Introduction	1
1.1 Lead Screws	1
1.2 The Audible Noise Problem.....	4
1.3 Thesis Overview.....	6
1.4 Contributions.....	8
Chapter 2 Literature Review.....	10
2.1 Friction-induced Vibration.....	10
2.1.1 Negative Damping.....	12
2.1.2 Kinematic constraint instability.....	14
2.1.3 Mode Coupling.....	15
2.2 Lead Screw Drives	18
Chapter 3 Mathematical Modeling of Lead Screw Drives	20
3.1 Lead Screw and Nut – A Kinematic Pair	21
3.2 Velocity-dependent Coefficient of Friction	25
3.3 Basic 1-DOF Model	26
3.3.1 Inverted Basic Model	28
3.3.2 Basic Model with Fixed Nut.....	29
3.3.3 Basic Model with Fixed Lead Screw.....	29
3.4 Anti-backlash Nut	30
3.5 Compliance in Lead Screw and Nut Threads.....	32
3.6 Axial Compliance in Lead Screw Supports	33
3.7 Compliance in Threads and Lead Screw Supports.....	34
3.8 A Complete System Model	35

3.9 Some Remarks Regarding the System Models	37
Chapter 4 An Experimental Case Study	40
4.1 Preliminary Observations	40
4.2 Step 1: Friction and System Parameter Identification.....	44
4.3 Experiment Results	49
4.3.1 DC Motor and Gearbox	49
4.3.2 Identification Results.....	50
4.4 Step 2: Fine-tuning	54
4.5 Parameter Studies	62
4.5.1 Effect of Input Angular Velocity.....	62
4.5.2 Effect of Damping	62
4.5.3 Effect of Stiffness	63
4.6 Conclusions	64
Chapter 5 Negative Damping	66
5.1 Equation of Motion	66
5.2 Eigenvalue Analysis.....	68
5.2.1 Numerical Examples	70
5.3 First-order Averaging.....	71
5.3.1 Assumptions	72
5.3.2 Equation of Motion in Standard Form.....	73
5.3.3 First Order Averaging.....	76
5.3.4 Steady State Solutions	78
5.3.5 Numerical Simulation Results	80
5.4 Conclusions	84
Chapter 6 Kinematic Constraint and Mode Coupling Instability	
Mechanisms	86
6.1 Kinematic Constraint Instability in 1-DOF Lead Screw Model	86
6.1.1 A Note Regarding the Solution of the Equation of Motion.....	87

6.1.2 Examples	88
6.1.3 Region of Attraction of the Stable Steady-sliding Fixed Point	92
6.2 Stability Analysis of the 2-DOF Lead Screw Model with Compliant Threads.....	94
6.2.1 Undamped System.....	97
6.2.2 Damped System.....	102
6.3 Stability Analysis of a 2-DOF Model with Axially Compliant Lead Screw Supports	109
6.3.1 Undamped System.....	111
6.3.2 Damped System.....	117
6.4 Mode Coupling in a 3-DOF System.....	124
6.5 Conclusions	128
Chapter 7 Vibration Control	131
7.1 Mathematical Model	132
7.1.1 A Note on the Friction Model.....	135
7.2 Parameter Uncertainty	135
7.3 Sliding Mode Control for Rigid Drives.....	137
7.3.1 Numerical Examples	141
7.4 Sliding Mode Controller for Flexible Drive.....	147
7.4.1 The Sliding Phase	148
7.4.2 The Reaching Phase	160
7.4.3 Feedforward Input	163
7.4.4 Continuous Sliding Mode Controller	165
7.4.5 Variable Velocity Set Point	170
7.4.6 Numerical Examples	172
7.5 Conclusions	183
Chapter 8 Results Summary and Future Work	185
8.1 Results Summary.....	185
8.2 Future Work	188
Appendices.....	190
Appendix A Test Setups.....	191

Appendix B First Order Averaging Theorem – Periodic Case	197
Appendix C A Definite Integral Used in Averaging.....	201
Appendix D Steady-state Solutions of the Averaged 1-DOF Lead Screw Model	204
Appendix E Higher-order Averaging.....	216
Appendix F First-order Averaging Applied to the 2-DOF Lead Screw Model with Axially Compliant Supports.....	225
Appendix G Similarities in the Conditions for Local Stability of the Steady-sliding Fixed Point Between the 2-DOF Model of Section 3.5 and the 2-DOF model of Section 3.6.....	233
Appendix H Further Observations on the Mode Coupling Instability in Lead Screw Drives	236
Appendix I Theorems Cited in Chapter 7	247
Bibliography	250

List of Figures

Figure 1-1: Lead screw design factors.....	2
Figure 1-2: Meshing “Stub Acme” lead screw and nut (cut view). Detail: radial and axial clearances.	3
Figure 1-3: A powered seat adjuster.....	5
Figure 1-4: Time-frequency signature of the sound recorded from the powered seat adjuster	5
Figure 1-5: Components of the lead screw drive mechanism found in a type of variable volume pump	6
Figure 1-6: Time-frequency signature of the sound recorded from the pump	6
Figure 2-1: Stribeck curve [25].	11
Figure 2-2: 1-DOF mass-on-a-conveyer model.....	13
Figure 2-3: Simple model to demonstrate kinematic constraint instability [29].	14
Figure 2-4: A simple 2-DOF model capable of exhibiting mode coupling instability [47].	16
Figure 3-1: Lead screw drive system.....	20
Figure 3-2: Sign convention for contact forces between nut and lead screw	22
Figure 3-3: Effect of lead angle on the measurement of thread angle.....	23
Figure 3-4: Geometry of the threads on two different section planes	23
Figure 3-5: Forces acting on a thread	24
Figure 3-6: Velocity dependent coefficient of friction.....	25
Figure 3-7: 1-DOF model of a lead screw system.....	27
Figure 3-8: Inverted basic 1-DOF model	28
Figure 3-9: Basic 1-DOF model with fixed nut.....	29
Figure 3-10: Basic 1-DOF model with fixed lead screw	30
Figure 3-11: Lead screw model with anti-backlash nut	31
Figure 3-12: 2-DOF lead screw drive model including thread compliance	32
Figure 3-13: 2-DOF lead screw drive model including compliance in the supports.....	34
Figure 3-14: 3-DOF lead screw drive model including compliance in the supports and compliance in the lead screw and nut threads.....	35
Figure 3-15: A 4-DOF lead screw drive system model.....	36
Figure 4-1: Test setup for complete seat adjuster.....	41
Figure 4-2: Sample test results from complete seat adjuster tests	42

Figure 4-3: Audible noise frequency content for the test results shown in Figure 4-2 (at 8s). Peak amplitude at 162Hz.....	42
Figure 4-4: Single-track test setup.....	43
Figure 4-5: Sample test results from single-track tests.....	43
Figure 4-6: Audible noise frequency content for the test results shown in Figure 4-5 (at 3s). Peak amplitude at 150Hz.....	44
Figure 4-7: Schematic view of the test setup.....	45
Figure 4-8: Resistive torque of the motor and the gearbox. Dots: measurements, dashed line: fitted line to the data points.....	50
Figure 4-9: Collection of data points showing Torque/Speed/Force.....	51
Figure 4-10: Sample measurement results. Variation of motor torque with applied axial load at constant speeds. Dots: measurements, solid line: fitted line to the data points	52
Figure 4-11: Variation of β_0 with motor angular velocity	52
Figure 4-12: Variation of β_1 with motor angular velocity	53
Figure 4-13: Identified velocity dependent coefficient of friction	54
Figure 4-14: Experimentally obtained variation of limit cycle vibration amplitude with input angular velocity (gearbox output) and axial force.....	55
Figure 4-15: a) A sample of test results showing stick-slip in open-loop tests, b) zoomed view. Black: lead screw angular velocity; grey: DC motor angular velocity	55
Figure 4-16: Measurement vs. simulation example. Inputs: $R = 152.9(N), \omega_G = 35.6(rad/s)$ - Parameters: $k = 1.18(Nm/rad), c = 1.86 \times 10^{-4}(Nms/rad)$ a) phase plot, b) frequency response. Gray: measurements, black: simulation.....	57
Figure 4-17: Measurement vs. simulation example. Inputs: $R = 273.9(N), \omega_G = 34.3(rad/s)$ - Parameters: $k = 1.31(Nm/rad), c = 3.37 \times 10^{-4}(Nms/rad)$ a) phase plot, b) frequency response. Gray: measurements, black: simulation.....	57
Figure 4-18: Measurement vs. simulation example. Inputs: $R = 314.3(N), \omega_G = 40.3(rad/s)$ - Parameters: $k = 1.65(Nm/rad), c = 3.04 \times 10^{-4}(Nms/rad)$ a) phase plot, b) frequency response. Gray: measurements, black: simulation.....	58
Figure 4-19: Measurement vs. simulation example. Inputs: $R = 327.5(N), \omega_G = 83.7(rad/s)$ - Parameters: $k = 1.75(Nm/rad), c = 4.07 \times 10^{-4}(Nms/rad)$ a) phase plot, b) frequency response. Gray: measurements, black: simulation.....	58

Figure 4-20: Measurement vs. simulation example. Inputs: $R = 330.8(N)$, $\omega_G = 37.3(rad/s)$ - Parameters: $k = 1.88(Nm/rad)$, $c = 5.79 \times 10^{-4}(Nms/rad)$ a) phase plot, b) frequency response. Gray: measurements, black: simulation.....	59
Figure 4-21: Measurement vs. simulation example. Inputs: $R = 336.7(N)$, $\omega_G = 27.9(rad/s)$ - Parameters: $k = 1.67(Nm/rad)$, $c = 4.00 \times 10^{-4}(Nms/rad)$ a) phase plot, b) frequency response. Gray: measurements, black: simulation.....	59
Figure 4-22: Variation of coupling stiffness, k , with gearbox output velocity and axial force	60
Figure 4-23: Variation of friction boundary effect, $1/r_1$, with gearbox output velocity and axial force	60
Figure 4-24: Variation of lead screw support damping, c ($\times 10^{-3}$), with gearbox output velocity and axial force	61
Figure 4-25: Variation of friction scaling, s_μ , with gearbox output velocity and axial force	61
Figure 4-26: Contour plots of the steady state vibration amplitude vs. applied axial force and gearbox output speed.....	62
Figure 4-27: Effect of lead screw rotational damping on the threshold of instabilities. The thick black line corresponds to the instability threshold in Figure 4-26.	63
Figure 4-28: The effects of coupling stiffness and axial loading on the dynamic behavior of the lead screw - Gearbox output angular velocity 40 (rad/s)	64
Figure 5-1: Local stability of fixed points of the 1-DOF lead screw system.	69
Figure 5-2: system trajectories for $c = 2 \times 10^{-4} < c_{cr}$; unstable steady-sliding fixed point (0,0).....	71
Figure 5-3: system trajectories for $c = 3 \times 10^{-4} > c_{cr}$; stable steady-sliding fixed point (0,0)	71
Figure 5-4: First order averaging results. $c=2 \times 10^{-4}$ Grey: truncated equation of motion; Black: amplitude of vibration from first order averaging	81
Figure 5-5: First order averaging results. $c=3 \times 10^{-4}$ Grey: truncated equation of motion; Black: amplitude of vibration from first order averaging	81
Figure 5-6: First order averaging results. $c=2 \times 10^{-4}$ Grey: original equation of motion; Black: amplitude of vibration from first order averaging	82
Figure 5-7: First order averaging results. $c=3 \times 10^{-4}$ Grey: original equation of motion; Black: amplitude of vibration from first order averaging	82
Figure 5-8: Bifurcation diagram of the averaged amplitude equation. “—” Stable; “- -” Unstable	83
Figure 5-9: Effect of Stribeck friction on bifurcation.....	84

Figure 5-10: Effect of negative damping on bifurcation.....	84
Figure 6-1: Evolution of the eigenvalues as the translating mass, m , is varied.....	89
Figure 6-2: System trajectories for constant μ . (a) $m = 10 < m_{cr}$ (b) $m = 11 > m_{cr}$	90
Figure 6-3: Instability caused by kinematic constraint - 2DOF model with very high contact stiffness and damping. (a) phase-plane, (b) contact normal force.....	90
Figure 6-4: Effect of damping on the unstable system.....	91
Figure 6-5: Effects of damping on the steady-state vibration of the lead screw system under kinematic constraint instability.....	92
Figure 6-6: Effect contact parameters on the response of the system under kinematic constraint instability.....	92
Figure 6-7: System trajectories for $R=-10$ (N), $\omega=40$ (rad/s), and $c=c_{cr}$	94
Figure 6-8: Stability of the 2-DOF system as contact stiffness and coefficient of friction are varied. $m = 5$ and $R\omega>0$. Hatched region: unstable.....	100
Figure 6-9: Variation of the real and imaginary parts of the eigenvalues as the contact stiffness is varied. $\mu = 0.2$, $m = 5$	100
Figure 6-10: Stability of the 2-DOF system as contact stiffness and coefficient of friction are varied, when $m = 15$ and $R\omega>0$. The ▨ hatched area: mode coupling instability region; the ▩ hatched area: secondary kinematic constraint instability region.....	101
Figure 6-11: Variation of the real part (a) and imaginary part (b) of the eigenvalues as the contact stiffness is varied. $\mu = 0.218$, $m = 15$	102
Figure 6-12: Regions of stability of the 2-DOF model with damping. Black: stable, white: unstable. $R\omega>0$, $m=5$, $c_c=10^2$, and $c=4\times 10^{-5}$	104
Figure 6-13: Variation of the real part of the eigenvalues (a) and the natural frequencies (b), as the contact stiffness is varied. $\mu = 0.15$, $m = 5$, $c_c=10^2$, and $c=4\times 10^{-5}$	105
Figure 6-14: Regions of stability of the 2-DOF model with damping. Black: stable, white: unstable. $R\omega>0$, $m=5$, $c_c=2\times 10^3$, and $c=4\times 10^{-4}$	106
Figure 6-15: Variation of the real part of the eigenvalues (a) and the natural frequencies (b), as the contact stiffness is varied. $\mu = 0.15$, $m = 5$, $c_c=2\times 10^3$, and $c=4\times 10^{-4}$	106
Figure 6-16: Regions of stability of the 2-DOF model with damping. Black: stable, white: unstable, Grey: region of instability of the undamped system $R\omega>0$, $m=15$, $c_c=2\times 10^3$, and $c=4\times 10^{-4}$	107
Figure 6-17: Variation of the real part of the eigenvalues (a) and the natural frequencies (b), as the contact stiffness is varied. $m = 15$, $c_c=2\times 10^3$, and $c=4\times 10^{-4}$. Solid: $\mu = 0.15$; dashed $\mu = 0.2$... 107	107

Figure 6-18: Regions of stability of the 2-DOF model with damping. Black: stable, white: unstable, Grey: region of instability of the undamped system. $R\omega > 0$, $m=15$, $c_c=4 \times 10^4$, and $c=8 \times 10^{-3}$ 109

Figure 6-19: Variation of the real part of the eigenvalues (a) and the natural frequencies (b), as the contact stiffness is varied. $m = 15$, $c_c=4 \times 10^4$, $c=8 \times 10^{-3}$, and $\mu = 0.218$ 109

Figure 6-20: Stability of the 2-DOF system as support stiffness and coefficient of friction are varied. $m = 5$ and $R\omega > 0$. Hatched region: unstable..... 114

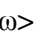
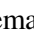
Figure 6-21: Stability of the 2-DOF system as support stiffness and coefficient of friction are varied, when $m = 15$ and $R\omega > 0$. The  hatched area: mode coupling instability region; the  hatched area: secondary kinematic constraint instability region..... 115

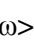
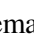
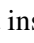
Figure 6-22: Stability of the 2-DOF system as support stiffness and coefficient of friction are varied, when $m = 15$ and $R\omega > 0$. The  hatched area: mode coupling instability region; the  hatched area: secondary kinematic constraint instability region, and; the  hatched area: primary kinematic constraint instability region. 116

Figure 6-23: Variation of the real parts (a) and imaginary parts (b) of the eigenvalues as the contact stiffness is varied. $k_1 = 4 \times 10^6$, $m = 15$, and $m_1 = 11.6$ 116

Figure 6-24: Regions of stability of the 2-DOF model with damping. (a) $m_1=0.232$ kg, (b) $m_1=2.32$ kg, and (c) $m_1=11.6$ kg. Black: stable, white: unstable, and hatched: undamped instability region. $R\omega > 0$, $m=5$, $c_1=10^2$, and $c=2 \times 10^{-5}$ 118

Figure 6-25: Regions of stability of the 2-DOF model with damping. (a) $m_1=0.232$ kg, (b) $m_1=2.32$ kg, and (c) $m_1=23.2$ kg. Black: stable, white: unstable, and hatched: undamped instability region. $R\omega > 0$, $m=5$, $c_1=2 \times 10^3$, and $c=4 \times 10^{-4}$ 119

Figure 6-26: Regions of stability of the 2-DOF model with damping. (a) $m_1=0.232$ kg, (b) $m_1=2.32$ kg, and (c) $m_1=11.6$ kg. Black: stable, white: unstable, and, hatched: undamped instability region. $R\omega > 0$, $m=15$, $c_1=2 \times 10^3$, and $c=4 \times 10^{-4}$ 120

Figure 6-27: Variations of real parts of the eigenvalues (a) and damped natural frequencies (b) as a function of lead screw support axial stiffness, k_1 . $\mu = 0.11, 0.12, 0.13$ 121

Figure 6-28: Variations of the real part of eigenvalues (a) and the damped natural frequencies (b) as a function of the coefficient of friction, μ . $k_1= 4 \times 10^6$ 122

Figure 6-29: Regions of stability of the 2-DOF model with damping. (a) $m_1=0.232$ kg, (b) $m_1=2.32$ kg, and (c) $m_1=11.6$ kg. Black: stable, white: unstable, and hatched: undamped instability region. $R\omega > 0$, $m=15$, $c_1=2 \times 10^4$, and $c=4 \times 10^{-3}$ 123

Figure 6-30: Variations of real part of the eigenvalues (a) and damped natural frequencies (b) as a function of lead screw support axial stiffness, k_1 . $\mu = 0.2$.	124
Figure 6-31: Variations of the real part of eigenvalues (a) and the damped natural frequencies (b) as a function of the coefficient of friction, μ . $k_1 = 5 \times 10^6$. (c) Close-up view of the real part of eigenvalues	124
Figure 6-32: a) Evolution of the three natural frequencies of the undamped 3-DOF system (with constant coefficient of friction) as a function of k_c and k_1 . b) Stability map.	127
Figure 6-33: Local stability of fixed points of the 3-DOF lead screw system with constant coefficient of friction. Black: stable, white: unstable	128
Figure 7-1: lead screw drive model	133
Figure 7-2: System trajectories under the action of the continuous sliding mode controller. Dashed: $x(0) = (0, -10)$ solid: $x(0) = (0, 10)$; dashed-dot: boundary layer	142
Figure 7-3: Controlled input. Dashed: $x(0) = (0, -10)$ solid: $x(0) = (0, 10)$	142
Figure 7-4: System trajectories under the action of the continuous sliding mode controller. Dashed: $x(0) = (0, -10)$ solid: $x(0) = (0, 10)$; dashed-dot: boundary layer	143
Figure 7-5: Controlled input. Dashed: $x(0) = (0, -10)$ solid: $x(0) = (0, 10)$	144
Figure 7-6: Effect of β_0 on the performance of the controller.	145
Figure 7-7: System trajectories under the action of the continuous sliding mode controller. Dashed: $x(0) = (0, -10)$ solid: $x(0) = (0, 10)$; hatched region: bounds on the solution given by the stability conditions.	146
Figure 7-8: Close-up view of system trajectories showing limit-cycle behavior. Dashed: $x(0) = (0, -10)$ solid: $x(0) = (0, 10)$	146
Figure 7-9: A portion of velocity error time history	147
Figure 7-10: Smoothed absolute function	166
Figure 7-11: Controller performance of example #1; (a) lead screw velocity error, (b) motor velocity error	173
Figure 7-12: (a) Variation of the torsional deflection of the coupling, (b) variation of normal contact force	174
Figure 7-13: Controlled input of example #1	174
Figure 7-14: System's trajectory for example #1	175

Figure 7-15: Lead screw (a) and motor (b) angular velocities of the closed loop system. Black: system response; dashed gray: velocity set point	176
Figure 7-16: Controlled input of example #2	176
Figure 7-17: Effect of d_2 on the performance of the controller.	177
Figure 7-18: Effect of feedforward part on the performance of the controller. Gray: without feedforward; black: with feedforward	179
Figure 7-19: Controlled inputs of example #4. Black: with feedforward input; gray: without feedforward input.	179
Figure 7-20: Performance under the action of feedforward input alone	180
Figure 7-21: Smoothed coefficient of friction.....	181
Figure 7-22: Lead screw (a) and motor (b) angular velocities of the closed loop system. Black: system response; dashed gray: velocity set point	182
Figure 7-23: Close-up view of the transient vibrations of the lead screw	182
Figure 7-24: Controlled input for example #5.....	183
Figure A-1: Experimental setup for preliminary tests on the complete powered seat adjuster	191
Figure A-2: Data acquisition in Matlab/Simulink environment.....	192
Figure A-3: Experimental setup for the lead screw friction identification tests.....	193
Figure A-4: Instrumentation used in the friction identification test setup.....	194
Figure A-5: Sample test results. (a) Lead screw angular displacement, (b) Lead screw angular velocity.	195
Figure A-6: Near steady-state portion of a sample test results. (a) Lead screw angular velocity, (b) Axial load, and (c) Motor torque.....	196
Figure D-1: The velocity-dependent coefficient of friction.	205
Figure D-2: Schematic plot of amplitude equation for Case I.....	207
Figure D-3: Schematic plots of amplitude equation for Case II.....	208
Figure D-4: Schematic plots of amplitude equation for Case III - Scenario 1.	210
Figure D-5: The case of two positive zeros of (D.2)	211
Figure D-6: Schematic plot of amplitude equation for Case III - Scenario 3.....	211
Figure D-7: First example, $\mu_3 = 0$, $c = 10^{-4}$. Left - variation of the coefficient of friction with velocity; Right - variation of steady-state vibration amplitude with input angular velocity	214
Figure D-8: Second example, $\mu_2 = 0.1$, $\mu_3 = -5 \times 10^{-4}$. Left - variation of the coefficient of friction with velocity; Right - variation of steady-state vibration amplitude with input angular velocity	214

Figure D-9: Third example, $\mu_2 = 0.1$, $\mu_3 = 5 \times 10^{-4}$. Left - variation of the coefficient of friction with velocity; Right - variation of steady-state vibration amplitude with input angular velocity	215
Figure E-1: First, second, and third order averaging results. (a) Numerical averaging results; gray solid: nonlinear system equation; dotted black: first order averaging; dashed-dot: second order averaging; solid black: third order averaging, (b) black: measurements; gray: simulation results	224
Figure H-1: Averaged amplitude of vibration, y_1 (rad), as lead screw support damping, c , and contact damping c_c are varied	237
Figure H-2: Bifurcation of Poincare sections. a) Along the horizontal dashed line in Figure H-1 b) Along the vertical dashed line in Figure H-1.	238
Figure H-3: Effect of contact stiffness (a) Two-sided Poincare bifurcation diagram, (b) Real part of the eigenvalues	239
Figure H-4: (a) Black lines: Evolution of peak lead screw vibration frequencies, dashed grey lines: eigenfrequencies; (b) Frequency content of steady-state lead screw vibration at $k_c=4 \times 10^5$	240
Figure H-5: Effect of contact stiffness (a) Two-sided Poincare bifurcation diagram, (b) Real part of the eigenvalues	241
Figure H-6: (a) Black lines: Evolution of peak lead screw vibration frequencies, dashed grey lines: eigenfrequencies; (b) Frequency content of steady-state lead screw vibration at $k_c=9 \times 10^5$	241
Figure H-7: Effect of coupling stiffness (a) Two-sided Poincare bifurcation diagram, (b) Real part of the eigenvalues	242
Figure H-8: (a) Black lines: Evolution of peak lead screw vibration frequencies, dashed grey lines: eigenfrequencies; (b) Frequency content of steady-state lead screw vibration at $k=4$	243
Figure H-9: Effect of coupling stiffness (a) Two-sided Poincare bifurcation diagram, (b) Real part of the eigenvalues	244
Figure H-10: Black lines: Evolution of peak lead screw vibration frequencies, dotted grey lines: eigenfrequencies	244
Figure H-11: Simulation results for lead screw at $k=4$; (a) Vibration frequency content, (b) y_1 - y_2 projection of the trajectories, (c) Poincare section	245
Figure H-12: Simulation results for lead screw at $k=7$; (a) Vibration frequency content, (b) y_1 - y_2 projection of the trajectories, (c) Poincare section	245
Figure H-13: Simulation results for lead screw at $k=1$; (a) Vibration frequency content, (b) y_1 - y_2 projection of the trajectories, (c) Poincare section	246

List of Tables

Table 4-1: Known or assumed system parameter values	50
Table 4-2: Identified parameters	51
Table 4-3: Numerical values of the identified parameters	53
Table 5-1: Parameter values used in the simulations	70
Table 5-2: Parameter values used in the simulations	80
Table 6-1: Parameter values used in the simulations	89
Table 6-2: Elements of the Jacobian matrix for the 3-DOF model	126
Table 7-1: Parameter values used in the simulations	136
Table 7-2: Controller parameters for example #1	172
Table 7-3: Controller parameters for example #3	177
Table 7-4: Controller parameters for example #4	178
Table 7-5: Controller parameters for example #5	181
Table A-1: Partial list of components of the lead screw test setup.....	195
Table C-1: Parameter values used in the simulations.....	213
Table E-1: Parameter values used in the higher order averaging example.....	223

Chapter 1

Introduction

Lead screws are used in various motion delivery systems where power is transmitted by converting rotary to linear motion. Packaging industries, industrial automation, manufacturing, medical devices, and automotive applications are some of the areas where lead screws can be found. Lead screws come in many different shapes and sizes; they may be large enough to support and move a 140-ton theatre stage [1], lightweight enough to be considered for wearable robotic applications [2], or even small enough to derive micro-pumps used in medical applications for dispensing fluid volumes of less than 1ml with great precision [3].

The sliding nature of contact in lead screws puts great importance on the role of friction on the performance of these systems. In addition to efficiency concerns, driving torque requirements, or wear, friction can be the cause of dynamic instabilities in the lead screw drives, resulting in self-excited vibrations which deteriorates the performance of the system and may cause unacceptable levels of audible noise.

In Section 1.1, an overview of the lead screw features and design aspects is presented. Application areas, benefits, and drawbacks of lead screws are discussed in this section. Two real-world examples, where the lead screw drive generates unacceptable levels of audible noise due to friction-induced vibrations, are presented in Section 1.2. The present research is motivated by these two examples.

1.1 Lead Screws

A very interesting historical account of the development of screws from *Archimedes'* water snail to the works of *Leonardo da Vinci* and up to the twentieth century is given in [4]. In this reference, geometrical specifications of “translating screws” – as opposed to fastening screws – are presented. In applications where transmitting power (rather than positioning) is of primary importance, translating lead screws are also known as “power screws” [5,6]. When used in vertical applications, these

systems are sometimes called “screw jacks” [1].

Set forth by the general conditions under which lead screws are traditionally used, the mechanics of the lead screws is limited to the factors affecting their static or quasi-static performance, such as efficiency, driving torque requirements, and load capacity [4-6]. There are, however, numerous other important aspects involved in the successful design of a lead screw drive system. Some of these issues are summarized in Figure 1-1. It is important to mention that, to some degree, almost all of these issues influence the other aspects of the lead screw design.

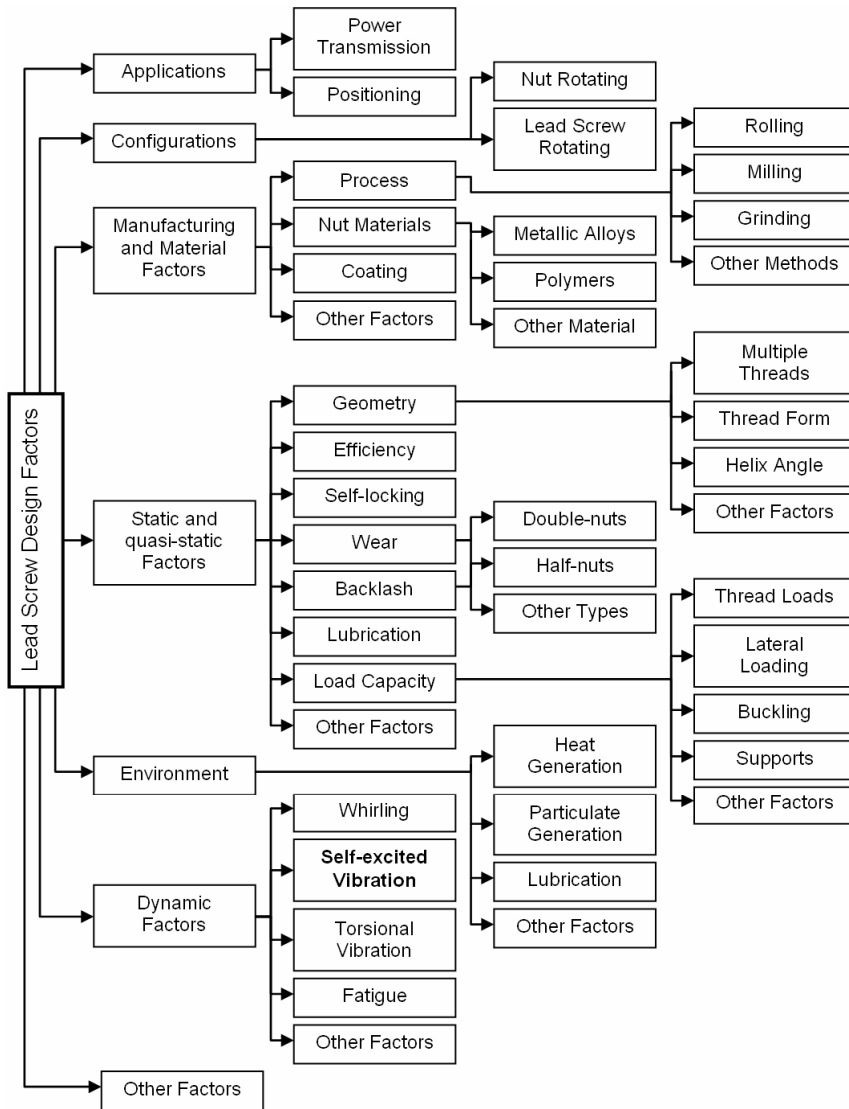


Figure 1-1: Lead screw design factors

Starting from the applications of the lead screws, there are two general areas: applications where transmission of power is of primary importance, and applications where accurate positioning of the translating part is the prime objective. The former is the focus of this research. In either application area, the conversion of rotary to linear motion can be achieved by either rotating the lead screw or rotating the nut. The two examples presented in the next section demonstrate each of these two configurations.

There are a number of thread geometries available for lead screws that are designed to address various requirements such as ease of manufacturing, load carrying capacity, and the quality of fit [4]. The most popular of these geometries are the Acme and stub-Acme types¹. See Figure 1-2 for the schematic view of a meshing stub-Acme lead screw and nut.

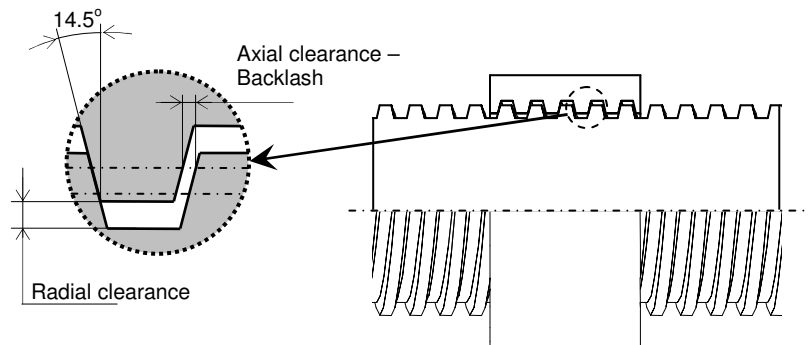


Figure 1-2: Meshing “Stub Acme” lead screw and nut (cut view). Detail: radial and axial clearances

Manufacturers offer a wide range of products in response to diverse applications where lead screws are utilized. For positioning stages, high precision ground lead screws with or without anti-backlash nuts are offered as an alternative to the more costly but much more efficient ballscrew driven stages [7,8]. There are various designs developed by the manufacturers for the anti-backlash nut. These nuts essentially have two halves connected with preloaded springs that move with respect to one another to compensate for backlash and wear [7,9-11,16]. The drawback of using these nuts is in the increased friction force, which lowers the efficiency and increases the required driving torque.

In addition to their lower cost compared to ballscrews, there are a number of distinct features that make a lead screw drive the favorable choice in many applications. These features include [13-15]:

- Quieter operation due to the absence of re-circulating balls used in ballscrews,

¹ The features of this design are further discussed in Section 3.1

- Smaller moving mass and smaller packaging,
- Availability of high helix angles resulting in very fast leads,
- Availability of very fine threads for high resolution applications,
- Possibility of self-locking to prevent the drive from being backdrivable thus eliminating the need for a separate brake system,
- Lower average particulate generation over the life of the system,
- Elimination of the need for periodic lubrication with the use of self-lubricating polymer nuts, and
- Possibility to work in washed-down environments.

Design factors given in Figure 1-1 are discussed by the manufacturers as part of their public technical information or product selection guidelines (see for example [9-12,16,17]). There is, however, a major exception: friction-induced vibration. This important factor – the subject of this research – has been barely touched by the scientific community, as will be discussed in Chapter 2.

1.2 The Audible Noise Problem

This research was motivated by two real-world examples where lead screws are used to convert rotary motion into translation. In both of these examples, the system produces unacceptable levels of audible noise under normal operating conditions.

The first example involves the horizontal motion drive of an automotive powered seat adjuster. The complete automotive powered seat adjuster is shown in Figure 1-3. The horizontal drive is constructed of two parallel lead screw slider systems. Torque is transmitted from a DC motor to the lead screws through two worm gearboxes. Two flexible couplings connect the gearboxes to the motor and to the two lead screws. The nuts are stationary and are connected to the seat frame. The lead screw sliders together with the motor and gearboxes move with the seat as lead screws advance in the nuts. In many cases, an extra force applied (by the passenger) in the direction of motion causes the system to generate audible noise, which is unacceptable to the car manufacturer.

In laboratory tests, under certain load and travel speed conditions, the seat adjuster produced a significant audible noise with the dominant frequency of around 150Hz. A sample of these test results is shown in Figure 1-4. This system is studied in detail in Chapter 4.

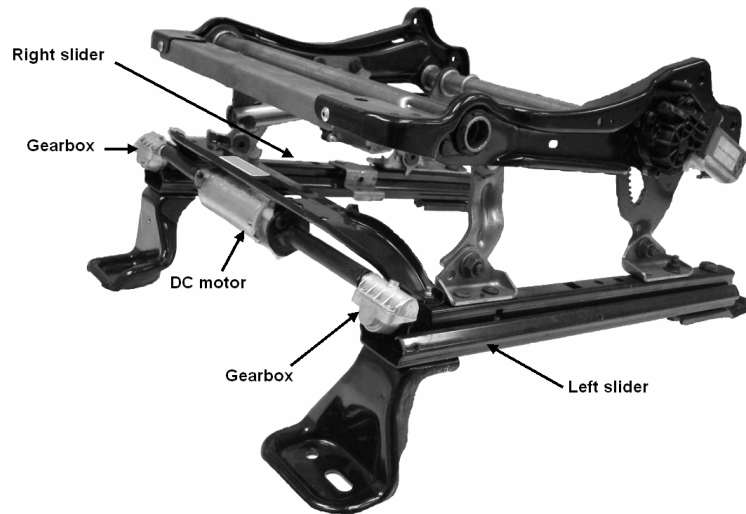


Figure 1-3: A powered seat adjuster

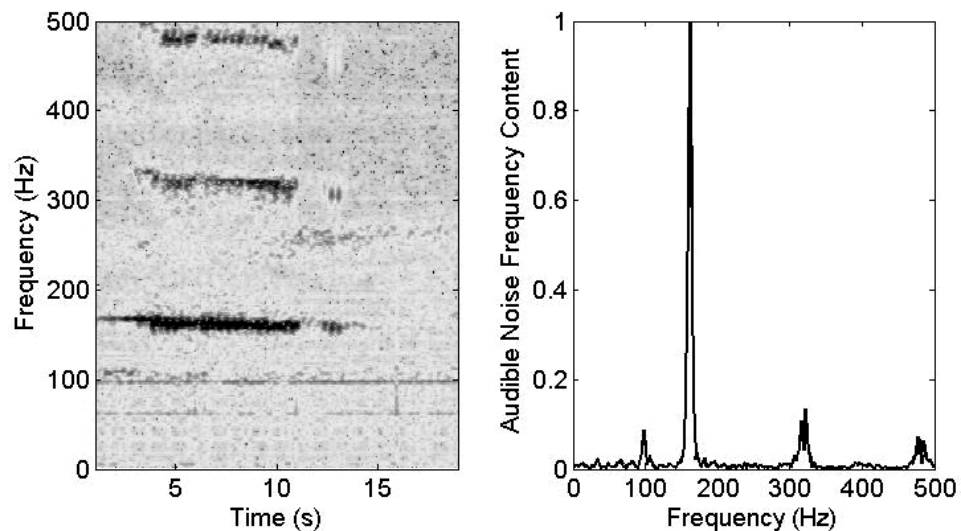


Figure 1-4: Time-frequency signature of the sound recorded from the powered seat adjuster

The second example is a micro-pump for medical applications. The lead screw drive components are shown in Figure 1-5. A stepper motor rotates the nut, which is integrated into the rotor. The rotary motion is converted by the lead screw to translation, which drives the piston. By moving the piston back and forth, the pump aspirates and then dispenses predetermined volumes of fluid. Figure 1-6 shows results of a test performed on the pump when the fluid lines were not connected. It is interesting to see that the pump generated noise with different frequency contents in aspirate and dispense phases. Similar to the case of the powered seat adjuster, preliminary observations suggest

that the source of vibration is the friction-induced vibration of the lead screw drive. Further experimental and theoretical study of this system, however, is not undertaken in this research.

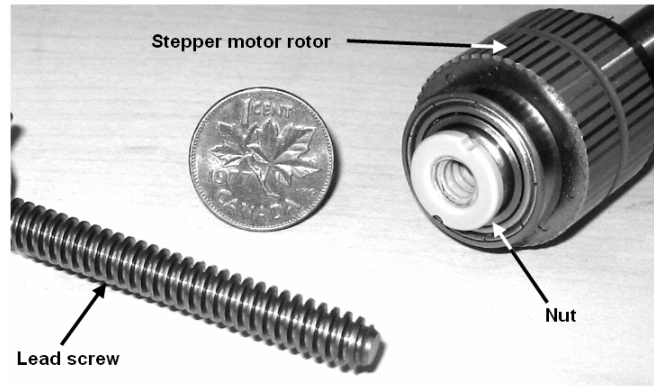


Figure 1-5: Components of the lead screw drive mechanism found in a type of variable volume pump

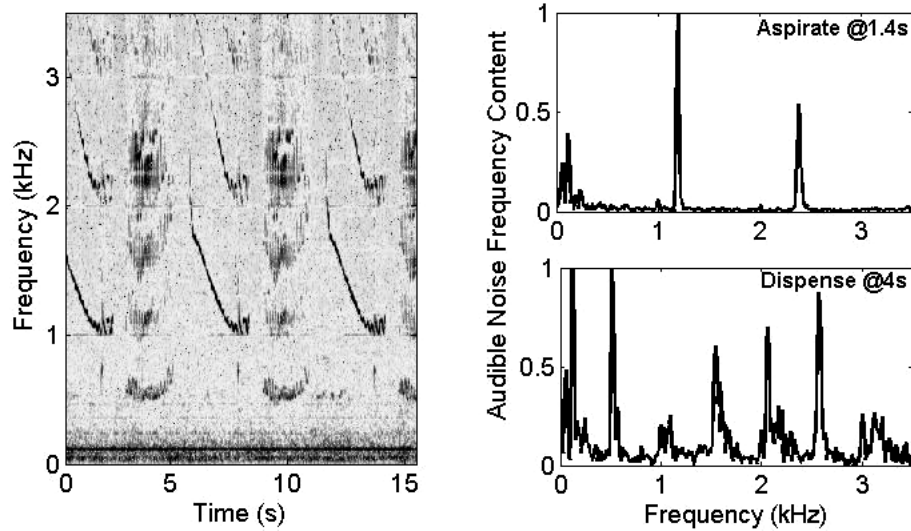


Figure 1-6: Time-frequency signature of the sound recorded from the pump

1.3 Thesis Overview

This thesis consists of eight chapters and nine appendices. After the present introductory chapter, a review of the relevant previous work is presented, in Chapter 2. This review is divided into two parts. In the first part, Section 2.1, the general subject of friction-induced vibration in dynamical systems is

reviewed and the three major instability mechanisms relevant to the lead screw systems are studied. In the second part, Section 2.2, publications on the lead screw dynamics are reviewed.

The mathematical models of lead screw systems used in this study are developed in Chapter 3. These models cover a wide range of configurations. In Chapter 4, an experimental case study is presented. In this study, a horizontal drive of an automotive powered seat adjuster is considered. A two-step system and friction parameters identification approach is developed and applied to the experimental data. The identified parameters are used in a mathematical model of the system to perform parameter studies through numerical simulations.

The friction-induced instability caused by the negative slope in the friction-velocity curve is the subject of Chapter 5. In Section 5.1, eigenvalue analysis is performed on a one degree-of-freedom (DOF) lead screw model to establish conditions for the negative damping instability mechanism to occur. The method of averaging is used in Section 5.2 to further study the system's behavior. In this analysis, a more complete picture of the system stability properties is obtained.

The kinematic constraint and mode coupling instability mechanisms are studied in detail in Chapter 6. In Section 6.1, the parametric conditions for instability due to kinematic constraint mechanism for a 1-DOF model are derived. Using the eigenvalue analysis of the linearized systems, stability conditions for the steady-sliding fixed point are derived for two different 2-DOF models in Section 6.1 and 6.2. These sections cover both kinematic constraint and mode coupling instability mechanisms. Mode coupling instability in a 3-DOF system model is briefly discussed in Section 6.3.

Chapter 7 discusses ways to actively attenuate vibration in lead screw drives caused by the negative damping instability mechanism. In Section 7.1, a robust sliding mode controller is developed for a 1-DOF simplified system model that assumes all of the rotating parts (from driver, *i.e.* motor, to lead screw) are all rigidly connected. This assumption is relaxed in Section 7.2 and another sliding mode controller is developed to regulate lead screw angular velocity in the face of uncertainty in friction and other system parameters. In the proof of stability of this novel controller, the first order averaging method is used extensively.

Conclusions drawn in this thesis are summarized in Chapter 8. Also in that chapter, areas for future research are identified and presented.

For the sake of the continuity of the main results, some additional materials and contributions are relegated to the appendices. In Appendix A, details of the test setups used in the study of the powered seat adjuster (discussed in this chapter and Chapter 4) are presented. A modified first order averaging theorem which is used in Chapters 5 and 7 is stated and proven in Appendix B. In Appendix C, steps

taken to evaluate a definite integral encountered in the first order averaged equations are presented. The existence and the stability of the steady-state solutions of the first order averaged equation of 1-DOF lead screw drive (Chapter 5), are discussed in Appendix D.

Two extensions of the first order averaging results of Chapter 5 are given in Appendices E and F. In Appendix E, general expressions for the second and third order averaging methods are presented. Also in this appendix, a numerical example is presented to demonstrate the improved accuracy of the higher order averaged equations compared to the first order averaged equation in the prediction of the amplitude of steady-state vibrations. In appendix F, the first order averaging method is applied to the equations of motion of a 2-DOF lead screw system to study the effects of the negative damping instability mechanism.

The kinematic constraint and mode coupling instability mechanisms are explored further in Appendices G and H. In Appendix G, the conditions for the local stability of the steady-sliding fixed points of two different 2-DOF lead screw models are compared and important similarities and differences are pointed out. In Appendix H, several numerical simulation results of a 2-DOF lead screw model are presented and the effects of various system parameters on the nonlinear behavior of the system and the mode coupling instability mechanism are discussed.

Finally, in Appendix I, theorems cited in the proof of stability of the second sliding mode controller developed in Chapter 7 (Section 7.4) are included for reference.

1.4 Contributions

The current research was motivated by real-world problems and was aimed to present a comprehensive study covering the field of friction-induced vibration in lead screw drives. The significance of this work is further emphasized by the noticeable lack of previous studies on the dynamic behavior of lead screw drives that adequately account for the friction-induced instability mechanisms. The major contributions of this work can be summarized as follows:

- **Mathematical models:** The mathematical models developed in Chapter 3 present a unified framework for the study of lead screw dynamics taking into account rotation/translation and loading directions as well as important system elements.
- **Friction parameter identification:** A novel two-step identification approach is developed that is capable of identifying friction as well as damping and stiffness parameters. The presented experimental results confirm the applicability of the developed method as well as the utility of the mathematical models in accurately predicting the vibratory behavior of the

lead screw drive systems.

- Friction-induced instability mechanisms: Parametric conditions for the three types of friction-induced instability mechanisms (*i.e.* negative damping, mode coupling, and kinematic constraint) are established in a unified framework.
- Comprehensive study of the negative damping friction-induced instability mechanism utilizing the averaging method: In addition to presenting a complete picture of the stability properties of the nonlinear system, the obtained results highlight the possibility of using the perturbation technique (specially, higher order averaging) as an accurate and efficient method to predict the steady-state amplitude of vibration in parameter studies.
- Comprehensive treatment of the kinematic constraint instability mechanism in lead screw drives: The possibility of friction-induced instability due to kinematic constraint is studied in detail for 1-DOF and 2-DOF models. Exclusive to Multi-DOF models, a secondary kinematic constraint mechanism is identified and its role on the expansion of the unstable domain in the space of system parameters is explored.
- Comprehensive treatment of the mode coupling instability mechanism in lead screw drives: The mode coupling instability, as one of the major mechanisms of friction-induced vibration in lead screw systems, is studied and parametric stability conditions are derived.
- Active vibration control: Two robust sliding mode controllers that effectively regulate the lead screw drive velocity in the face of parameters uncertainty, are developed.

Chapter 2

Literature Review

In this chapter, the major previous works published on the friction-induced vibration of the dynamical systems including lead screws are reviewed. The friction-induced instability mechanisms are reviewed in Section 2.1. Literature on the effects of friction on lead screw systems are reviewed in Section 2.2.

2.1 Friction-induced Vibration

A historical review of structural and mechanical systems with friction is given by Feeny *et al.* [18]. Their paper starts from the first human experiences in fire-making and early inventions of the ancient cultures to the early works of *Leonardo da Vinci*, and expands to the modern-day scientific advances in friction utilization and prevention.

An essential part of any study on the behavior of a dynamical system with friction is to appropriately account for the friction effect using a sufficiently accurate friction model. There are numerous works found in the literature on the various friction models for simulation and analysis of dynamical systems. In one of the first survey papers on friction modeling by Armstrong-Helouvry *et al.* [19], various friction models are studied. These models can be divided into the following two categories:

- Models that are based on the micro-mechanical interaction between rough surfaces and aim to explain the friction force.
- Models that incorporate various time or system dependent parameters to reproduce the effect of friction in a dynamical system.

The latter category is the subject of numerous works as can be seen in review papers by Ibrahim [20], Awrejcewicz and Olejnik [21], and Berger [22]. As reported in these works, friction can be considered dependent on any of the following factors: relative sliding velocity, acceleration, friction

memory, pre-slip displacement, normal load, dwell time, temperature, etc.

The friction models used in the dynamic modeling of systems can be further divided into *static* models and *dynamic* models. In the dynamic friction models such as the so-called LuGre model [23], the friction force is dependent on additional state variables that are governed by nonlinear differential equations stemming from the model for the average deflection of the contacting surfaces. At the price of increased complexity of the system dynamics, these models are capable of reproducing various features of friction such as velocity and acceleration dependence, pre-slip displacement, and hysteresis effect.

Depending on the specific problem being investigated, appropriate friction model should be chosen to reflect the relevant features of the physical system. The simplest approximate friction model may be given by (see for example [19,22])

$$F_f = \mu(v)N \operatorname{sgn}(v) \quad (2.1)$$

where F_f is the friction force, v is the relative sliding velocity, $\mu(v)$ is the velocity-dependent coefficient of friction, and N is the normal force pressing the two sliding surfaces together. This model is extensively used in the study of friction-induced vibration.

When some form of lubrication is present between the sliding bodies, the variations of friction with velocity is typically explained by the Stribeck curve [24]. As shown in Figure 2-1, four different regimes are identified in this model [25].

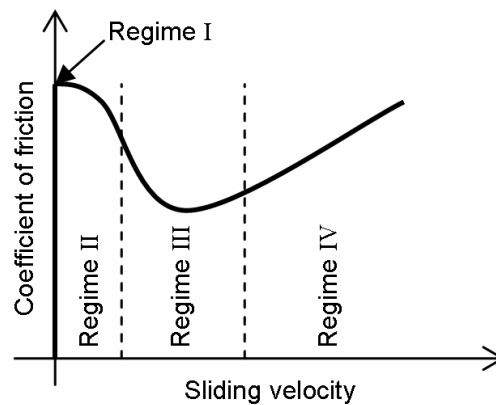


Figure 2-1: Stribeck curve [25].

The first regime is the static friction where lubricant does not prevent the contact of the asperities

of the two surfaces and friction acts similar to the no lubricant situation. In the second regime, the sliding velocity is not enough to build a fluid film between the surfaces and lubrication has insignificant effect. In the third regime with the increase of velocity, lubricant enters the load-bearing region, which results in partial lubrication. In this regime, increasing the sliding velocity decreases friction. Finally in the fourth regime, the solid-to-solid contact is eliminated and the load is fully supported by the fluid. In this regime, the friction force is the result of the shear resistance in the fluid and increases linearly with velocity.

Different models have been proposed to reproduce this type of velocity-dependent friction (see for example [26,27]). The important feature of these models is the existence of a region of negative slope in the friction-velocity curve, which may lead to self-excited vibrations. This type of instability is discussed in Section 2.1.1 below.

Wherever sliding motion exists in machines and mechanisms, friction-induced vibration may occur, and when it does, it can have severe effects on the function of the system. Excessive noise, diminished accuracy, and reduced life are some of the adverse consequences of friction-induced vibration. To this end, lead screw systems are no exception, since the lead screw threads slide against meshing nut threads as the system operates.

Numerous researchers have studied self-excited vibration phenomena in variety of frictional mechanisms [20-21,28]. Possibly the closest mechanism to a lead screw drive in terms of dynamics and friction-induced instabilities, is a disk brake. Fortunately, there are innumerable publications found in the literature that are dedicated to various aspects of disk brake noise and vibrations. Major experimental and theoretical works on the automotive disk brake squeal problem are reviewed in a paper by Kinkaid *et al.* [29]. Major self-excited vibration mechanisms in the systems with friction relevant to the lead screw drives can be categorized into three types [28-31]:

1. Decreasing friction force with relative velocity or negative damping,
2. Kinematic constraint instability,
3. Mode coupling.

2.1.1 Negative Damping

The negative slope in the friction/sliding velocity curve or the difference between static and kinematic coefficients of friction can lead to the so-called stick-slip vibrations (see for example [24,32]). In most instances, researchers adopted the well-known mass-on-a-conveyer model to study the stick-slip vibration (See for example [33,34,27]). This simple model is shown in Figure 2-2. Here, for

simplicity, the coefficient of friction is considered to decrease linearly with relative velocity.

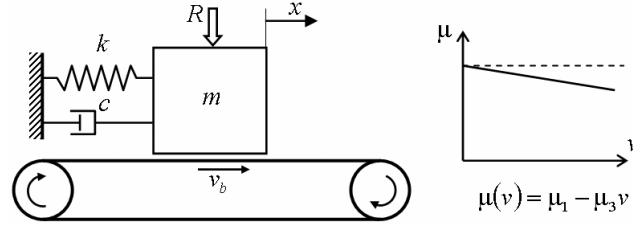


Figure 2-2: 1-DOF mass-on-a-conveyer model

The equation of motion for this model can be written as

$$m\ddot{x} + c\dot{x} + kx = N\mu(v_b - \dot{x})\text{sgn}(v_b - \dot{x}) \quad (2.2)$$

where $N > 0$ is the normal force between the mass and the conveyer and $v_b > 0$ is the conveyer's constant velocity. Transferring the steady-sliding state to the origin gives

$$m\ddot{y} + c\dot{y} + ky = N[\mu(v_b - \dot{y})\text{sgn}(v_b - \dot{y}) - \mu(v_b)] \quad (2.3)$$

where $y = x - x_0$ and $x_0 = \frac{N}{k}(\mu_1 - \mu_3 v_b)$.

Considering small perturbations around the steady-sliding fixed point where $v_b - \dot{y} > 0$, linearized equation of motion is found from (2.3) as

$$m\ddot{y} + (c - N\mu_3)\dot{y} + ky = 0 \quad (2.4)$$

It is obvious that when $c < N\mu_3$, the system (2.4) is unstable. In this situation, the vibration amplitude grows until it reaches the stick-slip boundary, *i.e.* $v_b - \dot{y} = 0$.

Using an exponentially decreasing model for the coefficient of friction, Hetzler *et al.* [34] used the method of averaging ([35]) to study the steady-state solutions of a system similar to the one shown in Figure 2-2. They showed that as damping is increased, the unstable steady-sliding fixed point goes through a subcritical Hopf-bifurcation ([36]), resulting in an unstable limit cycle that defines the region of attraction of the stable fixed point. Thomsen and Fidlin [37] also used averaging techniques to derive approximate expressions for the amplitude of stick-slip and pure-slip (when no sticking occurs) vibrations in a model similar to Figure 2-2. They used a third-order polynomial to describe

the velocity-dependent coefficient of friction.

In cases where the coefficient of friction is a nonlinear function of sliding velocity (*e.g.* humped friction model), the presence of one or more sections of negative slope in the friction-sliding velocity curve can lead to negative damping and self-excited vibration. In this type of friction instability, no sticking occurs between the two rubbing surfaces (see for example [20,38,39]).

2.1.2 Kinematic constraint instability

When friction is present, the constraint equation used to model kinematic pairs in dynamical systems can lead to instabilities even when the coefficient of friction is assumed to be constant (see for example [28] and references therein). In the context of constrained multi-body system dynamics with friction, the same mechanism is the cause of “jamming” or “wedging” [40]. In the study of disc brake systems, this type of instability is sometimes referred to as “sprag-slip” vibration (see for example [29] and references therein). This type of instability is usually characterized by violation of the solution existence or uniqueness conditions of the system’s equations of motion [41].

The simplest example to demonstrate the kinematic instability is shown in Figure 2-3 [29]. In the model shown, a massless rigid rod pivoted at point O is contacting a rigid moving plane. A force L is pressing the free end of the rod against the moving plane. The normal and friction force applied to the rod are given by N and $F_f = \mu_k N$ where μ_k is the constant kinetic coefficient of friction. It can be shown that at equilibrium

$$N = \frac{L}{1 - \mu_k \tan \theta} \quad (2.5)$$

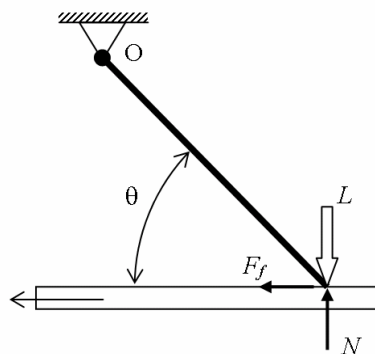


Figure 2-3: Simple model to demonstrate kinematic constraint instability [29].

From (2.5) it is evident that if $\theta \rightarrow \tan^{-1}(1/\mu_k)$, then $N \rightarrow \infty$ and further motion becomes impossible. In a more realistic setting where some flexibility is assumed, the motion continues by deflection of the parts (see for example Hoffmann and Gaul [42]). After sufficient deformation of the contacting bodies, slippage occurs which allows the bodies to assume their original configuration and the cycle continues. This situation is known as the sprag-slip limit cycle.

2.1.3 Mode Coupling

In the context of the linear dynamical systems, the effects of non-conservative forces on stability are well understood (see for example [43]). Consider the equations of motion of a second order undamped multi-DOF linear autonomous system as¹

$$\mathbf{M}\ddot{\mathbf{q}} + (\mathbf{K} + \mathbf{S}(\eta))\mathbf{q} = \mathbf{0} \quad (2.6)$$

where \mathbf{q} is the vector of generalized coordinates, \mathbf{M} is a positive-definite symmetric inertia matrix, \mathbf{K} is the symmetric stiffness matrix, and $\mathbf{S}(\eta)$ is an asymmetric matrix originating from the non-conservative forces, and η is a parameter of interest. The natural frequencies of this system are found from the solutions of the characteristic equation given by

$$\Delta(\omega^2, \eta) = \det(\mathbf{K} + \mathbf{S}(\eta) - \omega^2\mathbf{M}) \quad (2.7)$$

Assuming the initial system ($\eta = \eta_0$) is stable, the stability may be lost by divergence or flutter as the parameter η is varied. The divergence instability boundary ($\eta = \eta_d$) is found from ([43])

$$\det(\mathbf{K} + \mathbf{S}(\eta)) = 0 \quad (2.8)$$

At this critical value, one of the roots of (2.7) vanishes. The flutter instability boundary can be found by setting

$$\frac{\partial \Delta(\omega^2, \eta)}{\partial \omega^2} = 0 \quad (2.9)$$

where Δ is given by (2.7). The flutter boundary ($\eta = \eta_f$) is characterized by the coalescence of two of the system natural frequencies. By further variation of the parameter beyond its critical value, two

¹ These systems are also known as *circulatory* systems.

roots become complex conjugate. In cases where $\mathbf{S}(\eta)$ is skew-symmetric, system (2.6) can only become unstable through flutter instability as divergence is not possible [43]. The addition of velocity-dependent forces to this system yields

$$\mathbf{M}\ddot{\mathbf{q}} + (\mathbf{C} + \mathbf{G})\dot{\mathbf{q}} + (\mathbf{K} + \mathbf{S})\mathbf{q} = \mathbf{0} \quad (2.10)$$

where \mathbf{C} is positive semi-definite matrix and $\mathbf{G} = -\mathbf{G}^T$ defines the gyroscopic forces. It has been shown that the addition of damping can have a complex effect on the stability of the system and it may even destabilize the otherwise stable system [43]. For further details on this subject, see also [44].

The role of friction as a follower force in destroying the symmetry of the stiffness matrix resulting in flutter instability was first used to explain brake squeal [29]. Ono *et al.* [45] and Mottershead and Chan [46] studied hard disk drive instability using a similar concept.

Consider the 2-DOF system shown in Figure 2-4 studied by Hoffman and Gaul [47]. This model consists of a point mass sliding on a conveyer. The mass is suspended using vertical and horizontal linear spring and dampers. An additional spring placed at 45° angle is also considered which acts as the coupling between vertical and horizontal motions. The friction force is modeled using Coulomb friction law; $F_t = \mu F_n$ where μ is the constant coefficient of friction. Also the conveyer belt is moving with constant velocity of $v_b > 0$. The downward force R is assumed large enough to ensure contact between mass and conveyer belt is not lost.

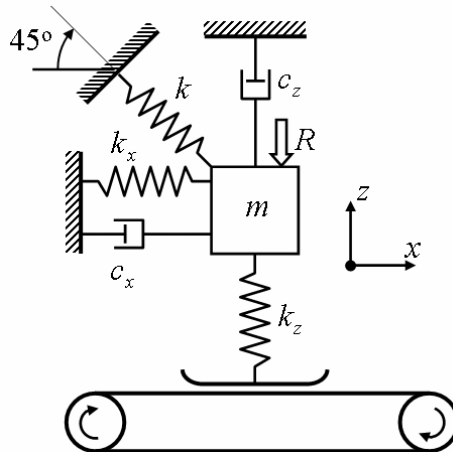


Figure 2-4: A simple 2-DOF model capable of exhibiting mode coupling instability [47].

The equation of motion for this system can be written in matrix form as

$$\begin{bmatrix} m & 0 \\ 0 & m \end{bmatrix} \begin{bmatrix} \ddot{x} \\ \ddot{z} \end{bmatrix} + \begin{bmatrix} c_x & 0 \\ 0 & c_z \end{bmatrix} \begin{bmatrix} \dot{x} \\ \dot{z} \end{bmatrix} + \begin{bmatrix} k_x + \frac{1}{2}k & -\frac{1}{2}k \\ -\frac{1}{2}k & k_z + \frac{1}{2}k \end{bmatrix} \begin{bmatrix} x \\ z \end{bmatrix} = \begin{bmatrix} -\mu k_z z \operatorname{sgn}(v_b - \dot{x}) \\ -R \end{bmatrix} \quad (2.11)$$

Shifting the equilibrium point (steady sliding state) to the origin by setting $\tilde{x} = x - x_0$ and $\tilde{z} = z - z_0$, where

$$\begin{bmatrix} x_0 \\ z_0 \end{bmatrix} = \begin{bmatrix} k_x + \frac{1}{2}k & -\frac{1}{2}k + \mu k_z \\ -\frac{1}{2}k & k_z + \frac{1}{2}k \end{bmatrix}^{-1} \begin{bmatrix} 0 \\ -R \end{bmatrix} \quad (2.12)$$

gives

$$\begin{bmatrix} m & 0 \\ 0 & m \end{bmatrix} \begin{bmatrix} \ddot{\tilde{x}} \\ \ddot{\tilde{z}} \end{bmatrix} + \begin{bmatrix} c_x & 0 \\ 0 & c_z \end{bmatrix} \begin{bmatrix} \dot{\tilde{x}} \\ \dot{\tilde{z}} \end{bmatrix} + \begin{bmatrix} k_x + \frac{1}{2}k & -\frac{1}{2}k + \mu k_z \\ -\frac{1}{2}k & k_z + \frac{1}{2}k \end{bmatrix} \begin{bmatrix} \tilde{x} \\ \tilde{z} \end{bmatrix} = \begin{bmatrix} \mu k_z (\tilde{z} + z_0) [1 - \operatorname{sgn}(v_b - \dot{\tilde{x}})] \\ 0 \end{bmatrix} \quad (2.13)$$

The symmetry-breaking role of friction is clearly shown in (2.13). Note that the right-hand-side of this equation non-zero only when $\dot{\tilde{x}} \leq -v_b$. In a small neighborhood of the origin, (2.13) simplifies to a linear homogeneous differential equation

$$\begin{bmatrix} m & 0 \\ 0 & m \end{bmatrix} \begin{bmatrix} \ddot{\tilde{x}} \\ \ddot{\tilde{z}} \end{bmatrix} + \begin{bmatrix} c_x & 0 \\ 0 & c_z \end{bmatrix} \begin{bmatrix} \dot{\tilde{x}} \\ \dot{\tilde{z}} \end{bmatrix} + \begin{bmatrix} k_x + \frac{1}{2}k & -\frac{1}{2}k + \mu k_z \\ -\frac{1}{2}k & k_z + \frac{1}{2}k \end{bmatrix} \begin{bmatrix} \tilde{x} \\ \tilde{z} \end{bmatrix} = \begin{bmatrix} 0 \\ 0 \end{bmatrix} \quad (2.14)$$

Comparing (2.14) with (2.10), it can be concluded that

$$\mathbf{M} = \begin{bmatrix} m & 0 \\ 0 & m \end{bmatrix}, \mathbf{C} = \begin{bmatrix} c_x & 0 \\ 0 & c_z \end{bmatrix}, \mathbf{G} = \mathbf{0}, \mathbf{K} = \begin{bmatrix} k_x + \frac{1}{2}k & -\frac{1}{2}k \\ -\frac{1}{2}k & k_z + \frac{1}{2}k \end{bmatrix}, \text{ and } \mathbf{S}(\mu) = \begin{bmatrix} 0 & \mu k_z \\ 0 & 0 \end{bmatrix}$$

Neglecting damping¹, from (2.9) the flutter instability threshold is calculated as

$$\mu_f = \frac{2m(k_x + k_z + k)^2 - 2k_x k_z - k_z k - k_x k}{k_z k} \quad (2.15)$$

If $\mu = \mu_f$ the two natural frequency become identical, given by

¹ For further discussions including the effects of damping and numerical examples refer to the original paper [47] and also [48].

$$\omega_1^2 = \omega_1^2 = \sqrt{\frac{k_x + k_z + k}{2}} \quad (2.16)$$

Note that (2.16) can be obtained from (2.9). Increasing the coefficient of friction beyond its flutter critical value, $\mu > \mu_f$, results in the a pair of complex conjugate squared natural frequencies, which indicates instability of the steady sliding fixed point.

Recently, a great number of papers were published on the systems exhibiting mode coupling instability due to friction and the complex effect damping on such systems. See papers by Hoffmann and his coworkers [49-51] and Jézéquel and his coworkers [52-59]. Other recent works on this subject include [60-64].

2.2 Lead Screw Drives

As mentioned earlier, when it comes to translation lead screws, very few published works are found that discuss the dynamics of these systems and the effect of friction on their vibratory behavior.

Olofsson and Ekerfors [65] investigated the friction-induced noise of screw-nut mechanisms. They discussed the tribological aspects of lubricated interaction between lead screw and nut threads, which accounts for the Stribeck friction. Based on experimental results, they have concluded that: a) the squeaking noise is the result of self-excited vibration between lead screw and nut threads; b) in the system studied (consisting of a long and slender screw), these vibrations excite bending mode shapes of the lead screw, and; c) the squeak noise is generated only when the nut is in the vicinity of one of the nodes of the bending mode shape of the lead screw.

In a study of the effect of friction on the existence and uniqueness of the solutions of the equation of motion of dynamical systems, Dupont [41] considered a 1-DOF model of a lead screw system. He investigated the situations under which no solution existed and clearly identified one of the sources of instability in the lead screw systems; *i.e.* the kinematic constraint instability mechanism. For the self-locking screws, he found that there is a certain limiting ratio between the lead screw inertia (rotating part) and the mass of the translating part, beyond which no solution exists.

Based on a case study, Gallina and Giovagnoni [1] discussed the design of screw jack mechanisms to avoid self-excited vibration. They developed a 2-DOF model of a lead screw system which included lead screw rotation (coupled with the nut translation) and lead screw axial displacement. Using eigenvalue analysis of the linearized equations, they found relationships that define the stability domain in terms of the parameters of the system. They concluded that to avoid vibration in self-

locking derives, lead screw should have low axial and high torsional stiffness. Gallina [66] further expanded this study and, using both eigenvalue analysis and experiments, showed that by increasing lead screw inertia it is possible to avoid instability under certain conditions.

Oledzki [67] studied self-locking mechanisms. He classified all types of mechanical drives, including worm gears and lead screws, with the emphasis on the possibility of self-locking. A unified notation was used to present geometrical features of the drives and to derive the equations of motion of a general kinematic pair. He also modeled the kinematic pair using elastic contacts instead of rigid contacts. The simulation results presented showed the possibility of “stick-slip” vibrations.

Generally, in high-accuracy linear positioning applications, “ball-screws” are used because of their low friction, high lead accuracy, and backlash-free operation [68]. Consequently, the majority of works in the literature regarding position control and dynamics of screw drives focus on ball-screws [69-76]. Lead screws are also used for similar positioning applications. For example, Otsuka [69] compared a high-precision lead screw drive equipped with an anti-backlash nut with two types of ball-screw drives for nanometer positioning applications. The experimental results obtained showed the possibility of achieving nanometer accuracy with all three systems. Particular to the lead screw, the nonlinear behavior of the drive due to the stick-slip phenomenon was studied. The anti-backlash nuts were found to have an adverse effect due to preloading of the threads and increased friction.

Sato, *et al.* [77] considered the dynamics of a lead screw positioning system with backlash. They set up an experiment using a sliding table, a lead screw, and a DC motor. In their experiments the table position, screw rotation angle, and DC motor current were measured. Although they did not undertake detailed modeling of lead screw and nut interaction, they were able to estimate lead screw/nut friction using a disturbance observer under the action of a linear proportional plus derivative feedback controller.

It is worth mentioning that lead screw drives were also used in redundant positioning systems for only coarse table motion [70,71]. In these systems, a high-precision parallel positioning system such as a piezo actuator is used for fine-tuning. Another example is the work by Sato, *et al.* [78], where they introduced an active lead screw mechanism. By using two nuts connected together by a piezoelectric actuator, they were able to actively control backlash to achieve position accuracy of better than 10 *nm*.

Chapter 3

Mathematical Modeling of Lead Screw Drives

In this chapter, a collection of mathematical models are developed which are used throughout this thesis to study the dynamic behavior of lead screw systems. Depending on the system elements considered and the type of analysis undertaken, different models are developed with varying number of degrees of freedom.

Figure 3-1 shows a typical lead screw drive system. A motor – possibly through a gearbox – rotates the lead screw via a coupling. The rotational motion is converted to translation at the lead screw-nut interface and transferred to the moving mass. The weight of the moving mass is supported by bearings. The lead screw is held in place by support bearings at its either end.

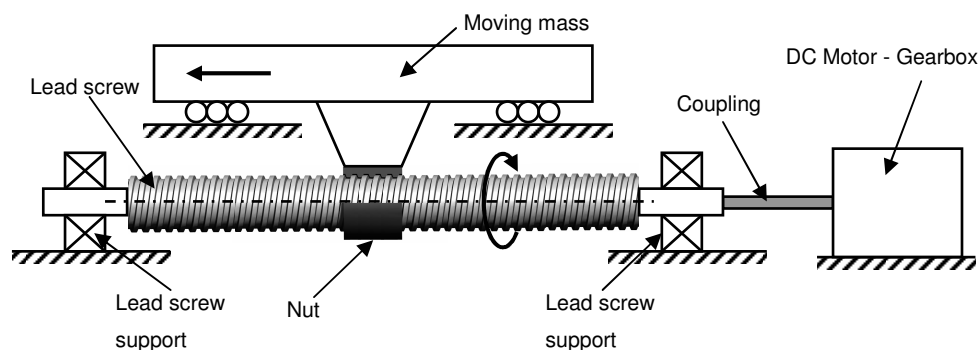


Figure 3-1: Lead screw drive system

In Section 3.1, a set of meshing lead screw and nut is considered as a kinematic pair and related kinematic and kinetic relationships are presented. The velocity-dependent friction model used in this thesis is discussed in Section 3.2. The basic 1-DOF lead screw drive model is developed in Section 3.3. This model will be used in Chapters 5 and 6 to study negative friction gradient and kinematic constraint instability mechanisms, respectively. A model of lead screw with anti-backlash nut is

presented in Section 3.4 and the role of preloaded nut on the increased friction is highlighted. Additional DOFs are introduced to the model in Sections 3.5, 3.6, and 3.7 to account for the flexibility of threads and the axial flexibility of lead screw supports. These models are used in Chapter 6 to investigate the mode coupling and kinematic constraint instability mechanisms. The 2-DOF model of Section 3.5 is also used in Chapter 4 to obtain simulation results based on the identified system parameters. By combining the DOFs of the models of Sections 3.5 and 3.6, a 3-DOF model of lead screw drives is developed in Section 3.7. This model is used in Chapter 6 to study the mode coupling instability mechanism. In Section 3.8, a complete system model is presented that includes all of the elements of a typical linear drive system. This model is used in Chapter 4 as the basis of the developed friction parameters identification method. Robust controllers are developed for simplified versions of this model in Chapter 7.

3.1 Lead Screw and Nut – A Kinematic Pair

The rotary motion is converted to linear translation at the interface of lead screw and nut threads. The kinematic relationship defining a lead screw is simply¹

$$x = r_m \tan \lambda \cdot \theta \quad (3.1)$$

where θ is the lead screw rotation, x is the nut translation, λ is the pitch angle, and r_m is the pitch circle radius.

The interaction between contacting lead screw and nut threads can be easily visualized by considering unrolled lead screw and nut threads [5]. This way, the rotation of lead screw is replaced by an equivalent translation. Assuming one thread pair to be in contact at any given instant, Figure 3-2 shows the interaction of the lead screw and nut threads for both left-handed and right-handed screws. The sign conventions used for the contact force, N , is shown in this figure. In the configurations shown, when the right-handed lead screw is rotated clockwise/moved up (rotated counterclockwise/moved down) the nut moves backward/right (forward/left). For the left-handed screw, the direction of motion of the nut is reversed. Also, when the nut threads are in contact with the leading (trailing) lead screw threads, the normal component of contact force, N , is considered to be positive (negative).

The friction force is given by

¹ By properly orienting the x -axis, this relationship applies to both left-hand and right-hand threads.

$$F_f = \mu|N|\text{sgn}(v_s) \quad (3.2)$$

where μ is the coefficient of friction¹ and v_s is the relative sliding velocity. The friction force acts tangent to the contacting thread surfaces and always opposes the direction of motion but does not change direction when normal force, N , changes direction.

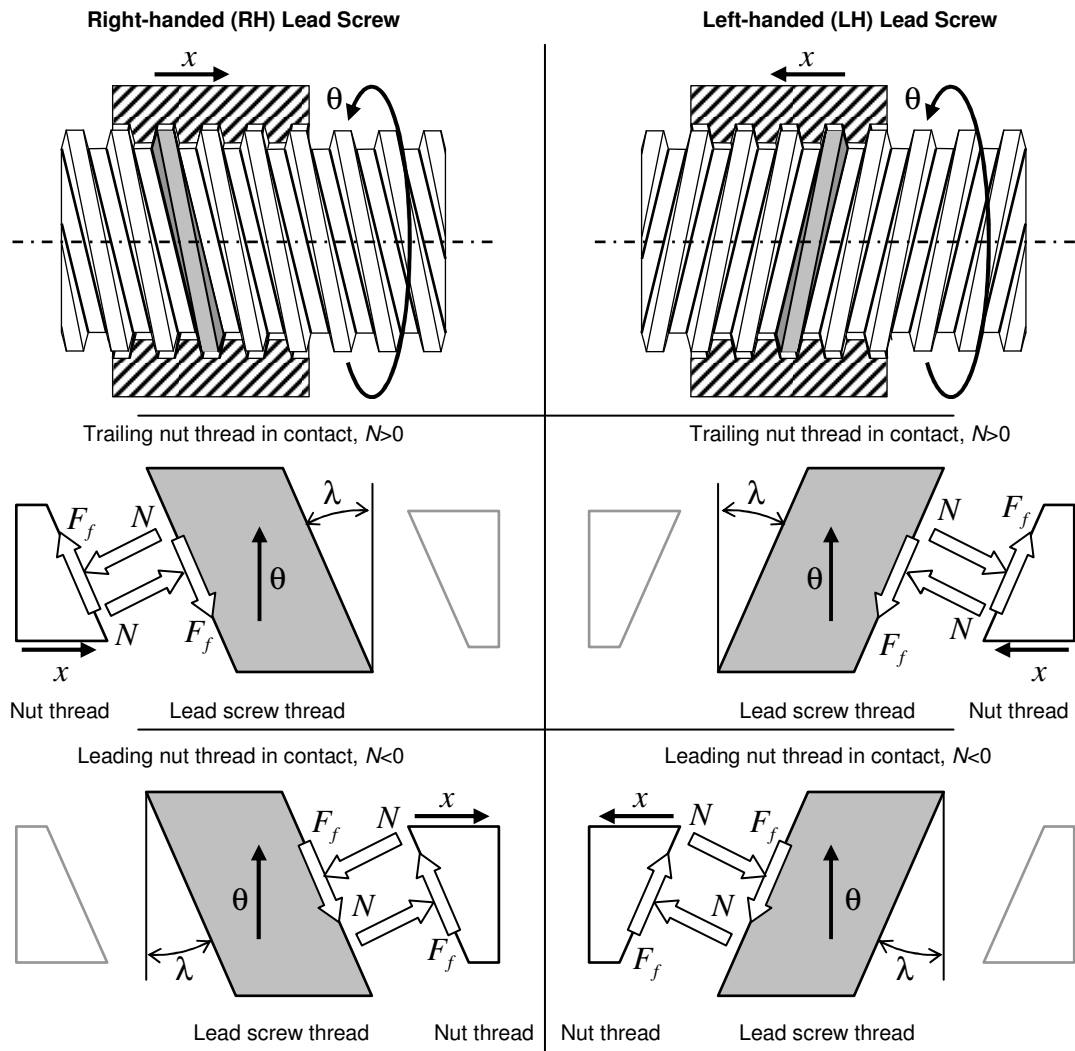


Figure 3-2: Sign convention for contact forces between nut and lead screw

Before moving on to the dynamic models of lead screw systems, the effects of thread geometry on

¹ See Section 3.2.

the contact forces are considered here. The force interaction shown in Figure 3-2 is essentially correct for the square threads where the normal force is parallel to the lead screw axis. For Acme or other types of threads, a slight modification is needed to take into account the thread angle.

Figure 3-3 shows the thread semi-angles as measured on a section through the axis of a screw, ψ_a and as measured on a section perpendicular to the helix, ψ_n . Using the geometric relationship in Figure 3-4, one can write [79]

$$\tan \psi_n = \frac{x_n}{y}, \quad \tan \psi_a = \frac{x_a}{y} \quad (3.3)$$

$$x_n = x_a \cos \lambda \quad (3.4)$$

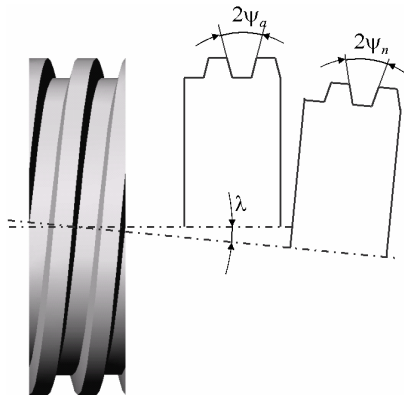


Figure 3-3: Effect of lead angle on the measurement of thread angle

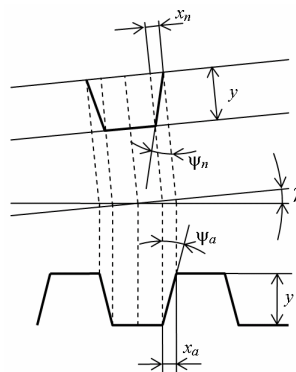


Figure 3-4: Geometry of the threads on two different section planes

Combining (3.3) and (3.4) gives

$$\tan \psi_n = \tan \psi_a \cos \lambda \quad (3.5)$$

Figure 3-5 shows a portion of the lead screw with localized contact force \hat{N} (perpendicular to the thread surface) and friction force F_f . The X-axis of XYZ coordinate system is parallel to the lead screw axis. The x-Z plane is perpendicular to the helix. The projection of contact force on the x-y (or X-Y) plane is calculated as,

$$N = \hat{N} \cos \psi_n \quad (3.6)$$

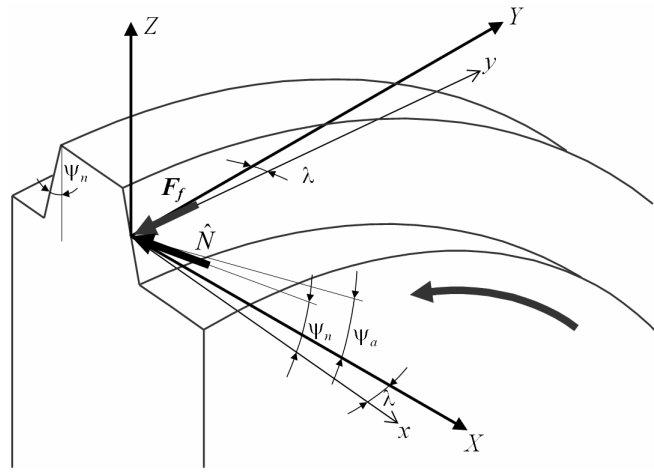


Figure 3-5: Forces acting on a thread

Since \hat{N} is the normal force, using (3.2) the friction force for trapezoid threads is calculated by $F_f = \hat{\mu} |\hat{N}| \text{sgn}(\dot{\theta})$, where $\hat{\mu}$ is the true coefficient of friction. One can define the *apparent* coefficient of friction as

$$\mu = \hat{\mu} \cos \psi_n = \mu (\tan^2 \psi_a \cos^2 \lambda + 1)^{-\frac{1}{2}} \quad (3.7)$$

Using (3.6) and (3.7), the friction force is written conveniently as $F_f = \mu |N| \text{sgn}(\dot{\theta})$, which is the same as (3.2) and will be used throughout this work.

3.2 Velocity-dependent Coefficient of Friction

The rubbing action of contacting lead screw threads against nut threads is assumed to be the main source of friction in the systems considered in this thesis. As mentioned in Chapter 2, numerous velocity-dependent coefficient of friction models can be found in the literature [19,21,22]. These models generally include the following three parts:

1. Coulomb or constant friction
2. Stribeck friction
3. Viscous or linear friction

In this work, the following model for the friction coefficient is considered¹

$$\mu = \tilde{\mu}_1 + \tilde{\mu}_2 \left(e^{-\frac{|v_s|}{v_0}} - 1 \right) + \tilde{\mu}_3 |v_s| \quad (3.8)$$

where $\tilde{\mu}_1$, $\tilde{\mu}_2$, and $\tilde{\mu}_3$ represent Coulomb, Stribeck, and viscous friction coefficients, respectively. v_s is the relative sliding velocity between contacting nut threads and lead screw threads. Also, v_0 controls the velocity range of the Stribeck effect. See Figure 3-6 for a schematic view of the velocity dependent coefficient of friction given by (3.8).

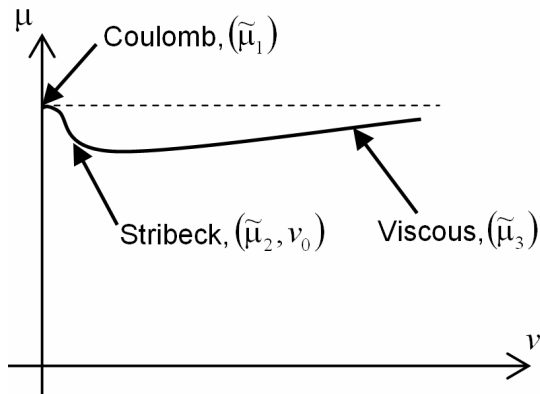


Figure 3-6: Velocity dependent coefficient of friction

The reasons for choosing this friction model are twofold. The model structure allows for the three above-mentioned components of friction to be easily separated for the purpose of focused analysis. In

¹ This model is sometimes known as the Tustin model [26].

addition, it was found that this particular formula lends itself very well to the experimental observations reported in Chapter 4.

Based on Figure 3-3, the sliding velocity can be written as

$$v_s = \frac{r_m}{\cos \lambda} \dot{\theta} \quad (3.9)$$

Substituting (3.9) into (3.8) and rearranging,

$$\mu = \mu_1 + \mu_2 e^{-r_0 |\dot{\theta}|} + \mu_3 |\dot{\theta}| \quad (3.10)$$

where $r_0 = \frac{r_m}{\cos \lambda v_0}$, $\mu_1 = \tilde{\mu}_1 - \tilde{\mu}_2$, $\mu_2 = \tilde{\mu}_2$, and $\mu_3 = \tilde{\mu}_3 \frac{r_m}{\cos \lambda}$. In the remainder of this thesis

(3.10) is used as the basic model for the velocity dependent coefficient of friction.

3.3 Basic 1-DOF Model

Figure 3-7 shows 1-DOF lead screw drive models with both right-handed (RH) and left-handed (LH) lead screws. Note that, with the chosen x -axis direction, the kinematic relationship (3.1) holds for both LH and RH lead screws. In these models, θ_i is the input rotational displacement applied to the lead screw through a flexible coupling (torsional spring k). R is the axial force applied to the nut and c is the linear damping coefficient of the lead screw supports. I and m designate inertia of the lead screw and mass of the translating part, respectively.

Based on the force diagrams shown in Figure 3-2, and irrespective of the hand of the lead screw, it can be written¹

$$I\ddot{\theta} = k(\theta_i - \theta) - c\dot{\theta} + r_m (N \sin \lambda - F_f \cos \lambda) - T_0 \operatorname{sgn}(\dot{\theta}) \quad (3.11)$$

and

$$m\ddot{x} = -N \cos \lambda - F_f \sin \lambda + R - F_0 \operatorname{sgn}(\dot{x}) \quad (3.12)$$

¹ Based on the selected conventions for the axes and forces in Figure 3-7, the equations of motion for the drives with left-handed screws are identical to those with right-handed screws. As a result, from this point on, the handedness of the lead screw is assumed to be known but is not included in the discussions.

where the terms $T_0 \operatorname{sgn}(\dot{\theta})$ and $F_0 \operatorname{sgn}(\dot{x})$ represent the friction in lead screw supports and the bearings of the translating mass, respectively.

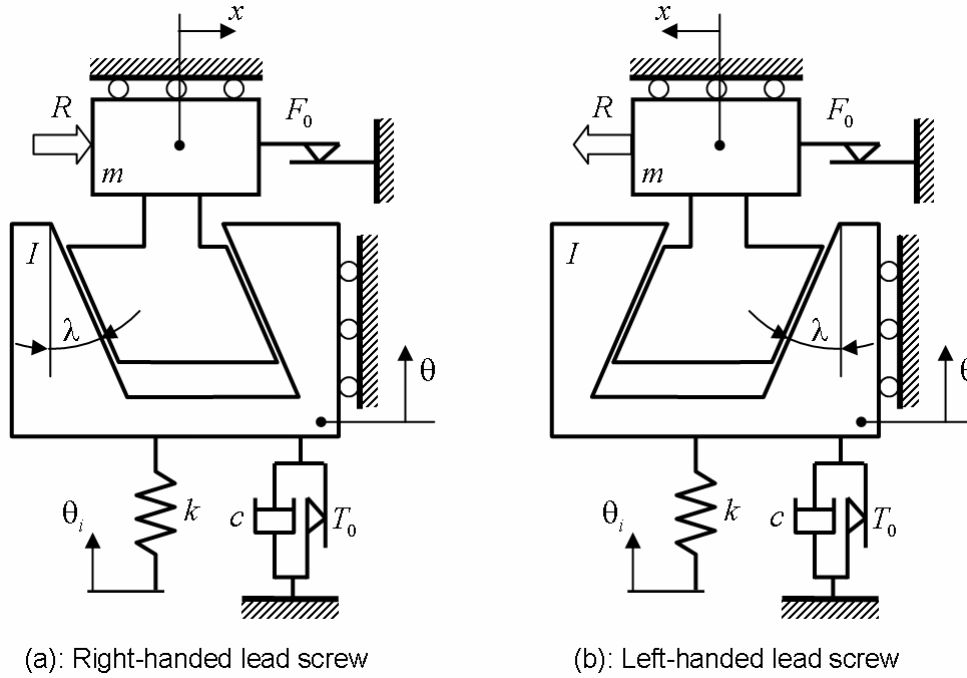


Figure 3-7: 1-DOF model of a lead screw system

Eliminating N between (3.11) and (3.12), yields

$$(I - r_m \tan \lambda \xi m) \ddot{\theta} + k\theta + c\dot{\theta} = k\theta_i - \xi(R - F_0 \operatorname{sgn}(\dot{\theta})) - T_0 \operatorname{sgn}(\dot{\theta}) \quad (3.13)$$

where (3.1) and (3.2) were used and

$$\xi = r_m \frac{\mu_s - \tan \lambda}{1 + \mu_s \tan \lambda} \quad (3.14)$$

where

$$\mu_s = \mu \operatorname{sgn}(\dot{\theta} N) \quad (3.15)$$

was used for abbreviation. The normal contact force is calculated as

$$N = \frac{(R - F_0 \operatorname{sgn}(\dot{\theta}))I + mr_m \tan \lambda [k(\theta - \theta_i) + c\dot{\theta} + T_0 \operatorname{sgn}(\dot{\theta})]}{(\cos \lambda + \mu_s \sin \lambda)(I - r_m \tan \lambda \xi m)} \quad (3.16)$$

Note that due to the appearance of $\operatorname{sgn}(N)$, through μ_s , in the denominator of (3.16), this equation can only be solved iteratively for N .

The equation of motion derived in this section can also describe other variations to the basic model. These models reflect other possible configurations that may be found in various applications. In Section 3.3.1, the inverted basic model is introduced where unlike the model of this section, nut is rotated causing the lead screw translate. A configuration with fixed nut and another with fixed lead screw are presented in Sections 3.3.2 and 3.3.3, respectively. In these two models, the rotating part also translates.

3.3.1 Inverted Basic Model

In some applications, the nut is rotated which causes the lead screw to translate¹. Figure 3-8 shows this configuration for a simple 1-DOF model. It can be shown that for this configuration, the equation of motion is identical to (3.13).

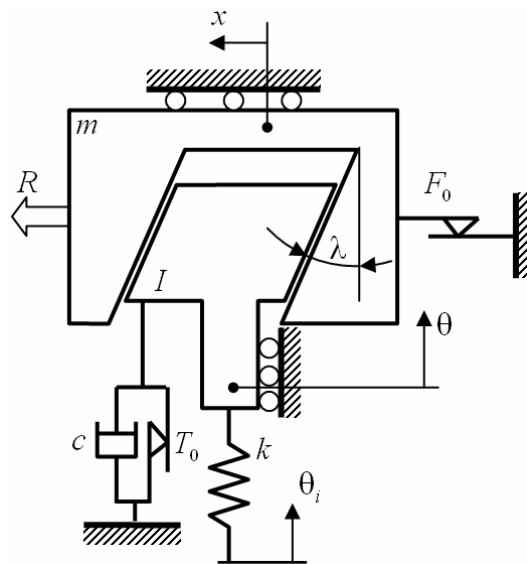


Figure 3-8: Inverted basic 1-DOF model

¹ See, for example, the micro-pump shown in Figure 1-5.

3.3.2 Basic Model with Fixed Nut

In another possible configuration, the nut may be fixed¹ and the lead screw rotation is converted to its translation together with other connected parts (*i.e.* motor, frame, payload, etc.). This configuration is shown in Figure 3-9. As mentioned before, the equation of motion of this system is also given by (3.13).

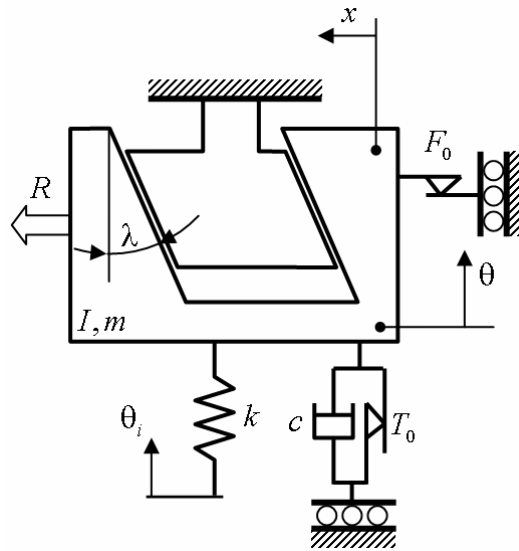


Figure 3-9: Basic 1-DOF model with fixed nut

3.3.3 Basic Model with Fixed Lead Screw

The last variation of the basic lead screw drive model considered here is shown in Figure 3-10. In this configuration, the lead screw is fixed in place and the nut rotates, causing it to translate along the lead screw together with other moving parts (*i.e.* motor, gearbox, payload, etc.). The equation of motion of this system is also given by (3.13).

¹ See, for example, the powered seat adjuster in Figure 1-3.

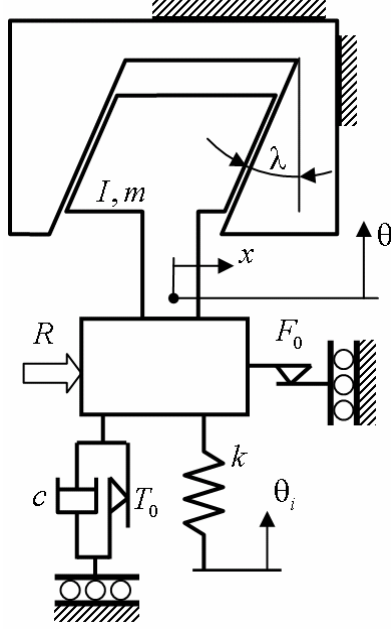


Figure 3-10: Basic 1-DOF model with fixed lead screw

3.4 Anti-backlash Nut

As mentioned in Chapter 1, anti-backlash nuts are commonly used to counter the effects of backlash and wear in a lead screw drive. An anti-backlash nut is usually made of two parts that are connected together through a preloaded spring. Figure 3-11 shows a schematic model of a lead screw drive with a two-part nut. The spring k_n is preloaded such that a force $P = k_n \delta_n$ acts between the two halves of the nut and where δ_n is the initial compression of the spring. Neglecting the mass of the nut, the Newton's second law gives

$$I\ddot{\theta} = k(\theta_i - \theta) - c\dot{\theta} + r_m (N_1 \sin \lambda - \mu \operatorname{sgn}(\dot{\theta}) N_1 \cos \lambda) + r_m (-N_2 \sin \lambda - \mu \operatorname{sgn}(\dot{\theta}) N_2 \cos \lambda) - T_0 \operatorname{sgn}(\dot{\theta}) \quad (3.17)$$

$$m\ddot{x} = -N_1 \cos \lambda - \mu \operatorname{sgn}(\dot{\theta}) N_1 \sin \lambda + R - F_0 \operatorname{sgn}(\dot{x}) + P \quad (3.18)$$

where

$$P = N_2 \cos \lambda - \mu \operatorname{sgn}(\dot{\theta}) N_2 \sin \lambda \quad (3.19)$$

where $N_1 > 0$ and $N_2 > 0$ are the thread contact forces corresponding to left and right parts of the nut, respectively. Combining (3.17), (3.18), and (3.19) and using (3.1), gives

$$(I - r_m \tan \lambda \xi_1 m) \ddot{\theta} + k\theta + c\dot{\theta} = k\theta_i - \xi_1 (R - F_0 \operatorname{sgn}(\dot{\theta})) - T_0 \operatorname{sgn}(\dot{\theta}) - (\xi_1 + \xi_2)P \quad (3.20)$$

where

$$\begin{aligned} \xi_1 &= r_m \frac{\mu \operatorname{sgn}(\dot{\theta}) - \tan \lambda}{1 + \mu \operatorname{sgn}(\dot{\theta}) \tan \lambda} \\ \xi_2 &= r_m \frac{\mu \operatorname{sgn}(\dot{\theta}) + \tan \lambda}{1 - \mu \operatorname{sgn}(\dot{\theta}) \tan \lambda} \end{aligned} \quad (3.21)$$

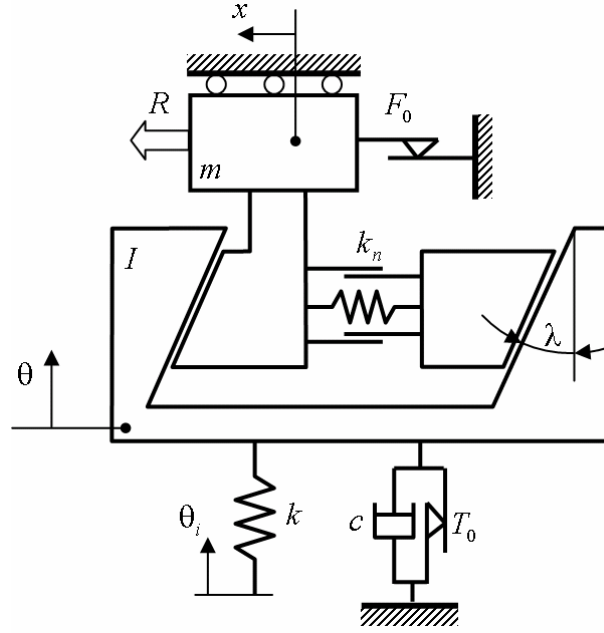


Figure 3-11: Lead screw model with anti-backlash nut

Compared with (3.13), $-(\xi_1 + \xi_2)P$ term is the additional resistive torque caused by the preloaded nut. The contact force N_1 (for left threads in Figure 3-11) is found as

$$N_1 = \frac{(R - F_0 \operatorname{sgn}(\dot{\theta}))I + mr_m \tan \lambda [k(\theta - \theta_i) + c\dot{\theta} + T_0 \operatorname{sgn}(\dot{\theta})] + (I + r_m \tan \lambda \xi_1 m)P}{(\cos \lambda + \mu \operatorname{sgn}(\dot{\theta}) \sin \lambda)(I - r_m \tan \lambda \xi_1 m)} \quad (3.22)$$

where, again, compared with (3.16), the contact force is increased due to the preload P .

Note that the above simplified formulation is valid as long as $N_1 > 0$. If this condition is violated, (*i.e.* the left contact is broken) for the duration of such motion, the number of DOFs is increased to

two. In such cases, which may be caused by large $-R > 0$, the dynamics of the system is more complicated since the impact of the threads and repeated loss of contact should be considered.

3.5 Compliance in Lead Screw and Nut Threads

In Section 3.3, the lead screw and nut were modeled as a kinematic pair leading to an iterative equation for determining the sign of the contact force. The analysis may be greatly simplified by assuming some degree of compliance in the lead screw and/or nut threads¹. Figure 3-12 shows the same system as in Figure 3-7(b) except for the contact between threads which is now modeled by springs and dampers. With this change, the number of DOFs is increased to two.

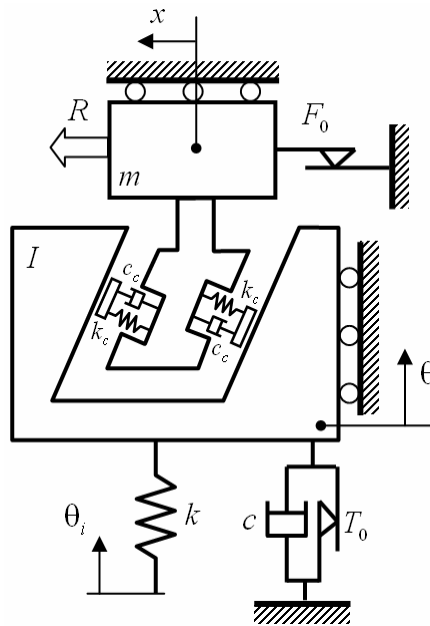


Figure 3-12: 2-DOF lead screw drive model including thread compliance

Conforming to the sign convention defined in Figure 3-2, the deflection (or interference) of threads can be calculated as

$$\delta = x \cos \lambda - r_m \theta \sin \lambda \quad (3.23)$$

The simplest way to approximate the contact force is by modeling the force/deflection relationship

¹ Refer to Section 6.1.1.

of the threads as that of linear springs and dampers. Thus

$$N = k_c \delta + c_c \dot{\delta} \quad (3.24)$$

Substituting (3.24) into (3.11) and (3.12) and using (3.23) yields¹

$$I\ddot{\theta} = k(\theta_i - \theta) - c\dot{\theta} + r_m k_c (x \cos \lambda - r_m \theta \sin \lambda)(\sin \lambda - \mu_s \cos \lambda) + r_m c_c (\dot{x} \cos \lambda - r_m \dot{\theta} \sin \lambda)(\sin \lambda - \mu_s \cos \lambda) - T_0 \operatorname{sgn}(\dot{\theta}) \quad (3.25)$$

$$m\ddot{x} = -k_c (x \cos \lambda - r_m \theta \sin \lambda)(\cos \lambda + \mu_s \sin \lambda) - c_c (\dot{x} \cos \lambda - r_m \dot{\theta} \sin \lambda)(\cos \lambda + \mu_s \sin \lambda) + R - F_0 \operatorname{sgn}(\dot{x}) \quad (3.26)$$

where μ_s is defined by (3.15).

3.6 Axial Compliance in Lead Screw Supports

Another important source of flexibility in the system may be the compliance in the lead screw supports. To model this feature, as shown in Figure 3-13, spring k_1 and damping c_1 are added to the basic model of Section 3.3, which allows the lead screw to move axially.

Similar to Section 3.3, (3.11) and (3.12) give force/acceleration relationships for lead screw rotation and nut translation, respectively. Moreover, the lead screw translation DOF is governed by

$$m_1 \ddot{x}_1 = -k_1 x_1 - c_1 \dot{x}_1 + N \cos \lambda + F_f \sin \lambda \quad (3.27)$$

The kinematic relationship between θ , x , and x_1 is given as

$$x - x_1 = r_m \tan \lambda \theta \quad (3.28)$$

Eliminating N between (3.11) and (3.12) and also between (3.12) and (3.27) and using (3.28) and (3.2) yields

$$(I - r_m \tan \lambda \xi m) \ddot{\theta} - \xi m \ddot{x}_1 = k(\theta_i - \theta) - c\dot{\theta} - \xi(R - F_0 \operatorname{sgn}(\dot{x})) - T_0 \operatorname{sgn}(\dot{\theta}) \quad (3.29)$$

¹ For the model of this section, the relative velocity given by (3.9) should be changed to $v_s = \frac{r_m}{\cos \lambda} \dot{\theta} + \dot{\delta} \tan \lambda$. However, in practical situations where the lead angle (λ) is small and threads are almost rigid the term $\dot{\delta} \tan \lambda$ is negligible and it is omitted.

$$(m_1 + m)\ddot{x}_1 + mr_m \tan \lambda \ddot{\theta} = -k_1 x_1 - c_1 \dot{x}_1 + R - F_0 \operatorname{sgn}(\dot{x}) \quad (3.30)$$

where ξ is given by (3.14).

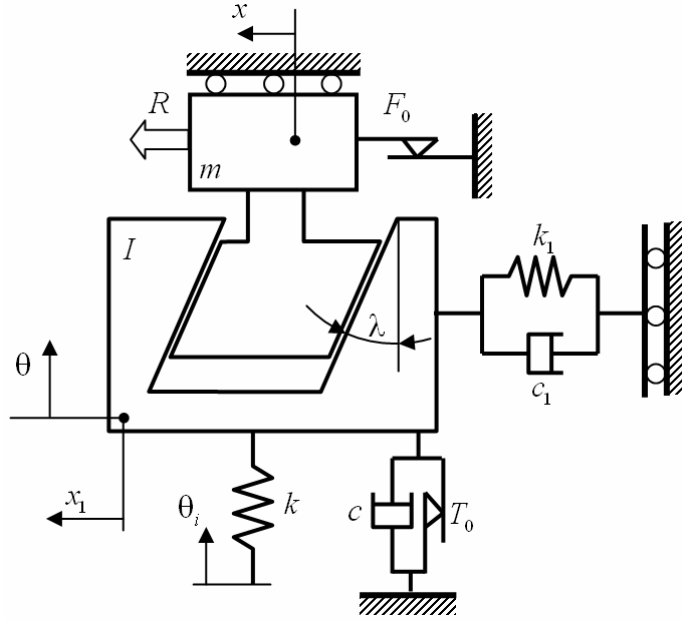


Figure 3-13: 2-DOF lead screw drive model including compliance in the supports

The normal contact force is calculated as

$$N = \frac{\frac{I}{m}(R - F_0 \operatorname{sgn}(\dot{x})) + \frac{I}{m_1} k_1 x_1 + \frac{I}{m_1} c_1 \dot{x}_1 - r_m \tan \lambda k(\theta_i - \theta) + r_m \tan \lambda (c\dot{\theta} + T_0 \operatorname{sgn}(\dot{\theta}))}{(\cos \lambda + \mu_s \sin \lambda) \left[\left(\frac{I}{m} + \frac{I}{m_1} \right) - r_m \tan \lambda \xi \right]} \quad (3.31)$$

3.7 Compliance in Threads and Lead Screw Supports

By combining the two models presented in Sections 3.5 and 3.6, a 3-DOF model of the lead screw drive results, which is shown in Figure 3-14. The equations of motion of this system are defined by (3.11), (3.12), and (3.27). The only change is in the calculation of contact force N given by (3.24); the threads deflection, instead of (3.23), is calculated by

$$\delta = (x - x_1) \cos \lambda - r_m \theta \sin \lambda \quad (3.32)$$

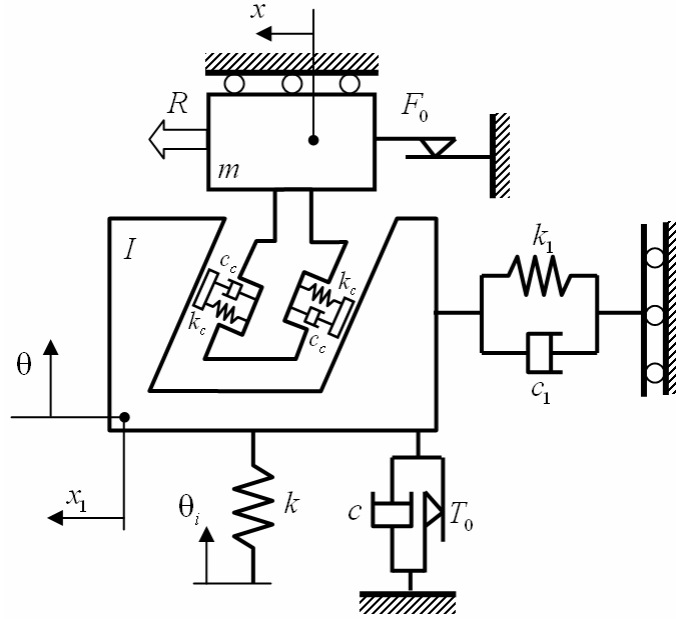


Figure 3-14: 3-DOF lead screw drive model including compliance in the supports and compliance in the lead screw and nut threads

3.8 A Complete System Model

In this section, another model is developed which includes other elements in the power transmission chain, namely a DC motor and a worm gearbox. Figure 3-15 shows the 4-DOF configuration considered.

For the motor, Newton's second law gives

$$I_M \ddot{\theta}_M = T_M - T_{fM} \operatorname{sgn} \dot{\theta}_M + k_1 (\theta_W - \theta_M) - c_M \dot{\theta}_M \quad (3.33)$$

where θ_M is the rotor's angular displacement, I_M is the inertia of the rotor, T_M is generated (input) torque, T_{fM} and c_M are the internal friction and damping of the motor, respectively. Also, k_1 is the torsional stiffness of the coupling connecting the motor to the gearbox, and θ_W designates the angular displacement of the worm.

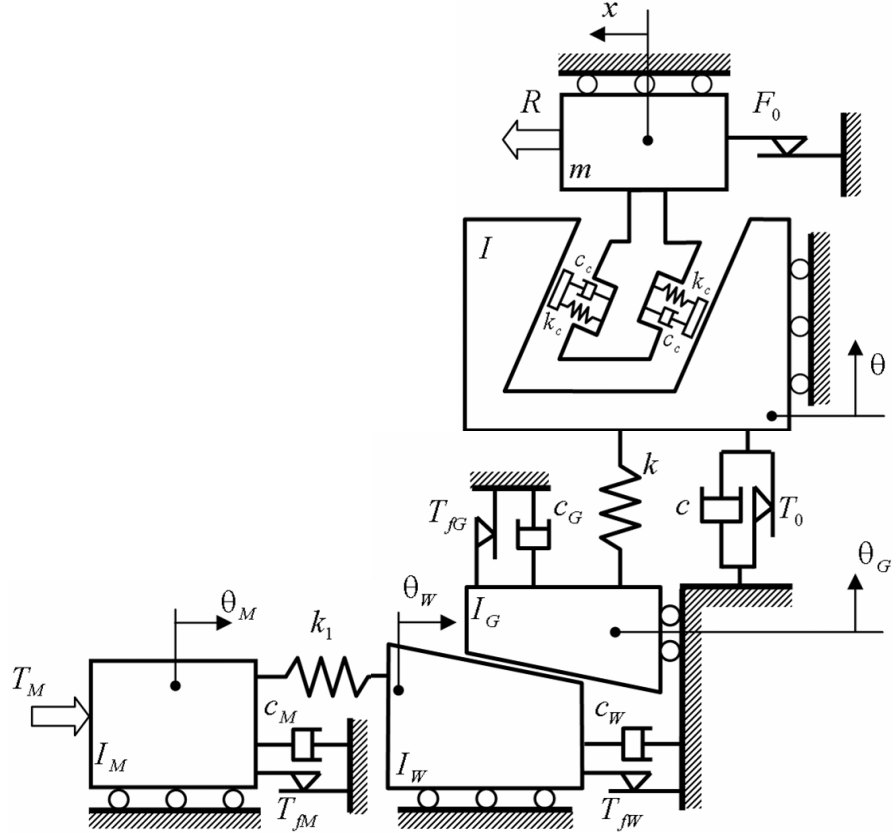


Figure 3-15: A 4-DOF lead screw drive system model

For lead screw and nut, similar to (3.11) and (3.12), one can write

$$I\ddot{\theta} = k(\theta_G - \theta) - c\dot{\theta} + r_m(N \sin \lambda - F_f \cos \lambda) - T_0 \operatorname{sgn}(\dot{\theta}) \quad (3.34)$$

$$m\ddot{x} = -N \cos \lambda - F_f \sin \lambda + R - F_0 \operatorname{sgn}(\dot{x}) \quad (3.35)$$

where N is given by (3.24). For the worm and worm gear, Newton's second law gives

$$I_w \ddot{\theta}_w = k_1(\theta_M - \theta_w) - c_w \dot{\theta}_w - \frac{d_w}{2} (W \sin \lambda_w + \mu_{wG} |W| \operatorname{sgn} \dot{\theta}_w \cos \lambda_w) - T_{fw} \operatorname{sgn} \dot{\theta}_w \quad (3.36)$$

$$I_G \ddot{\theta}_G = k(\theta - \theta_G) - c_G \dot{\theta}_G + \frac{d_G}{2} (W \cos \lambda_w - \mu_{wG} |W| \operatorname{sgn} \dot{\theta}_G \sin \lambda_w) - T_{fg} \operatorname{sgn} \dot{\theta}_G \quad (3.37)$$

where I_w and I_G are the inertia of the worm and worm-gear, respectively. θ_G is the angular displacement of the gear. d_w and d_G are the pitch diameters of worm and worm gear, respectively.

W is the normal component of the contact force between meshing worm threads and gear teeth. T_{fW} and T_{fG} are the internal friction torque of the worm and the worm gear, respectively. λ_w is the pitch angle of the worm and μ_{wG} is the coefficient of friction of the meshing worm and worm gear.

Eliminating W between (3.36) and (3.37) gives

$$\begin{aligned} & (I_w + \alpha_w \xi_w I_G) \ddot{\theta}_G + (c_w + \alpha_w \xi_w c_G) \dot{\theta}_G + (k_1 + \alpha_w \xi_w k) \theta_G \\ & - k_1 \alpha_w \theta_M - \alpha_w \xi_w k \theta + (\alpha_w T_{fW} + \alpha_w \xi_w T_{fG}) \operatorname{sgn} \dot{\theta}_G = 0 \end{aligned} \quad (3.38)$$

where

$$\alpha_w = \frac{d_w}{d_G} \tan \lambda_w \quad (3.39)$$

is the gearbox ratio¹ (i.e. $\theta_G = \alpha_w \theta_w$) and

$$\xi_w = \frac{d_w (\tan \lambda_w + \mu_{wG} \operatorname{sgn}(\dot{\theta}_w W))}{d_G (1 - \mu_{wG} \operatorname{sgn}(\dot{\theta}_G W) \tan \lambda_w)} \quad (3.40)$$

The equations of motion for the 4-DOF model in Figure 3-15 are given by (3.33), (3.34), (3.35), and (3.38).

3.9 Some Remarks Regarding the System Models

Depending on the configuration of an actual lead screw drive, one or more of models presented in this chapter may be suitable to accurately capture the most prominent and/or relevant features of the system's dynamical behavior. This is certainly the case in the subsequent chapters of this thesis. However, many other features are not included in this work. The features include:

- Dependence of friction on position: As the lead screw turns, the nut progresses along the lead screw threads creating the possibility of a position-dependent coefficient of friction. In this work, the mathematical friction model is assumed to be independent of position for simplicity of mathematical modeling. From an experimental point view, as the case of

¹ For the worm gearbox considered here, $\alpha_w = n_w / n_G$ where n_G is the number of gear teeth and n_w is the number of worm starts.

Chapter 4, the identified friction (and other possible position-dependent parameters) may be considered as an averaged value for the working portion of the lead screw.

- **Nonlinearity:** The only nonlinear effect considered in this work comes from friction. However, many other sources of nonlinearity are possible in a lead screw drive, which are excluded here to simplify the study of the friction-induced vibrations. Most notable factors are: presence of nonlinearity in the contact forces of threads caused by deflection, nonlinear torsional stiffness of the couplings, and discontinuity due to backlash.
- **Torsional deflection of lead screw:** For a long and/or slender lead screw, the frequency of the first few torsional modes of vibration may be low enough to influence the system dynamics. Moreover, the winding/unwinding action of torsional deflections may affect the threads clearance and the overall load distribution causing further deviation from the models considered here. In this work, the lead screws are considered sufficiently stiff and modeled as rigid bodies.
- **Axial deflection of lead screw:** Similar to the previous point, this effect may influence the lead screw-nut interaction in two ways: by introducing new modes of vibration and by affecting the threads clearance and load distribution.
- **Lateral deflection of lead screw:** Three situations may lead to this type of vibration: lateral loading, excessive axial loading leading to buckling (a factor for long slender lead screws), and finally whirling (for very high rotation speeds). All these situations are considered to be outside the scope of this work.
- **Misalignment:** Design and/or assembly problems may lead to axial offset of the centerlines of lead screw and nut. The misalignment may also occur in the form of a skewed nut. In both of these cases (which are excluded from the current research), thread contact and load distribution may be effected severely.
- **Manufacturing issues:** Depending on the manufacturing method and quality of the product, lead screws can suffer from lead error (particularly in longer designs). There may be external contaminants or surface defects on lead screw or nut. Although these and other similar issues may have significant impact on the function of a lead screw drive, they are

excluded from this fundamental study of the friction-induced vibration.

- **Additional elements:** The study of lead screw drives, or any other mechanical system, can be augmented by other mechanical elements (*e.g.* a vibrating component on the moving part, additional DOF due to the flexibility of the moving part, external time-dependent forcing, etc.). These cases are outside the scope of this work and depending on the problem they represent, may warrant a separate study.
- **Backlash:** Lead screw drives generally suffer from backlash. Here, backlash is not considered since the focus is on the effects of friction on power screws where the resisting load is considered to be constant and the system is considered to be moving with a constant input velocity. Backlash certainly will play a major role in “positioning” applications of lead screws, a subject that is outside the scope of this work.
- **Wear:** Throughout the operating life of lead screw drives, wear causes changes to the contacting surfaces, thereby affecting the load distribution across the threads. This effect is considered to be outside of the current study.

Chapter 4

An Experimental Case Study

As mentioned in the Section 1.2, one of the motivations behind this research was the excessive audible noise generated from the horizontal drive of an automotive seat adjuster. In this chapter, the experimental work, theoretical modeling, and system parameter identification of the horizontal drive mechanism of this seat adjuster are presented.

In Section 4.1 some preliminary observations are made regarding the audible noise generated by the system. These observations are followed by a focused study on the role of friction as the source of vibrations and the generation of audible noise. The details of the parameter identification approach, which consists of two steps, are presented in Sections 4.2 and 4.4. In the first step, parameter identification formulations are formed based on the steady-state pure-slip behavior of the system. In this step, external settings (*i.e.* applied axial force and preset motor angular velocity) are related to the friction and damping elements of the system, making it possible to identify various parameters from experimental results using the least squares technique. Identified results for the lead screw drive of the seat adjuster are presented in Section 4.3. In the second step, Section 4.4, identified parameters are fine-tuned based on the open-loop vibrating behavior of the system. In this step, an optimization technique is utilized to match the model response to the measurements when the system trajectory follows a limit cycle. Parameter studies based on the fine-tuned model are given in Section 4.5. Conclusions are summarized in Section 4.6.

4.1 Preliminary Observations

The first step in finding the causes of excessive audible noise in an operating mechanical system may be to analyze the noise signal and the external conditions under which such a noise is generated. In this section, some of the preliminary observations made on the powered seat adjuster investigated

here are presented¹.

In the first step, a series of tests were performed on the complete seat adjuster. Figure 4-1 shows the test setup and instrumentation used to study the complete seat adjuster². A pneumatic cylinder mounted on the wall was used to apply axial force.

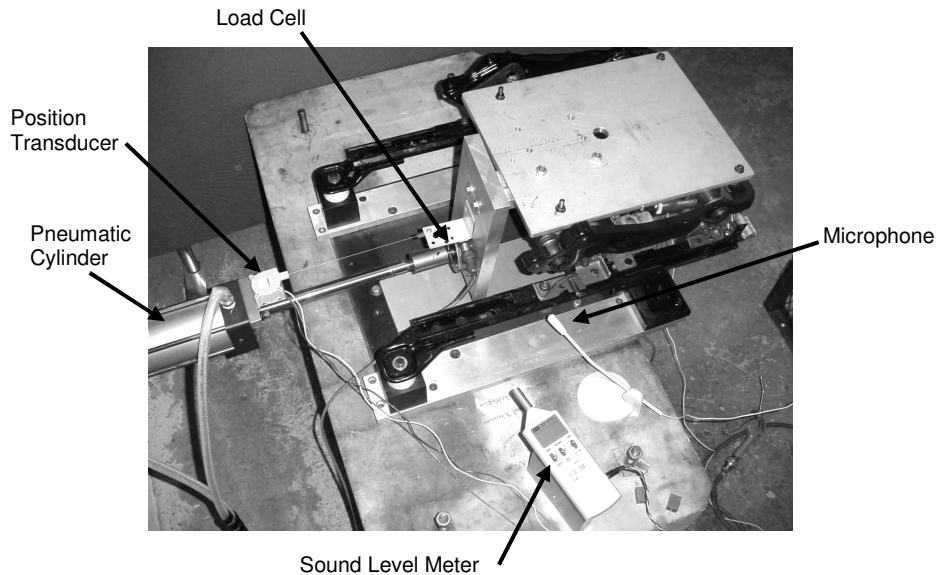


Figure 4-1: Test setup for complete seat adjuster

A sample these measurements are presented in Figure 4-2. As shown in Figure 4-2(c), the applied force of approximately $180N$ caused the seat adjuster to generated audible noise. Figure 4-2(d) shows that seat was traveling at a velocity of approximately $7mm/s$. The sound level meter measurements in Figure 4-2(b) shows an approximately $10dB$ jump occurred in the noise level (from the background noise level) during a portion of the seat travel. During the same interval, the audible noise time-frequency plot in Figure 4-2(a) clearly shows the sustained presence of noise with a dominant frequency of approximately $160Hz$. The frequency content of the noise signal is also shown in Figure 4-3 at $t = 8s$.

¹ See Section 1.2 for the details of the seat adjuster mechanism.

² For the instrumentation details see Appendix A

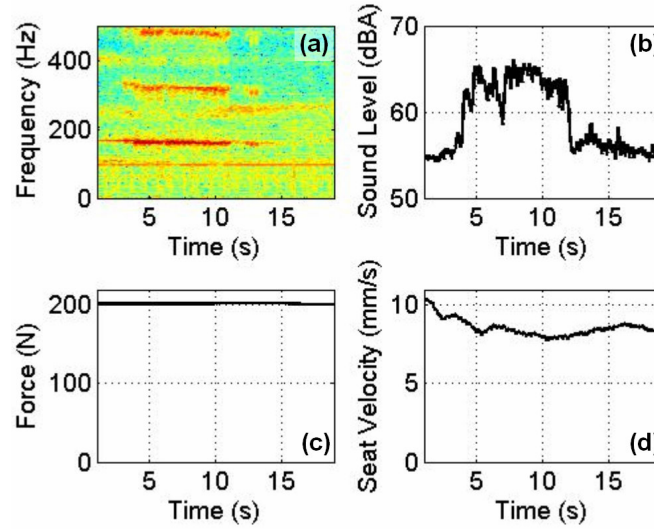


Figure 4-2: Sample test results from complete seat adjuster tests.

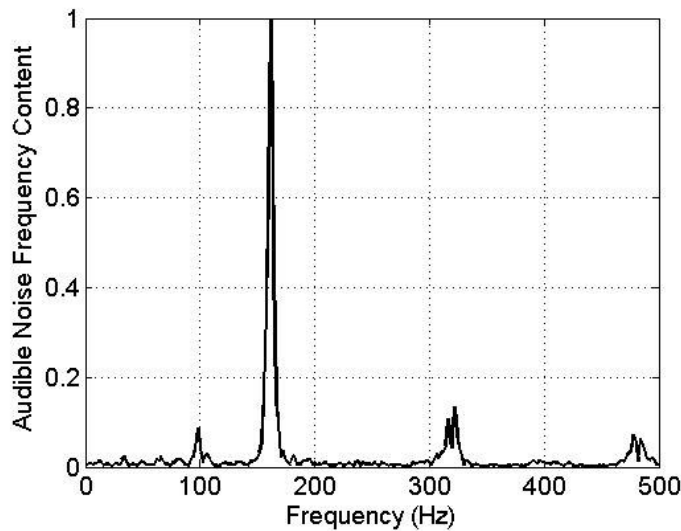


Figure 4-3: Audible noise frequency content for the test results shown in Figure 4-2 (at 8s). Peak amplitude at 162Hz

The investigation was then continued by a second series of tests focusing only on the sliders comprising the horizontal motion system of the seat adjuster. As mentioned earlier, the two sliders are equipped with lead screw systems driven by a single DC motor. The test setup for this series of test is shown in Figure 4-4, which is similar to the setup used for the complete seat adjuster tests.

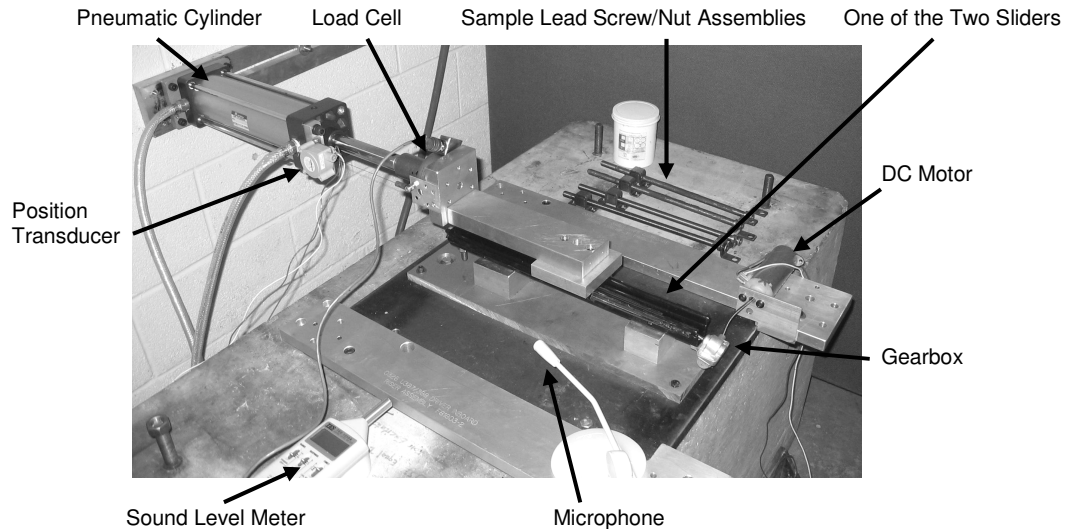


Figure 4-4: Single-track test setup

Sample measurement results from one of the single slider tests are presented in Figure 4-5. In this test, a horizontal force of about $200N$ (Figure 4-5(c)) was needed to induce the noise at a traveling velocity of approximately $20mm/s$ (Figure 4-5(d)). The audible noise continued for about $4s$ with a dominant frequency of about $150Hz$ (Figure 4-5(a)) accompanied by an almost $20dB$ increase in the noise level (Figure 4-5(b)).

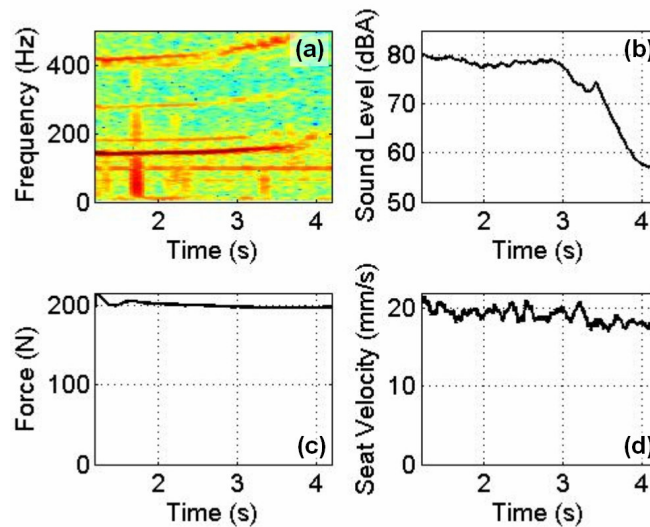


Figure 4-5: Sample test results from single-track tests.

The frequency spectrum of the recorded noise at $t = 3s$ is plotted in Figure 4-6. This plot clearly shows the dominant signal frequency of 150Hz.

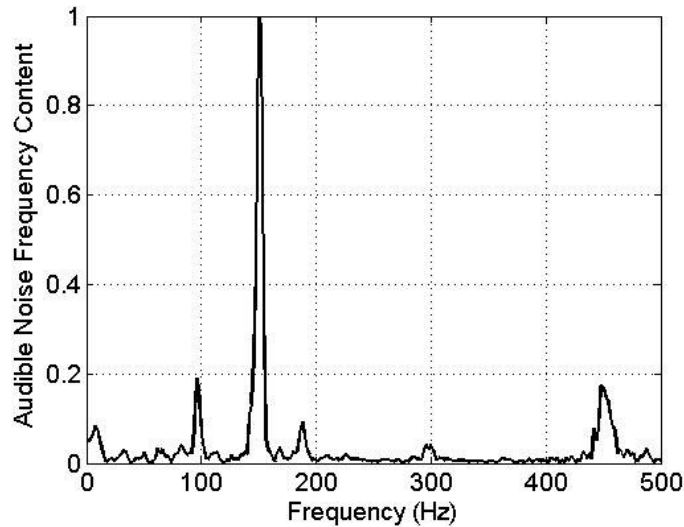


Figure 4-6: Audible noise frequency content for the test results shown in Figure 4-5 (at 3s). Peak amplitude at 150Hz

These tests and many similar others under different force and velocity settings revealed a strong correlation between the two test setups, confirming the initial guess as to the source of audible noise: *friction-induced vibration in the lead screw drive*.

4.2 Step 1: Friction and System Parameter Identification

The first step in the friction identification process is formulated based on the system response under steady-state pure-slip conditions (*i.e.* no rotational vibrations and constant lead screw angular velocity). The aim of this formulation is to relate the measurable system inputs and states to the internal friction and damping parameters through the mathematical model described in Section 3.8. This model corresponds to the third test setup¹ developed for these studies, which is shown in Figure 4-7.

¹ For the instrumentation details see Appendix A

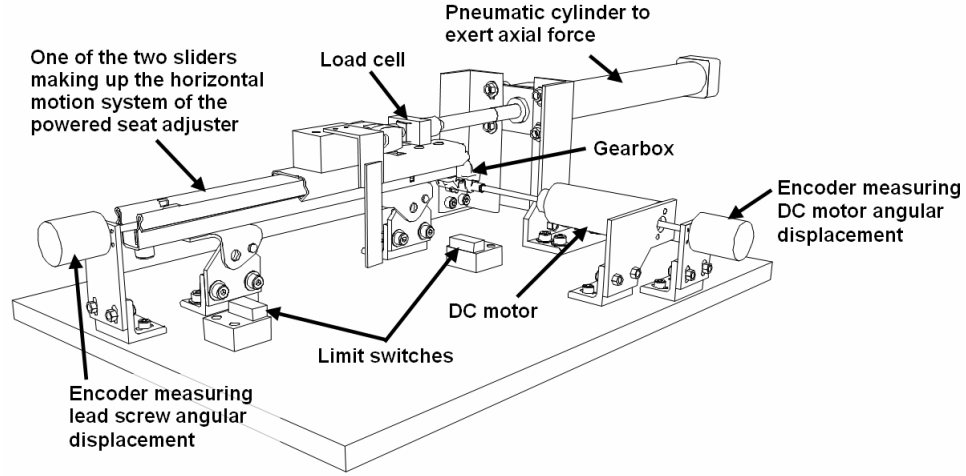


Figure 4-7: Schematic view of the test setup

Similar to the test setup shown in Figure 4-4, only one of the two sliders was included in the setup. The working parts of the test setup were taken from an actual seat adjuster. Two encoders were used to measure the angular displacement of the lead screw and the motor. A load cell was used to measure the force exerted by the pneumatic cylinder. The input voltage and current to the DC motor were also measured. With the help of a controller regulating the current input to the DC motor [80,81], the slider was set to move at constant preset velocities in the applicable range. At each test, the following quantities become available as averaged values over the considered travel stroke of the nut:

- Motor angular velocity, ω_M
- Motor torque, T_M
- Axial Force, R

The angular velocity of the motor is calculated by numerical differentiation of its measured angular displacement. The motor torque is calculated from the measured input current and the known motor's torque constant.

The steady state relationships are derived from (3.33), (3.34), (3.35), and (3.38) by setting all accelerations to zero and assuming positive angular velocities. The steady-state equations are found as

$$T_M - T_{fM} + k_1(\alpha_w^{-1}\theta_G - \theta_M) - c_M \omega_M = 0 \quad (4.1)$$

$$k(\theta_G - \theta) - c\omega - T_0 + r_m(N \sin \lambda - F_f \cos \lambda) = 0 \quad (4.2)$$

$$-N \cos \lambda - F_f \sin \lambda - F_0 + R = 0 \quad (4.3)$$

$$\begin{aligned} (c_W + \alpha_W \xi_{W0} c_G) \omega_G + (k_1 + \alpha_W \xi_{W0} k) \theta_G - k_1 \alpha_W \theta_M \\ - \alpha_W \xi_{W0} k \theta + (\alpha_W T_{fW} + \alpha_W \xi_{W0} T_{fG}) = 0 \end{aligned} \quad (4.4)$$

where $\omega = \omega_G = \alpha_W \omega_M$ are the constant angular velocities and

$$\xi_{W0} = \frac{d_W (\tan \lambda_W + \mu_{WG})}{d_G (1 - \mu_{WG} \tan \lambda_W)} \quad (4.5)$$

Eliminating N between (4.2) and (4.3) gives

$$k(\theta_G - \theta) - c\omega - T_0 - \xi_0(R - F_0) = 0 \quad (4.6)$$

where

$$\xi_0 = r_m \frac{\mu \operatorname{sgn}(N) - \tan \lambda}{1 + \mu \operatorname{sgn}(N) \tan \lambda} \quad (4.7)$$

Since the aim of this study is to investigate cases where the axial load is applied *in the direction* of motion, N is assumed to be positive. Consequently, at steady-state for $R > F_0$, (4.7) is simplified to

$$\xi_0 = r_m \frac{\mu - \tan \lambda}{1 + \mu \tan \lambda} \approx r_m (\mu - \tan \lambda) \quad (4.8)$$

where the approximation is obtained by assuming $\mu \tan \lambda \ll 1$. Combining (4.1), (4.4), and (4.6) yields

$$T_M = C\omega_M + T_f + \xi_{W0} \xi_0 (R - F_0) \quad (4.9)$$

where

$$C = C_0 + \alpha_W \xi_{W0} c \quad (4.10)$$

$$T_f = T_{f0} + \xi_{W0} T_0 \quad (4.11)$$

and

$$C_0 = c_W + \alpha_W \xi_{W0} c_G + c_M \quad (4.12)$$

$$T_{f0} = T_{fM} + T_{fW} + \xi_{w0} T_{fG} \quad (4.13)$$

To separate *force* effects from the *velocity* effects, (4.9) is rearranged as

$$T_M = \beta_0(\omega_M) + (R - F_0)\beta_1(\omega_M) \quad (4.14)$$

where

$$\beta_0(\omega_M) = T_f + C\omega_M \quad (4.15)$$

$$\beta_1(\omega_M) = \xi_{w0} \cdot \xi_0(\omega_M) \quad (4.16)$$

For each motor speed setting, $\omega_M^{(i)}$, the straight line described by (4.14) can be fitted to the experimental data points $\langle R^{(j)}, T_M^{(i,j)} \rangle$ to obtain $\beta_0^{(i)}$ and $\beta_1^{(i)}$ as functions of motor angular velocity.

Based on (4.15), another straight line can be fitted to $\langle \omega_M^{(i)}, \beta_0^{(i)} \rangle$ data points to obtain T_f and C .

Expanding the second velocity dependent coefficient, $\beta_1(\omega_M)$, using (4.8), gives

$$\beta_1(\omega) = \xi_{w0} \frac{d_m}{2} (\mu(\omega) - \tan \lambda) \quad (4.17)$$

At steady-state velocity of $\omega = \alpha_w \omega_M$, the coefficient of friction defined by (3.10) becomes

$$\mu = \mu_1 + \mu_2 e^{-r_0 \alpha_w \omega_M} + \mu_3 \alpha_w \omega_M \quad (4.18)$$

Substituting (4.18) into (4.17) and rearranging gives

$$\beta_1(\omega_M) = \begin{bmatrix} 1 & e^{-r_0 \alpha_w \omega_M} & \omega_M \end{bmatrix} \begin{bmatrix} \gamma_0 \\ \gamma_1 \\ \gamma_2 \end{bmatrix} \quad (4.19)$$

where

$$\gamma_0 = r_m \xi_{w0} (\mu_1 - \tan \lambda) \quad (4.20)$$

$$\gamma_1 = r_m \xi_{w0} \mu_2 \quad (4.21)$$

$$\gamma_2 = r_m \xi_{w0} \alpha_w \mu_3 \quad (4.22)$$

Now the curve described by (4.19) can be fitted to the previously obtained data points (*i.e.* $\langle \omega_M^{(i)}, \beta_1^{(i)} \rangle$) to estimate the three new parameters; $\hat{\gamma}_0$, $\hat{\gamma}_1$, and $\hat{\gamma}_2$. Using the least squares technique, one finds

$$\hat{\mathbf{\Gamma}} = (\mathbf{A}^T \mathbf{A})^{-1} \mathbf{A}^T \mathbf{B} \quad (4.23)$$

where

$$\hat{\mathbf{\Gamma}} = [\hat{\gamma}_0 \quad \hat{\gamma}_1 \quad \hat{\gamma}_2]^T \quad (4.24)$$

and

$$\mathbf{A} = \begin{bmatrix} 1 & e^{-r_0 \alpha_w \omega_w^{(1)}} & \omega_w^{(1)} \\ 1 & e^{-r_0 \alpha_w \omega_w^{(2)}} & \omega_w^{(2)} \\ \vdots & \vdots & \vdots \\ 1 & e^{-r_0 \alpha_w \omega_w^{(n)}} & \omega_w^{(n)} \end{bmatrix} \quad (4.25)$$

$$\mathbf{B} = \begin{bmatrix} \beta_1^{(1)} \\ \beta_1^{(2)} \\ \vdots \\ \beta_1^{(n)} \end{bmatrix} \quad (4.26)$$

where n is the total number of data points available. Note that \mathbf{A} given by (4.25) is dependent on r_0 , which is one of the unknown parameters describing the Stribeck effect in the assumed model of the velocity dependent coefficient of friction. To rectify this problem, a simple optimization routine is used to find the best value for r_0 such that the curve fitting error of (4.23) is minimized. Define

$$\begin{bmatrix} e_{(1)}(r_0) \\ e_{(2)}(r_0) \\ \vdots \\ e_{(n)}(r_0) \end{bmatrix} = \mathbf{B} - \mathbf{A}(r_0) \begin{bmatrix} \hat{\gamma}_0(r_0) \\ \hat{\gamma}_1(r_0) \\ \hat{\gamma}_2(r_0) \end{bmatrix} \quad (4.27)$$

where dependence on r_0 is made explicit. The optimized value of r_0 given by \hat{r}_0 is now found simply as

$$\hat{r}_0 = \arg \min_{r_{0\min} \leq r_0 \leq r_{0\max}} \sum_{i=1}^n e_{(i)}^2(r_0) \quad (4.28)$$

This task may be performed using a number of numerical optimization techniques. In the next section, $\sum_{i=1}^n e_{(i)}^2(r_0)$ is simply computed and plotted over a range of appropriate values, $r_0 > 0$, and the minimum is found graphically.

4.3 Experiment Results

In this section, the parameter identification approach described in Section 4.2 is applied to the measurements performed using the test setup shown in Figure 4-7.

Before exploring the friction torque produced at the contact between lead screw and nut threads, a preliminary step is required to estimate and isolate internal damping (4.12) and friction (4.13) of the DC motor and the gearbox. This step is present first in Section 4.3.1 and then the lead screw friction and damping identification results are presented in Section 4.3.2.

4.3.1 DC Motor and Gearbox

In a series of preliminary tests, DC motor and gearbox were disconnected from the lead screw, and the input current of the DC motor was measured at different levels of preset constant angular velocities. Figure 4-8 shows the results of these tests. By fitting a straight line to these data points using the least squares technique, the overall damping, C_0 , and residual friction torque, T_{f0} , were estimated. These results together with other known system parameters are given in Table 4-1.

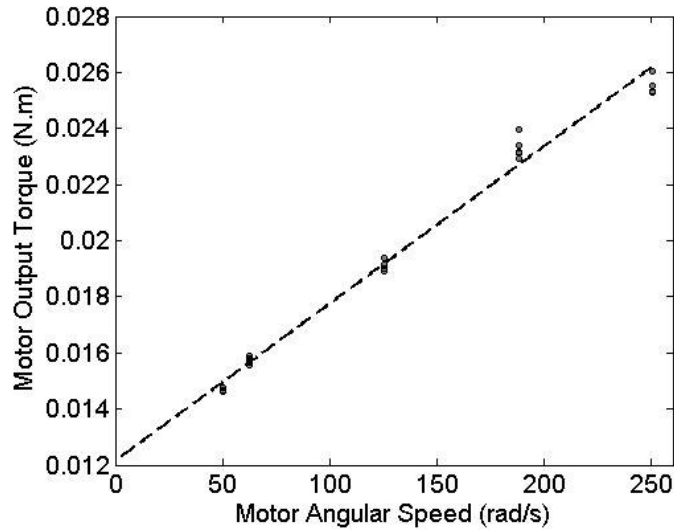


Figure 4-8: Resistive torque of the motor and the gearbox.
Dots: measurements, dashed line: fitted line to the data points

Table 4-1: Known or assumed system parameter values

Parameter	Value
Lead screw pitch diameter, d_m	10.366 mm
Lead screw lead angle, λ	5.57°
Mass of translating parts, m	3.8 kg
Average resistance of the slider, F_0	<2 N
Assumed contact stiffness – lead screw and nut, k_c	10^8 N/m
Assumed contact damping – lead screw and nut, c_c	10^6 kg/s
Lead screw inertia, I	3.12×10^{-6} kg.m ²
Worm pitch diameter, d_w	9.442 mm
Worm gear pitch diameter, d_G	20.04 mm
Worm lead angle, λ_w	18.53°
Gearbox ratio, α_w	3/19
Nominal torsional stiffness of the coupling, k	1.12 N.m/rad
Assumed coefficient of friction of gearbox mesh, μ_{wG}	0.2
Overall DC motor and the gearbox internal damping, C_0	0.0121 N.m
Overall DC motor and the gearbox internal friction, T_{f0}	5.61×10^{-5} N.m.rad/s

4.3.2 Identification Results

Figure 4-9 shows data points collected from all of the measurements performed. In this figure, motor

torque (measured from motor input current) is plotted against measured force and measured speed. Fluctuation in the supply air pressure to the cylinder, together with the speed-dependent internal friction of the piston rod, caused variations in the applied force from one experiment to the next.

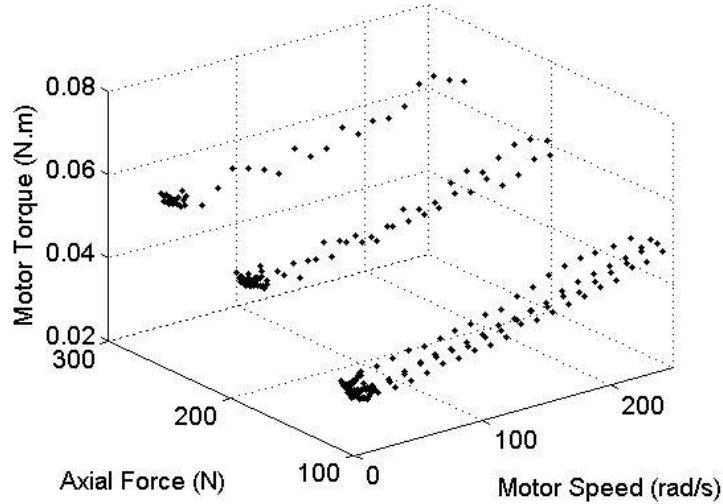


Figure 4-9: Collection of data points showing Torque/Speed/Force

As described in the previous section, a straight line is fitted to the data points at each velocity setting, which gives variation of motor torque versus applied axial force according to (4.14) for each of the available velocity set points. Figure 4-10 shows a few samples of these curve fittings¹. The curve fitting results according to (4.15) and (4.19) are shown in Figure 4-11 and Figure 4-12, respectively. The estimated parameters are listed in Table 4-2.

Table 4-2: Identified parameters

Parameter	Value	Unit
T_f	0.0146	<i>N.m</i>
C	7.34e-005	<i>N.m.s/rad</i>
r_0	0.38	<i>s/rad</i>
γ_0	1.54e-003	<i>m</i>
γ_1	2.59e-005	<i>m</i>
γ_2	-8.99e-008	<i>m</i>

¹ In these calculations, the effect of F_0 was neglected since preliminary observations showed that the slider friction force is consistently less than $2N$, which is less than 2% of the applied force, R .

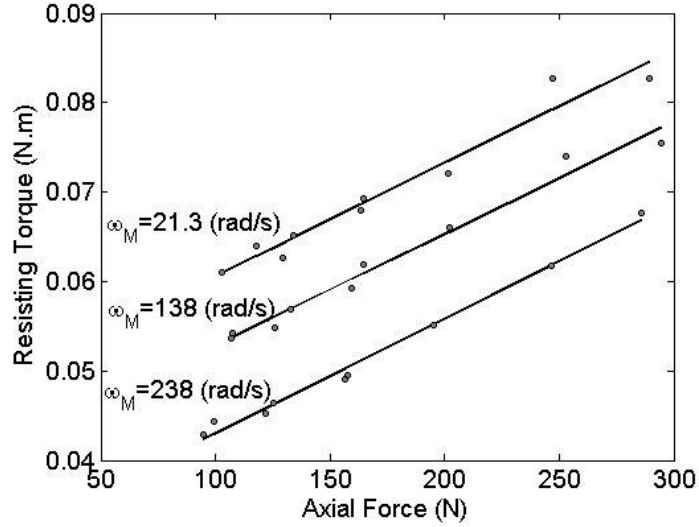


Figure 4-10: Sample measurement results. Variation of motor torque with applied axial load at constant speeds. Dots: measurements, solid line: fitted line to the data points

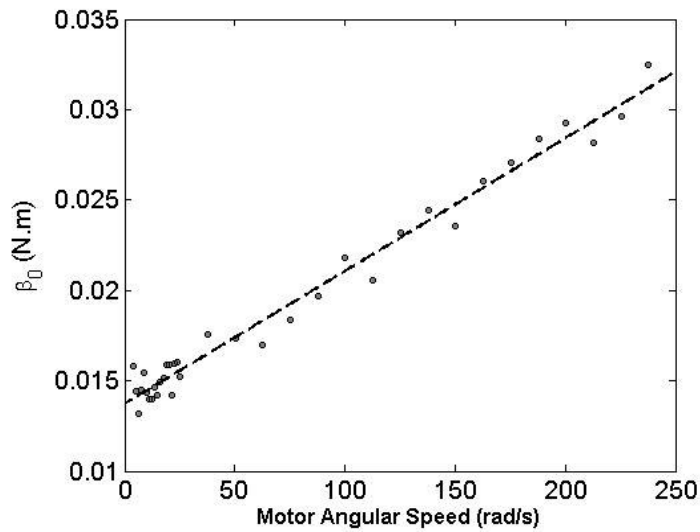


Figure 4-11: Variation of β_0 with motor angular velocity

Based on (4.11) and using values of T_{f0} from Table 4-1 and T_f from Table 4-2, the residual friction of the lead screw supports, T_0 is found to be

$$T_0 \approx 0.01 \text{ N.m}$$

where based on the parameter values in Table 4-2 and (4.5), $\xi_{w0} \approx 0.27$ was used.

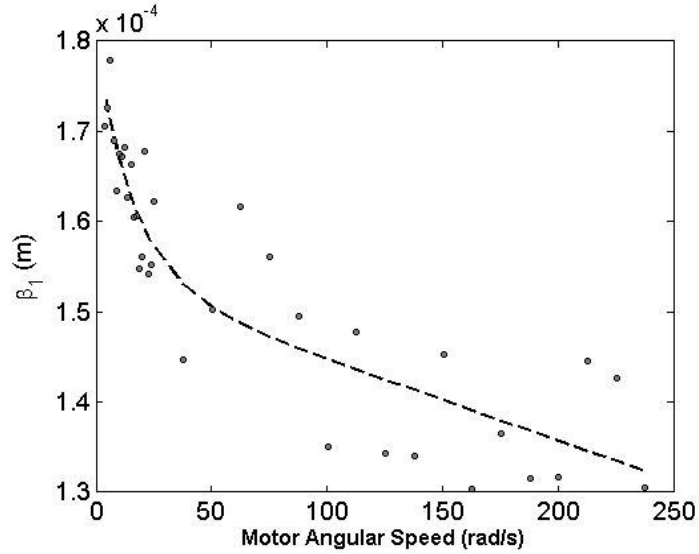


Figure 4-12: Variation of β_1 with motor angular velocity

Also using (4.10) and C_0 from Table 4-1 and C from Table 4-2, the damping coefficient of the end support is found to be

$$c \approx 4 \times 10^{-4} \text{ N.m.s/rad}$$

This value is adjusted in Section 4.4, since the system's stability (in simulations) depends heavily on the damping of the lead screw, and in the experimental results, there was quite a bit of variability.

Using (4.20), (4.21), and (4.22) and their identified values in Table 4-2, the three friction parameters defined by (4.18) can be calculated. These values are listed in Table 4-3 and the resulting velocity-dependent coefficient of friction is plotted in Figure 4-13.

Table 4-3: Numerical values of the identified parameters

Parameter	Value	Unit
μ_1	2.18e-1	-
μ_2	2.03e-2	-
μ_3	-4.47e-4	s/rad

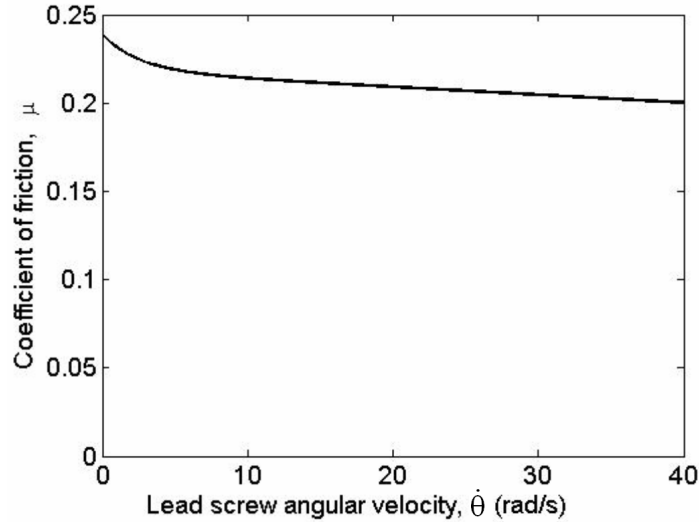


Figure 4-13: Identified velocity dependent coefficient of friction

4.4 Step 2: Fine-tuning

The identification formulation in the Section 4.2 depends on the knowledge of the sliding coefficient of friction of the gearbox (μ_{wG} is given in Table 4-1) through the appearance of ξ_{w0} in (4.10), (4.11), (4.20), (4.21), and (4.22). Uncertainty in the value of this parameter, together with the unknown nonlinearity of the coupling stiffness, necessitates a further step of parameter identification and fine-tuning.

The approach in Section 4.2 was based on steady state (no vibration) conditions. Accordingly, in Section 4.3, tests were performed while keeping the angular velocity of the lead screw nearly constant under the action of a speed controller. In this section, results from a series of tests on the system without the controller (normal operating conditions) are used to fine-tune the model through identifying variations in damping, stiffness, and friction.

Figure 4-14 shows the changes in the vibration amplitude as the applied axial force and the input angular velocity of lead screw is changed. Each point in Figure 4-14 represents the averaged experimental values of amplitude of vibration over a 2 ms interval, where a limit cycle was detected. These results show that the amplitude of vibration increases with gearbox output angular velocity. Figure 4-15(a) shows a sample of the test results. In the close-up view in Figure 4-15 (b), the stick-slip rotational vibration of lead screw can be seen clearly.

Note that in the actual lead screw system, various parameters (*e.g.* lubrication, surface conditions,

and load distribution on lead screw and nut threads) change as the nut translates along the lead screw. This means that the estimated parameters obtained from the measurements are effectively the averaged values over the distance that the nut was set to translate along the lead screw in the tests.

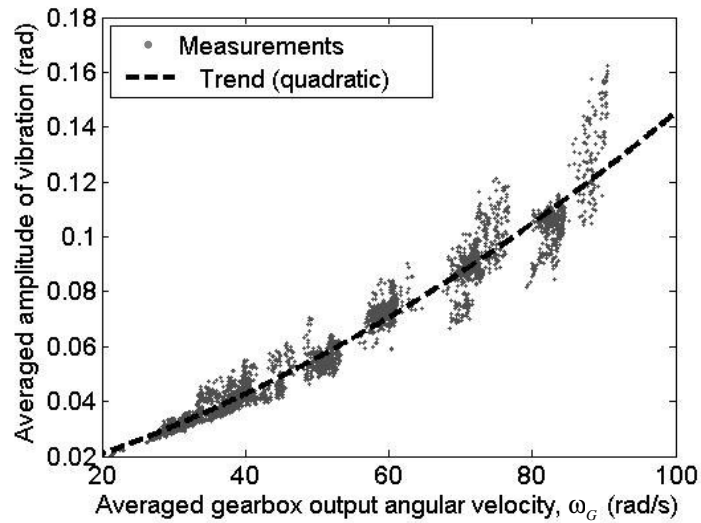


Figure 4-14: Experimentally obtained variation of limit cycle vibration amplitude with input angular velocity (gearbox output) and axial force

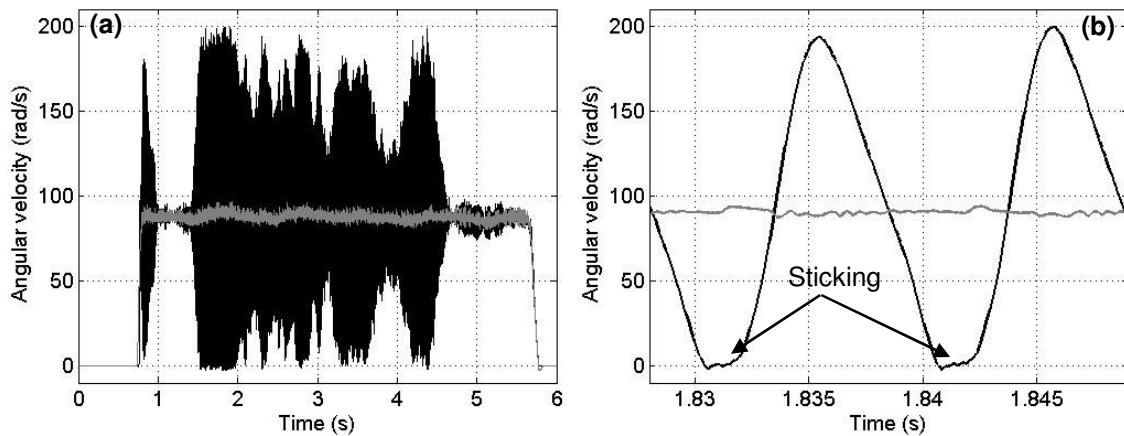


Figure 4-15: a) A sample of test results showing stick-slip in open-loop tests, b) zoomed view. Black: lead screw angular velocity; grey: DC motor angular velocity

Consider the following cost function

$$\Psi(k, c, s_\mu, r_1) = \frac{\sum_{i=1}^n (\dot{\theta}^M(i) - \dot{\theta}^S(i))^2}{\left(\max_i \dot{\theta}^M(i)\right)^2} + \frac{\sum_{i=1}^n (\tilde{\theta}^M(i) - \tilde{\theta}^S(i))^2}{\left(\max_i \tilde{\theta}^M(i)\right)^2} \quad (4.29)$$

which calculates the weighted sum of squared differences between measured (superscript M) and simulated (superscript S) angular displacement ($\tilde{\theta}^M, \tilde{\theta}^S$) and angular velocity ($\dot{\theta}^M, \dot{\theta}^S$). The “ \sim ” signifies that the mean value is removed. Also, n is the number of data points included in the time window during which the measured system trajectory follows a limit-cycle.

Additional parameters in the cost function Ψ in (4.29) are defined by the following modifications to the velocity-dependent coefficient of friction defined by (3.10)

$$\mu = s_\mu \left(\mu_1 + \mu_2 e^{-\tau_0 |\dot{\theta}|} + \tilde{\mu}_3 |\dot{\theta}| \right) \left(1 - e^{-\tau_1 |\dot{\theta}|} \right) \quad (4.30)$$

where $0.9 < s_\mu < 1.1$ is a scaling added to the identified friction to account for any variations in μ_{WG} from one experiment to the next. In addition, the friction coefficient is smoothed over near zero relative velocities to facilitate numerical integration and improve conformity of the simulation results to the test data as the trajectories approach the zero sliding velocity boundary.

Because of the high gear ratio of the worm gear, friction-induced vibrations of the lead screw do not cause considerable fluctuations in the angular velocity of the DC motor (See Figure 4-15, for example). Hence, from this point on, in the numerical simulations, it is assumed that the angular velocity output of gearbox, $\dot{\theta}_G$, is constant. The resulting simplified model is given in Section 3.5.

The parameters minimizing Eq. (4.30) are found for every incidence where a limit cycle is found in the measured response (Figure 4-14) over a wide range of gearbox output angular velocities and applied axial forces. In Figures 4-16 to 4-21, sample results are shown that compare measurements with the simulation results obtained from the 2-DOF model of Section 3.5 with the fine-tuned parameters.

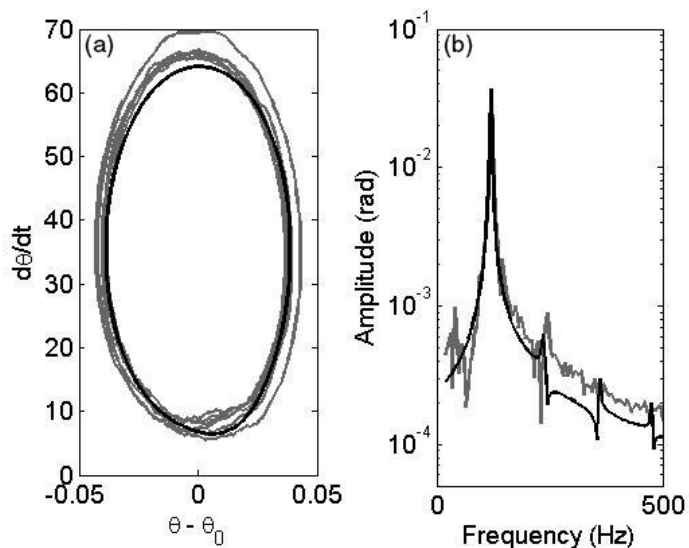


Figure 4-16: Measurement vs. simulation example.

Inputs: $R = 152.9(N)$, $\omega_G = 35.6(rad/s)$ - **Parameters:** $k = 1.18(Nm/rad)$, $c = 1.86 \times 10^{-4}(Nms/rad)$

a) phase plot, b) frequency response. Gray: measurements, black: simulation

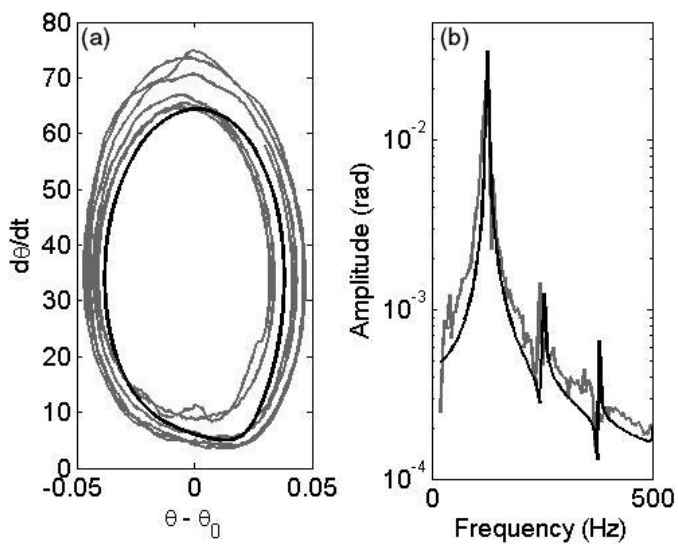


Figure 4-17: Measurement vs. simulation example.

Inputs: $R = 273.9(N)$, $\omega_G = 34.3(rad/s)$ - **Parameters:** $k = 1.31(Nm/rad)$, $c = 3.37 \times 10^{-4}(Nms/rad)$

a) phase plot, b) frequency response. Gray: measurements, black: simulation

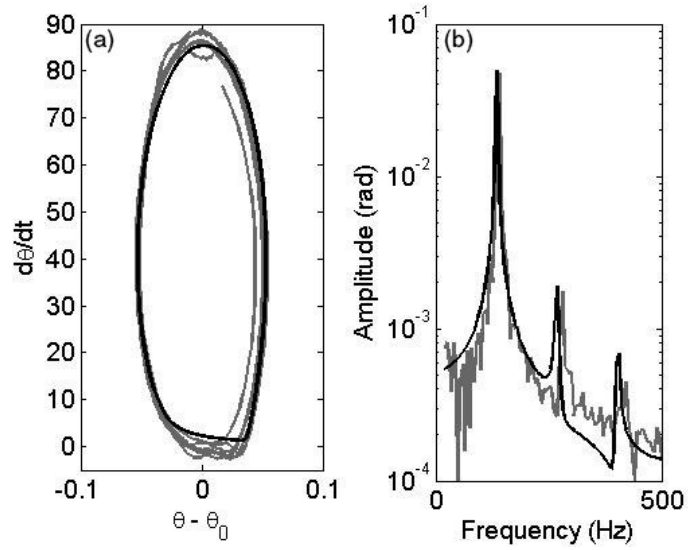


Figure 4-18: Measurement vs. simulation example.

Inputs: $R = 314.3(N), \omega_G = 40.3(rad/s)$ - **Parameters:** $k = 1.65(Nm/rad), c = 3.04 \times 10^{-4}(Nms/rad)$
a) phase plot, b) frequency response. Gray: measurements, black: simulation

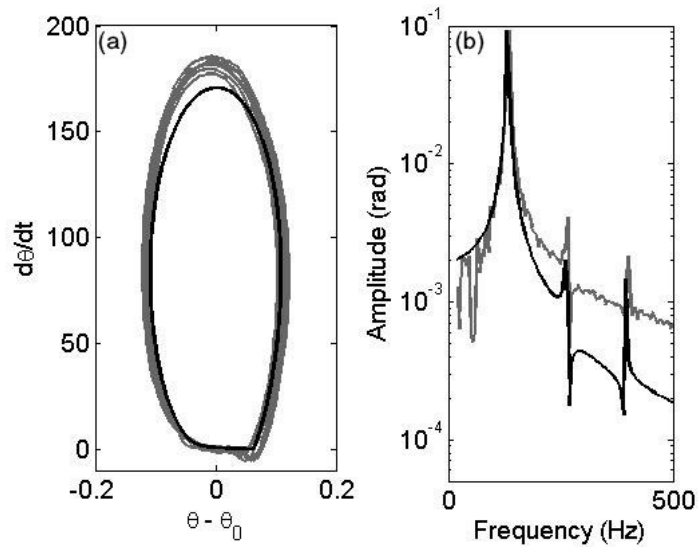


Figure 4-19: Measurement vs. simulation example.

Inputs: $R = 327.5(N), \omega_G = 83.7(rad/s)$ - **Parameters:** $k = 1.75(Nm/rad), c = 4.07 \times 10^{-4}(Nms/rad)$
a) phase plot, b) frequency response. Gray: measurements, black: simulation

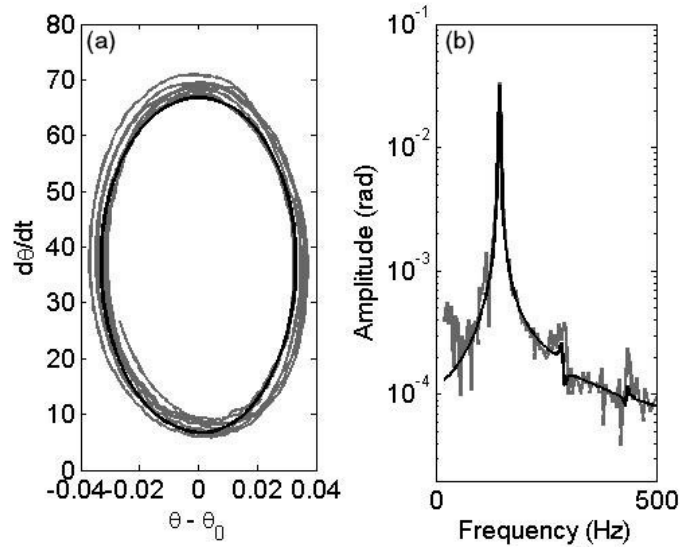


Figure 4-20: Measurement vs. simulation example.

Inputs: $R = 330.8(N), \omega_G = 37.3(rad/s)$ - **Parameters:** $k = 1.88(Nm/rad), c = 5.79 \times 10^{-4}(Nms/rad)$
a) phase plot, b) frequency response. Gray: measurements, black: simulation

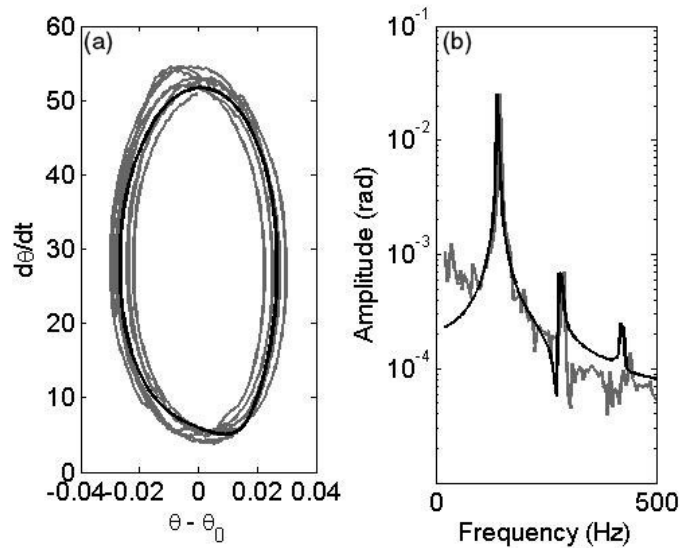


Figure 4-21: Measurement vs. simulation example.

Inputs: $R = 336.7(N), \omega_G = 27.9(rad/s)$ - **Parameters:** $k = 1.67(Nm/rad), c = 4.00 \times 10^{-4}(Nms/rad)$
a) phase plot, b) frequency response. Gray: measurements, black: simulation

These results show the effectiveness of the fine-tuning step in matching the dynamical behavior of the model with that of the real system.

In order to perform parameter studies through simulation, two-variable bilinear fitting was

performed for each of the four parameters in (4.29) with respect to the gearbox output angular velocity, ω_G , and the applied axial force, R . Contour plots in Figures 4-22 to 4-25 show the results of these fittings.

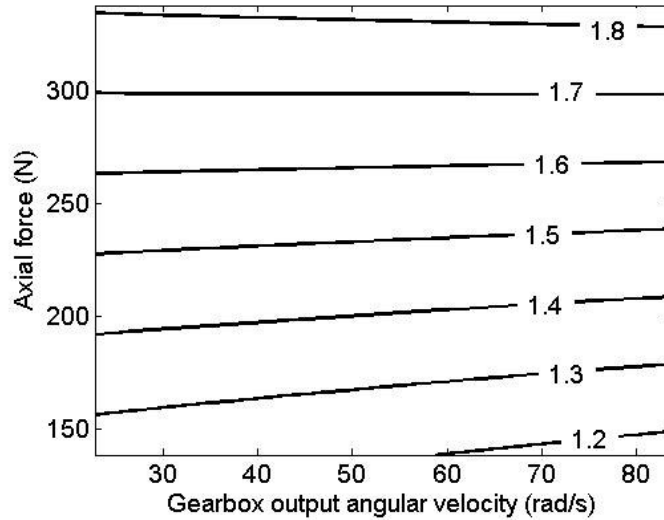


Figure 4-22: Variation of coupling stiffness, k , with gearbox output velocity and axial force

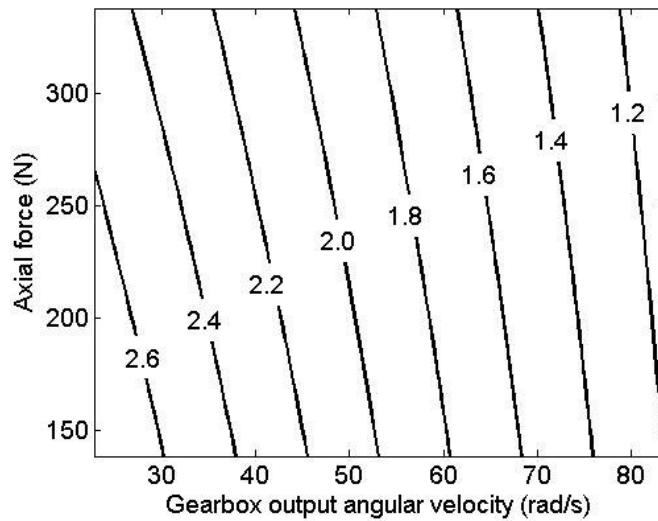


Figure 4-23: Variation of friction boundary effect, $1/r_1$, with gearbox output velocity and axial force

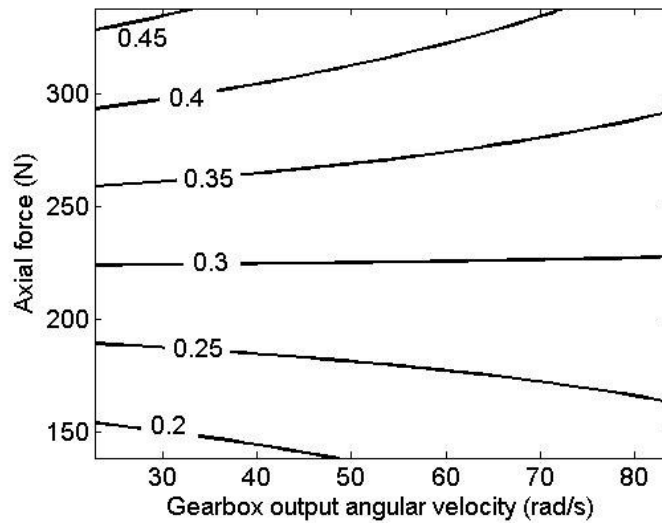


Figure 4-24: Variation of lead screw support damping, c ($\times 10^{-3}$), with gearbox output velocity and axial force

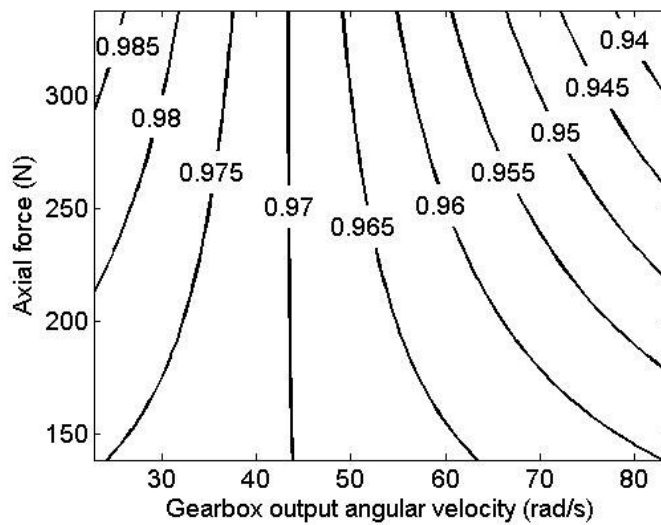


Figure 4-25: Variation of friction scaling, s_{μ} , with gearbox output velocity and axial force

It is interesting to note that, as expected, coupling stiffness varies mainly with the axial force and exhibits a “work-hardening” behavior. Also, the friction scaling (s_{μ}) was found to be very close to one which shows that the initial estimate for μ_{WG} was quite accurate.

4.5 Parameter Studies

Using the identified and fine-tuned model parameters, various performance maps can be obtained to study the effects of the variation of system parameters on the initiation of limit cycles and the amplitude of steady-state vibrations. The amplitude of vibrations is directly related to the generated audible noise from the system. In the following, the effects of input angular velocity, damping of the lead screw supports, and coupling stiffness are investigated.

4.5.1 Effect of Input Angular Velocity

Figure 4-26 shows the contours of steady-state vibration amplitudes as a function of gearbox output angular velocity and the applied axial force. It can be seen from this figure that, beyond a certain value of applied axial force, increasing the angular velocity increases the amplitude of vibration. This finding is well correlated with the subjective tests on the audible noise intensity levels from the lead screw system and the experimental results in Figure 4-14

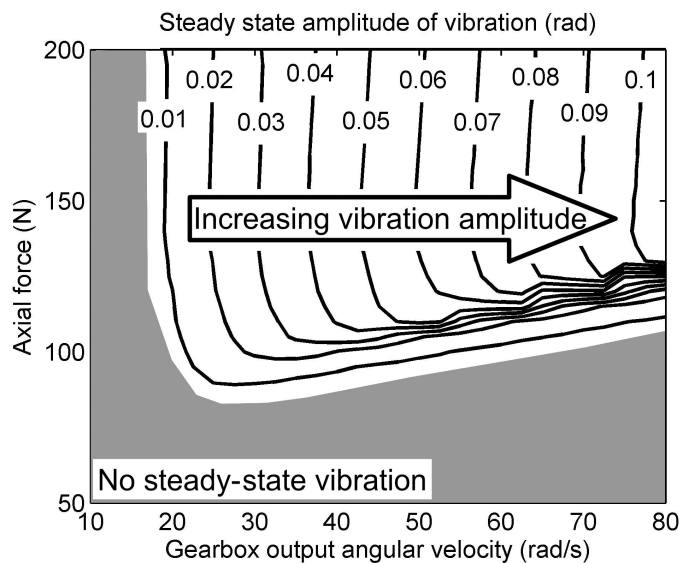


Figure 4-26: Contour plots of the steady state vibration amplitude vs. applied axial force and gearbox output speed

4.5.2 Effect of Damping

To investigate the effect of damping on the threshold of instabilities, the above simulations were repeated for three values of the constant damping coefficient. Figure 4-27 shows the result of these

simulations where a vibration amplitude of 0.01 (*rad*) has been taken as the approximate threshold of stable/unstable regions. It can be seen that, by increasing the damping, instabilities occur at higher levels of axial force. This phenomenon will be analyzed further in Chapter 5 using the eigenvalue analysis method and the method of averaging.

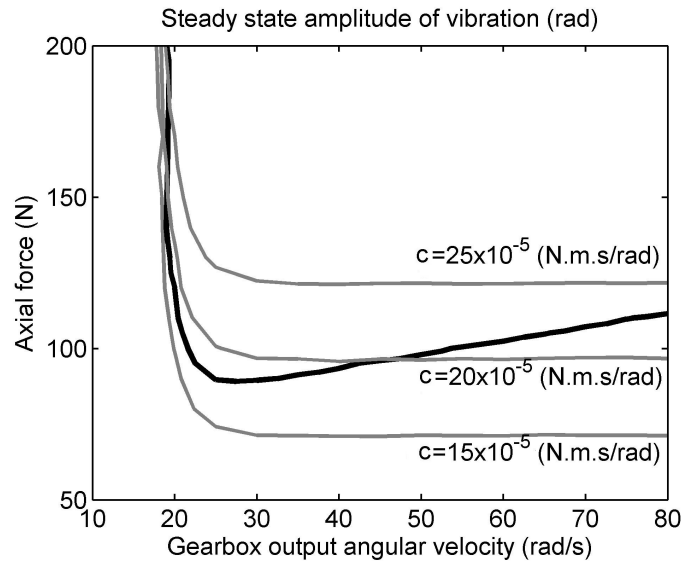


Figure 4-27: Effect of lead screw rotational damping on the threshold of instabilities. The thick black line corresponds to the instability threshold in Figure 4-26.

4.5.3 Effect of Stiffness

The effect of the torsional stiffness of the coupling was also considered. Figure 4-28 shows the variation of the vibration amplitude as a function of applied axial force and the torsional stiffness of the coupling. This map was obtained from numerical simulations assuming $\omega_G = 40$ (rad/s). Similar plots can be obtained for other preset angular velocities.

Figure 4-28 shows that if the applied force is below 100 N, by either increasing *or* decreasing the stiffness of the coupling from its current design value, rotational vibration leading to excessive noise may be eliminated. Note that the horizontal axis is a scaling parameter applied to the coupling stiffness of the system. At higher axial loads, by using stiffer couplings – beyond 10 times the current value – much lower vibration amplitudes are obtained. However, other design requirements may prevent the use of a high stiffness coupling in the system. This finding opens the door for two possible design modifications, which can either eliminate the steady-state rotational vibrations or

reduce its amplitude in such a way that no audible noise is emitted from the system. The former is accomplished by incorporating a very soft flexible shaft and the latter by replacing the flexible shaft with a solid shaft, which guarantees high torsional stiffness. Experimental results showed that by implementing each of the above solutions, in identical situations, the audible noise is eliminated from the originally noisy system.

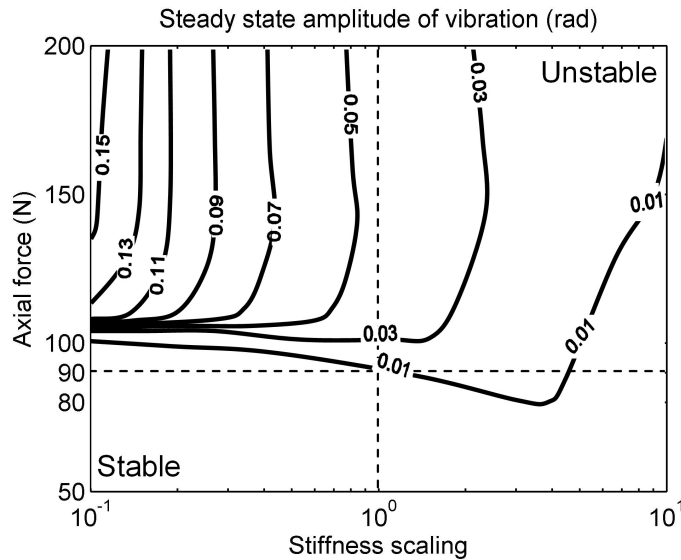


Figure 4-28: The effects of coupling stiffness and axial loading on the dynamic behavior of the lead screw - Gearbox output angular velocity 40 (rad/s)

4.6 Conclusions

In this chapter, a two-step identification/fine-tuning approach is developed to estimate various friction and damping parameters of the system. In the first step, using the steady-sliding test results, the velocity effects (*i.e.* damping and velocity-dependent parts of friction) were separated from the force effects (*i.e.* coulomb coefficient of friction) and appropriate parameters were estimated using the least squares technique. Then, using the open-loop test results in which limit cycles were observed, effective load-dependent torsional stiffness of the lead screw system was estimated by minimizing a cost function that quantified the difference between measured and calculated displacements and velocities. In this step, friction and damping parameters were also adjusted so that maximum conformity between measurements and simulation results was achieved. The presented numerical simulations showed the accuracy of the identified mathematical model of the lead screw system under a wide range axial loading and input speed settings.

Parameter studies were performed to assess the effects of lead screw rotational damping and coupling torsional stiffness on the onset of instabilities. Simulation results showed that by increasing the damping, instabilities occur at higher levels of applied force. In addition, it was shown that the torsional stiffness of the coupling could change the axial loading range (dependent on the input speed) where the system generates significant audible noise.

Chapter 5

Negative Damping

The conversion of rotary to translational motion in a lead screw system occurs at the meshing lead screw and nut threads. The contacting threads slide against each other creating a friction force opposing the direction of motion. The friction-induced instability mechanisms in dynamical systems were introduced in Chapter 2. In this chapter, the role of the velocity-dependent friction coefficient on the stability of lead screw systems is studied. As observed and reported in numerous previous works found in the literature, a decreasing coefficient of friction with relative sliding velocity can effectively act as a source of *negative damping* causing instabilities that lead to self-excited vibration¹. In this study, the 1-DOF model of Section 3.3 is used, which captures all of the essential features of the system dynamics pertaining to the negative damping instability mechanism.

The equation of motion of the 1-DOF lead screw model is presented in Section 5.1. In Section 5.2, eigenvalue analysis method is used to study the local stability of the steady-sliding state and to derive parametric conditions for the negative damping instability mechanism. This study is expanded in Section 5.3, using the method of first order averaging. A complete picture of the stability properties of the system is obtained in this section. The results from the averaging analysis can also be used to predict the amplitude of vibrations when instability occurs and to study the effect of various system parameters on the steady state vibrations. This concept is important in understanding the role of friction-induced vibration on the generation of audible noise from a lead screw drive mechanism. A summary of results and conclusions is given in Section 5.3.

5.1 Equation of Motion

To study the negative damping instability mechanism, the 1-DOF model of Section 3.3 is chosen.

¹ See Section 2.1.1.

Neglecting F_0 and T_0 for simplicity, (3.13) becomes

$$\Gamma\ddot{\theta} + k\theta + c\dot{\theta} = k\theta_i - \xi R \quad (5.1)$$

where

$$\Gamma = I - r_m \tan \lambda \xi m \quad (5.2)$$

and ξ is given by (3.14). Also, the velocity-dependent coefficient of friction is defined by (3.10).

Let $z = \theta - \theta_i$ then $\dot{z} = \dot{\theta} - \omega$ and $\ddot{z} = \ddot{\theta}$ where $\omega = d\theta_i/dt$ is a constant representing the input angular velocity. Substituting this change of variable into (5.1), gives

$$\Gamma\ddot{z} + c\dot{z} + kz = -c\omega - \xi R \quad (5.3)$$

At steady-sliding we have $\ddot{z} = 0$, $\dot{z} = 0$, and $z = z_0$. Substituting these values in (5.3) yields

$$z_0 = -\frac{c\omega + \xi_0 R}{k} \quad (5.4)$$

where

$$\xi_0 = r_m \frac{\mu_0 \operatorname{sgn}(R\omega) - \tan \lambda}{1 + \mu_0 \operatorname{sgn}(R\omega) \tan \lambda} \quad (5.5)$$

and

$$\mu_0 = \mu_1 + \mu_2 e^{-r_0|\omega|} + \mu_3 |\omega| \quad (5.6)$$

The change of variable $u = z - z_0$ converts (5.3) to

$$\Gamma\ddot{u} + c\dot{u} + ku = (\xi_0 - \xi)R \quad (5.7)$$

Also, (3.10) becomes

$$\mu(\dot{u}) = \mu_1 + \mu_2 e^{-r_0|\dot{u} + \omega|} + \mu_3 |\dot{u} + \omega| \quad (5.8)$$

Furthermore, the equation for the contact force, which was given by (3.16), is simplified to

$$N = \frac{\Gamma_0 R + m r_m \tan \lambda (ku + c\dot{u})}{(\cos \lambda + \mu_s \sin \lambda) \Gamma} \quad (5.9)$$

where Γ_0 is found from (5.2) by replacing ξ with ξ_0 and the abbreviation (3.15) is now written as

$$\mu_s(u, \dot{u}) = \mu(\dot{u}) \operatorname{sgn}(N(u, \dot{u})) \operatorname{sgn}(\dot{u} + \omega) \quad (5.10)$$

5.2 Eigenvalue Analysis

The equations of motion in state-space form can be formulated by the following change of variables

$$y_1 = u, \quad y_2 = \dot{u} \quad (5.11)$$

Assuming $\Gamma \neq 0$, (5.7) is represented by two first-order differential equations

$$\begin{cases} \dot{y}_1 = y_2 \\ \dot{y}_2 = \frac{-ky_1 - cy_2 - (\xi - \xi_0)R}{\Gamma} \end{cases} \quad (5.12)$$

The stability of the system's fixed point (*i.e.* the origin) can be locally evaluated by calculating the eigenvalues of the Jacobian matrix of (5.12). Rewriting (5.12) as $\dot{\mathbf{Y}} = \mathbf{f}(\mathbf{Y})$ where $\mathbf{Y} = [y_1 \quad y_2]^T$ and $\mathbf{f} = [f_1(\mathbf{Y}) \quad f_2(\mathbf{Y})]^T$, the Jacobian matrix is written as

$$\mathbf{A} = \left. \frac{\partial \mathbf{f}}{\partial \mathbf{Y}} \right|_{\mathbf{Y}=0} \quad (5.13)$$

Assuming ω and R to be away from zero, carrying out the differentiations yields

$$\mathbf{A} = \begin{bmatrix} 0 & 1 \\ -\frac{k}{\Gamma_0} & -\frac{c + \hat{c}}{\Gamma_0} \end{bmatrix}, \Gamma_0 \neq 0 \quad (5.14)$$

where $\Gamma_0 = I - r_m \tan \lambda \xi_0 m$ and

$$\hat{c} = \frac{r_m (1 + \tan^2 \lambda) R}{(1 + \mu_0 \operatorname{sgn}(R\omega) \tan \lambda)^2} d_\mu \quad (5.15)$$

where d_μ is the gradient of the coefficient of friction curve vs. relative velocity and is given by

$$d_\mu = -r_0 \mu_2 e^{-r_0 |\omega|} + \mu_3 \quad (5.16)$$

Note that \hat{c} is the equivalent damping coefficient due to the velocity dependent friction and

becomes negative if $d_\mu < 0$. The eigenvalues of the Jacobian matrix evaluated at the fixed point (*i.e.* A) are given by

$$e_1, e_2 = -\frac{c + \hat{c}}{2\Gamma_0} \pm \frac{1}{2|\Gamma_0|} \sqrt{(c + \hat{c})^2 - 4k\Gamma_0} \quad (5.17)$$

When $\Gamma_0 > 0$ ¹, the steady sliding fixed point becomes unstable if

$$c + \hat{c} < 0 \quad (5.18)$$

The above instability threshold can be stated alternatively in terms of the applied axial force, R . The system is unstable if

$$|R| > -c \frac{(1 + \mu_0 \operatorname{sgn}(R\omega) \tan \lambda)^2}{r_m (1 + \tan^2 \lambda) d_\mu} \text{ and } d_\mu < 0 \quad (5.19)$$

Stable/unstable regions according to (5.19) for varying values of R and μ_3 is shown schematically in Figure 5-1.

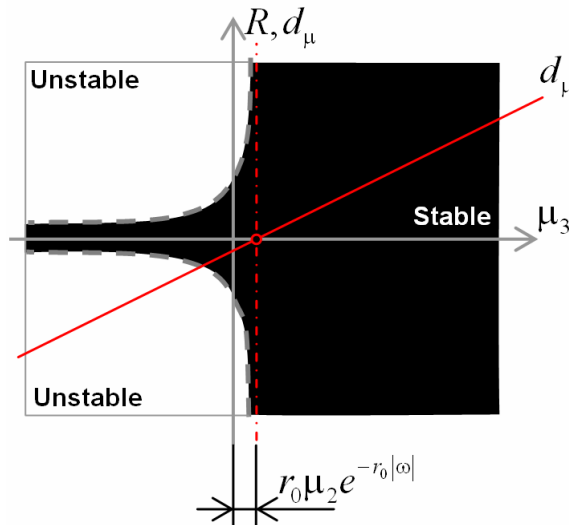


Figure 5-1: Local stability of fixed points of the 1-DOF lead screw system.

¹ Violation of this inequality may also lead to instability. In Chapter 6, this type of instability is discussed in detail.

Expectedly, when negative friction damping is present ($d_\mu < 0$), there is a limiting value of axial force, beyond which the system becomes unstable. This limit proportionally increases by increasing the damping in the lead screw supports. It is interesting to note that these findings are in agreement with the experimental results reported in Chapter 4.

5.2.1 Numerical Examples

The parameter values used in the numerical examples presented here are given in Table 5-1. Most of these values are taken from experimental study of Chapter 4 given in Table 4-1 and Table 4-3.

Table 5-1: Parameter values used in the simulations

Parameter	Value	Parameter	Value
d_m	10.37 mm	μ_1	0.218
λ	5.57°	μ_2	0.0203
I	$3.12 \times 10^{-6} \text{ kg.m}^2$	μ_3	$-4.47 \times 10^{-4} \text{ s/rad}$
k	1 N.m/rad	r_0	0.38 rad/s
c	$20 \times 10^{-5} \text{ Nms/rad}$	R	$\pm 100 \text{ N}$
m	3.8 kg	ω	$\pm 40 \text{ rad/s}$

For an axial force of $R = \pm 100 \text{ N}$ and input angular velocity of $\omega = \pm 40 \text{ rad/s}$, the critical damping coefficients, $c = c_{cr}$, according to (5.19) are found as

$$\text{If } \text{sgn}(R\omega) = +1 \text{ then } c_{cr} \approx 2.25 \times 10^{-4}$$

$$\text{If } \text{sgn}(R\omega) = -1 \text{ then } c_{cr} \approx 2.43 \times 10^{-4}$$

Figure 5-2 and Figure 5-3 show the system trajectories for $c < c_{cr}$ and $c > c_{cr}$, respectively. In each simulation the initial conditions was $\mathbf{y}_0 = (0, -\omega)$. As expected, for the damping level below (above) the critical value, the fixed point is unstable (stable). In the unstable cases, system trajectories are attracted to a limit cycle. Using the method of averaging, in the next section the periodic solutions of the nonlinear equation of motion (limit cycles) are studied and the amplitude of steady-state vibrations are estimated.

It is interesting to note that results in Figure 5-2 show that, in cases where force and angular velocity have the same sign (*i.e.* force assisting the motion), the displacement amplitude is considerably smaller than cases where the axial force resists the motion (*i.e.* $R\omega < 0$).

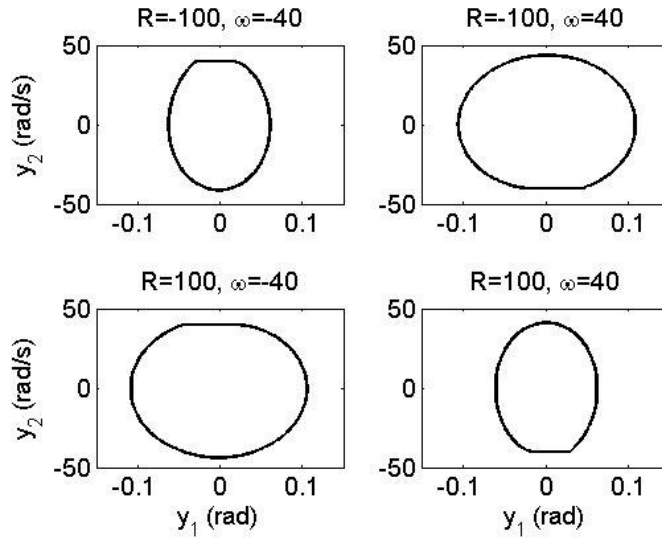


Figure 5-2: system trajectories for $c = 2 \times 10^{-4} < c_{cr}$; unstable steady-sliding fixed point (0,0)

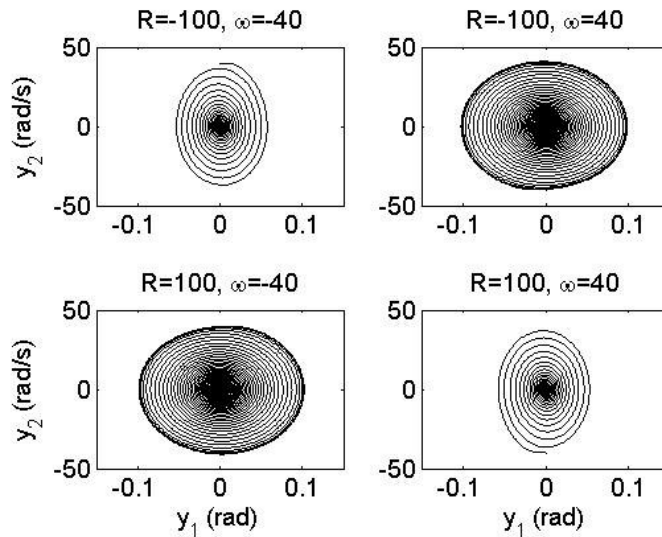


Figure 5-3: system trajectories for $c = 3 \times 10^{-4} > c_{cr}$; stable steady-sliding fixed point (0,0)

5.3 First-order Averaging

The eigenvalue analysis of the previous section does not reveal any information regarding the behavior of the nonlinear system once instability occurs. The existence of periodic solutions (limit cycles), region of attraction of the stable trivial solution, and the effects of system parameters on these features as well as the size of the limit cycles (amplitude of steady-state vibrations) are important

issues that are addressed in this section. The powerful method of averaging is the perturbation technique utilized here to study the behavior of the 1-DOF lead screw model as a *weakly nonlinear system*. For the lead screw equation of motion to be considered as a weakly nonlinear system, the friction and damping coefficients must be small. The relative smallness requirement of these parameters will be put into a more concrete setting later in the section.

Before performing the averaging, (5.7) must be transformed to *standard form* [35]. To that end, some simplifications are necessary. In the following sections, first the equation of motion is simplified and then converted into a non-dimensionalized form. In the next step, a small parameter, ε , is introduced and the new dimensionless parameters are ordered to reach an approximate weakly nonlinear equation of motion accurate up to $O(\varepsilon)$.

5.3.1 Assumptions

As mentioned earlier, the current study is only concerned with the instability caused by negative damping. Thus, it is assumed that $\Gamma > 0$ for all \dot{u} .

From (5.10), it is easy to see that the equation of motion of the 1-DOF lead screw has a discontinuity whenever $\dot{\theta}$ crosses zero. To deal with this situation, the coefficient of friction is smoothed at zero relative velocity (*i.e.* $\dot{u} + \omega = 0$) according to

$$\mu(\dot{u}) = \left(\mu_1 + \mu_2 e^{-r_1|\dot{u}+\omega|} + \mu_3 |\dot{u} + \omega| \right) \left(1 - e^{-r_1|\dot{u}+\omega|} \right) \quad (5.20)$$

where $r_1 > 0$ is a relatively large number. Note that in Chapter 4, a similar friction-velocity relationship was used¹. Substituting (5.20) into (5.10) yields

$$\mu_s(u, \dot{u}) = \left(\mu_1 + \mu_2 e^{-r_1|\dot{u}+\omega|} + \mu_3 |\dot{u} + \omega| \right) \left(1 - e^{-r_1|\dot{u}+\omega|} \right) \text{sgn}(\dot{u} + \omega) \text{sgn}(N(u, \dot{u})) \quad (5.21)$$

It must be noted that, although (5.21) is discontinuous at $N(u, \dot{u}) = 0$, the differential equation of the system, given by (5.7), is continuous, since in its original form, given by (3.11) and (3.12), only the product μN appears.

From (5.9), we have

¹ Similar smoothed friction models were used by others, see for example [34,82,83].

$$\text{sgn } N = \text{sgn} \left(\frac{\Gamma_0 R}{m r_m \tan \lambda} + k u + c \dot{u} \right) \quad (5.22)$$

5.3.2 Equation of Motion in Standard Form

The first step towards transforming the equation of motion to a proper form for averaging is to non-dimensionalize the parameters. This is an important step to appropriately “order” each parameter according to its “size”. Expanding (5.7), yields

$$\left(I - r_m^2 \tan \lambda \frac{\mu_s - \tan \lambda}{1 + \mu_s \tan \lambda} m \right) \ddot{u} + c \dot{u} + k u = r_m \left(\frac{\mu_0 \text{sgn}(R\omega) - \tan \lambda}{1 + \mu_0 \text{sgn}(R\omega) \tan \lambda} - \frac{\mu_s - \tan \lambda}{1 + \mu_s \tan \lambda} \right) R \quad (5.23)$$

Introduce the dimensionless time $\tau = \Omega t$, where

$$\Omega = \sqrt{k/I} \quad (5.24)$$

The derivative with respect to τ is given as

$$\frac{d(\cdot)}{dt} = \Omega \frac{d(\cdot)}{d\tau} \quad (5.25)$$

Also, define non-dimensional parameters

$$\hat{m} = r_m^2 \frac{m}{I} \tan \lambda \quad (5.26)$$

$$\tilde{c} = \frac{c}{\sqrt{kI}} \quad (5.27)$$

$$\hat{R} = \frac{\Omega}{|\omega|} \frac{r_m}{k} R, \omega \neq 0 \quad (5.28)$$

Using these new parameters, (5.23) is transformed to

$$\left(1 - \frac{\mu_s - \tan \lambda}{1 + \mu_s \tan \lambda} \hat{m} \right) u'' + \tilde{c} u' + u = \frac{|\omega|}{\Omega} \left(\frac{\mu_0 \text{sgn}(R\omega) - \tan \lambda}{1 + \mu_0 \text{sgn}(R\omega) \tan \lambda} - \frac{\mu_s - \tan \lambda}{1 + \mu_s \tan \lambda} \right) \hat{R} \quad (5.29)$$

where prime denotes derivate with respect to τ . Now that the equation of motion is in its non-

dimensionalized form, based on physical insight, parameters are ordered using the small positive parameter ε . The new parameters,

$$\hat{\mu}_s = \frac{\mu_s}{\tan \lambda}, \hat{\mu}_0 = \frac{\mu_0}{\tan \lambda} \quad (5.30)$$

$$\hat{c} = \frac{\tilde{c}}{\tan \lambda} \quad (5.31)$$

together with \hat{m} and \hat{R} are all assumed to be $O(1)$ with respect to ε where $\varepsilon = \tan \lambda$ is taken as the small parameter. Assuming, $|\omega|/\Omega = \rho\varepsilon$ where ρ is $O(1)$ and scaling u as

$$u = \varepsilon\rho v \quad (5.32)$$

gives

$$[1 - \varepsilon\Xi_1(v, v', \varepsilon)\hat{m}]v'' + \varepsilon\hat{c}v' + v = \varepsilon\hat{R}[\Xi_0(\varepsilon) - \Xi_1(v', \varepsilon)] \quad (5.33)$$

where

$$\Xi_0(\varepsilon) = \frac{\text{sgn}(R\omega)\hat{\mu}_0 - 1}{1 + \varepsilon^2 \text{sgn}(R\omega)\hat{\mu}_0} \quad (5.34)$$

$$\Xi_1(v, v', \varepsilon) = \frac{\hat{\mu}_s(v, v', \varepsilon) - 1}{1 + \varepsilon^2 \hat{\mu}_s(v', \varepsilon)} \quad (5.35)$$

Also, the expression for the *signed* velocity-dependent coefficient of friction, $\hat{\mu}_s(v', \varepsilon)$, in terms new dimensionless parameters, is

$$\begin{aligned} \hat{\mu}_s(v, v', \varepsilon) = & \left(\hat{\mu}_1 + \hat{\mu}_2 e^{-\hat{\tau}_0 \|\omega|v' + \omega|} + \hat{\mu}_3 \|\omega|v' + \omega| \right) \left(1 - e^{-\hat{\tau}_1 \|\omega|v' + \omega|} \right) \\ & \times \text{sgn}(\|\omega|v' + \omega|) \text{sgn} \left(\frac{\hat{R}}{\hat{m}} - \varepsilon\Xi_0(\varepsilon)\hat{R} + v + \varepsilon\hat{c}v' \right) \end{aligned} \quad (5.36)$$

where $\hat{\mu}_i = \mu_i / \tan \lambda$, $i = 1, 2, 3$. After rearranging, (5.33) becomes;

$$v'' + v = \varepsilon f(v, v', \varepsilon) \quad (5.37)$$

where,

$$f(v, v', \varepsilon) = -(1 - \varepsilon \Xi_1 \widehat{m})^{-1} [\widehat{c}v' + \widehat{m} \Xi_1 v + \widehat{R}(\Xi_1 - \Xi_0)] \quad (5.38)$$

It is important to notice that, despite the presence of the two sign functions (*i.e.* $\text{sgn}(v' + 1)$ and $\text{sgn}\left(\frac{\widehat{R}}{\widehat{m}} - \varepsilon \frac{\widehat{\mu}_0 - 1}{1 + \varepsilon^2 \widehat{\mu}_0} \widehat{R} + v + \varepsilon \widehat{c}v'\right)$) in (5.38), $f(v, v', \varepsilon)$ is bounded and Lipschitz continuous with respect to its arguments for $(v, v', \varepsilon) \in D \times [0, \varepsilon_0]$, and D is any compact subset of \mathfrak{R}^2 and $\varepsilon_0 > 0$ is some constant. To show this, we only need to investigate $f(v, v', \varepsilon)$ at instances where $v' + 1 = 0$ and $N = 0$ (which is equivalent to $\widehat{R}/\widehat{m} - \varepsilon \Xi_0(\varepsilon) \widehat{R} + v + \varepsilon \widehat{c}v' = 0$). For the first case, notice that $\widehat{\mu}_s(v, -1, \varepsilon) = 0$ and $\widehat{\mu}_s$ is continuous at $v' = -1$, provided that $N \neq 0$. Furthermore

$$\lim_{v' \rightarrow -1^+} \frac{\partial \widehat{\mu}_s(v, v', \varepsilon)}{\partial v'} = \lim_{v' \rightarrow -1^-} \frac{\partial \widehat{\mu}_s(v, v', \varepsilon)}{\partial v'} = (\widehat{\mu}_1 + \widehat{\mu}_2) r_1 \omega \text{sgn}(N), \quad N \neq 0$$

uniformly in ε . Also, $\frac{\partial \widehat{\mu}_s(v, v', \varepsilon)}{\partial v} = 0$ and $\frac{\partial \widehat{\mu}_s(v, v', \varepsilon)}{\partial \varepsilon} = 0$ for all (v, v') in the domain D and $N \neq 0$.

For the second case, let $\delta(v, v', \varepsilon) = \widehat{R}/\widehat{m} - \varepsilon \Xi_0(\varepsilon) \widehat{R} + v + \varepsilon \widehat{c}v'$. Substituting this relationship into (5.38) gives $f(v, v', \varepsilon) = -\varepsilon^{-1} \left\{ \delta [1 - \varepsilon \Xi_1(v, v', \varepsilon) \widehat{m}]^{-1} - (\widehat{R}/\widehat{m} + v) \right\}$. Since $\Xi_1(v, v', \varepsilon)$ is bounded and continuous on $D \times [0, \varepsilon_0] - \{v, v', \varepsilon | \delta(v, v', \varepsilon) \neq 0\}$, and also since $1 - \varepsilon \Xi_1(v, v', \varepsilon) \widehat{m}$ is away from zero¹, $f(v, v', \varepsilon)$ is continuous on $D \times [0, \varepsilon_0]$. Also it is easy to see that $\lim_{\delta \rightarrow 0^+} \frac{\partial f}{\partial v}(v, v', \varepsilon)$,

$$\lim_{\delta \rightarrow 0^-} \frac{\partial f}{\partial v}(v, v', \varepsilon), \quad \lim_{\delta \rightarrow 0^+} \frac{\partial f}{\partial v'}(v, v', \varepsilon), \quad \lim_{\delta \rightarrow 0^-} \frac{\partial f}{\partial v'}(v, v', \varepsilon), \quad \lim_{\delta \rightarrow 0^+} \frac{\partial f}{\partial \varepsilon}(v, v', \varepsilon), \quad \text{and} \quad \lim_{\delta \rightarrow 0^-} \frac{\partial f}{\partial \varepsilon}(v, v', \varepsilon)$$

exist and are bounded, thus confirming the Lipschitz continuity of (5.38) with respect to its arguments.

To transform (5.37) into the standard form, the following change of variables is used

$$v = a \cos \varphi, \quad v' = -a \sin \varphi \quad (5.39)$$

This leads to

¹ This is the consequence of initial assumption $\Gamma > 0$ (see section 5.3.1).

$$a' = -\varepsilon f(a \cos \varphi, -a \sin \varphi, \varepsilon) \sin \varphi \quad (5.40)$$

$$\varphi' = 1 - \frac{\varepsilon}{a} f(a \cos \varphi, -a \sin \varphi, \varepsilon) \cos \varphi \quad (5.41)$$

Since φ' is away from zero¹, dividing (5.40) by (5.41) yields

$$\frac{da}{d\varphi} = -\varepsilon \frac{f(a \cos \varphi, -a \sin \varphi, \varepsilon) \sin \varphi}{1 - \frac{\varepsilon}{a} f(a \cos \varphi, -a \sin \varphi, \varepsilon) \cos \varphi} \equiv \varepsilon g(\varphi, a, \varepsilon) \quad (5.42)$$

5.3.3 First Order Averaging

In this section, the averaging method ([35]) is applied to (5.42). To obtain the first order averaged equations, the right-hand side of (5.42) must be averaged over a period (*i.e.* $T = 2\pi$) while keeping a constant². This gives

$$\begin{aligned} a' &= \frac{\varepsilon}{2\pi} \int_0^{2\pi} g(\varphi, a, 0) d\varphi \\ &= -\frac{\varepsilon}{2\pi} \int_0^{2\pi} f(a \cos \varphi, -a \sin \varphi, 0) \sin \varphi d\varphi \end{aligned} \quad (5.43)$$

There are a few variations on the basic theorem for the periodic first order averaging [35,44, 84]. In Appendix B, a slightly modified version of the theorem proven in [44] is presented and proved which establishes the error estimate of the averaged system, (5.43), with respect to the original differential equation, (5.42). Substituting (5.39) into (5.38) and then substituting the result into (5.43) gives

¹ Note that the change of variable (5.39) is only allowed in situations where the RHS of (5.41) remains bounded as a approaches zero [84]. Here, this change of variables is allowed when R is away from zero, since after expanding (5.38) using power series, we get $f(a \cos \varphi, -a \sin \varphi, \varepsilon) = a\tilde{f}(a, \varphi, \varepsilon)$ for some bounded function $\tilde{f}(a, \varphi)$ for $0 \leq a < a_0$ and for sufficiently small $a_0 < 1$ such that $N \neq 0$.

² For simplicity of notation, from this point on, prime denotes differentiation with respect to φ .

$$\begin{aligned}
a' = & -\frac{\varepsilon}{2\pi} \int_0^{2\pi} (\widehat{c}a \sin^2 \varphi + \widehat{m}a \sin \varphi \cos \varphi + \widehat{\mu}_0 \widehat{R} \sin \varphi) d\varphi \\
& + \frac{\varepsilon}{2\pi} \int_0^{2\pi} (\widehat{m}a \sin \varphi \cos \varphi + \widehat{R} \sin \varphi) \widehat{\mu}_s d\varphi
\end{aligned} \tag{5.44}$$

After carrying out the integration of the first term, becomes

$$a' = -\varepsilon \frac{\widehat{c}a}{2} + \frac{\varepsilon}{2\pi} \int_0^{2\pi} (\widehat{m}a \sin \varphi \cos \varphi + \widehat{R} \sin \varphi) \widehat{\mu}_s(\varphi, a) d\varphi \tag{5.45}$$

where

$$\begin{aligned}
\widehat{\mu}_s(\varphi, a) = & \left(\widehat{\mu}_1 + \widehat{\mu}_2 e^{-r_0|\omega - |\omega|a \sin \varphi|} + \widehat{\mu}_3 |\omega - |\omega|a \sin \varphi| \right) \left(1 - e^{-r_1|\omega - |\omega|a \sin \varphi|} \right) \\
& \times \operatorname{sgn}(\omega - |\omega|a \sin \varphi) \operatorname{sgn} \left(\frac{\widehat{R}}{\widehat{m}} + a \cos \varphi \right)
\end{aligned} \tag{5.46}$$

The averaged differential equation given by (5.45) is too complicated to be approached analytically. Limiting our study to the situations where $\omega > 0$ and also where $R > 0$ is large enough such that N remains positive over the domain of interest, $\widehat{\mu}_s$ simplifies to

$$\widehat{\mu}_s(\varphi, a) = \left(\widehat{\mu}_1 + \widehat{\mu}_2 e^{-r_0\omega|1-a \sin \varphi|} + \widehat{\mu}_3 \omega |1-a \sin \varphi| \right) \left(1 - e^{-r_1\omega|1-a \sin \varphi|} \right) \operatorname{sgn}(1-a \sin \varphi) \tag{5.47}$$

Substituting (5.47) into (5.45) and simplifying yields

$$a' = -\varepsilon \frac{\widehat{c}a}{2} + \frac{\varepsilon}{2\pi} \widehat{R} \int_0^{2\pi} \sin \varphi \widehat{\mu}_s(\varphi, a) d\varphi \tag{5.48}$$

In addition to the assumption of $N > 0$, if the maximum amplitude is limited to 1, *i.e.* $0 \leq a \leq 1$, (5.47) further simplifies to

$$\widehat{\mu}_s(\varphi, a) = \left(\widehat{\mu}_1 + \widehat{\mu}_2 e^{r_0\omega a \sin \varphi} - \widehat{\mu}_3 a \sin \varphi \right) \left(1 - r_2 e^{r_1\omega a \sin \varphi} \right) \tag{5.49}$$

where $r_2 = e^{-r_1\omega}$ and also

$$\widehat{\mu}_1 = \widehat{\mu}_1 + \widehat{\mu}_3 \omega \tag{5.50}$$

$$\widehat{\mu}_2 = \widehat{\mu}_2 e^{-r_0\omega} \tag{5.51}$$

$$\widehat{\mu}_3 = \widehat{\mu}_3 \omega \quad (5.52)$$

Substituting (5.49) into (5.48) and simplifying gives

$$\begin{aligned} a' = & -\varepsilon \frac{(\widehat{c} + \widehat{\mu}_3 \widehat{R})a}{2} + \frac{\varepsilon}{2\pi} \widehat{\mu}_2 \widehat{R} \int_0^{2\pi} \sin \varphi e^{r_0 \omega a \sin \varphi} d\varphi - \frac{\varepsilon}{2\pi} r_2 \widehat{\mu}_1 \widehat{R} \int_0^{2\pi} \sin \varphi e^{r_1 \omega a \sin \varphi} d\varphi \\ & + \frac{\varepsilon}{2\pi} r_2 \widehat{\mu}_3 a \widehat{R} \int_0^{2\pi} \sin^2 \varphi e^{r_1 \omega a \sin \varphi} d\varphi - \frac{\varepsilon}{2\pi} r_2 \widehat{\mu}_2 \widehat{R} \int_0^{2\pi} \sin \varphi e^{(r_0 + r_1) \omega a \sin \varphi} d\varphi \end{aligned} \quad (5.53)$$

Carrying out the rest of the integrations, one finds

$$\begin{aligned} a' = & -\varepsilon \frac{\widehat{c} + \widehat{\mu}_3 \widehat{R}}{2} a + \varepsilon \widehat{\mu}_2 \widehat{R} \Lambda_{1,0}(r_0 \omega a) - \varepsilon r_2 \widehat{\mu}_1 \widehat{R} \Lambda_{1,0}(r_1 \omega a) \\ & + \varepsilon r_2 \widehat{\mu}_3 a \widehat{R} \Lambda_{2,0}(r_1 \omega a) - \varepsilon r_2 \widehat{\mu}_2 \widehat{R} \Lambda_{1,0}((r_0 + r_1) \omega a) \end{aligned} \quad (5.54)$$

where

$$\Lambda_{n,m}(\zeta) = \frac{1}{2\pi} \int_0^{2\pi} \sin^n \phi \cos^m \phi e^{\zeta \sin \phi} d\phi \quad (5.55)$$

General formulae for (5.55) are derived in Appendix C. For the integrals in (5.54), one finds

$$\Lambda_{1,0}(\zeta) = \sum_{n=1}^{\infty} \frac{n}{2^{2n-1} (n!)^2} \zeta^{2n-1} \quad (5.56)$$

$$\Lambda_{2,0}(\zeta) = \sum_{n=1}^{\infty} \frac{(2n-1)n}{2^{2n-1} (n!)^2} \zeta^{2n-2} \quad (5.57)$$

In the next section, steady state solutions of (5.54) are studied. It must be noted that, in cases where stable (unstable) non-trivial solutions exist and $a = a^* \leq 1$, the above averaging process guarantees that the original system, (5.29), has stable (unstable) limit cycle in an $O(\varepsilon)$ neighborhood of the circle $r = \omega a^* / \Omega$, with a period $O(\varepsilon)$ to 2π for sufficiently small $\varepsilon > 0$ [84].

5.3.4 Steady State Solutions

Substituting (5.56) and (5.57) into (5.54) and rearranging

$$\begin{aligned}
a' = & -\varepsilon \frac{\widehat{c} + \widehat{\mu}_3 \widehat{R}}{2} a \\
& + \varepsilon \widehat{R} \sum_{n=1}^{\infty} \frac{n \omega^{2n-2}}{2^{2n-1} (n!)^2} \left(r_2 \widehat{\mu}_3 (2n-1) r_1^{2n-2} + \widehat{\mu}_2 \omega r_0^{2n-1} - r_2 \widehat{\mu}_1 \omega r_1^{2n-1} - r_2 \widehat{\mu}_2 \omega (r_0 + r_1)^{2n-1} \right) a^{2n-1}
\end{aligned} \tag{5.58}$$

It is obvious that $a = 0$ is the trivial solution. To determine its stability, da'/da is derived and evaluated at $a = 0$. From (5.58)

$$\left. \frac{da'}{da} \right|_{a=0} = \frac{\varepsilon}{2} \left[-(\widehat{c} + \widehat{\mu}_3 \widehat{R}) + \widehat{R} (r_2 \widehat{\mu}_3 + \widehat{\mu}_2 \omega r_0 - r_2 \widehat{\mu}_1 \omega r_1 - r_2 \widehat{\mu}_2 \omega (r_0 + r_1)) \right] \tag{5.59}$$

From (5.59), one can find a parametric condition for the stability of the trivial solution (*i.e.* $\left. \frac{da'}{da} \right|_{a=0} < 0$), which is found to be

$$\widehat{c} > \widehat{R} \left((r_2 - 1) \widehat{\mu}_3 + \widehat{\mu}_2 \omega r_0 - r_2 \widehat{\mu}_1 \omega r_1 - r_2 \widehat{\mu}_2 \omega (r_0 + r_1) \right) \tag{5.60}$$

By substituting the original system parameters, (5.60) is simplified to

$$c > c_{cr} = -r_m R \left. \frac{\partial \mu}{\partial u} \right|_{u=0} \tag{5.61}$$

It is interesting to note that, (5.61) is accurate to $O(\varepsilon^2)$ when compared to what was found from linear eigenvalue analysis ((5.15) and (5.16)):

$$c > -r_m R \frac{1 + \tan^2 \lambda}{(1 + \mu_0 \tan \lambda)^2} \left. \frac{\partial \mu}{\partial y_2} \right|_{y_2=0}, \quad R > 0, \omega > 0 \tag{5.62}$$

Unfortunately, the other possible solutions (*i.e.* stable or unstable limit cycles) can only be found numerically due to the complexity of the averaged equations. However, some important insights can be gained by examining (5.58). In Appendix D, it is shown that, depending on the system parameters one of the following three cases defines the dynamic behavior of the averaged system:

1. The trivial solution is stable and no other solution exists.
2. The trivial solution is stable and is surrounded by an unstable limit cycle, which defines the region of attraction of the trivial solution. The unstable limit cycle is inside a stable limit cycle.

3. The trivial solution is unstable and is surrounded by a stable limit cycle.

Two natural extensions of the averaging results of this section are included as appendices. In Appendix E, the possibility of using higher-order averaging to improve the accuracy of the predicted vibration amplitudes of the 1-DOF is shown. The method of first-order averaging is applied to a 2-DOF model of Section 3.6 in Appendix F.

5.3.5 Numerical Simulation Results

In this section, a few numerical examples are presented. In these examples the system's parameter values, unless otherwise specified, are those listed in Table 5-2. For the parameter values and the initial conditions selected, all simulation results satisfy $v' \geq -1$ and $N > 0$ conditions. As a result, the simplified averaged system equation given by (5.53) or (5.58) is used. Computationally, it is much more efficient to use (5.53) instead of the infinite sum of (5.58).

Table 5-2: Parameter values used in the simulations

Parameter	Value	Parameter	Value
d_m	10.37 mm	μ_1	0.218
λ	5.57°	μ_2	0.0203
I	$3.12 \times 10^{-6} \text{ kg.m}^2$	μ_3	$-4.47 \times 10^{-4} \text{ s/rad}$
k	1 N.m/rad	r_0	0.38 rad/s
c	$20 \times 10^{-5} \text{ Nms/rad}$	r_1	2 rad/s
m	1kg	ω	40 rad/s
R	100 N		

Figure 5-4 and Figure 5-5 show comparisons between numerical integration of the approximate (truncated) equation of motion given by

$$v'' + v = \epsilon f(v, v', 0) \quad (5.63)$$

and the fixed points of the averaged amplitude equation, (5.53), for two values of lead screw damping; $c = 2 \times 10^{-4} < c_{cr}$ and $c = 3 \times 10^{-4} > c_{cr}$, respectively. Note that in these figures, both amplitudes are scaled by ω/Ω to reflect the physical system's vibration levels.

Results show very accurate prediction of the steady-state amplitude of vibration by the first order averaging method. However, when compared with the original (untruncated) equation of motion,

(5.37), the averaging results have some differences as shown in Figure 5-6 and Figure 5-7. This deviation is caused by the effects of the higher order terms omitted from the first order averaging process. It must be noted that, the steady-sliding amplitudes of vibration in Figure 5-6 and Figure 5-7 are predicted very accurately by the averaged equation for the parameter values given in Table 5-2.

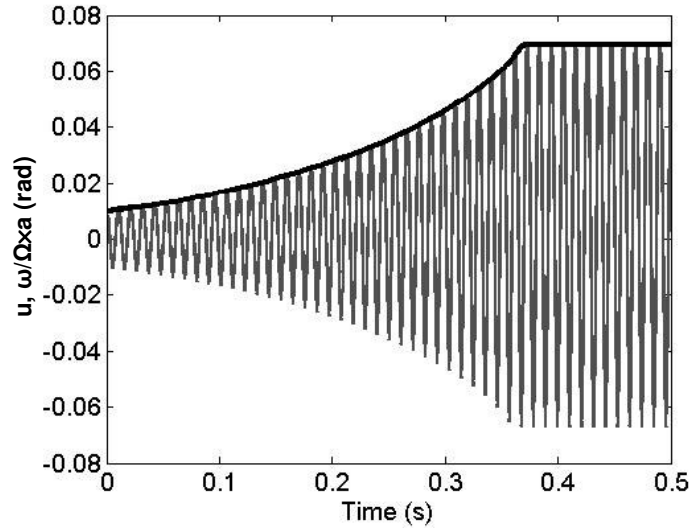


Figure 5-4: First order averaging results. $c=2 \times 10^{-4}$
Grey: truncated equation of motion; Black: amplitude of vibration from first order averaging

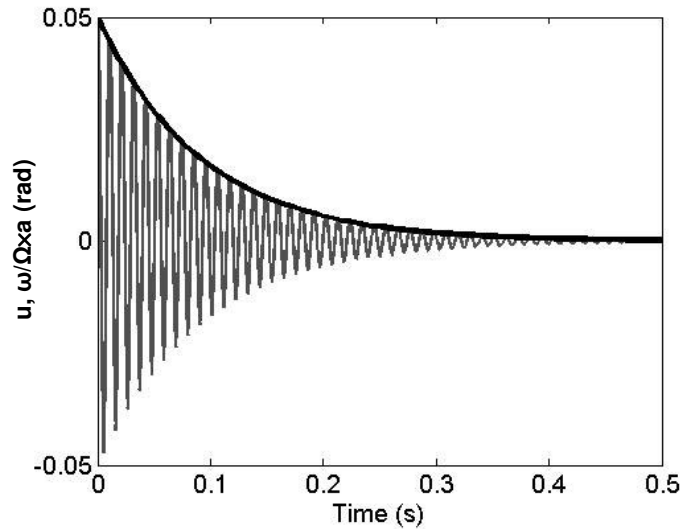


Figure 5-5: First order averaging results. $c=3 \times 10^{-4}$
Grey: truncated equation of motion; Black: amplitude of vibration from first order averaging

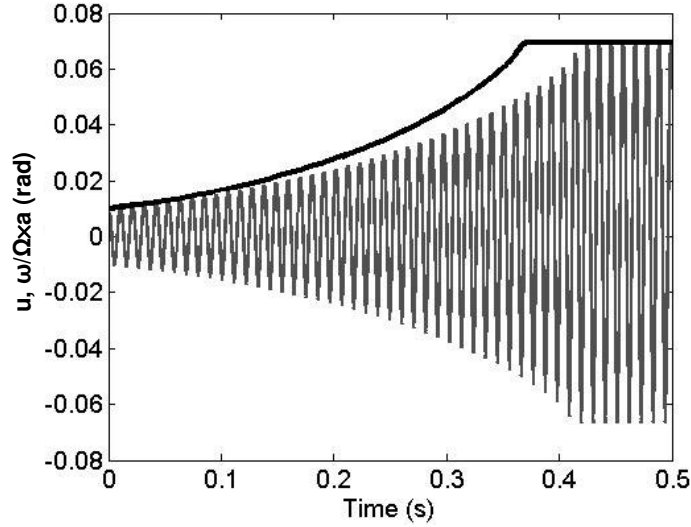


Figure 5-6: First order averaging results. $c=2 \times 10^{-4}$
Grey: original equation of motion; Black: amplitude of vibration from first order averaging

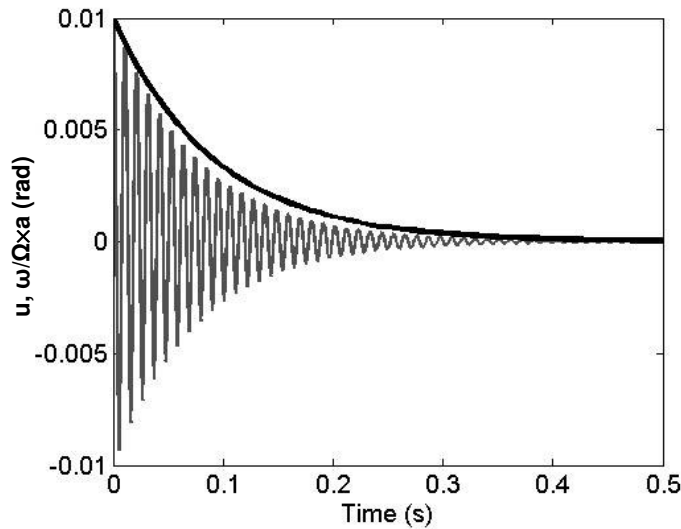


Figure 5-7: First order averaging results. $c=3 \times 10^{-4}$
Grey: original equation of motion; Black: amplitude of vibration from first order averaging

Figure 5-8 shows the bifurcation diagram of the amplitude equation, (5.53), where the damping coefficient, c , is taken as the control parameter. The trivial solution (*i.e.* the fixed point of the original system) undergoes a subcritical pitch-fork bifurcation [36] at approximately $c_{cr} = 2.32 \times 10^{-4} \text{ N.m.s/rad}$. It can be shown that this bifurcation corresponds to a Hopf bifurcation of the original system [36]. The unstable branch, shown by the dotted line, determines the domain of

attraction of the trivial or steady-sliding fixed point.

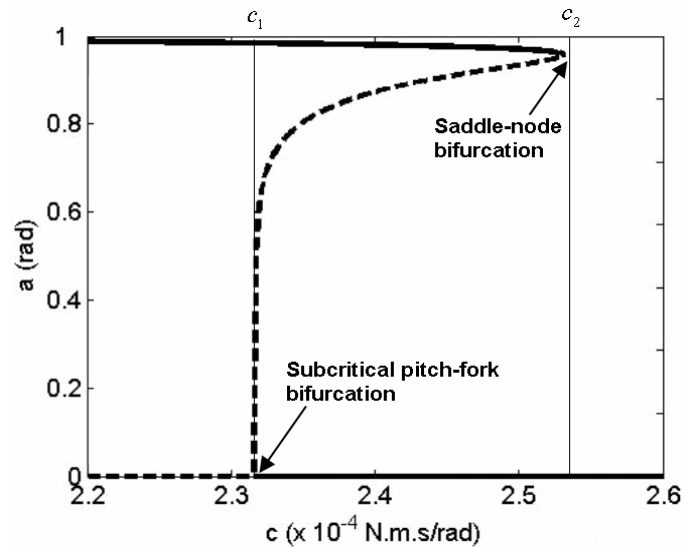


Figure 5-8: Bifurcation diagram of the averaged amplitude equation.
 “—” Stable; “- -” Unstable

The limiting values c_1 and c_2 in Figure 5-8 correspond to the limits discussed in Appendix D, Section D.3.

Figure 5-9 and Figure 5-10 show the effect of Stribeck friction (μ_2) and linear negative friction (μ_3) parameters on the amplitude bifurcation diagram, respectively. In these figure, bifurcation plots are drawn with respect to the applied axial force, R , as the control parameter. As shown, μ_2 controls the domain of attraction of the stable trivial solution without significant change to the limiting value of R . The reason for this is that the term $\mu_2 e^{-r_0 \omega}$ is negligible for the considered values of r_0 and ω (see (5.60)). However, μ_3 directly controls the threshold of instability of the trivial or steady-state solution.

Further examples and discussions are presented in Appendix D.

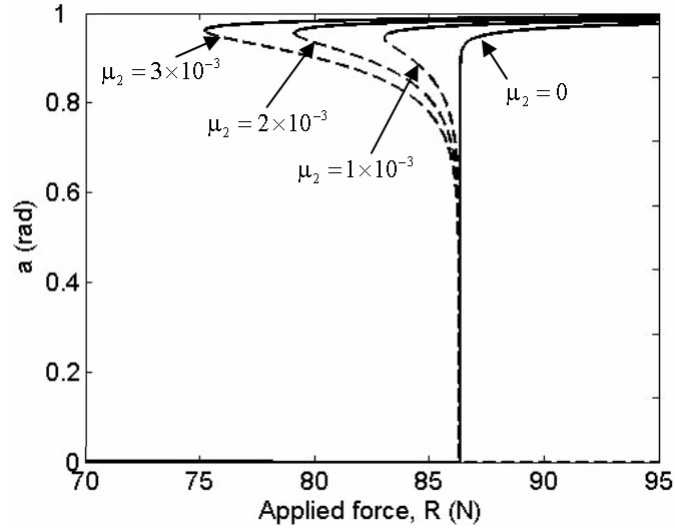


Figure 5-9: Effect of Stribeck friction on bifurcation

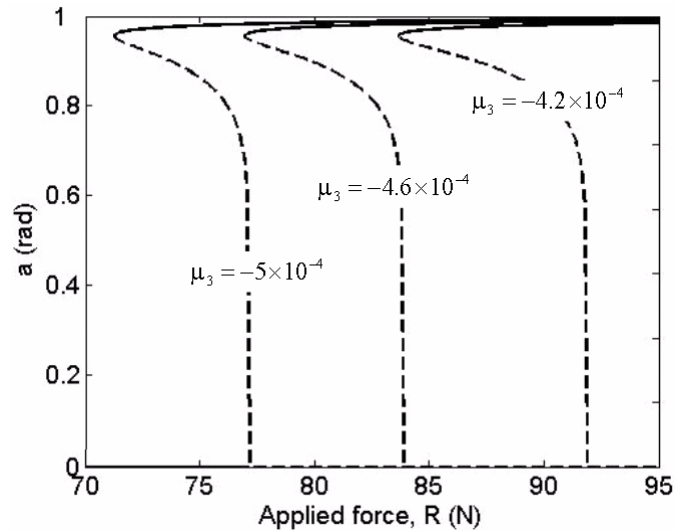


Figure 5-10: Effect of negative damping on bifurcation.

5.4 Conclusions

In this chapter, using the 1-DOF model of a lead screw drive developed in Section 3.3, the instability caused by the negative gradient of the friction coefficient with respect to velocity was studied. The local stability of the steady-sliding fixed point of the system was studied by examining the eigenvalues of the Jacobian of the linearized system. It was shown that the steady-sliding fixed point of the system loses stability if the condition given by either (5.18) or (5.19) is satisfied.

The eigenvalue analysis result was extended by the application of the method of averaging. It was shown (see Appendix D) that depending on the system parameters, one the following cases define the dynamic behavior of the system:

1. The trivial solution is stable and no other solution exists.
2. The trivial solution is stable and is surrounded by an unstable limit cycle that defines the region of attraction of the trivial solution. The unstable limit cycle is inside a stable limit cycle. The presence of Stribeck effect is a necessary condition in this scenario.
3. The trivial solution is unstable and is surrounded by a stable limit cycle.

The numerical simulation results presented, also showed the applicability of the averaging results in approximating the amplitude of periodic vibrations. The accuracy of the approximations – as presented in Appendix E – can be improved by using higher order averaging.

Chapter 6

Kinematic Constraint and Mode Coupling

Instability Mechanisms

In Chapter 2, three friction-induced instability mechanisms were introduced. Negative damping instability was studied in the previous chapter. In this chapter, the two remaining instability mechanisms, *i.e.* “kinematic constraint” and “mode coupling”, are studied. In contrast to the negative damping instability, these two mechanisms can affect a system even when the coefficient of friction is constant. The mode coupling instability mechanism is exclusive to multi-DOF systems.

In Section 6.1, the kinematic constraint instability mechanism is studied using the basic 1-DOF lead screw model of Section 3.3. Mode coupling instability is studied in Sections 6.2 and 6.3 using the 2-DOF models of Section 3.5 and Section 3.6, respectively. In these sections, the kinematic constraint instability is also studied. Mode coupling in the 3-DOF model of Section 3.7 is discussed in Section 6.4. In each section, numerical examples are given to demonstrate the findings. Conclusions drawn in this chapter are reviewed in Section 6.5.

6.1 Kinematic Constraint Instability in 1-DOF Lead Screw Model

To study the kinematic constraint instability, the same 1-DOF model used in the previous chapter is considered here. For simplicity, a constant coefficient of friction is assumed (*i.e.* $\mu = \mu_0 = \mu_1$). The eigenvalues of the Jacobian matrix given by (5.17) are simplified to

$$e_1, e_2 = -\frac{c}{2\Gamma_0} \pm \frac{1}{2|\Gamma_0|} \sqrt{c^2 - 4k\Gamma_0} \quad (6.1)$$

From (6.1), it is evident that regardless of the linear damping ($c \geq 0$), divergence instability occurs

whenever $\Gamma_0 < 0$. In terms of systems' parameters, the fixed point is unstable whenever the following inequalities hold simultaneously:

$$\begin{aligned}
 I) \quad & \mu > \tan \lambda \\
 II) \quad & R\omega > 0 \\
 III) \quad & \Gamma_0 = I - r_m \tan \lambda \xi_0 m < 0
 \end{aligned} \tag{6.2}$$

The first condition in (6.2) is the “self-locking” condition in lead screw drives [5,67]. The second condition states that instability can only occur if the axial force (load) is applied in the direction of motion (assisting)¹. The third condition establishes a limiting ratio between lead screw inertia and the translating mass².

6.1.1 A Note Regarding the Solution of the Equation of Motion

Before presenting a numerical example, it is worthwhile to study the unstable behavior of the system when conditions (6.2) are fulfilled. Setting F_0 and T_0 to zero for simplicity, the contact force given by (3.16) becomes

$$N = \frac{(I - mr_m \tan \lambda \xi_0)R + mr_m \tan \lambda (ku + c\dot{u})}{(\cos \lambda + \mu_s \sin \lambda)(I - mr_m \tan \lambda \xi)} \tag{6.3}$$

where the change of variables (5.11) was used. Limiting our study to a case where $R > 0$ and $\omega > 0$, (5.5) simplifies to

$$\xi_0 = r_m \frac{\mu_0 - \tan \lambda}{1 + \mu_0 \tan \lambda} \tag{6.4}$$

Also, in the case of a constant coefficient of friction with $\dot{u} + \omega > 0$, ξ given by (3.14) reduces to

$$\xi = r_m \frac{\mu_0 \operatorname{sgn}(N) - \tan \lambda}{1 + \mu_0(N) \tan \lambda} \tag{6.5}$$

It can be seen that, under the kinematic constraint instability conditions, if

¹ See Section 6.1.3 below for further discussions.

² This relationship holds for other system configurations (See Section 3.3) where I and m designate the inertia of the rotating parts and translating parts of the lead screw drive, respectively.

$$mr_m \tan \lambda (ku + c\dot{u}) > -(I - mr_m \tan \lambda \xi_0)R \quad (6.6)$$

then (6.3) has no solutions; setting $\text{sgn}(N) = 1$ in the RHS of (6.3) results in a negative contact force, and setting $\text{sgn}(N) = -1$ results in a positive contact force. If such a situation happens, further motion is impossible and the lead screw is to be considered stationary (*i.e.* $\dot{u} + \omega = 0$). The instantaneous lead screw seizure is accompanied by an infinite impulse-like normal force.

On the other hand, if under the same conditions as above

$$mr_m \tan \lambda (ku + c\dot{u}) < -(I - mr_m \tan \lambda \xi_0)R \quad (6.7)$$

then (6.3) has two distinct solutions:

$$N = \frac{(I - mr_m \tan \lambda \xi_0)R + mr_m \tan \lambda (ku + c\dot{u})}{(\cos \lambda + \mu \sin \lambda)(I - mr_m \tan \lambda \xi_+)} , \quad N > 0 \quad (6.8)$$

and

$$N = \frac{(I - mr_m \tan \lambda \xi_0)R + mr_m \tan \lambda (ku + c\dot{u})}{(\cos \lambda + \mu \sin \lambda)(I - mr_m \tan \lambda \xi_-)} , \quad N < 0 \quad (6.9)$$

where $\xi_+ = \xi_0 = r_m \frac{\mu_0 - \tan \lambda}{1 + \mu_0 \tan \lambda}$ and $\xi_- = -r_m \frac{\mu_0 + \tan \lambda}{1 - \mu_0 \tan \lambda}$.

These two solutions in turn lead to two different possible solutions for the equation of motion given in state-space form by (5.12). One finds

$$N > 0 \rightarrow \ddot{u} = \frac{-(ku + c\dot{u})}{I - mr_m \tan \lambda \xi_+} \quad \text{and} \quad N < 0 \rightarrow \ddot{u} = \frac{-(ku + c\dot{u})}{I - mr_m \tan \lambda \xi_-} \quad (6.10)$$

Dupont [41] has studied the problem of existence and uniqueness in the forward dynamics equations of frictional systems and reported similar results for a lead screw. A possible way to resolve this problem is to give the contacting bodies flexibility [85, 86]. This is done in the model presented in Section 3.5, where nut and lead screw threads can deform. In the numerical example presented next, both rigid and flexible models are used to simulate the “sprag-slip” behavior of the lead screw.

6.1.2 Examples

The parameters values used in the numerical simulations of this section are listed in Table 6-1. First,

notice that the self-locking condition is satisfied for the selected value of the constant coefficient of friction (*i.e.* $\mu = 0.218 > \tan(5.57^\circ) = 0.0975$).

Table 6-1: Parameter values used in the simulations

Parameter	Value	Parameter	Value
d_m	10.37 mm	c	20×10^{-5} Nms/rad
λ	5.57°	R	100 N
I	3.12×10^{-6} kg.m ²	μ	0.218
k	1 N.m/rad	ω	40 rad/s

Using (6.2), the critical translating mass is found to be; $m_{cr} \approx 10.10$ (kg). Figure 6-1 shows the evolution of the real and imaginary parts of the two eigenvalues given by (6.1) as the translating mass, m , is varied. For $m > m_{cr}$, the system loses stability due to divergence.

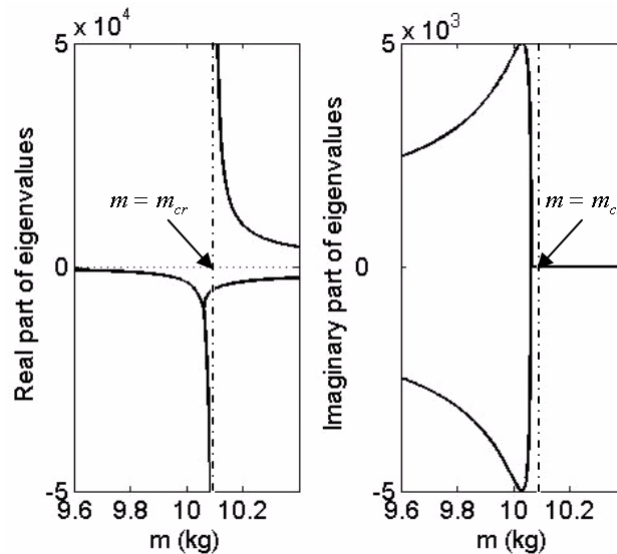


Figure 6-1: Evolution of the eigenvalues as the translating mass, m , is varied.

Figure 6-2(a) and Figure 6-2(b) show the phase plane plots of the 1-DOF model for $m = 10$ (kg) and $m = 11$ (kg), respectively. It can be seen that, by crossing the kinematic instability threshold, the system becomes unstable. This instability is characterized by a violent motion accompanied by very high decelerations and contact forces.

To see what happens during the “sprag” phase, the same system parameters are used in the numerical simulation of the 2-DOF model of Section 3.5. In this example, very high contact stiffness

and damping values are selected; $k_c = c_c = 10^8$. The $y_1 - y_2$ projection of the trajectories shown in Figure 6-3(a) is almost indistinguishable from the 1-DOF system trajectories plotted in Figure 6-2(b). The impulse-like peaks in the contact force as the system goes through the “sprag” phase is shown in Figure 6-3(b). For the selected values of the contact stiffness and damping, this force peaks to about 320 kN.

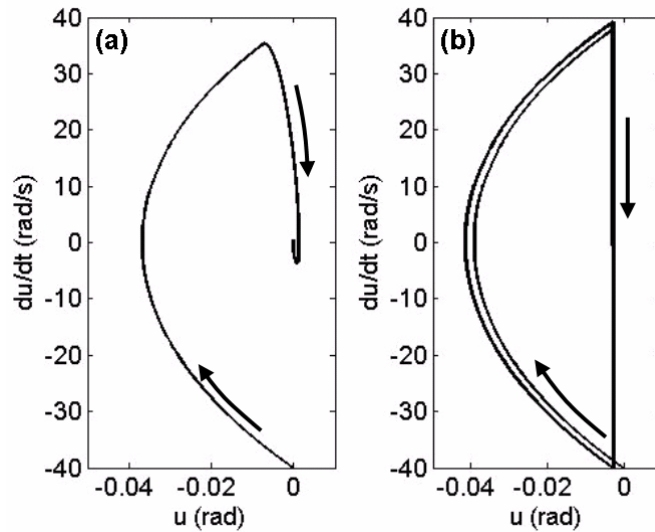


Figure 6-2: System trajectories for constant μ . (a) $m = 10 < m_{cr}$ (b) $m = 11 > m_{cr}$

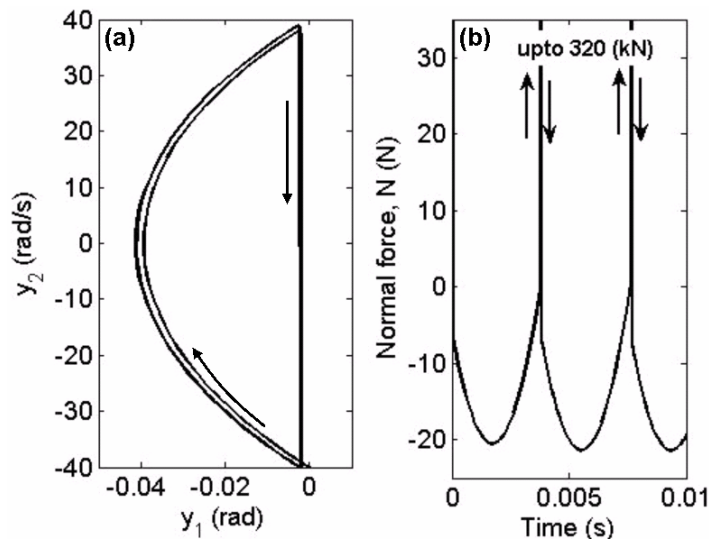


Figure 6-3: Instability caused by kinematic constraint - 2DOF model with very high contact stiffness and damping. (a) phase-plane, (b) contact normal force

As mentioned earlier, damping does not affect the stability of the 1-DOF model when the kinematic constraint instability mechanism is active. However, damping has a considerable effect on

the behavior of the nonlinear system. Figure 6-4 shows phase plots of the 1-DOF model with three levels of lead screw support damping.

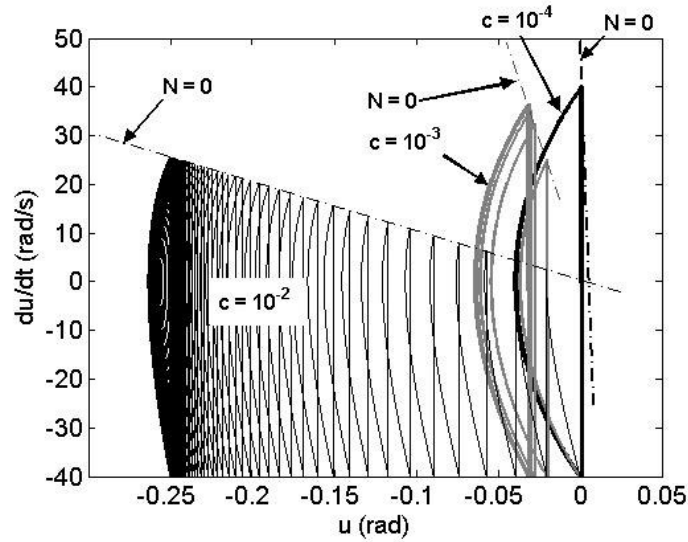


Figure 6-4: Effect of damping on the unstable system

For each of these three simulation results, the line $N(u, \dot{u}) = 0$ is also drawn. In agreement with the discussions of Section 6.1.1, the onset of lead screw seizure is the point where the trajectory reaches this line. Note that from (6.3), the line $N(u, \dot{u}) = 0$ is given by

$$\dot{u} = -\frac{k}{c}u - \left(\frac{I - mr_m \tan \lambda \xi_0}{mr_m \tan \lambda} \right) R \quad (6.11)$$

As damping is increased, the amplitude of vibrations is slightly reduced. As shown in Figure 6-5, increasing damping increases the mean deflection of coupling element, which increases the mean thread normal force.

The results presented in Figure 6-3 were obtained using a 2-DOF with very high contact stiffness and damping. As shown in Figure 6-6, by decreasing the contact parameters (*i.e.* k_c and c_c) the trajectories become smoother and the deflection of the coupling element (*i.e.* torsional spring, k) becomes positive during the sprag phase. In the next section, the stability of this 2-DOF model is studied in detail.

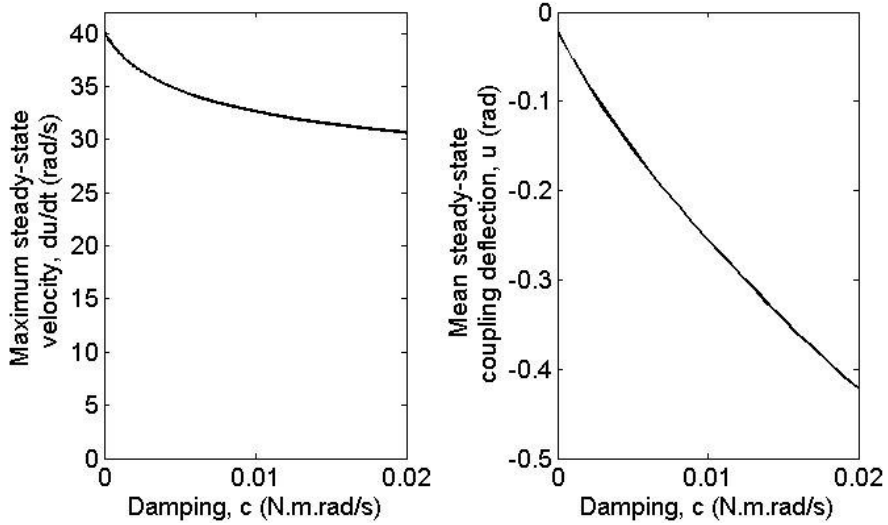


Figure 6-5: Effects of damping on the steady-state vibration of the lead screw system under kinematic constraint instability

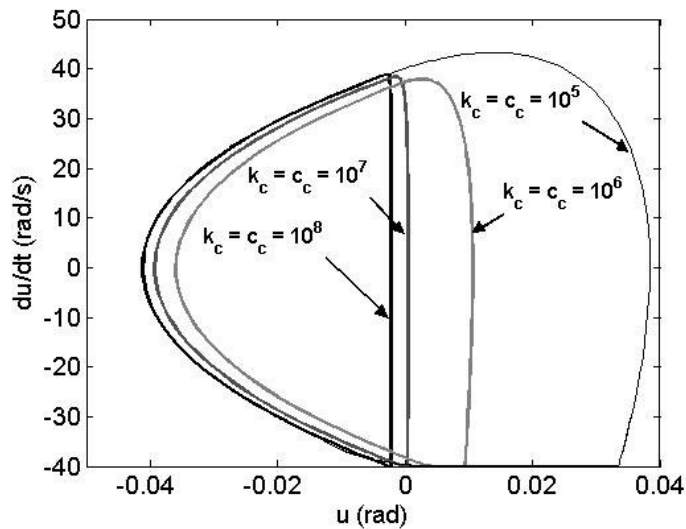


Figure 6-6: Effect contact parameters on the response of the system under kinematic constraint instability

6.1.3 Region of Attraction of the Stable Steady-sliding Fixed Point

The linear eigenvalue analysis of Section 6.1 showed that when the conditions given by (6.2) are *not* satisfied and $c > 0$, the trivial fixed point of the system is asymptotically stable. However, there can be situations where the region of attraction of the stable fixed point is quite small, leading to instabilities even when (6.2) does not hold.

Consider the case where $\mu_0 > \tan \lambda$, $R < 0$, and $\omega > 0$. It is obvious that only the first condition of (6.2) is satisfied and hence the steady-sliding fixed point is stable. Further, assume that $I - r_m^2 \tan \lambda \frac{\mu_0 - \tan \lambda}{1 + \mu_0 \tan \lambda} m < 0$ (this is the third condition of (6.2) if $R > 0$). First, notice that for any initial condition such that $N(u(0), \dot{u}(0)) > 0$, no motion is possible and velocity instantaneously resets to zero (*i.e.* $\dot{u}(0^+) = -\omega$). This behavior conforms to the same argument as in Section 6.1.1, when no solution exists (*i.e.* setting $\text{sgn}(N) = 1$ in (6.3) results in a negative contact force and setting $\text{sgn}(N) = -1$ yields a positive contact force). At this point (*i.e.* $(u(0), -\omega)$), if N is negative, the system's trajectory follows a path below the $\dot{u} = -\omega$ line (*i.e.* reversed rotation of the lead screw) and reaches the $N = 0$ line again. This cycle continues until the point $\left(-\frac{(I - mr_m \tan \lambda \xi_0)R}{kmr_m \tan \lambda} + \frac{c\omega}{k}, -\omega \right)$, where the $N = 0$ line intersects the horizontal $\dot{u} = -\omega$ line. Also note that initial motion from conditions where $N(u(0), \dot{u}(0)) < 0$ and $\dot{u}(0) < -\omega$ is not possible (this also follows a similar argument as Section 6.1.1), and the system's trajectory instantaneously transfers to $(u(0), -\omega)$ from which the motion continues towards to origin.

The solutions that start from initial conditions, satisfying $N(u(0), \dot{u}(0)) < 0$ and $\dot{u}(0) \geq -\omega$ are attracted towards the origin and, if they do not touch the $N = 0$ line, reach it asymptotically. Because of the assumption of constant coefficient of friction, (5.7) is simplified and these solutions satisfy

$$\Gamma_0 \ddot{u} + c\dot{u} + ku = 0 \quad (6.12)$$

If any of these trajectories reach the $N = 0$ line say at $t = t_1$, then the motion stops instantaneously and starts from the rest at $(u(t_1), -\omega)$. This pattern continues and may even result in a limit cycle at steady state. Otherwise, the solution reaches the origin asymptotically.

Figure 6-7(a) shows two trajectories starting well away from the equilibrium point for $R = -50N$ and $c = 10^{-3} \text{ N.m.s/rad}$. Other system parameters are taken from Table 6-1. Although trajectories cross the $N = 0$ line, the origin is stable. In Figure 6-7(b), the applied axial force is increased to $R = -10N$ while the other parameters are unchanged. In this case, the system trajectories are attracted to a limit cycle.

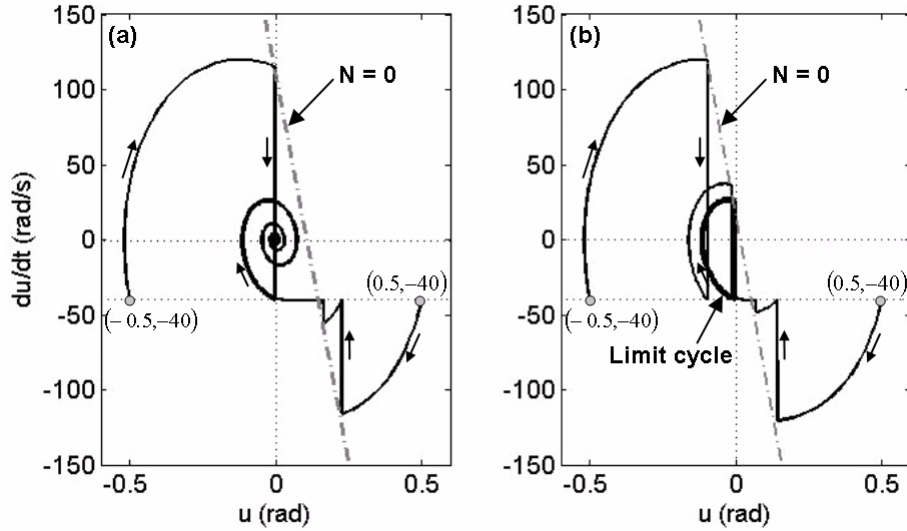


Figure 6-7: System trajectories for $\omega=40$ (rad/s). (a) $R=-50$ (N); (b) $R=-10$ (N)

From the above discussions, one can conclude that, if $-R$ is large enough such that every trajectory starting from $(u_0, -\omega)$ where $u_0 \leq -\frac{(I - mr_m \tan \lambda \xi_0)R}{kmr_m \tan \lambda} + \frac{c\omega}{k}$ asymptotically reach the origin, the steady-sliding fixed point is globally stable. Otherwise, the region of attraction is only a subset of \mathcal{R}^2 .

6.2 Stability Analysis of the 2-DOF Lead Screw Model with Compliant Threads

In this section, the 2-DOF model of Section 3.5 with constant coefficient of friction is considered. In what follows, first, the equations of motion of the system are simplified and the steady-sliding fixed point is transferred to the origin by introducing a suitable change of variables. Then, the local stability of the steady-sliding fixed point is studied by evaluating the eigenvalues of the Jacobian matrix of the linearized system. In Section 6.2.1, the case of an undamped system is analyzed and necessary and sufficient conditions for instability are derived. The case of a damped system, which is somewhat more complicated, is treated in Section 6.2.2. The analyses presented involve both analytical and numerical approaches.

The equations of motion given are given by (3.25) and (3.26)

$$I\ddot{\theta} = k(\theta_i - \theta) - c\dot{\theta} + r_m k_c (x \cos \lambda - r_m \theta \sin \lambda)(\sin \lambda - \mu_s \cos \lambda) + r_m c_c (\dot{x} \cos \lambda - r_m \dot{\theta} \sin \lambda)(\sin \lambda - \mu_s \cos \lambda) \quad (6.13)$$

$$m\ddot{x} = -k_c (x \cos \lambda - r_m \theta \sin \lambda)(\cos \lambda + \mu_s \sin \lambda) - c_c (\dot{x} \cos \lambda - r_m \dot{\theta} \sin \lambda)(\cos \lambda + \mu_s \sin \lambda) + R \quad (6.14)$$

where μ_s is defined by (3.15). Also, here F_0 and T_0 are neglected for simplicity. To simplify the subsequent analysis, the steady-sliding fixed point of the system is transferred to the origin. Towards that end, let

$$\begin{aligned} u_1 &= \theta - \theta_i \\ u_2 &= x - r_m \tan \lambda \theta_i \end{aligned} \quad (6.15)$$

Substituting (6.15) into (6.13) and (6.14) and setting $\dot{u}_1 = \dot{u}_2 = \ddot{u}_1 = \ddot{u}_2 = 0$ yields $u_1 = u_{10}$ and $u_2 = u_{20}$ where

$$u_{10} = -\frac{c}{k} \omega - \frac{\xi_0}{k} R \quad (6.16)$$

$$u_{20} = \frac{1}{k_c \cos^2 \lambda} \frac{R}{1 + \mu_0 \operatorname{sgn}(R\omega) \tan \lambda} + r_m \tan \lambda u_{10} \quad (6.17)$$

where ξ_0 is given by (5.5). To transfer the fixed point to the origin, let

$$\begin{aligned} y_1 &= \theta - u_{10} - \theta_i \\ y_2 &= \frac{x - u_{20}}{r_m \tan \lambda} - \theta_i \end{aligned} \quad (6.18)$$

Substituting (6.18) into (6.13) and (6.14) and rearranging yields

$$\mathbf{M}\ddot{\mathbf{y}} + \mathbf{C}\dot{\mathbf{y}} + \mathbf{K}\mathbf{y} = \mathbf{f}(\mathbf{y}, \dot{\mathbf{y}}) \quad (6.19)$$

where $\mathbf{y} = [y_1 \quad y_2]^T$ and

$$\mathbf{M} = \begin{bmatrix} I & 0 \\ 0 & \hat{m} \end{bmatrix} \quad (6.20)$$

$$\mathbf{K} = \begin{bmatrix} k + \hat{k}_c - \mu_0 \operatorname{sgn}(R\omega) \cot \lambda \hat{k}_c & -\hat{k}_c + \mu_0 \operatorname{sgn}(R\omega) \cot \lambda \hat{k}_c \\ -\hat{k}_c - \mu_0 \operatorname{sgn}(R\omega) \tan \lambda \hat{k}_c & \hat{k}_c + \mu_0 \operatorname{sgn}(R\omega) \tan \lambda \hat{k}_c \end{bmatrix} \quad (6.21)$$

$$\mathbf{C} = \begin{bmatrix} c + \hat{c}_c - \mu_0 \operatorname{sgn}(R\omega) \cot \lambda \hat{c}_c & -\hat{c}_c + \mu_0 \operatorname{sgn}(R\omega) \cot \lambda \hat{c}_c \\ -\hat{c}_c - \mu_0 \operatorname{sgn}(R\omega) \tan \lambda \hat{c}_c & \hat{c}_c + \mu_0 \operatorname{sgn}(R\omega) \tan \lambda \hat{c}_c \end{bmatrix} \quad (6.22)$$

$$\mathbf{f}(\mathbf{y}, \dot{\mathbf{y}}) = (\mu_0 \operatorname{sgn}(R\omega) - \mu \operatorname{sgn}(N(\dot{y}_1 + \omega))) (\hat{k}_c y_2 - \hat{k}_c y_1 + \hat{c}_c \dot{y}_2 - \hat{c}_c \dot{y}_1 + \hat{R}) \begin{bmatrix} \cot \lambda \\ \tan \lambda \end{bmatrix} \quad (6.23)$$

where N is given by (3.24) and

$$\hat{k}_c = r_m^2 \sin^2 \lambda k_c \quad (6.24)$$

$$\hat{c}_c = r_m^2 \sin^2 \lambda c_c \quad (6.25)$$

$$\hat{m} = r_m^2 \tan^2 \lambda m \quad (6.26)$$

$$\hat{R} = \frac{r_m \tan \lambda}{1 + \mu_0 \operatorname{sgn}(R\omega) \tan \lambda} R. \quad (6.27)$$

Note that for a constant coefficient of friction ($\mu = \mu_0$), the nonlinear force vector given by (6.23) is non-zero only when the response trajectory reaches the stick-slip boundary ($v_s = 0$) or when the contact force changes sign. Setting the force vector to zero gives the linearized version of the equations of motion for the case of constant coefficient of friction. One finds

$$\mathbf{M}\ddot{\mathbf{y}} + \mathbf{C}\dot{\mathbf{y}} + \mathbf{K}\mathbf{y} = 0 \quad (6.28)$$

From (6.21) and (6.22), the role of friction in breaking the symmetry of the stiffness matrix and the damping matrix is evident. Because of this effect, either by varying the constant coefficient of friction (μ_1), the coupling torsional stiffness (k), or the contact stiffness (k_c), the linearized system (6.28) can have identical undamped natural frequencies, which defines the onset of the flutter instability [43].

6.2.1 Undamped System

The natural frequencies of the undamped system are the roots of the following equation

$$\det(\mathbf{K} - \omega^2 \mathbf{M}) = 0 \quad (6.29)$$

which is a quadratic equation in ω^2 . Expanding (6.29) yields

$$a_4 \omega^4 + a_2 \omega^2 + a_0 = 0 \quad (6.30)$$

where

$$\begin{aligned} a_4 &= \hat{m}I \\ a_2 &= \hat{k}_c \hat{m} \cot \lambda (\mu \operatorname{sgn}(R\omega) - \tan \lambda) - \hat{k}_c I (1 + \mu \operatorname{sgn}(R\omega) \tan \lambda) - k\hat{m} \\ a_0 &= k\hat{k}_c (1 + \mu \operatorname{sgn}(R\omega) \tan \lambda) \end{aligned} \quad (6.31)$$

Since $a_4 > 0$ and $a_0 > 0$ ¹, instability occurs (*i.e.* natural frequencies become complex numbers) whenever

$$a_2 > 0 \quad (6.32)$$

or

$$a_2^2 - 4a_0 a_4 < 0 \quad (6.33)$$

Instability condition given by (6.32) can be rearranged as

$$a_2 = -(1 + \mu \operatorname{sgn}(R\omega) \tan \lambda) \hat{k}_c (I - \xi_0 r_m \tan \lambda m) - k\hat{m} > 0 \quad (6.34)$$

where ξ_0 is given by (5.5) and also (6.26) was used. Obviously, if $\Gamma_0 = I - \xi_0 r_m \tan \lambda m > 0$, inequality (6.34) cannot be satisfied. On the other hand, if $\operatorname{sgn}(R\omega) = 1$ and $\mu > \tan \lambda$ then for suitable values of system parameters, the inequality $\Gamma_0 < 0$ is satisfied. In this case, the system is unstable if

¹ In this work, it is assumed that the condition; $\mu < \cot \lambda$ always holds. Violation of this condition would require a very high coefficient of friction in a lead screw with a helix angle greater than 45°, which is not encountered in any practical situation [4].

$$\cos^2 \lambda (1 + \mu \tan \lambda) \left(\xi_0 r_m \tan \lambda - \frac{I}{m} \right) > \frac{k}{k_c} \quad (6.35)$$

where (6.24) and (6.26) were used. It is interesting to note that the necessary (but not sufficient) condition for instability to occur according to (6.35) is the same as the kinematic constraint instability conditions derived in the previous section for the 1-DOF model. Here, this type of instability is called the “secondary kinematic constraint” instability mechanism to distinguish it from the case of the previous section, where $\text{sgn}(R\omega) = 1$, $\mu > \tan \lambda$, and $\Gamma_0 < 0$ were sufficient conditions for instability.

Moreover, since $a_2 = 0$ satisfies (6.33), the boundary that is defined by $a_2 = 0$ is inside the region defined by (6.33). As $k_c \rightarrow \infty$, the undamped 2-DOF model reduces to the 1-DOF model of the previous section and (6.35) becomes the same as the condition for the kinematic constraint instability of the 1-DOF model.

The second instability condition, given by (6.33), represents the mode coupling (flutter) instability. The equation for the flutter instability boundary (*i.e.* coalescence of the two real natural frequencies) is found by replacing the less-than sign with the equal sign in (6.33). After some manipulations, one finds

$$b_1 \hat{k}_c^2 + b_2 k \hat{k}_c + b_3 k^2 = 0 \quad (6.36)$$

where

$$\begin{aligned} b_1 &= [\hat{m}(1 - \mu \text{sgn}(R\omega) \cot \lambda) + I(1 + \mu \text{sgn}(R\omega) \tan \lambda)]^2 \\ b_2 &= 2\hat{m}[\hat{m}(1 - \mu \text{sgn}(R\omega) \cot \lambda) - I(1 + \mu \text{sgn}(R\omega) \tan \lambda)] \\ b_3 &= \hat{m}^2 \end{aligned} \quad (6.37)$$

This equation is quadratic in k and \hat{k}_c and can be solved to find parametric relationships for the onset of the flutter instability. The conditions for the solutions to be real positive numbers are (either for k as a function of \hat{k}_c or vice versa)

$$b_2^2 - 4b_1b_3 \geq 0 \quad (6.38)$$

$$b_2 < 0 \quad (6.39)$$

Inequality (6.38) can be expressed as

$$16\hat{m}^3 I(1 - \mu \operatorname{sgn}(R\omega) \cot \lambda)(1 + \mu \operatorname{sgn}(R\omega) \tan \lambda) \leq 0 \quad (6.40)$$

which holds if and only if $\xi_0 > 0$. This in turn requires that

$$\mu \geq \tan \lambda \quad \wedge \quad R\omega > 0 \quad (6.41)$$

The second inequality (6.39) can be expressed as

$$(1 + \mu \operatorname{sgn}(R\omega) \tan \lambda)(I + r_m \tan \lambda \xi_0 m) > 0 \quad (6.42)$$

which is satisfied for $\xi_0 > 0$.

Hence, for the undamped system, mode coupling can only happen in the self-locking lead screw drives where $R\omega > 0$ (*i.e.* where the applied force is in the direction of the translation).

6.2.1.1 Numerical Examples and Discussion

Figure 6-8 shows the stability region of the 2-DOF model (6.29) for the parameters values in Table 6-1 and $m = 5$. Note that $\Gamma_0(\mu) > 0$ for $0 \leq \mu \leq 0.3$. As a result, stability is not affected by (6.32). The hatched region corresponds to the parameter range, where the two natural frequencies are complex and the system is unstable. The boundary of this region is the flutter instability boundary defined by $\omega_1 = \omega_2$.

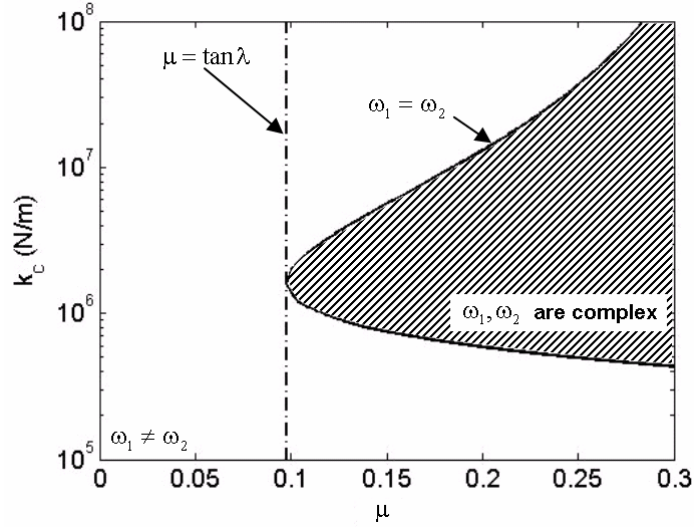


Figure 6-8: Stability of the 2-DOF system as contact stiffness and coefficient of friction are varied. $m = 5$ and $R\omega > 0$. Hatched region: unstable.

It is interesting to note that the flutter boundary is tangent to the $\mu = \tan \lambda$ line (at $k_c \approx 1.7 \times 10^6$). As predicted in the above, the instability region lies entirely on the right of this line. Figure 6-9 shows the variation of the real and imaginary parts of the eigenvalues of the undamped system for $\mu = 0.2 > \tan \lambda$. It can be seen that flutter instability occurs as the two natural frequencies merge. Further increase of the contact stiffness uncouples the two modes and the stability is restored.

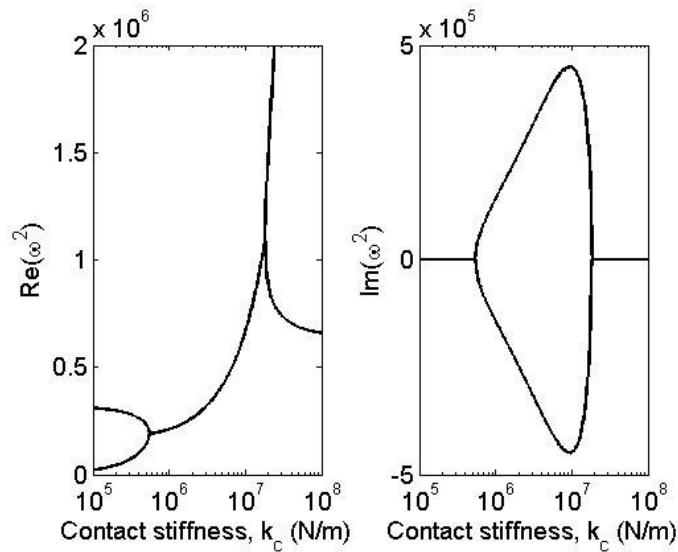


Figure 6-9: Variation of the real and imaginary parts of the eigenvalues as the contact stiffness is varied. $\mu = 0.2$, $m = 5$.

For larger values of the translating mass, m , inequality (6.32) can also become active in the considered ranges of parameters, thus creating a mixed situation where both mode coupling and secondary kinematic constraint instability mechanisms influence the stability of the system. An example of this situation is given by the stability map of Figure 6-10. The translating mass is increased to $m = 15\text{kg}$, resulting in Γ_0 vanishing at $\mu \approx 0.178$. The hatched regions in this figure show parameter ranges where these two mechanisms are active.

Consider the variation of the system parameters μ and k_c along the dashed line in Figure 6-10. In the stable region, the two frequencies are distinct real numbers. At the flutter instability boundary, the two frequencies merge, *i.e.* $\omega_{1,2}^2 = a, a > 0$. By further increasing the parameters, the frequencies become complex-valued, *i.e.* $\omega_{1,2}^2 = a \pm ib, a, b > 0$. At the secondary kinematic constraint instability boundary the real part of $\omega_{1,2}^2$ vanishes, *i.e.* $\omega_{1,2}^2 = \pm ib, b > 0$. If the parameters are increased even further, the real part of the squared frequencies becomes negative, *i.e.* $\omega_{1,2}^2 = -a \pm ib, a, b > 0$. At the second boundary of flutter instability, the squared frequencies are identical and purely imaginary, *i.e.* $\omega_{1,2}^2 = -a, a > 0$. Beyond this threshold, squared frequencies are different but remain purely imaginary.

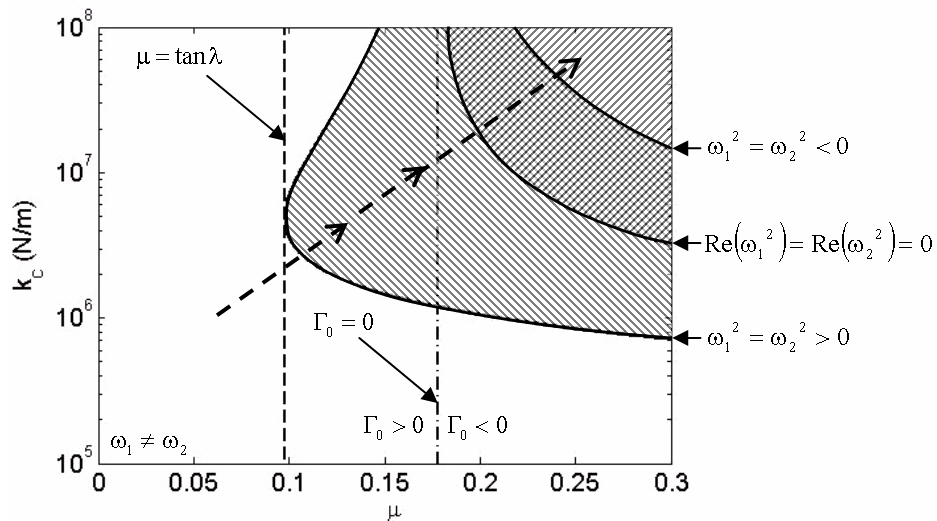


Figure 6-10: Stability of the 2-DOF system as contact stiffness and coefficient of friction are varied, when $m = 15$ and $R\omega > 0$. The $\text{diagonal hatched area}$: mode coupling instability region; the $\text{cross-hatched area}$: secondary kinematic constraint instability region.

The variation of the real and imaginary parts of eigenvalues (*i.e.* natural frequencies) for $\mu = 0.218 > 0.178$ as k_c is varied is plotted in Figure 6-11. Mode coupling instability occurs at the flutter boundary: $k_c = 9.65 \times 10^5$. It is interesting to note that, due to the secondary kinematic constraint instability, the systems remains unstable even when k_c is large enough that the two modes decouple.

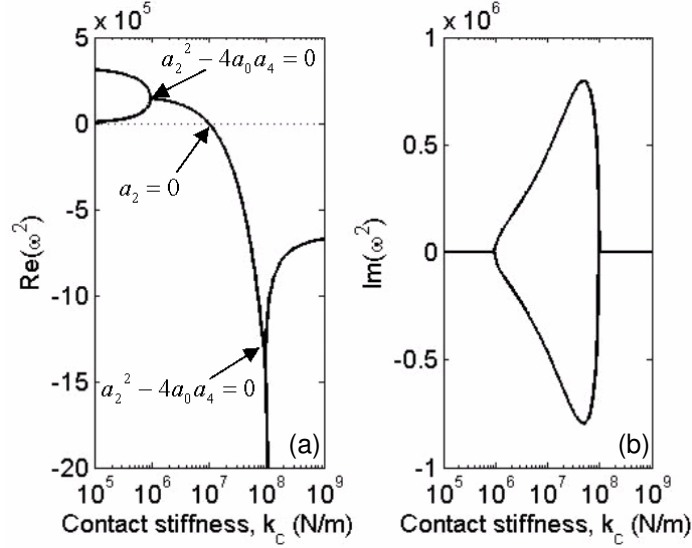


Figure 6-11: Variation of the real part (a) and imaginary part (b) of the eigenvalues as the contact stiffness is varied. $\mu = 0.218$, $m = 15$.

6.2.2 Damped System

The eigenvalues of the damped 2-DOF system ($\eta_i, i = 1 \dots 4$) are the solutions of the fourth-order equation

$$\det(\eta^2 \mathbf{M} + \eta \mathbf{C} + \mathbf{K}) = 0 \quad (6.43)$$

Assuming all of the system parameters to be non-negative, the stability conditions based on the Routh-Hurwitz criterion are found as

$$D_2 = \hat{c}_c D_1 + c \hat{m} > 0 \quad (6.44)$$

$$D_3 = \hat{k}_c D_1 + k \hat{m} + c \hat{c}_c (1 + \mu \operatorname{sgn}(R\omega) \tan \lambda) > 0 \quad (6.45)$$

$$D_2 D_3 - \hat{m} I (c \hat{k}_c + \hat{c}_c k) (1 + \mu \operatorname{sgn}(R\omega) \tan \lambda) > 0 \quad (6.46)$$

$$\{D_2 D_3 - \hat{m} I (c \hat{k}_c + \hat{c}_c k) (1 + \mu \operatorname{sgn}(R\omega) \tan \lambda)\} (c \hat{k}_c + \hat{c}_c k) - k \hat{k}_c D_2^2 > 0 \quad (6.47)$$

where

$$D_1 = I(1 + \mu \operatorname{sgn}(R\omega) \tan \lambda) + \hat{m}(1 - \mu \operatorname{sgn}(R\omega) \cot \lambda) \quad (6.48)$$

These inequalities are too complicated to be useful in establishing closed-form parametric stability boundaries. However, some important special cases can be proven, which are listed here.

- Special Case No. 1: The system's fixed point is *stable* when the force is applied opposite to the nut translation direction, *i.e.* $R\omega < 0$.
- Special Case No. 2: The system's fixed point is *stable* when the force is applied in the direction of the nut translation and the lead screw drive is not self-locking, *i.e.* $R\omega > 0$ and $\mu < \tan \lambda$.

It is clear that self-locking, as well as application of the load onto the nut in the direction of travel, are the two necessary (but not sufficient) conditions for the instability to occur.

- Special Case No. 3: The system's fixed point is *unstable* when $R\omega > 0$, $\mu > \tan \lambda$, and $c_c = 0 \wedge c \neq 0$.
- Special Case No. 4: The system's fixed point is *unstable* when $R\omega > 0$, $\mu > \tan \lambda$, and $c_c \neq 0 \wedge c = 0$.

The presence of damping only in the rotational DOF (*i.e.* lead screw support damping, c) or in the translating DOF (*i.e.* contact damping, c_c) destabilizes the system. Similar qualitative observations are found in the literature involving simple systems (see for example [87-90]).

- Special Case No. 5: For very large contact stiffness and damping (*i.e.* $k_c, c_c \rightarrow \infty$), the

system's fixed point is *stable* if $D_1 > 0$ and *unstable* if $D_1 < 0$ which agrees with the conditions for the kinematic constrain instability of the 1-DOF model in Section 6.1 since $\text{sgn } D_1 = \text{sgn } \Gamma_0$.

6.2.2.1 Numerical Examples and Discussions

In Figure 6-12, the two damping coefficients are chosen as $c_c = 10^2$ and $c = 2 \times 10^{-5}$. The other system parameters are selected as before, and $m = 5$. It can be seen that the addition of damping, contrary to common experiences, has reduced the stability region.

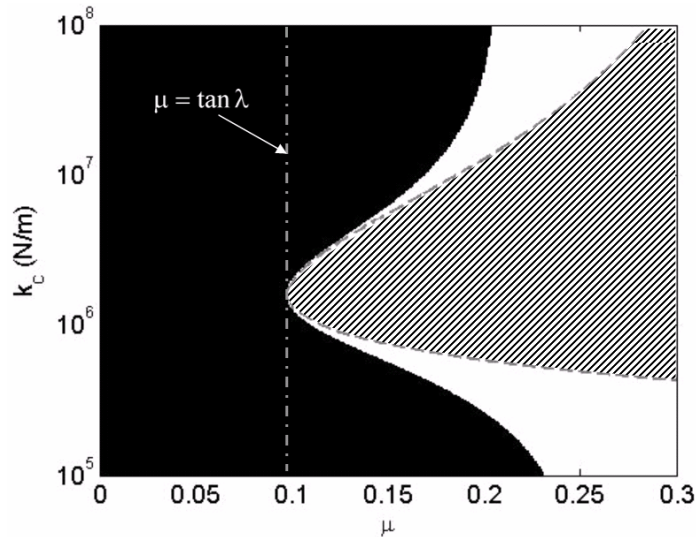


Figure 6-12: Regions of stability of the 2-DOF model with damping. Black: stable, white: unstable. $R\omega > 0$, $m=5$, $c_c=10^2$, and $c=4 \times 10^{-5}$.

Variation of the eigenvalues for this case are plotted in Figure 6-13 for $\mu = 0.15$. The coalescence of the natural frequencies can be seen in this figure. It must be noted that, due to the presence of damping, the two frequencies do not match exactly¹, and the instability region does not necessarily correspond to the range where they are close.

¹ Matching of the frequency of the two coupled modes is exact for the special case of proportional damping (see for example [90]).

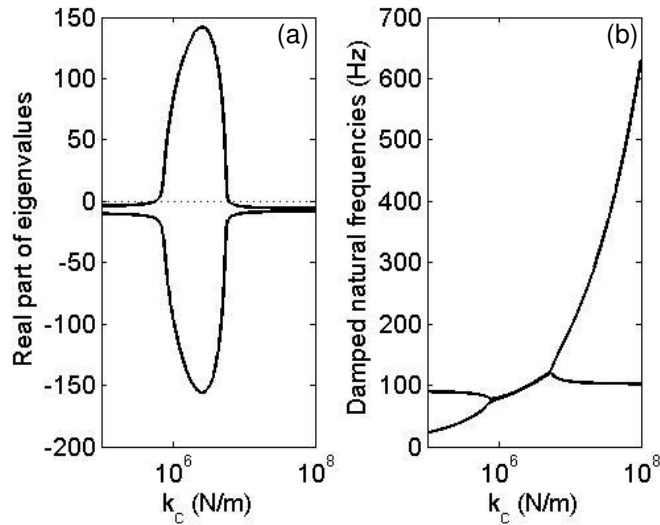


Figure 6-13: Variation of the real part of the eigenvalues (a) and the natural frequencies (b), as the contact stiffness is varied. $\mu = 0.15$, $m = 5$, $c_c = 10^2$, and $c = 4 \times 10^{-5}$.

By increasing the damping, as shown in Figure 6-14, the stable region is expanded beyond the instability region of the undamped system. In this figure the damping coefficients are $c_c = 2 \times 10^3$ and $c = 4 \times 10^{-4}$. Similar to Figure 6-13, Figure 6-15 shows that the evolution of the real and imaginary parts of the eigenvalues as k_c is varied, for $\mu = 0.15$. The increased damping has resulted in the “overdamping” of the lower mode of vibration for roughly $k_c < 1.96 \times 10^5$. More importantly, in this higher damping level, the range over which the two natural frequencies are close has been almost completely eliminated.

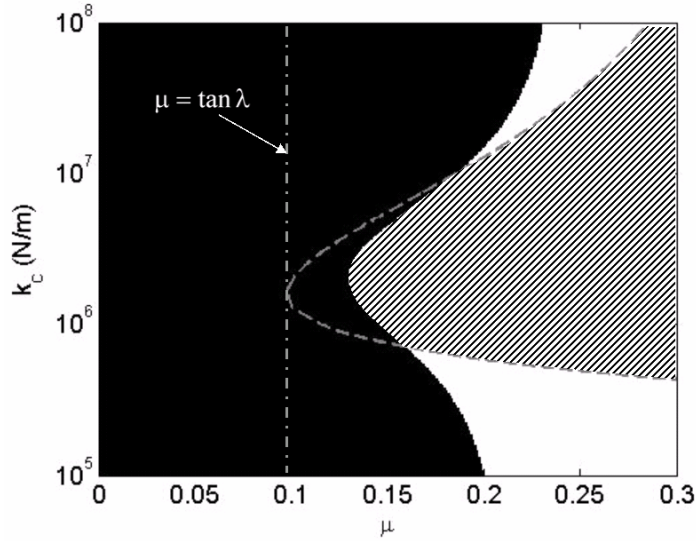


Figure 6-14: Regions of stability of the 2-DOF model with damping. Black: stable, white: unstable. $R\omega > 0$, $m = 5$, $c_c = 2 \times 10^3$, and $c = 4 \times 10^{-4}$.

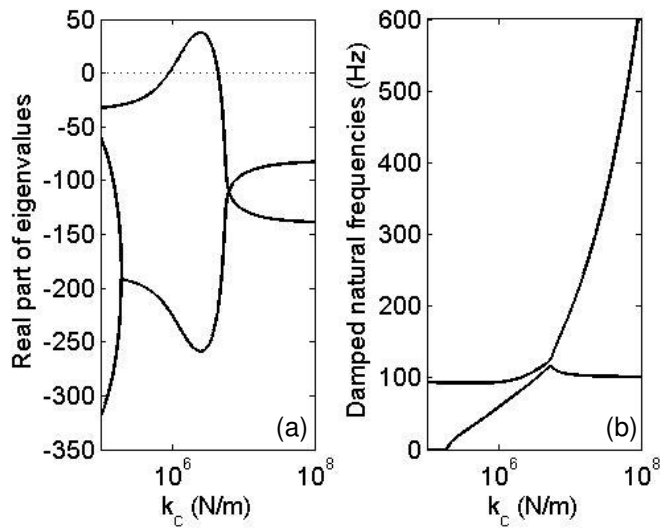


Figure 6-15: Variation of the real part of the eigenvalues (a) and the natural frequencies (b), as the contact stiffness is varied. $\mu = 0.15$, $m = 5$, $c_c = 2 \times 10^3$, and $c = 4 \times 10^{-4}$.

Similar to the undamped case, the effect of secondary kinematic constraint instability on the damped system is considered next. The translating mass is now increased to $m = 15 \text{ kg}$. At this value, Γ_0 changes sign at approximately $\mu = \mu_{skc} \approx 0.178$. Figure 6-16 shows the stability region of the system for $c_c = 2 \times 10^3$ and $c = 4 \times 10^{-4}$.

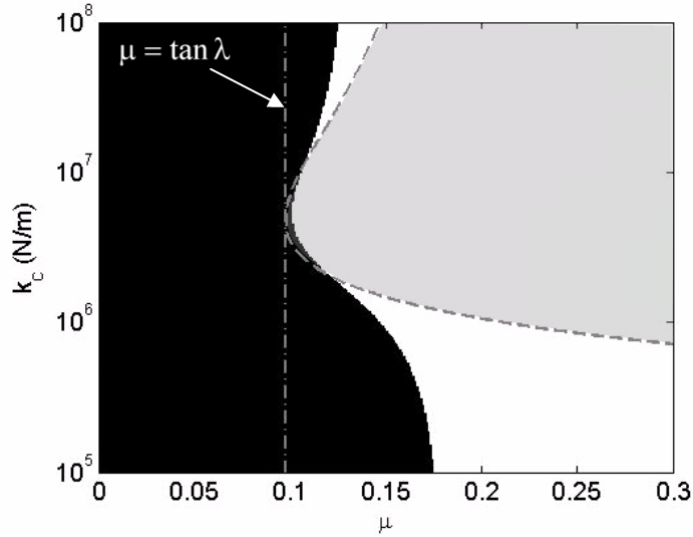


Figure 6-16: Regions of stability of the 2-DOF model with damping. Black: stable, white: unstable, Grey: region of instability of the undamped system $R\omega > 0$, $m=15$, $c_c=2 \times 10^3$, and $c=4 \times 10^{-4}$

As it was the case in the previous examples, the addition of damping has *decreased* the stable parameter ranges. The evolution of real and imaginary parts of the eigenvalues for two values of constant coefficient of friction is plotted in Figure 6-17.

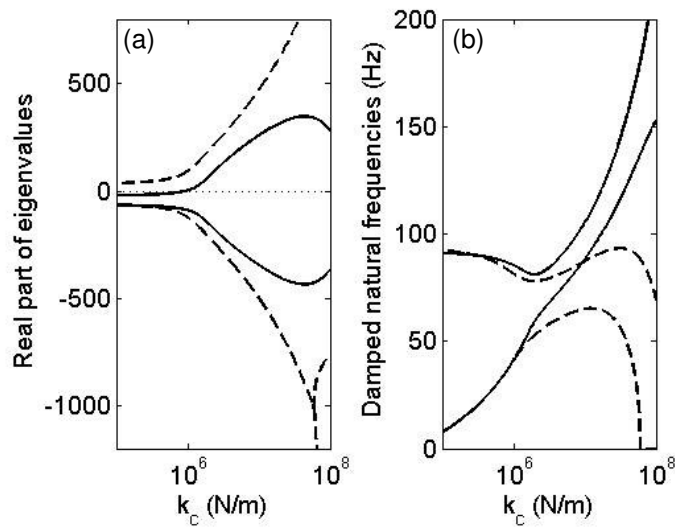


Figure 6-17: Variation of the real part of the eigenvalues (a) and the natural frequencies (b), as the contact stiffness is varied. $m = 15$, $c_c=2 \times 10^3$, and $c=4 \times 10^{-4}$. Solid: $\mu = 0.15$; dashed $\mu = 0.2$.

As shown, at $\mu = 0.15$ the system becomes unstable approximately for $k_c > 9.25 \times 10^5$. The system is unstable over the entire range contact stiffness values for $\mu = 0.2$.

By further increasing the damping coefficients, the stable region grows. However, due to the presence of secondary kinematic constraint instability (*i.e.* $\Gamma_0 < 0$), the stable region is bounded by the vertical line $D_2 = 0$ where D_2 is defined by (6.44). The bound in terms of the friction coefficient is found from this equation as

$$\mu_{dskc} = \tan \lambda \frac{1 + I/\hat{m} + c/\hat{c}_c}{1 - I/\hat{m} \tan^2 \lambda} \quad (6.49)$$

It is interesting to note that in (6.49) only the ratio of the two damping coefficients appears. Consequently, for a fixed ratio of c/\hat{c}_c , the system will be unstable for $\mu > \mu_{dskc}$ regardless of the size of damping coefficients. It must be mentioned that, for large c/\hat{c}_c , the bound obtained by (6.49) will be too high as instability may occur at much lower values of the coefficient of friction. On the other hand, for $c/\hat{c}_c \rightarrow 0$, $\mu_{dskc} \rightarrow \mu_{skc}$, where $\Gamma_0(\mu_{skc}) = 0$; this becomes the special case No. 4 mentioned above where the system is unstable for $\mu > \tan \lambda$.

Figure 6-18 shows the stability map of the system for $c_c = 4 \times 10^4$ and $c = 8 \times 10^{-3}$, which are 20 times higher than the values used in Figure 6-16. The ratio of damping coefficients here is $c/\hat{c}_c \approx 0.08$. The stable region is entirely on the left side of the vertical line defined by $\mu = \mu_{dskc}$.

In Figure 6-19, the evolution of the real and imaginary parts of the eigenvalues are plotted for the same parameter values as in Figure 6-18 and $\mu = 0.218$. The lower mode of vibration is overdamped almost over the entire range of k_c . The system becomes unstable for $k_c > 3.65 \times 10^7$.

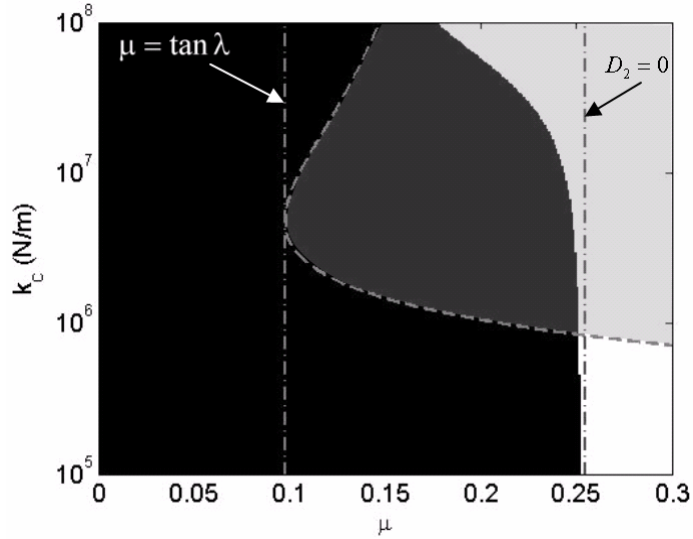


Figure 6-18: Regions of stability of the 2-DOF model with damping. Black: stable, white: unstable, Grey: region of instability of the undamped system. $R\omega > 0$, $m=15$, $c_c=4 \times 10^4$, and $c=8 \times 10^{-3}$

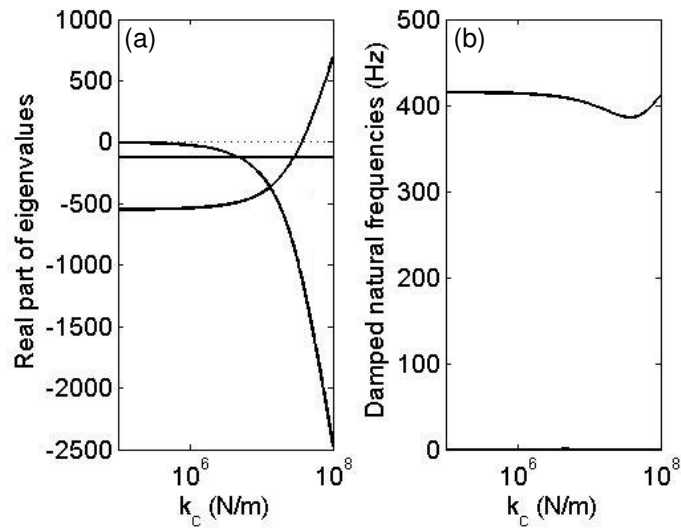


Figure 6-19: Variation of the real part of the eigenvalues (a) and the natural frequencies (b), as the contact stiffness is varied. $m = 15$, $c_c=4 \times 10^4$, $c=8 \times 10^{-3}$, and $\mu = 0.218$

6.3 Stability Analysis of a 2-DOF Model with Axially Compliant Lead Screw Supports

In this section, the 2-DOF model of Section 3.6 is considered. As will be discussed below, the

stability conditions of the lead screw model with axially compliant lead screw supports bears many resemblances to the study of previous section, where the source of flexibility was the compliant threads (see Appendix G for a comparison of the stability conditions of these two systems). There are some distinct and important differences that will be highlighted in what follows. First, the system model is simplified and converted to a suitable form for linearization and stability analysis. Then, similar to the previous section, the local stability of the steady sliding fixed point is analyzed using the eigenvalue analysis method. The stability of the undamped case is discussed in Section 6.3.1 while the system with damping is covered in Section 6.3.2. In these analyses, both mode coupling and kinematic constraint instability mechanisms are encountered.

The equations of motion are given by (3.29) and (3.30)

$$(I - \xi m r_m \tan \lambda) \ddot{\theta} - \xi m \ddot{x}_1 = k(\theta_i - \theta) - c\dot{\theta} - \xi R \quad (6.50)$$

$$(m_1 + m) \ddot{x}_1 + m r_m \tan \lambda \ddot{\theta} = -k_1 x_1 - c_1 \dot{x}_1 + R \quad (6.51)$$

where, once again, F_0 and T_0 are neglected for simplicity. To bring the steady-sliding fixed point to the origin, the following change of variables is used

$$\begin{aligned} \theta &= y_1 + \theta_i + u_{10} \\ x_1 &= r_m \tan \lambda y_2 + u_{20} \end{aligned} \quad (6.52)$$

where

$$u_{10} = \frac{-c\omega - \xi_0 R}{k} \quad (6.53)$$

$$u_{20} = \frac{R}{k_1} \quad (6.54)$$

Substituting (6.52) into (6.50) and (6.51) and after some simplifications

$$\mathbf{M}\ddot{\mathbf{y}} + \mathbf{C}\dot{\mathbf{y}} + \mathbf{K}\mathbf{y} = \mathbf{f}(\mathbf{y}, \dot{\mathbf{y}}) \quad (6.55)$$

where

$$\mathbf{M} = \begin{bmatrix} I - \xi m r_m \tan \lambda & -\xi m r_m \tan \lambda \\ m & m + m_1 \end{bmatrix} \quad (6.56)$$

$$\mathbf{C} = \begin{bmatrix} c & 0 \\ 0 & c_1 \end{bmatrix} \quad (6.57)$$

$$\mathbf{K} = \begin{bmatrix} k & 0 \\ 0 & k_1 \end{bmatrix} \quad (6.58)$$

$$\mathbf{f} = \begin{bmatrix} (\xi_0 - \xi)R \\ 0 \end{bmatrix} \quad (6.59)$$

Notice that, unlike the model studied in Section 6.2, here the inertia matrix is asymmetric, and stiffness and damping matrices are symmetric. For the case of constant coefficient of friction, the linearized equations of motion are given simply by

$$\mathbf{M}_0 \ddot{\mathbf{y}} + \mathbf{C} \dot{\mathbf{y}} + \mathbf{K} \mathbf{y} = 0 \quad (6.60)$$

where

$$\mathbf{M}_0 = \begin{bmatrix} I - \xi_0 m r_m \tan \lambda & -\xi_0 m r_m \tan \lambda \\ m & m + m_1 \end{bmatrix} \quad (6.61)$$

where ξ_0 is given by (5.5).

Similar to the steps taken in previous section, the case of undamped system is considered first, and then the damped system is studied.

6.3.1 Undamped System

The natural frequencies of the undamped system are the roots of the following equation:

$$\det(\mathbf{K} - \omega^2 \mathbf{M}_0) = 0 \quad (6.62)$$

which is a quadratic equation in ω^2 . Expanding (6.29) yields

$$a_4 \omega^4 + a_2 \omega^2 + a_0 = 0 \quad (6.63)$$

where

$$\begin{aligned}
a_4 &= I(m + m_1) - mm_1 \xi_0 r_m \tan \lambda \\
a_2 &= -k(m + m_1) - k_1(I - \xi_0 m r_m \tan \lambda) \\
a_0 &= kk_1
\end{aligned} \tag{6.64}$$

Since $a_0 > 0$, instability occurs (*i.e.* natural frequencies become complex numbers) whenever

$$a_4 < 0 \tag{6.65}$$

or

$$a_4 > 0 \wedge a_2 > 0 \tag{6.66}$$

or

$$a_2^2 - 4a_0 a_4 < 0 \tag{6.67}$$

In terms of system parameters, the instability condition given by (6.65) can be written as

$$\tilde{\Gamma}_0 = I - \tilde{m} \xi_0 r_m \tan \lambda < 0 \tag{6.68}$$

where

$$\tilde{m} = \frac{mm_1}{m + m_1} \tag{6.69}$$

The necessary condition for $\tilde{\Gamma}_0 < 0$ is $\xi_0 > 0$ which, in turn, requires $\text{sgn}(R\omega) = 1$ and $\mu > \tan \lambda$. It is interesting to note that (6.68) takes the form of the kinematic constraint instability condition given by (6.2) with \tilde{m} as an *equivalent* translating mass.

The instability condition (secondary kinematic constraint) according to (6.66) can be written as

$$\begin{aligned}
m_1(I - m \xi_0 r_m \tan \lambda) + mI &> 0 \\
k(m + m_1) + k_1(I - \xi_0 m r_m \tan \lambda) &< 0
\end{aligned} \tag{6.70}$$

For the instability to occur according to (6.70), the following conditions are necessary and sufficient

$$I - m \xi_0 r_m \tan \lambda < 0 \tag{6.71}$$

$$\frac{\xi_0 m r_m \tan \lambda - I}{m + m_1} > \frac{k}{k_1} \quad (6.72)$$

It is interesting to note that inequality (6.71) is the same as the kinematic constraint instability condition given by (6.2).

Finally, inequality (6.67) gives the necessary and sufficient for the mode coupling instability. Replacing the less-than sign with an equal sign for the instability boundary and after simplifications, one finds

$$b_1 k_1^2 + b_2 k k_1 + b_3 k^2 = 0 \quad (6.73)$$

where

$$\begin{aligned} b_1 &= (I - \xi_0 m r_m \tan \lambda)^2 \\ b_2 &= 2[m_1(\xi_0 m r_m \tan \lambda - I) - m(\xi_0 m r_m \tan \lambda + I)] \\ b_3 &= (m + m_1)^2 \end{aligned} \quad (6.74)$$

This equation is quadratic in k and k_1 and can be solved to find parametric relationships for the onset of the flutter instability. The conditions for the solutions to be real positive numbers are

$$b_2^2 - 4b_1 b_3 \geq 0 \quad (6.75)$$

$$b_2 < 0 \quad (6.76)$$

In terms of system parameters, inequality (6.75) becomes

$$16\xi_0 m^2 r_m \tan \lambda (m + m_1) \left[I - \left(\frac{m m_1}{m + m_1} \right) \xi_0 r_m \tan \lambda \right] \geq 0 \quad (6.77)$$

which yields

$$I - \left(\frac{m m_1}{m + m_1} \right) \xi_0 r_m \tan \lambda \geq 0 \wedge \xi_0 > 0 \quad (6.78)$$

The second inequality given by (6.76), yields

$$\frac{m(m_1 - m)}{m + m_1} \xi_0 r_m \tan \lambda - I < 0 \quad (6.79)$$

which is satisfied whenever (6.78) is satisfied. From (6.68) and (6.78), it can be concluded the mode coupling and the (primary) kinematic constraint instability regions have no overlap in the parameter space.

6.3.1.1 Numerical Examples and Discussion

Figure 6-20 shows the stability region of the undamped 2-DOF model in the $k_1 - \mu$ parameter space. Other system parameter values not given in the figure are selected according to Table 6-1. The hatched region corresponds to the parameter range where the two natural frequencies are complex and the system is unstable. The boundary of this region is the flutter instability threshold defined by $\omega_1 = \omega_2$. In this figure, flutter boundary is plotted for two other higher values of the lead screw mass, m_1 . For small values of lead screw mass, this plot is almost identical to Figure 6-8.

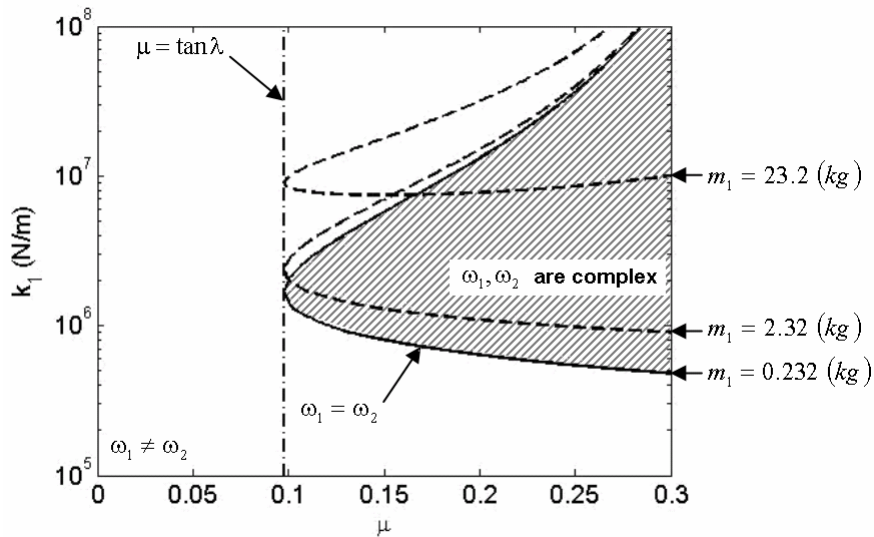


Figure 6-20: Stability of the 2-DOF system as support stiffness and coefficient of friction are varied. $m = 5$ and $R_{\omega} > 0$. Hatched region: unstable.

By increasing the translating mass to $m = 15$, the condition (6.71) is satisfied for approximately $\mu > \mu_{skc} \approx 0.178$. As shown in Figure 6-21, there are two overlapping areas in the $k_1 - \mu$ parameter space that constitute the unstable region. These regions correspond to the mode coupling and secondary kinematic constraint instability mechanisms.

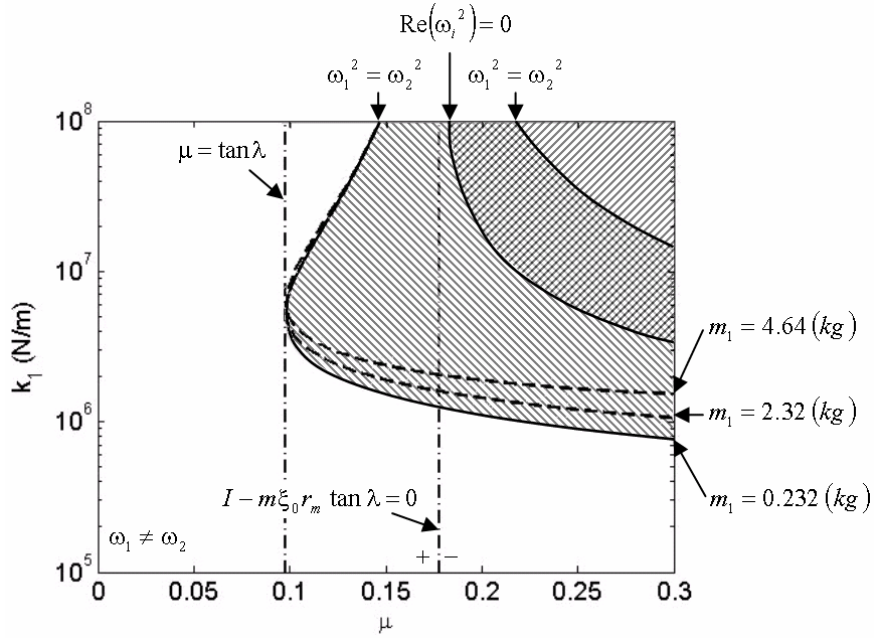


Figure 6-21: Stability of the 2-DOF system as support stiffness and coefficient of friction are varied, when $m = 15$ and $R\omega > 0$. The ▨ hatched area: mode coupling instability region; the ▩ hatched area: secondary kinematic constraint instability region.

For the above mentioned value of the translating mass, if $m_1 = 11.6$, then condition (6.68) is satisfied for $\mu > \mu_{kc} \approx 0.285$. As a result, the vertical line $\mu \approx 0.285$ becomes the *divergence* boundary in the parameter space, as shown in Figure 6-22.

The variation of the real and imaginary parts of the eigenvalues (*i.e.* ω^2) are plotted in Figure 6-23 for $k_1 = 4 \times 10^6$ as a function coefficient of friction. For this value of the support stiffness, the system becomes unstable due to mode coupling as the real part of the two eigenfrequencies merge. A second instability region also exists for $\mu > 0.285$, where the system becomes unstable due to the kinematic constraint. Similar to the results of Section 6.1, at the threshold of the kinematic constrain instability, one eigenvalue is at infinity.

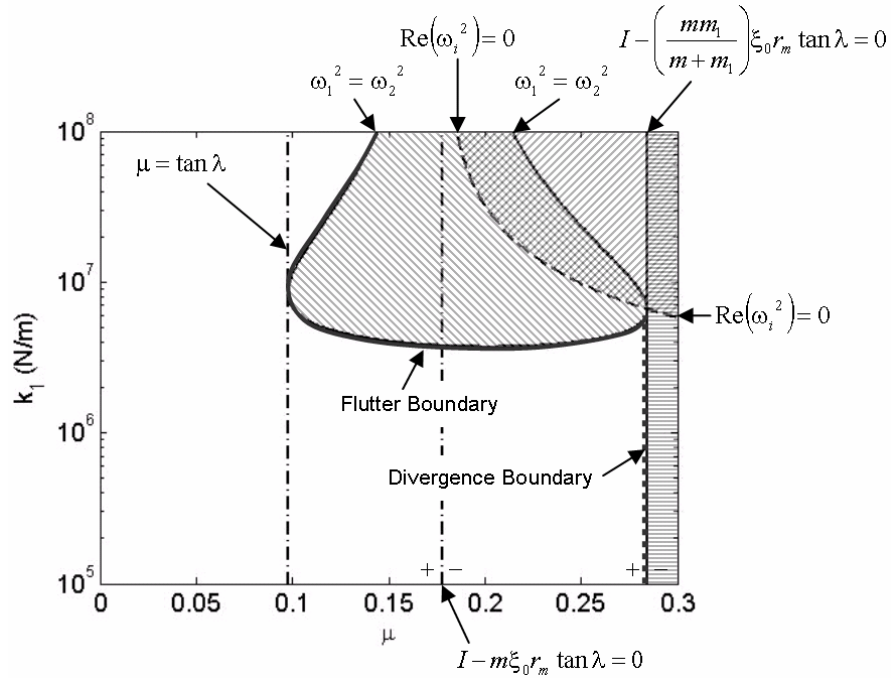


Figure 6-22: Stability of the 2-DOF system as support stiffness and coefficient of friction are varied, when $m = 15$ and $R\omega > 0$. The  hatched area: mode coupling instability region; the  hatched area: secondary kinematic constraint instability region, and; the  hatched area: primary kinematic constraint instability region.

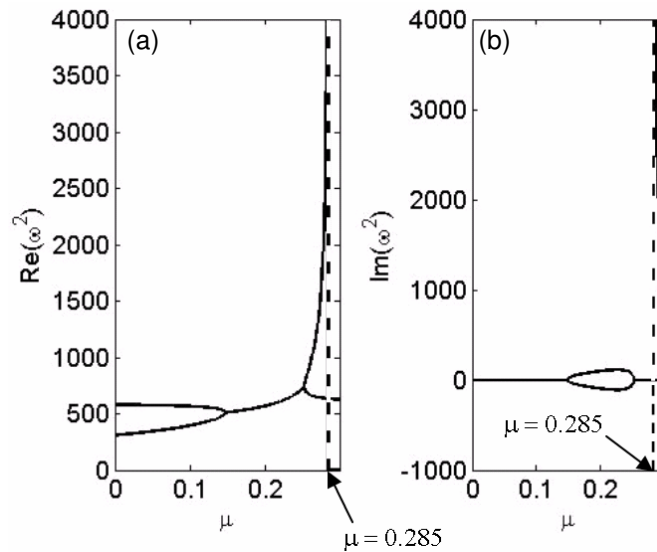


Figure 6-23: Variation of the real parts (a) and imaginary parts (b) of the eigenvalues as the contact stiffness is varied. $k_1 = 4 \times 10^6$, $m = 15$, and $m_1 = 11.6$

6.3.2 Damped System

The eigenvalues of the damped 2-DOF system ($\eta_i, i=1\dots 4$) are the solutions of the fourth-order equation

$$\det(\eta^2 \mathbf{M}_0 + \eta \mathbf{C} + \mathbf{K}) = 0 \quad (6.80)$$

Assuming all of the system parameters to be non-negative numbers, the stability conditions based on the Routh-Hurwitz criterion are found to be

$$D_1 = I(m + m_1) - mm_1 \xi_0 r_m \tan \lambda > 0 \quad (6.81)$$

$$D_2 = c(m + m_1) + c_1(I - \xi_0 r_m \tan \lambda m) > 0 \quad (6.82)$$

$$D_3 = k(m + m_1) + cc_1 + k_1(I - \xi_0 m r_m \tan \lambda) > 0 \quad (6.83)$$

$$D_2 D_3 - (kc_1 + ck_1) D_1 > 0 \quad (6.84)$$

$$\{D_2 D_3 - (kc_1 + ck_1) D_1\} (kc_1 + ck_1) - kk_1 D_2^2 > 0 \quad (6.85)$$

Once again, the resulting conditions are too complex to be useful for parametric study of stability. However, as shown in Appendix G, there are many similarities between these conditions and those derived for the 2-DOF model in Section 6.2. Expectedly, similar special cases as in Section 6.2.2 can be proven for the model of this section. These cases are listed here.

- Special Cases Nos. 1 and 2: The system's fixed point is *stable* if $\xi_0 < 0$. From the definition of ξ_0 , (5.5), it is easy to see that $\xi_0 < 0$ only if $R\omega < 0$ or $\mu < \tan \lambda$, which coincides with the first and second special cases of Section 6.2.2.
- Special Case No. 3: The system's fixed point is *unstable* when $R\omega > 0$, $\mu > \tan \lambda$, and $c_1 = 0 \wedge c \neq 0$.
- Special Case No. 4: The system's fixed point is *unstable* when $R\omega > 0$, $\mu > \tan \lambda$, and

$$c_1 \neq 0 \wedge c = 0.$$

- Special Case No. 5: The system's fixed point becomes *unstable* due the kinematic constrain instability mechanism when $D_1 < 0$.

6.3.2.1 Numerical Examples and Discussion

Figure 6-24 and Figure 6-25 show samples of the regions of stability of the system as μ_1 and k_1 are varied. The hatched region in these figures is copied from Figure 6-20 and corresponds to the region of instability of the undamped system. In Figure 6-24 the two damping coefficients were chosen as $c_1 = 10^2$ and $c = 2 \times 10^{-5}$. It can be seen that the addition of damping has reduced the stability region. However, by increasing the damping further, as shown in Figure 6-25, the stable region is expanded beyond the instability region of the undamped system. In this figure the damping coefficients were $c_1 = 2 \times 10^3$ and $c = 4 \times 10^{-4}$. In both series of examples, it can be seen that by increasing the lead screw mass, m_1 , the stability region grows towards the unstable region of the undamped system.

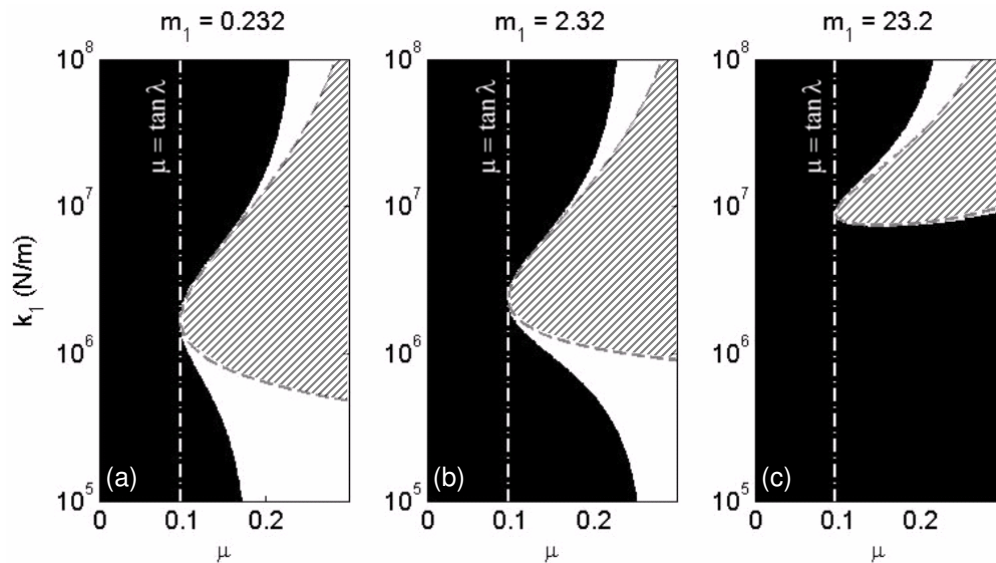


Figure 6-24: Regions of stability of the 2-DOF model with damping. (a) $m_1=0.232$ kg, (b) $m_1=2.32$ kg, and (c) $m_1=11.6$ kg. Black: stable, white: unstable, and hatched: undamped instability region. $R_{\omega} > 0$, $m=5$, $c_1=10^2$, and $c=2 \times 10^{-5}$

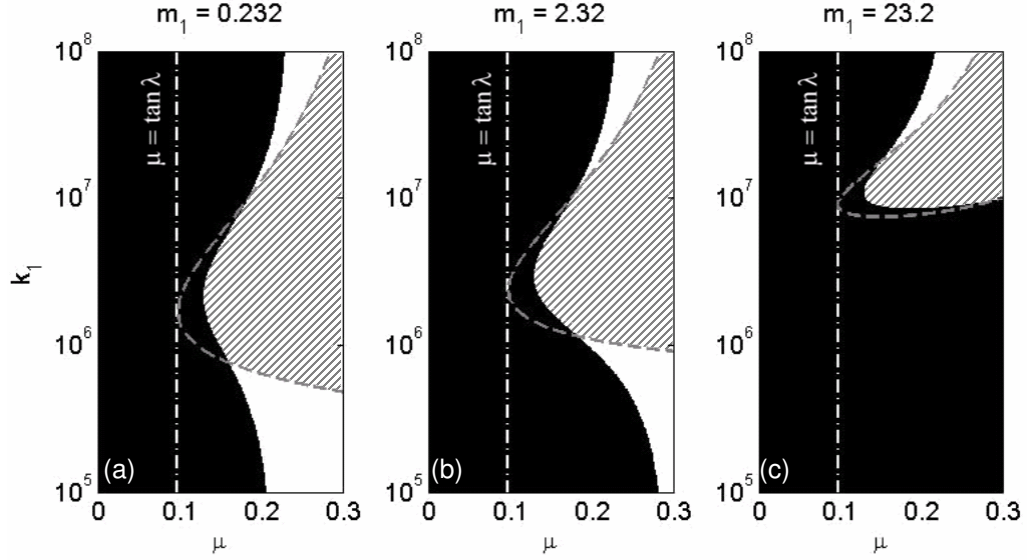


Figure 6-25: Regions of stability of the 2-DOF model with damping. (a) $m_1=0.232$ kg, (b) $m_1=2.32$ kg, and (c) $m_1=23.2$ kg. Black: stable, white: unstable, and hatched: undamped instability region. $R\omega>0$, $m=5$, $c_1=2\times 10^3$, and $c=4\times 10^{-4}$

If the translating mass is large enough such the solution of $\Gamma_0(\mu)=0$ lies in the considered range of the coefficient of friction, then an upper bound for the stable region may be found. The solution of $\Gamma_0(\mu)=0$ is given by

$$\mu_{skc} = \frac{\frac{I}{m} + r_m^2 \tan^2 \lambda}{\left(r_m^2 - \frac{I}{m}\right) \tan \lambda} \quad (6.86)$$

Replacing $>$ by $=$ in the second stability condition (6.82) gives this limiting value for the coefficient of friction. Solving $D_2 = 0$ for μ , yields

$$\mu_{dskc} = \frac{\left[\frac{c}{c_1} \left(1 + \frac{m_1}{m}\right) + \frac{I}{m}\right] + r_m^2 \tan^2 \lambda}{r_m^2 \tan \lambda - \left[\frac{c}{c_1} \left(1 + \frac{m_1}{m}\right) + \frac{I}{m}\right] \tan \lambda} \quad (6.87)$$

Similar to (6.49), only the ratio of the two damping coefficients appears in (6.87). As a result, for a fixed ratio, no matter how large the damping is, the stable region will be on the left side of the vertical

line $\mu = \mu_{dskc}$ in the $k_1 - \mu$ parameter plane. Note that, for large c/c_1 such that (6.87) does not yield a positive solution, other stability conditions must be checked. If $c/c_1 \rightarrow 0$, then $\mu_{dskc} \approx \mu_{skc}$. However, in this case, the system stability is defined by special case No. 4 above. On the other hand, for values of m_1 such that (6.81) is violated (kinematic constraint instability), then regardless of damping and stiffness parameters, the system is unstable for $\mu > \mu_{kc}$ where

$$\mu_{kc} = \frac{I \left(\frac{1}{m} + \frac{1}{m_1} \right) + r_m^2 \tan^2 \lambda}{\left(r_m^2 - I \left(\frac{1}{m} + \frac{1}{m_1} \right) \right) \tan \lambda} \quad (6.88)$$

Figure 6-26 shows the stability maps of the 2-DOF system for $m = 15\text{kg}$. At this value, $\Gamma_0(\mu) = 0$ at $\mu = \mu_{skc} \approx 0.178$. The damping values are the same as the previous example; $c_1 = 2 \times 10^3$ and $c = 4 \times 10^{-4}$. For $m_1 = 0.232$ and $m_1 = 2.32$, one has $\mu_{dskc} \approx 0.258$ and $\mu_{dskc} \approx 0.270$. Vertical lines for these two cases corresponding to $\mu = \mu_{dskc}$ are shown in Figure 6-26.

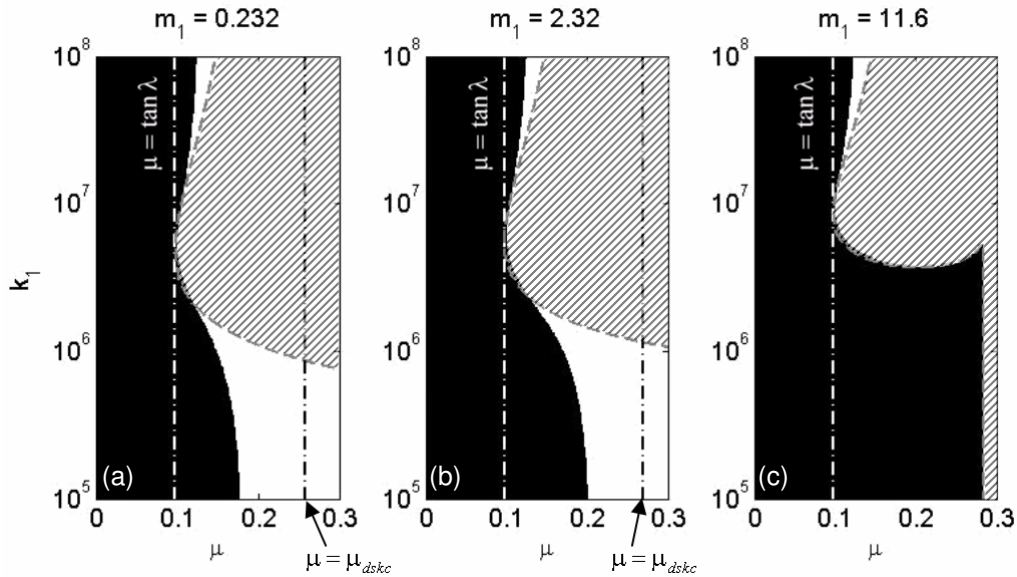


Figure 6-26: Regions of stability of the 2-DOF model with damping. (a) $m_1=0.232$ kg, (b) $m_1=2.32$ kg, and (c) $m_1=11.6$ kg. Black: stable, white: unstable, and, hatched: undamped instability region. $R_{\omega} > 0$, $m=15$, $c_1=2 \times 10^3$, and $c=4 \times 10^{-4}$

For $m_1 = 11.6$, the system is unstable due to kinematic constraint for $\mu > \mu_{kc} \approx 0.285$ regardless of the damping and stiffness parameters of the system. Figure 6-27 and Figure 6-28 show the evolution of the real and imaginary parts of the eigenvalues for $m_1 = 11.6$ as support stiffness (k_1) and coefficient of friction are varied, respectively.

In Figure 6-27, the real part of the eigenvalues and the damped natural frequencies are plotted for three close values of the constant coefficient of friction as the support stiffness is varied. It is interesting to note that, although the variation of the natural frequencies remains mostly unchanged, the stability of the system is very sensitive to the changes in the coefficient of friction.

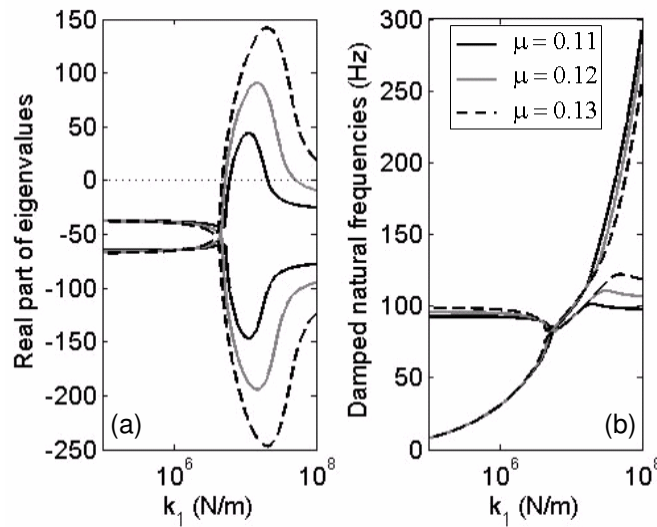


Figure 6-27: Variations of real parts of the eigenvalues (a) and damped natural frequencies (b) as a function of lead screw support axial stiffness, k_1 . $\mu = 0.11, 0.12, 0.13$

The plots in Figure 6-28 show the occurrence of the kinematic constraint instability at $\mu = \mu_{kc} \approx 0.285$. Similar to the undamped case and the 1-DOF model of Section 6.1, at the kinematic constraint instability boundary, one eigenvalue is at infinity. Also note that, in Figure 6-28 the system is unstable over a small range of coefficient of friction below the kinematic constraint boundary due to mode coupling.

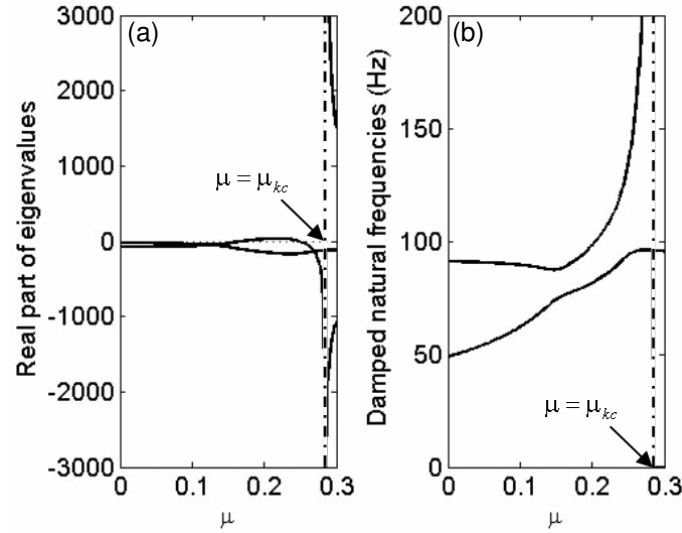


Figure 6-28: Variations of the real part of eigenvalues (a) and the damped natural frequencies (b) as a function of the coefficient of friction, μ . $k_1= 4 \times 10^6$.

Figure 6-29 shows similar stability maps as those in Figure 6-26 but with 20 times larger damping coefficients. As predicted, for the $m_1 = 0.232$ and $m_1 = 2.32$ cases, the proportional increase of the damping coefficients expanded the stability region towards the limiting $\mu = \mu_{dskc}$ line. For $m_1 = 11.6$, the limiting value of the coefficient of friction is unchanged compared to Figure 6-26, since the kinematic constraint threshold is independent of damping. For this case, however, the damping increase expanded the stability region into the mode coupling instability region of the undamped system.

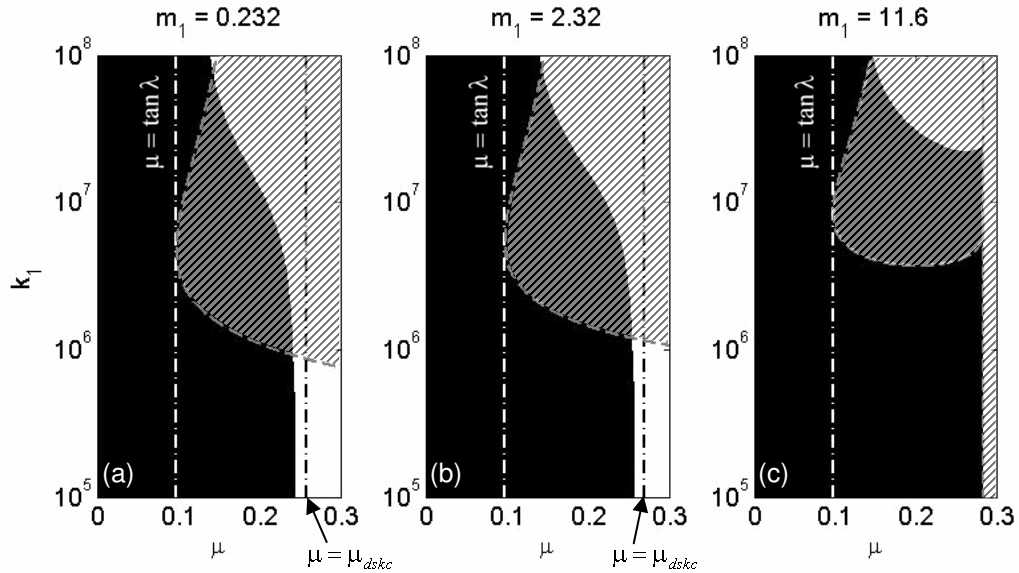


Figure 6-29: Regions of stability of the 2-DOF model with damping. (a) $m_1=0.232$ kg, (b) $m_1=2.32$ kg, and (c) $m_1=11.6$ kg. Black: stable, white: unstable, and hatched: undamped instability region. $R_{\omega}>0$, $m=15$, $c_1=2\times 10^4$, and $c=4\times 10^{-3}$.

For the case of $m_1 = 11.6$, Figure 6-30 shows the evolution of the real and imaginary parts of the eigenvalues as a function of support stiffness for $\mu = 0.2$. The increased damping has resulted in the overdamping of the lower vibration mode for most of the parameter range considered. The system loses stability due to mode coupling at $k_1 \approx 3.16\times 10^7$. In Figure 6-31, the evolution of the real and imaginary parts of the eigenvalues is shown as the coefficient of friction is varied for $k_1 = 5\times 10^6$. The system loses stability due to kinematic constraint at $\mu = \mu_{kc} \approx 0.285$, which is exactly the same value as in Figure 6-28.

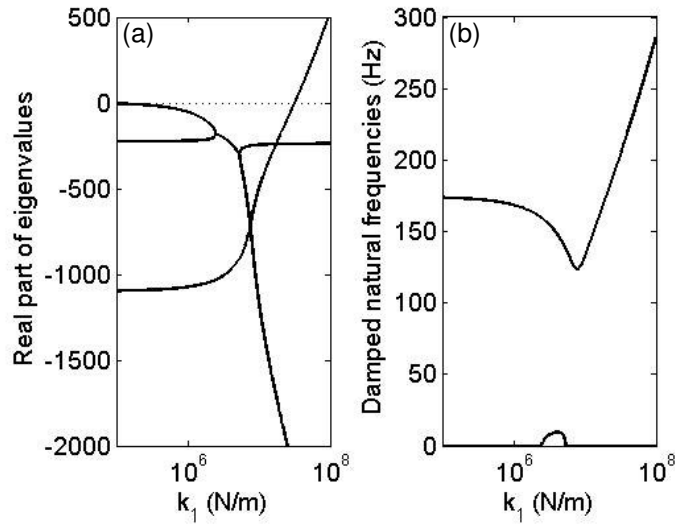


Figure 6-30: Variations of real part of the eigenvalues (a) and damped natural frequencies (b) as a function of lead screw support axial stiffness, k_1 . $\mu = 0.2$.

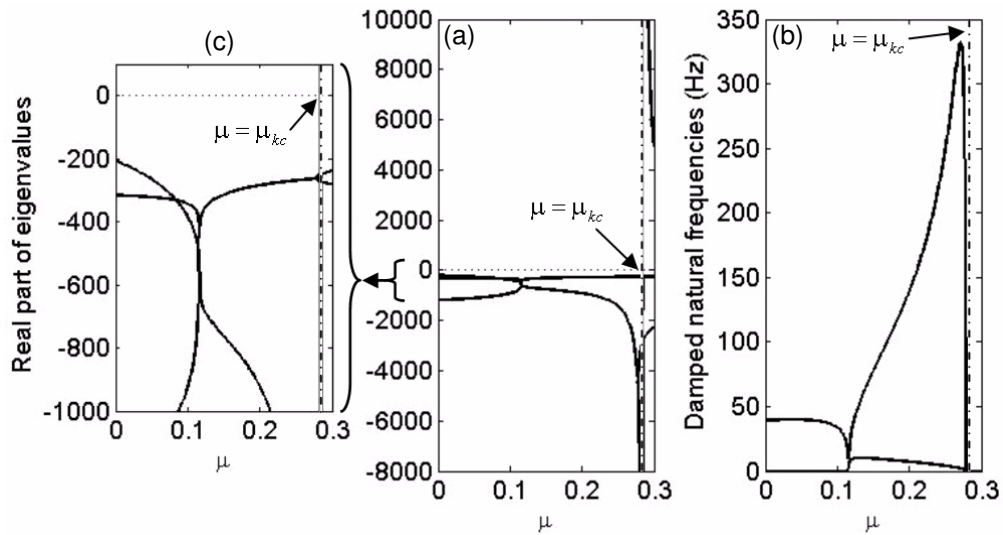


Figure 6-31: Variations of the real part of eigenvalues (a) and the damped natural frequencies (b) as a function of the coefficient of friction, μ . $k_1 = 5 \times 10^6$. (c) Close-up view of the real part of eigenvalues

6.4 Mode Coupling in a 3-DOF System

In this section, local stability of the fixed point of the 3-DOF model described in Section 3.7 is investigated. The focus of this section is on the mode coupling instability mechanism. Parameter

studies and comparisons are done numerically. Similar to what was done in Section 6.2 and Section 6.3, the equations of motion are first transformed to a suitable form corresponding to the steady-sliding fixed point. The equations of motion are given by (3.11), (3.12), and (3.27). Neglecting F_0 and T_0 , these equations simplify to

$$I\ddot{\theta} = k(\theta_i - \theta) - c\dot{\theta} + r_m(N \sin \lambda - F_f \cos \lambda) \quad (6.89)$$

$$m\ddot{x} = -N \cos \lambda - F_f \sin \lambda + R \quad (6.90)$$

$$m_1\ddot{x}_1 = -k_1x_1 - c_1\dot{x}_1 + N \cos \lambda + F_f \sin \lambda \quad (6.91)$$

Introducing the change of variables

$$\begin{aligned} u_1 &= \theta - \theta_i \\ u_2 &= x - r_m \tan \lambda \theta_i \\ u_3 &= x_1 \end{aligned} \quad (6.92)$$

into (6.89), (6.90), and (6.91) and setting all time derivatives to zero, the steady-sliding fixed point is found as

$$\begin{aligned} u_{10} &= -\frac{c\omega + \xi_0 R}{k} \\ u_{20} &= \frac{1}{k_c \cos^2 \lambda} \frac{R}{1 + \mu_{s0} \tan \lambda} + r_m \tan \lambda u_{10} + \frac{R}{k_1} \\ u_{30} &= \frac{R}{k_1} \end{aligned} \quad (6.93)$$

To transfer this point to the origin and present the system in state-space form, the following change of variables is applied

$$\begin{aligned} y_1 &= \theta - \theta_i - u_{10} \\ y_2 &= \dot{\theta} - \omega \\ y_3 &= x - r_m \tan \lambda \theta_i - u_{20} \\ y_4 &= \dot{x} - r_m \tan \lambda \omega \\ y_5 &= x_1 - u_{30} \\ y_6 &= \dot{x}_1 \end{aligned} \quad (6.94)$$

which results in a system of six first order differential equations

$$\dot{y}_i = f_i(\mathbf{y}), i = 1 \dots 6 \quad (6.95)$$

To study the stability of the steady-sliding fixed point, the eigenvalues of the Jacobian matrix are evaluated at $\mathbf{y} = \mathbf{0}$. The Jacobian matrix is given by ($R \neq 0, \omega \neq 0$)

$$\mathbf{A} = \left[\frac{\partial f_i}{\partial y_j} \Big|_{\mathbf{y}=\mathbf{0}} \right] = \begin{bmatrix} 0 & 1 & 0 & 0 & 0 & 0 \\ \gamma_{21} & \gamma_{22} & \gamma_{23} & \gamma_{24} & \gamma_{25} & \gamma_{26} \\ 0 & 0 & 0 & 1 & 0 & 0 \\ \gamma_{41} & \gamma_{42} & \gamma_{43} & \gamma_{44} & \gamma_{45} & \gamma_{46} \\ 0 & 0 & 0 & 0 & 0 & 1 \\ \gamma_{61} & \gamma_{62} & \gamma_{63} & \gamma_{64} & \gamma_{65} & \gamma_{66} \end{bmatrix} \quad (6.96)$$

where γ_{ij} 's are given in Table 6-2.

Table 6-2: Elements of the Jacobian matrix for the 3-DOF model

$\gamma_{21} = -\frac{k}{I} + \frac{\rho_{10} k_c r_m^2 \sin \lambda}{I}$	$\gamma_{41} = \frac{\rho_{20} k_c r_m \sin \lambda}{m}$	$\gamma_{61} = -\frac{\rho_{20} k_c r_m \sin \lambda}{m_1}$
$\gamma_{22} = -\frac{c}{I} + \frac{\rho_{10} c_c r_m^2 \sin \lambda}{I} - \frac{\eta_0 \cos \lambda}{I}$	$\gamma_{42} = \frac{\rho_{20} c_c r_m \sin \lambda}{m} - \frac{\eta_0 \sin \lambda}{m}$	$\gamma_{62} = -\frac{\rho_{20} c_c r_m \sin \lambda}{m_1} + \frac{\eta_0 \sin \lambda}{m_1}$
$\gamma_{23} = -\frac{r_m \rho_{10} k_c \cos \lambda}{I}$	$\gamma_{43} = -\frac{\rho_{20} k_c \cos \lambda}{m}$	$\gamma_{63} = \frac{\rho_{20} k_c \cos \lambda}{m_1}$
$\gamma_{24} = -\frac{r_m \rho_{10} c_c \cos \lambda}{I}$	$\gamma_{44} = -\frac{\rho_{20} c_c \cos \lambda}{m}$	$\gamma_{64} = \frac{\rho_{20} c_c \cos \lambda}{m_1}$
$\gamma_{25} = \frac{r_m \rho_{10} k_c \cos \lambda}{I}$	$\gamma_{45} = \frac{\rho_{20} k_c \cos \lambda}{m}$	$\gamma_{65} = -\frac{k_1}{m_1} - \frac{\rho_{20} k_c \cos \lambda}{m_1}$
$\gamma_{26} = \frac{r_m \rho_{10} c_c \cos \lambda}{I}$	$\gamma_{46} = \frac{\rho_{20} c_c \cos \lambda}{m}$	$\gamma_{66} = -\frac{c_1}{m_1} - \frac{\rho_{20} c_c \cos \lambda}{m_1}$
$\eta_0 = r_m k_c \cos \lambda (u_{30} - u_{50}) - k_c r_m \sin \lambda u_{10} d_\mu$		$d_\mu = -r_0 \mu_2 e^{-r_0 \omega } + \mu_3$
$\rho_{10} = -\sin \lambda + \mu_0 \operatorname{sgn}(R\omega) \cos \lambda$	$\rho_{20} = \cos \lambda + \mu_0 \operatorname{sgn}(R\omega) \sin \lambda$	

Figure 6-32(a) shows the variation of the three undamped natural frequencies of the 3-DOF model

with a constant coefficient of friction as a function of lead screw support stiffness (k_1) and contact stiffness (k_c). Lead screw parameters are taken as before with $m = 5 \text{ kg}$ and $m_1 = 0.232 \text{ kg}$. The corresponding stability map, which is obtained by examining the real part of the eigenvalues, is depicted in Figure 6-32(b). This map shows that the system becomes unstable whenever two of the system modes merge. Note that the parameter range where coupling between the first and the second modes occurs agrees with instability range of the undamped 2-DOF model of Section 3.5 (Figure 6-8) for large values of k_1 and also the undamped 2-DOF model of section 3.6 (Figure 6-20) for large values of k_c .

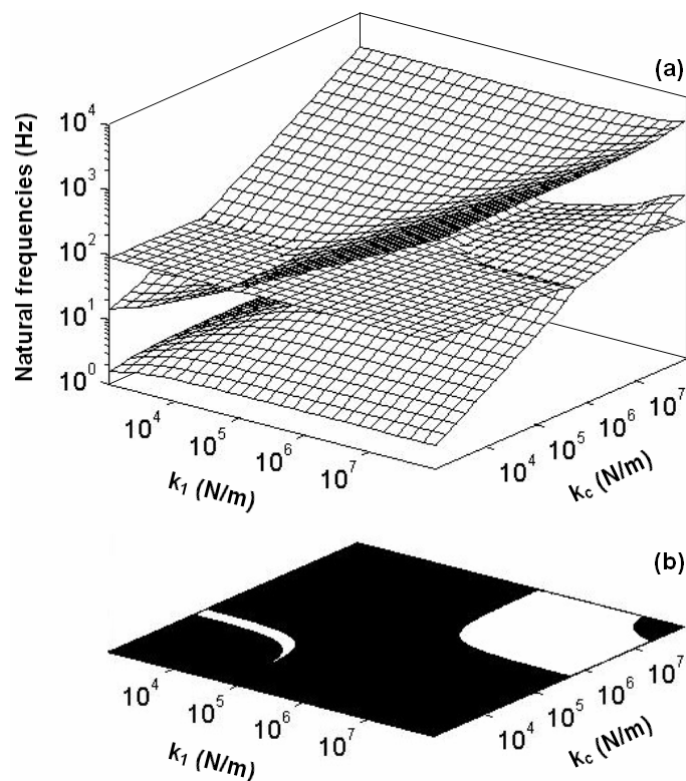


Figure 6-32: a) Evolution of the three natural frequencies of the undamped 3-DOF system (with constant coefficient of friction) as a function of k_c and k_1 . b) Stability map.

Figure 6-33 shows the stability maps of the 3-DOF model as the contact stiffness (k_c) and the support stiffness (k_1) are varied. In the 3 by 3 series of plots included in this figure, the contact damping coefficient (c_c) and lead support translational damping coefficient (c_1) take the values: 10,

10^2 , and $10^3 \text{ N}\cdot\text{s}/\text{m}$. Also the lead screw damping (angular) coefficient is chosen as $c = 3 \times 10^{-4} \text{ N}\cdot\text{m}\cdot\text{s}/\text{rad}$. Other parameters are selected as before. These plots clearly show the role of damping in both *stabilizing* an unstable fixed point and *destabilizing* a stable one. It is also interesting to note that, based on the symmetry of the plots and for the selected values and ranges of values of parameters, the stiffness and damping of the two translational DOFs (*i.e.* x and x_1) have a similar effect on the stability of the system.

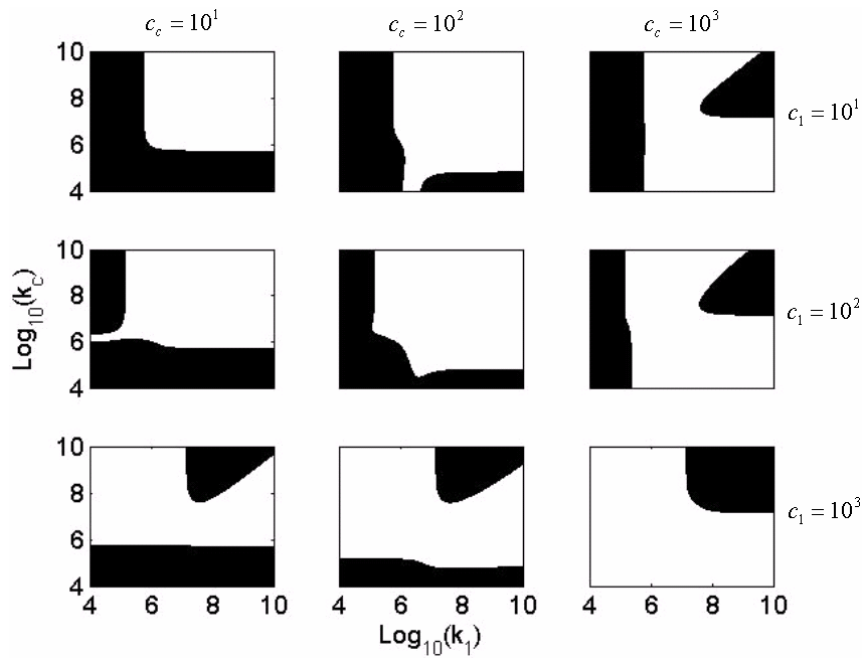


Figure 6-33: Local stability of fixed points of the 3-DOF lead screw system with constant coefficient of friction. Black: stable, white: unstable

6.5 Conclusions

In this chapter, the kinematic constraint and mode coupling instability mechanisms were studied. Together with negative damping instability studied in Chapter 5, these mechanisms constitute the three friction-induced instability mechanisms relevant to the lead screw systems.

It was found that both kinematic constraint and mode coupling instability mechanism share the same necessary conditions – namely, that the lead screw must be self-locking (*i.e.* $\mu > \tan \lambda$) and applied axial force must be in the same direction as the translating part (*i.e.* $R\omega > 0$). It was also

found that the quantity

$$\Gamma_0 = I - \left(r_m^2 \tan \lambda \frac{\mu - \tan \lambda}{1 + \mu \tan \lambda} \right) m,$$

plays a central role in almost all of the instability scenarios covered in this chapter.

Specific to the type of instability mechanism and the system model, parametric relationships were found that define the conditions for the local stability of the steady-sliding fixed point. An itemized list of the major findings is given here.

1. **Kinematic constraint instability in the 1-DOF basic lead screw model:** Inequality (6.2), *i.e.* $\Gamma_0 < 0$ defines the instability relationship in terms of friction, geometry, and the inertia of the rotating and translating parts of the lead screw drive.
2. **Mode coupling instability in the undamped 2-DOF model with compliant threads:** The flutter instability boundary is given by (6.36), which defines the parameter region where the two natural frequencies merge and become complex-valued.
3. **Secondary kinematic constraint instability in the undamped 2-DOF model with compliant threads:** For the parameter values that satisfy $\Gamma_0 < 0$, inequality (6.35) defines the conditions leading to secondary kinematic constrain instability, which overlaps and expands the mode coupling instability region.
4. **Mode coupling instability in the damped 2-DOF model with compliant threads:** The Routh-Hurwitz stability conditions are given by (6.44) to (6.47).
5. **Mode coupling instability in the undamped 2-DOF model with axially compliant supports:** The flutter instability boundary is given by (6.73), which defines the parameter region where the two natural frequencies merge and become complex-valued.
6. **Secondary kinematic constraint instability in the undamped 2-DOF model with axially compliant supports:** For the parameter values that satisfy $\Gamma_0 < 0$, inequality (6.72) defines the conditions for the secondary kinematic constrain instability, which overlaps and expands the mode coupling instability region.
7. **Kinematic constraint instability in the undamped 2-DOF model with axially compliant supports:** For the parameter values that satisfy both $\Gamma_0 < 0$ and inequality (6.68), *i.e.* $\tilde{\Gamma}_0 < 0$, the system is unstable and the line $\tilde{\Gamma}_0 = 0$ defines the divergence instability boundary.

8. **Mode coupling instability in the damped 2-DOF model with axially compliant supports:** The Routh-Hurwitz stability conditions are given by (6.82) to (6.85).
9. **Kinematic constraint instability in the damped 2-DOF model with axially compliant supports:** Since damping does not affect the instability caused by the kinematic constraint stability, conditions are the same as in the undamped case, *i.e.* $\tilde{\Gamma}_0 < 0$.

Mode coupling is by far the most complex instability mechanism of the three mechanisms considered in this work. In Appendix H, various numerical examples are given that show the complex effect of system parameters on the mode coupling instability and the resulting behavior of the system (*e.g.* amplitude and frequency of steady-state vibrations).

In this chapter, using a 3-DOF model, it was shown that when mode coupling instability mechanism can affect a system, all of the relevant DOFs must be included in the model. It was also shown that the compliance caused by the thread flexibility has similar effects on the stability of the system as the axial compliance in the lead screw supports.

Chapter 7

Vibration Control

When efforts towards designing a lead screw drive fail to guarantee vibration-free operation due to design constraints, material properties, or variations in the operating conditions, active vibration attenuation may become necessary. Other system performance requirements such as accurate tracking of certain position and velocity profiles, may also necessitate the use of closed-loop control.

In this chapter, robust control strategies are developed for lead screw drive systems with the main goal of suppressing vibrations caused by the negative damping instability mechanism while regulating the lead screw angular velocity to a constant reference velocity. Furthermore, the controllers are designed to perform these tasks in situations where there is significant uncertainty in the value of various system parameters.

The controllers developed here are based on the “sliding mode control” method, which was pioneered by Utkin [91]. The basic idea is to design a control input that confines the system’s trajectories to a predefined “sliding surface or manifold”. On this surface, the system dynamics are governed by an asymptotically stable differential equation. The control law that moves system trajectory to the sliding mode is typically discontinuous and switches between two values based on the states of the system. The popularity of this approach in the design of feedback controller stems from its robustness properties to model uncertainties [84,92]. Numerous published works are found in the literature on the applications of the sliding mode control to various mechanical systems (see for example the survey paper [93]).

The main drawback of the sliding mode control approach is what is known as chattering. In the implementation (or when the otherwise neglected dynamics of the actuators are included in the model), the delay in the switching action required by the discontinuous controller results in high frequency vibration that can deteriorate the performance of the controller or lead to instabilities [84,92].

A number of approaches were put forward by many researches that aim to reduce or eliminate chattering [94]. These methods include; continuous approximation of the discontinuous controller law [84,92,95,96], observer-based sliding mode control [94,97], and higher-order sliding mode control [98]. The most popular approach – the one adopted here – is the continuous sliding mode control by linear approximation of the control law or “boundary layer” method [96,99]. In this approach, in a small distance of the sliding (switching) surface (*i.e.* the boundary layer), the control law is replaced by an approximate linear high-gain feedback. Elimination of chattering with this approach usually leads to reduced performance of the controller, since the trajectories are only guaranteed to stay inside the boundary layer and not on the sliding surface. Integral sliding mode control is one of the approaches proposed to counteract this effect [99].

In this chapter, a simplified version of the model presented in Section 3.8 is considered. The mathematical model of this system presented in Section 7.1. The uncertainty in the system parameters is discussed in Section 7.2 and sample parameter values used in the simulations are given. In Section 7.3, a sliding mode controller is designed with the assumption that the entire drive from power generator (*e.g.* DC motor) to the moving load is rigidly connected, and thus the system is represented by a single DOF. The rigidity condition is relaxed in Section 7.4, leading to a 2-DOF system model. Another sliding mode controller is developed to deal with the added complexity of this model. The special feature of this controller is its ability to stabilize the system in the face of *unmatched uncertainties* [84]. Numerical simulation results are included that demonstrate the effectiveness of both of these controllers. Finally, the conclusions are presented in Section 7.5.

7.1 Mathematical Model

A slightly simplified version of the model presented in Section 3.8 is considered here as shown in Figure 7-1. For the motor, Newton’s second law gives;

$$J\ddot{\theta}_M = T_M - T_{fM} \operatorname{sgn} \dot{\theta}_M + k_2(\theta_w - \theta_M) - c_M \dot{\theta}_M \quad (7.1)$$

where θ_M is the rotor’s angular displacement, J is the inertia of the rotor, and T_M is the generated (input) torque. T_{fM} and c_M are the internal friction and damping of the motor, respectively. Also, k_1 is the torsional stiffness of the coupling connecting the motor to gearbox, and θ_w designates the input angular displacement of the gearbox. For the lead screw and nut, similar to (3.11) and (3.12), one can write

$$I\ddot{\theta} = k_1(\theta_G - \theta) - c\dot{\theta} + r_m(N \sin \lambda - F_f \cos \lambda) - T_0 \operatorname{sgn} \dot{\theta} \quad (7.2)$$

$$m\ddot{x} = -N \cos \lambda - F_f \sin \lambda + R - F_0 \operatorname{sgn} \dot{x} \quad (7.3)$$

where the terms $T_0 \operatorname{sgn} \dot{\theta}$ and $F_0 \operatorname{sgn} \dot{x}$ reflect the friction in lead screw supports and bearings of the translating mass, respectively. Also the normal contact force is given by (3.16), where $\theta_i = \theta_G$.

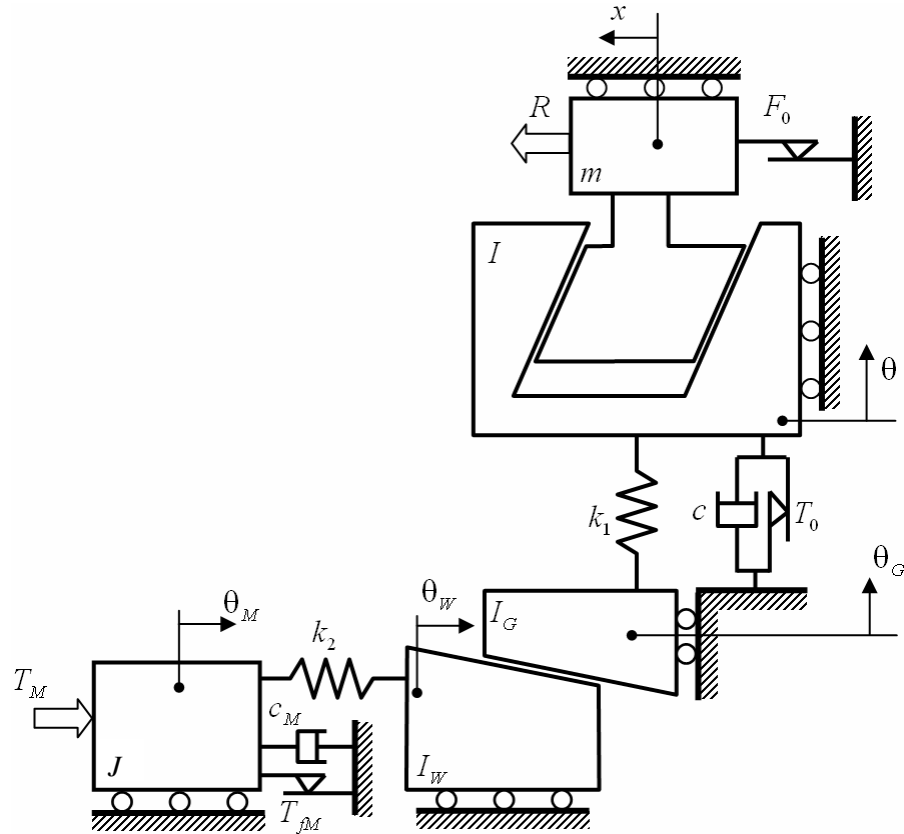


Figure 7-1: lead screw drive model

For simplicity, that the gearbox is assumed to be mass-less and frictionless. As a result, for the gearbox, the following kinematic relationship holds:

$$k_1(\theta - \theta_G) = r^{-1}k_2(\theta_w - \theta_M) \quad (7.4)$$

where

$$\theta_G = r\theta_w \quad (7.5)$$

Eliminating N between (7.2) and (7.3) yields

$$\Gamma\ddot{\theta} + k_1\dot{\theta} + c\dot{\theta} = k_1\theta_G - \xi(R - F_0 \operatorname{sgn} \dot{\theta}) - T_0 \operatorname{sgn} \dot{\theta} \quad (7.6)$$

where

$$\Gamma = I - r_m \tan \lambda \xi m \quad (7.7)$$

$$\xi = r_m \frac{\mu_s - \tan \lambda}{1 + \mu_s \tan \lambda} \quad (7.8)$$

and as before, $\mu_s = \mu \operatorname{sgn}(\dot{u} + \omega) \operatorname{sgn} N$. Also

$$\mu(\dot{u}) = (\mu_1 + \mu_2 e^{-\tau_0|\dot{u} + \omega|} + \mu_3 |\dot{u} + \omega|) (1 - e^{-\tau_1|\dot{u} + \omega|}) \quad (7.9)$$

From (7.4) and (7.5) one finds

$$\frac{k_1}{r^{-2}k_2 + k_1} \theta + \frac{r^{-1}k_2}{r^{-2}k_2 + k_1} \theta_M = \theta_G \quad (7.10)$$

Substituting (7.10) into (7.1) and (7.6) yields the equations of motion of the 2-DOF model

$$\Gamma\ddot{\theta} + k(\theta - r\theta_M) + c\dot{\theta} = -\xi(R - F_0 \operatorname{sgn} \dot{\theta}) - T_0 \operatorname{sgn} \dot{\theta} \quad (7.11)$$

$$J\ddot{\theta}_M = T_M - T_{fM} \operatorname{sgn} \dot{\theta}_M + rk(\theta - r\theta_M) - c_M \dot{\theta}_M \quad (7.12)$$

where

$$k = \frac{k_1 k_2}{k_2 + r^2 k_1} \quad (7.13)$$

The contact force, N , is given by

$$N = \frac{IR - IF_0 \operatorname{sgn} \dot{\theta} + mr_m \tan \lambda T_0 \operatorname{sgn} \dot{\theta} + mr_m \tan \lambda c \dot{\theta} - mr_m \tan \lambda k_1 (r\theta_M - \theta)}{\Gamma(\cos \lambda + \mu_s \sin \lambda)} \quad (7.14)$$

7.1.1 A Note on the Friction Model

The friction model (7.9) includes a linear term $\mu_3|\dot{u} + \omega|$ which could cause problems in the subsequent global stability analysis when $\mu_3 < 0$. Although, in practical situations, $|\mu_3|$ is small enough such that over the velocity range of interest μ does not become too close to zero, here we need to formally set a limit on the velocity ω_{\max} , such that for $\omega > \omega_{\max}$, the coefficient of friction tapers off and becomes a constant. The easiest way to accomplish this while keeping the smoothness properties of the friction model is to modify the velocity-dependent coefficient of friction to

$$\mu(\dot{u}) = \left(\mu_1 + \mu_2 e^{-r_1|\dot{u} + \omega|} + \mu_3 \omega_{\max} \tanh\left(\frac{|\dot{u} + \omega|}{\omega_{\max}}\right) \right) (1 - e^{-r_1|\dot{u} + \omega|}) \quad (7.15)$$

where $\omega_{\max} > 0$ is a large velocity such that $\mu_1 + \mu_3 \omega_{\max} > 0$.

The modified velocity-dependent coefficient of friction given by (7.15) is used in the subsequent sections only where global system properties are considered. In all other cases, it is assumed that $|\dot{u} + \omega| \ll \omega_{\max}$, such that the difference between (7.15) and (7.9) is negligible.

7.2 Parameter Uncertainty

As mentioned earlier, control strategies are sought that are robust to parameter uncertainties. The only information assumed here are the bounds on each of the parameters. In this section, some relationships for the upper and lower bounds of system parameters are presented which are used in the numerical examples presented in the subsequent sections.

From (7.15), one finds

$$0 \leq \mu(\omega) < \bar{\mu} \quad (7.16)$$

where

$$\begin{aligned} \bar{\mu} &= \mu_1 + \mu_2, & \mu_3 &\leq 0 \\ \bar{\mu} &= \mu_1 + \mu_2 + \mu_3 |\omega_{\max}|, & \mu_3 &> 0 \end{aligned} \quad (7.17)$$

Based on (7.16), the upper and lower bounds for ξ defined by (7.8) are given by

$$\underline{\xi} \leq \xi \leq \bar{\xi} \quad (7.18)$$

where

$$\underline{\xi} = -r_m \frac{\bar{\mu} + \tan \lambda}{1 - \bar{\mu} \tan \lambda} \quad \bar{\xi} = r_m \frac{\bar{\mu} - \tan \lambda}{1 + \bar{\mu} \tan \lambda} \quad (7.19)$$

Note that $\underline{\xi} < 0$ while $\bar{\xi} < \left| \frac{\xi}{\xi} \right|$ can be negative, positive or zero depending on the direction of motion. It follows from (7.7) and (7.18) that

$$\underline{\gamma} \leq \Gamma \leq \bar{\gamma} \quad (7.20)$$

where

$$\underline{\gamma} = \underline{I} - \bar{m} \bar{\xi} \quad \bar{\gamma} = \bar{I} - \bar{m} \underline{\xi} \quad (7.21)$$

It is assumed $\underline{\gamma} > 0$ to exclude parametric conditions where kinematic constraint instability can occur. In (7.21) it is assumed that $\underline{I} \leq I \leq \bar{I}$ and $0 \leq m \leq \bar{m}$. For all of the other system parameters in (7.11) and (7.12), only the knowledge of upper bound ($\bar{\quad}$) and lower bound ($\underline{\quad}$) are assumed to be available. Throughout this chapter, numerical simulation results are presented that are obtained using parameter values listed in Table 7-1. These values are mostly taken from the experimental case study of Chapter 4. The “Min.” and “Max.” columns are the assumed available bounds on the uncertain parameters. In addition, the “Nom.” column lists the nominal values.

Table 7-1: Parameter values used in the simulations

Parameter	True Value	Min.	Nom.	Max.	Unit
r_m	5.183	-	5.183	-	mm
λ	5.57°	-	5.57	-	deg
r	3/19	-	3/19	-	-
m	1.12kg	0.5	1.0	2	kg
I	3.12×10^{-6}	3.0×10^{-6}	3.1×10^{-6}	3.3×10^{-6}	kgm^2
J	8.5×10^{-5}	7.0×10^{-5}	8.5×10^{-5}	9.0×10^{-5}	kgm^2
k	1	0.75	1.0	1.5	Nm/rad
c	20×10^{-5}	10×10^{-5}	30×10^{-5}	40×10^{-5}	Nms/rad
c_M	5.1×10^{-3}	2×10^{-3}	6×10^{-3}	10×10^{-3}	Nms/rad
R	100	80	100	120	N
T_{JM}	1.2×10^{-2}	0	1×10^{-2}	2.0×10^{-2}	Nm

Table 7-1 (continued): Parameter values used in the simulations

Parameter	True Value	Min.	Nom.	Max.	Unit
μ_1	0.218	0.15	0.2	0.3	-
μ_2	0.0203	0.0	0.02	0.04	-
μ_3	-4.47×10^{-4}	-10×10^{-4}	-1×10^{-4}	0	s/rad
r_0	0.38	1	0.4	0.2	s/rad
r_1	2	0.2	2	5	s/rad
T_0	0	0	0	0	Nm
F_0	0	0	0	0	N

7.3 Sliding Mode Control¹ for Rigid Drives

The rigid drive is obtained by assuming k to be very large which yields

$$\theta = \theta_G = r\theta_W = r\theta_M \quad (7.22)$$

Eliminating $(\theta - r\theta_M)$ between (7.11) and (7.12) and using (7.22), yields

$$(J + r^2\Gamma)\ddot{\theta} = -(c_M + r^2c)\dot{\theta} + rT_M - rT_{fM} \operatorname{sgn} \dot{\theta} - r^2\xi(R - F_0 \operatorname{sgn} \dot{\theta}) - r^2T_0 \operatorname{sgn} \dot{\theta} \quad (7.23)$$

The normal contact force is now calculated from

$$N = \frac{(r^2I + J)(R - F_0 \operatorname{sgn} \dot{x}) + r_m \tan \lambda m (r^2T_0 \operatorname{sgn} \dot{\theta} + rT_{fM} \operatorname{sgn} \dot{\theta} - rT_M + c_M \dot{\theta} + r^2c\dot{\theta})}{(\cos \lambda + \mu_s \sin \lambda)(r^2\Gamma + J)} \quad (7.24)$$

The second order differential equation (7.23) can be written in state-space form as

$$\begin{aligned} \dot{x}_1 &= x_2 \\ \dot{x}_2 &= -C(x_2)x_2 + G(x_2)[u - \Delta(x_2)] \end{aligned} \quad (7.25)$$

where

$$\begin{aligned} x_1 &= \theta - \omega t \\ x_2 &= \dot{\theta} - \omega \end{aligned} \quad (7.26)$$

and ω is the reference constant lead screw angular velocity and $u = T_M$ is the controlled input. Also

¹ The approach followed in this section is taken from [84].

$$C(x) = \frac{c_M + r^2 c}{J + r^2 \Gamma} \quad (7.27)$$

$$G(x) = \frac{r}{J + r^2 \Gamma} \quad (7.28)$$

$$\Delta(x) = T_{fM} \operatorname{sgn}(x + \omega) + r\xi(R - F_0 \operatorname{sgn}(x + \omega)) + rT_0 \operatorname{sgn}(x + \omega) + (r^{-1}c_M + rc)\omega \quad (7.29)$$

Note that $0 < C_{\min} \leq C(x) < C_{\max}$, $0 < G_{\min} \leq G(x) < G_{\max}$, and $|\Delta(x)| \leq \Delta_{\max}$ where

$$C_{\min} = \frac{c_M + r^2 \underline{c}}{\underline{J} + r^2 \underline{\gamma}}, \quad C_{\max} = \frac{\bar{c}_M + r^2 \bar{c}}{\underline{J} + r^2 \underline{\gamma}} \quad (7.30)$$

$$G_{\min} = \frac{r}{\underline{J} + r^2 \underline{\gamma}}, \quad G_{\max} = \frac{r}{\underline{J} + r^2 \underline{\gamma}} \quad (7.31)$$

$$\Delta_{\max} = \bar{T}_{fM} + r\bar{T}_0 + r\xi(\bar{R} + \bar{F}_0) + (r^{-1}\bar{c}_M + r\bar{c})\omega \quad (7.32)$$

Let

$$s = ax_1 + x_2, \quad a > 0 \quad (7.33)$$

define the sliding surface. Note that when $s = 0$, we have $x_2 = -ax_1$, and if it is substituted in the first equation of (7.25), $\dot{x}_1 = -ax_1$ is exponentially stable. The differential equation governing s is found as

$$\begin{aligned} \dot{s} &= ax_2 + \dot{x}_2 \\ &= ax_2 - C(x_2)x_2 + G(x_2)[u - \Delta(x_2)] \end{aligned} \quad (7.34)$$

Select $\rho(x_2)$ such that

$$\begin{aligned} \left| \frac{ax_2 - C(x_2)x_2 - G(x_2)\Delta(x_2)}{G(x_2)} \right| &\leq \frac{|ax_2 - C(x_2)x_2 - G(x_2)\Delta(x_2)|}{G_{\min}} \\ &\leq \frac{(a + C_{\max})|x_2| + G_{\max}\Delta_{\max}}{G_{\min}} = \rho(x_2) \end{aligned} \quad (7.35)$$

Then the control input is chosen as

$$u = -\beta(x_2)\text{sgn}(s) \quad (7.36)$$

where

$$\beta(x_2) = \rho(x_2) + \beta_0 \quad (7.37)$$

for some $\beta_0 > 0$. With this controller, the Lyapunov function candidate for (7.34) is chosen as

$V = \frac{1}{2}s^2$. The derivative of V along the system trajectories is

$$\begin{aligned} \dot{V} &= s\dot{s} = s[ax_2 - C(x_2)x_2 - G(x_2)\Delta(x_2)] + sG(x_2)u \\ &\leq |s|\rho(x_2)G(x_2) + sG(x_2)u \\ &\leq |s|G(x_2)[\rho(x_2) - \beta(x_2)] \\ &\leq -\beta_0 G_{\min} |s| \end{aligned} \quad (7.38)$$

Therefore, the trajectories starting away from the sliding surface reach it in finite time and once on the sliding surface, cannot leave it. It was already shown that trajectories on the sliding surface are exponentially attracted to origin.

The controller given by (7.36) is discontinuous and suffers from the chattering problem in the implementation. One way to deal with this problem is to approximate (7.36) using a saturation function

$$u = -\beta(x_2)\text{sat}\left(\frac{s}{\epsilon}\right) \quad (7.39)$$

where the saturation function, $\text{sat}(\cdot)$, is defined as

$$\text{sat}(u) = \begin{cases} u & |u| \leq 1 \\ \text{sgn}(u) & |u| > 1 \end{cases}$$

Repeating the previous analysis, one finds that the system trajectories starting outside the boundary layer $\{|x| |s| \leq \epsilon\}$ reach it in finite time and once inside, cannot leave it. Inside the boundary layer the x_1 equation becomes

$$\dot{x}_1 = -ax_1 + s, \quad |s| \leq \epsilon \quad (7.40)$$

The derivative of $V_1 = \frac{1}{2}x_1^2$ satisfies

$$\dot{V}_1 = -ax_1^2 + sx_1 \leq -ax_1^2 + |x_1|\varepsilon \leq -a(1-\vartheta)x_1^2, \quad \forall |x_1| \geq \frac{\varepsilon}{a\vartheta} \quad (7.41)$$

where $0 < \vartheta < 1$. As a result, the trajectories reach the set

$$\Omega_\varepsilon = \left\{ |x_1| \leq \frac{\varepsilon}{a\vartheta}, |s| \leq \varepsilon \right\} \quad (7.42)$$

in finite time and remain inside it for all future time. This result shows ultimate boundedness with an ultimate bound that is a function of ε and can be made arbitrarily small. Further analysis is needed to see what happens inside Ω_ε , where the control is given by $u = -\beta(x_2)\left(\frac{ax_1 + x_2}{\varepsilon}\right)$. The closed-loop

system equations are

$$\begin{aligned} \dot{x}_1 &= x_2 \\ \dot{x}_2 &= -C(x_2)x_2 - G(x_2)\Delta(x_2) - G(x_2)\beta(x_2)\left(\frac{ax_1 + x_2}{\varepsilon}\right) \end{aligned} \quad (7.43)$$

This system has an equilibrium point at $(x_{10}, 0)$ where

$$x_{10} = -\varepsilon \frac{\Delta(0)}{a\beta(0)} \quad (7.44)$$

To shift the equilibrium point to origin, set $y_1 = x_1 - x_{10}$ and $y_2 = x_2$. The system's equations become

$$\begin{aligned} \dot{y}_1 &= y_2 \\ \dot{y}_2 &= -C(y_2)y_2 - G(y_2)\Delta(y_2) - G(y_2)\beta(y_2)\left(\frac{ay_1 + y_2}{\varepsilon} - \frac{\Delta(0)}{\beta(0)}\right) \end{aligned}$$

or

$$\begin{aligned} \dot{y}_1 &= y_2 \\ \dot{y}_2 &= -\frac{aG(y_2)\beta(y_2)}{\varepsilon}y_1 - \left[C(y_2) + \frac{G(y_2)\beta(y_2)}{\varepsilon} \right]y_2 + \Theta(y_2) \end{aligned} \quad (7.45)$$

where $\Theta(y_2) = G(y_2)\beta(y_2)\frac{\Delta(0)}{\beta(0)} - G(y_2)\Delta(y_2)$. Note that $\Theta(0) = 0$.

Inside Ω_ε , we have $\inf_{x \in \Omega_\varepsilon} x_2 = -\varepsilon$. Consequently, for $\varepsilon < |\omega|$, $\Theta(y_2)$ is a Lipschitz continuous function. From the Lipschitz continuity of Θ , assume $|\Theta(y)| < \kappa|y|$ for some κ . Take

$$V(y_1, y_2) = \frac{a}{2\varepsilon} y_1^2 + \int_0^{y_2} \frac{udu}{G(u)\beta(u)} \quad (7.46)$$

as a Lyapunov function candidate. Since $G(u) > 0$ and $\beta(u) > 0$ for $\forall u \in \Omega_\varepsilon$, it is obvious that V is a positive definite function of (y_1, y_2) . The derivative of V along the trajectories is found as

$$\begin{aligned} \dot{V} &= \frac{a}{\varepsilon} y_1 y_2 + \frac{y_2}{G(y_2)\beta(y_2)} \dot{y}_2 \\ &= \frac{a}{\varepsilon} y_1 y_2 + \frac{y_2}{G(y_2)\beta(y_2)} \left(-\frac{aG(y_2)\beta(y_2)}{\varepsilon} y_1 - \left[C(y_2) + \frac{G(y_2)\beta(y_2)}{\varepsilon} \right] y_2 + \Theta(y_2) \right) \\ &= -\left[\frac{C(y_2)}{G(y_2)\beta(y_2)} + \frac{1}{\varepsilon} \right] y_2^2 + \frac{y_2 \Theta(y_2)}{G(y_2)\beta(y_2)} \\ &\leq -\left[\frac{C(y_2) - \kappa}{G(y_2)\beta(y_2)} + \frac{1}{\varepsilon} \right] y_2^2 \end{aligned} \quad (7.47)$$

From (7.47) it is evident that \dot{V} can be made semi-negative definite by choosing ε small enough, regardless of the value of κ . Using LaSalle's invariance principle [84], and since the set $\{(y_1, y_2) \mid \dot{V}(y_1, y_2) = 0\}$ contains only the trivial trajectory $(0,0)$, one concludes that the point $(x_{10}, 0)$ is asymptotically stable.

7.3.1 Numerical Examples

The controller designed in this section is simply a linear proportional plus integrator controller followed by a saturation function. To illustrate the effectiveness of the developed controller, some numerical results are presented here. The parameter values are taken from Table 7-1.

7.3.1.1 Example #1

Figure 7-2 shows two system trajectories under the action of the sliding mode controller (7.39).

Controller parameters are selected as $a = 1000$, $\beta_0 = 0$, and $\varepsilon = 1$. The boundary layer is shown by two parallel dashed-dotted lines (*i.e.* $x_2 = -ax_1 \pm \varepsilon$). Inside the boundary layer, system (7.43) has an asymptotically attractive equilibrium point $(x_{10}, 0)$, given by (7.44). In this example, $x_{10} \approx -4 \times 10^{-4} \text{ rad}$. The controlled input time histories are shown in Figure 7-3.

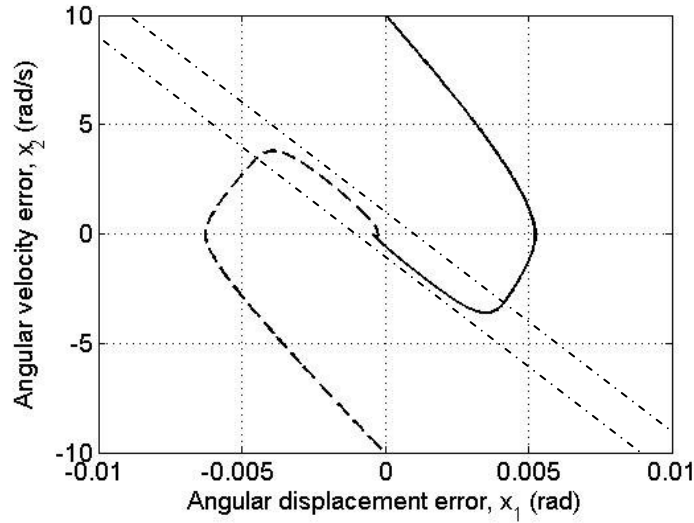


Figure 7-2: System trajectories under the action of the continuous sliding mode controller.
Dashed: $x(0) = (0, -10)$ solid: $x(0) = (0, 10)$; dashed-dot: boundary layer

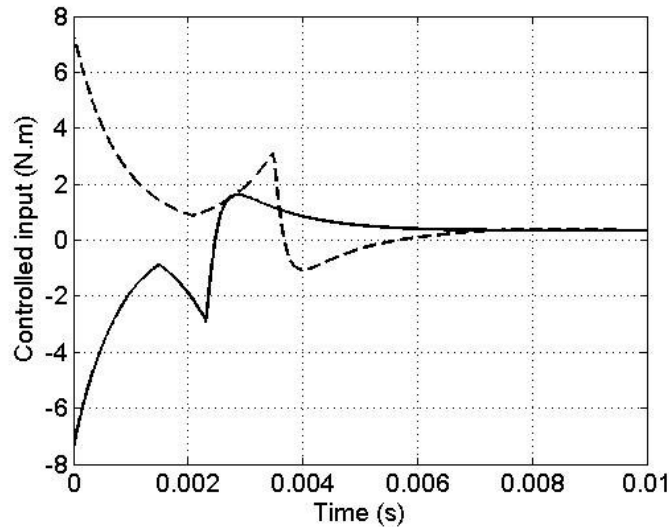


Figure 7-3: Controlled input. Dashed: $x(0) = (0, -10)$ solid: $x(0) = (0, 10)$

7.3.1.2 Example #2

Figure 7-4 and Figure 7-5 show simulation results obtained using the same settings as the above except for ϵ which was increased to 5 (resulting in a much wider boundary layer). Here, the time required to reach steady state is increased but the required input signal is smoother. In addition, the displacement error has increased to $x_{10} \approx -2 \times 10^{-3} \text{ rad}$ (about 20 times higher compared to the previous example).

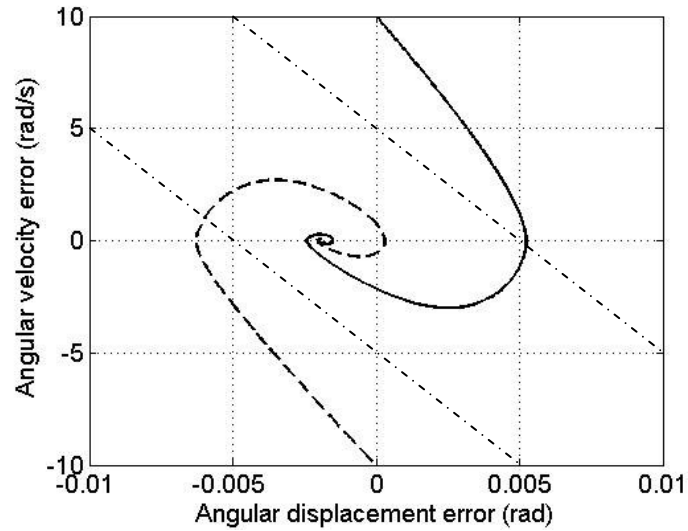


Figure 7-4: System trajectories under the action of the continuous sliding mode controller.
Dashed: $x(0) = (0, -10)$ solid: $x(0) = (0, 10)$; dashed-dot: boundary layer

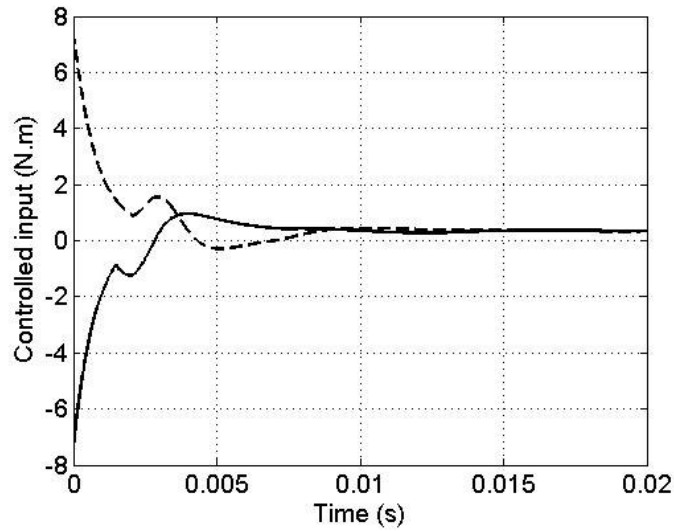


Figure 7-5: Controlled input. Dashed: $x(0) = (0, -10)$ solid: $x(0) = (0, 10)$

7.3.1.3 Example #3

Figure 7-6 shows system trajectories starting from $x(0) = (0, -10)$ (dashed lines) and starting from $x(0) = (0, 10)$ (solid lines) for two values of β_0 . Other control parameters are $a = 10000$ and $\varepsilon = 5$. Results show that by increasing β_0 , which increases the control gain as per (7.37), trajectories go through a shorter reaching phase. Moreover, the steady state displacement error decreases as given by (7.44). The steady state errors are -3×10^{-5} and -3×10^{-6} for $\beta_0 = 5$ and $\beta_0 = 50$, respectively.

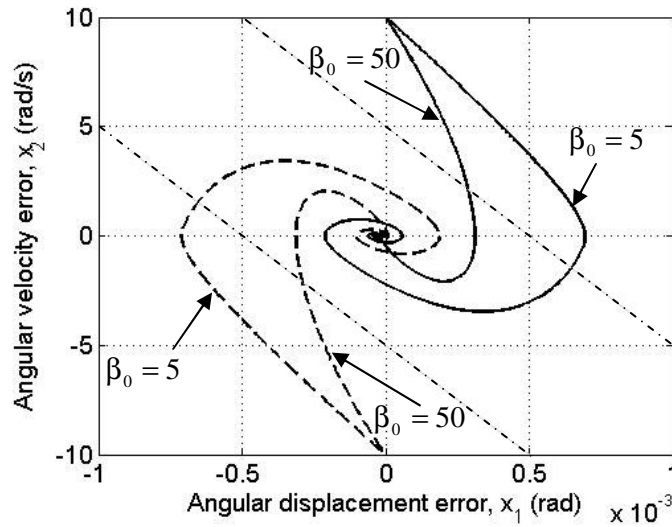


Figure 7-6: Effect of β_0 on the performance of the controller

7.3.1.4 Example #4

In the foregoing Lyapunov stability analysis, it was shown that to have asymptotic stability, ϵ must be chosen small enough according to (7.47). Otherwise, the best provable result would be the ultimate boundedness given by (7.42). In this example, parameters are chosen to demonstrate this situation. The control parameters are selected as $a = 50000$, $\epsilon = 5$, and $\beta_0 = 0.01$.

Figure 7-7 shows system trajectories starting from $x(0) = (0, -10)$ (dashed lines) and starting from $x(0) = (0, 10)$ (solid lines). It is clear from this figure that the two trajectories remain in the invariant set Ω_ϵ shown by the hatched region. In the close-up view depicted in Figure 7-8, it can be seen that the controlled system trajectories are attracted to a limit cycle. The pulsating behavior of the controlled system is shown in Figure 7-9. The velocity error varies between -0.73 to 1.43 rad/s.

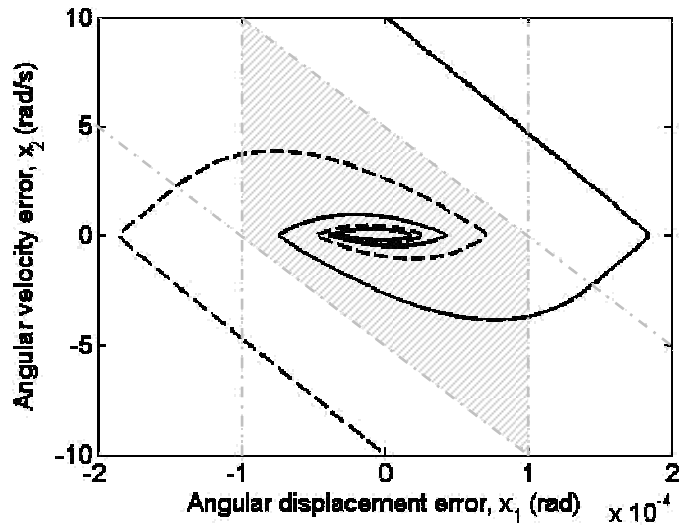


Figure 7-7: System trajectories under the action of the continuous sliding mode controller.
 Dashed: $x(0) = (0, -10)$ solid: $x(0) = (0, 10)$;
 hatched region: bounds on the solution given by the stability conditions.

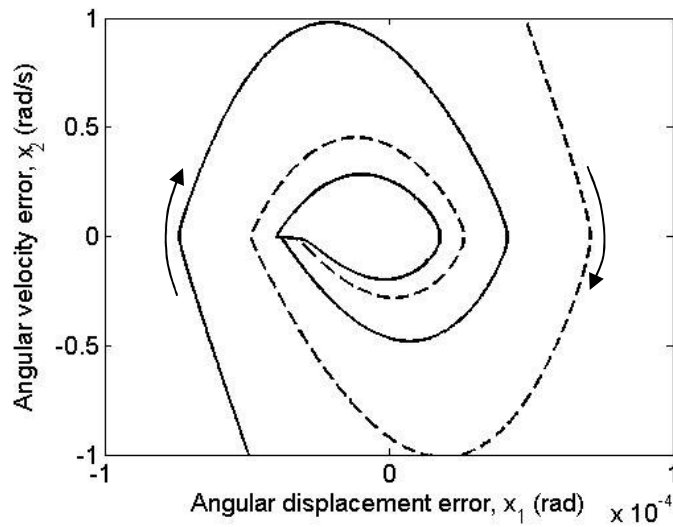


Figure 7-8: Close-up view of system trajectories showing limit-cycle behavior.
 Dashed: $x(0) = (0, -10)$ solid: $x(0) = (0, 10)$

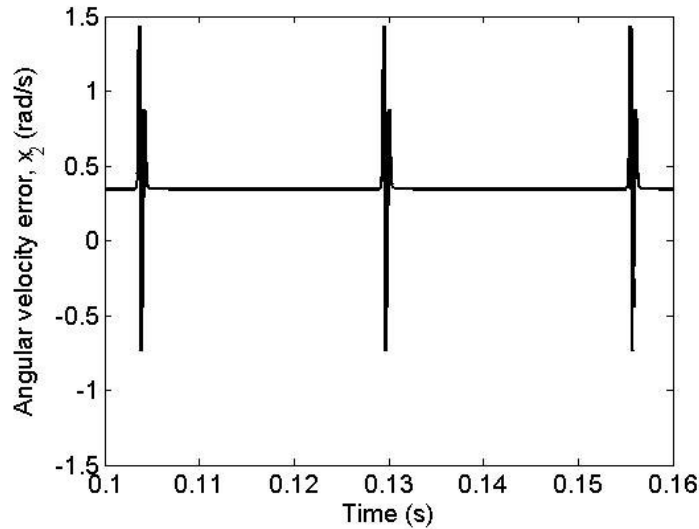


Figure 7-9: A portion of velocity error time history

For the selected parameters, according to (7.47), the limit cycle disappears for $\varepsilon \leq 0.8$ and trajectories converge asymptotically to the equilibrium point.

7.4 Sliding Mode Controller for Flexible Drive

The controller presented in Section 7.3 was designed for a simplified system model where the system elements are considered to be rigid and rigidly connected. The rigidity of the drive, however, is not a realistic assumption in many cases, and it is natural to assume some degree of flexibility in the couplings, gearbox, or even the lead screw itself. Here, a sliding mode controller is developed for the 2-DOF model presented in Section 7.1 that properly addresses the increased complexity of the model and the effect of the velocity-dependent coefficient of friction.

One of the challenges in designing a sliding mode controller (or any robust controller for that matter) is the appearance of the so-called *unmatched* uncertainties in the system model¹. Starting with (7.11) and (7.12), and introducing the following change of variables

¹ Unmatched uncertainties do not satisfy the matching condition. Under the matching condition, the uncertain terms appear in the state equation of the system at the same point as the control input [84].

$$\begin{aligned}
x_1 &= \theta - r\theta_M \\
x_2 &= \dot{\theta} - \omega \\
x_3 &= \dot{\theta}_M - r^{-1}\omega
\end{aligned} \tag{7.48}$$

the equations of motion in the state-space form with three states can be written as

$$\begin{aligned}
\dot{x}_1 &= x_2 - rx_3 \\
\dot{x}_2 &= -\frac{c}{\Gamma}x_2 - \frac{k}{\Gamma}x_1 - \frac{1}{\Gamma}\xi R - \frac{c}{\Gamma}\omega \\
\dot{x}_3 &= \frac{1}{J}u - \frac{1}{J}T_{JM} \operatorname{sgn}(x_3 + r^{-1}\omega) + \frac{rk}{J}x_1 - \frac{c_M}{J}x_3 - \frac{c_M}{J}r^{-1}\omega
\end{aligned} \tag{7.49}$$

where Γ and ξ are defined by (7.7) and (7.8), respectively and u is the controlled input. Also T_0 and F_0 were neglected for simplicity.

The first step in designing a sliding mode controller for (7.49) is to find the sliding surface: $x_3 = \varphi(x_1, x_2)$. Once confined to this surface, the system trajectories must asymptotically attract to the origin. This process can be viewed as finding a state feedback for the first two of the system equations when x_3 is seen as the control input.

$$\begin{aligned}
\dot{x}_1 &= x_2 - r\varphi(x_1, x_2) \\
\dot{x}_2 &= -\frac{c}{\Gamma}x_2 - \frac{k}{\Gamma}x_1 - \frac{1}{\Gamma}\xi R - \frac{c}{\Gamma}\omega
\end{aligned} \tag{7.50}$$

Once such a surface is found, the next step would be to design a controller action that brings the system trajectory from any initial point in the region of interest to the sliding surface $x_3 = \varphi(x_1, x_2)$.

Here the sliding surface is chosen as

$$x_3 = \frac{d_1}{r}x_1 - \frac{d_2}{r}x_2 \tag{7.51}$$

where d_1 and d_2 are constants to be determined.

7.4.1 The Sliding Phase

Upon substituting (7.51) into the first two equations of (7.49), the governing equations of the sliding motion are found as

$$\begin{bmatrix} \dot{x}_1 \\ \dot{x}_2 \end{bmatrix} = \begin{bmatrix} -d_1 x_1 + (d_2 + 1)x_2 \\ -\Gamma^{-1} k x_1 - \Gamma^{-1} c x_2 - \Gamma^{-1} \xi R - \Gamma^{-1} c \omega \end{bmatrix} \quad (7.52)$$

Converting (7.52) to a second order differential equation, gives

$$\Gamma \ddot{x}_1 + (c + \Gamma d_1) \dot{x}_1 + ((d_2 + 1)k + c d_1) x_1 = -(d_2 + 1)(c \omega + \xi R) \quad (7.53)$$

where the lead screw angular velocity error, x_2 (argument of ξ and Γ functions) is given by

$$x_2 = \frac{\dot{x}_1 + d_1 x_1}{d_2 + 1} \quad (7.54)$$

Inspired by the results of Section 5.3, one would expect that a similar analysis using the averaging method should reveal that there is a positive constant \tilde{d}_1 (dependent on d_2 and other system parameters), such that setting $d_1 > \tilde{d}_1$ would lead to asymptotic (exponential) stability of the equilibrium point of (7.53).

The equilibrium point, (x_{10}, x_{20}) , of (7.52) is the solution of

$$\begin{bmatrix} -d_1 x_{10} + (d_2 + 1)x_{20} \\ -k x_{10} - c x_{20} - \xi_0 R - c \omega \end{bmatrix} = \begin{bmatrix} 0 \\ 0 \end{bmatrix} \quad (7.55)$$

where

$$\xi_0 = r_m \frac{\mu_0 \operatorname{sgn}(R) \operatorname{sgn}(x_{20} + \omega) - \tan \lambda}{1 + \mu_0 \operatorname{sgn}(R) \operatorname{sgn}(x_{20} + \omega) \tan \lambda} \quad (7.56)$$

and

$$\mu_0 = \mu(x_{20}) \quad (7.57)$$

where $\mu(\cdot)$ is defined by (7.15).

From (7.55), x_{10} is found as the unique solution of the following equation

$$\left(k + \frac{c d_1}{d_2 + 1} \right) x_{10} + \xi_0 R + c \omega = 0 \quad (7.58)$$

and

$$x_{20} = \frac{d_1}{d_2 + 1} x_{10} \quad (7.59)$$

Let

$$z = x_1 - x_{10} \quad (7.60)$$

then (7.53) becomes

$$\Gamma \ddot{z} + (c + \Gamma d_1) \dot{z} + ((d_2 + 1)k + cd_1)z = (d_2 + 1)R(\xi_0 - \xi) \quad (7.61)$$

The contact force, N , is simplified from (7.14) to

$$N = \frac{\Gamma_0 R + mr_m \tan \lambda c \left(\frac{\dot{z} + d_1 z}{d_2 + 1} \right) + mr_m \tan \lambda kz}{\Gamma(\cos \lambda + \mu_s \sin \lambda)} \quad (7.62)$$

Let $\tau = \Omega t$ where

$$\Omega = \sqrt{\frac{(d_2 + 1)k}{I}} \quad (7.63)$$

Note that compared with (5.24), the natural frequency of the undamped unperturbed system is multiplied by $\sqrt{d_2 + 1}$. Also, define the non-dimensional parameters

$$\hat{m} = r_m^2 \frac{m}{I} \tan \lambda \quad (7.64)$$

$$\tilde{c} = \frac{c}{\sqrt{(d_2 + 1)kI}} \quad (7.65)$$

$$\hat{R} = \frac{\Omega}{|\omega|} \frac{r_m}{k} R \quad (7.66)$$

Note that (7.64) and (7.66) are the same as (5.26) and (5.28), respectively. (7.65) differs from (5.27) by a factor of $1/\sqrt{d_2 + 1}$. Also, define

$$\tilde{d} = d_1 \sqrt{\frac{I}{(d_2+1)k}} = \frac{d_1}{\Omega} \quad (7.67)$$

Using these new parameters, (7.61) is transformed to

$$\begin{aligned} & \left(1 - \frac{\mu_s - \tan \lambda}{1 + \mu_s \tan \lambda} \hat{m}\right) z'' + \tilde{c} z' + \tilde{d} \left(1 - \frac{\mu_s - \tan \lambda}{1 + \mu_s \tan \lambda} \hat{m}\right) z' + z + \tilde{c} \tilde{d} z \\ & = \left(\frac{\mu_0 \operatorname{sgn}(R\omega) - \tan \lambda}{1 + \mu_0 \operatorname{sgn}(R\omega) \tan \lambda} - \frac{\mu_s - \tan \lambda}{1 + \mu_s \tan \lambda} \right) \frac{|\omega|}{\Omega} \hat{R} \end{aligned} \quad (7.68)$$

where prime denotes derivate with respect to the dimensionless time τ . Now that the equation of motion is in its non-dimensionalized form, similar to Section 5.3.1, parameters are ordered using the small positive parameter ε . The new parameters

$$\hat{\mu}_s = \frac{\mu_s}{\tan \lambda}, \quad \hat{\mu}_0 = \frac{\mu_0}{\tan \lambda} \quad (7.69)$$

$$\hat{d} = \frac{\tilde{d}}{\tan \lambda} \quad (7.70)$$

$$\hat{c} = \frac{\tilde{c}}{\tan \lambda} \quad (7.71)$$

together with \hat{m} and \hat{R} are all assumed to be $O(1)$ with respect ε where $\varepsilon = \tan \lambda$ is taken as the small parameter. Finally, z is scaled as $z = \varepsilon \rho v$, where $\rho > 0$ is $O(1)$ and it is assumed

$$|\omega|/\Omega = \rho \varepsilon \quad (7.72)$$

The system equation, (7.68), becomes

$$\begin{aligned} & [1 - \varepsilon \Xi_1(v, v', \varepsilon) \hat{m}] v'' + \varepsilon \hat{c} v' + \varepsilon \hat{d} [1 - \varepsilon \Xi_1(v, v', \varepsilon) \hat{m}] v' \\ & + v + \varepsilon^2 \hat{c} \hat{d} v = \varepsilon \hat{R} [\Xi_0(\varepsilon) - \Xi_1(v, v', \varepsilon)] \end{aligned} \quad (7.73)$$

where, similar to (5.34) and (5.35),

$$\Xi_0(\varepsilon) = \frac{\operatorname{sgn}(R\omega) \hat{\mu}_0 - 1}{1 + \varepsilon^2 \operatorname{sgn}(R\omega) \hat{\mu}_0} \quad (7.74)$$

$$\Xi_1(v, v', \varepsilon) = \frac{\hat{\mu}_s(v, v', \varepsilon) - 1}{1 + \varepsilon^2 \hat{\mu}_s(v, v', \varepsilon)} \quad (7.75)$$

Also, the expression for the *signed* velocity-dependent coefficient of friction, $\hat{\mu}_s(v, v', \varepsilon)$, in terms of the new dimensionless parameters is

$$\hat{\mu}_s(v, v', \varepsilon) = \hat{\mu}(v, v', \varepsilon) \operatorname{sgn}(\zeta) \operatorname{sgn}(N(v, v', \varepsilon)) \quad (7.76)$$

where

$$\hat{\mu}(v, v', \varepsilon) = \left(\hat{\mu}_1 + \hat{\mu}_2 e^{-\tau_0 |\zeta|} + \hat{\mu}_3 \omega_{\max} \tanh(|\zeta| / \omega_{\max}) \right) (1 - e^{-\tau_1 |\zeta|}) \quad (7.77)$$

and $\hat{\mu}_i = \mu_i / \tan \lambda$, $i = 1, 2, 3$, and

$$\zeta(v, v', \varepsilon) = \frac{|\omega|}{d_2 + 1} v' + \varepsilon \rho \frac{d_1}{d_2 + 1} v + \frac{d_1 x_{10}}{d_2 + 1} + \omega \quad (7.78)$$

Also, from (7.62), one finds

$$\operatorname{sgn}(N) = \operatorname{sgn} \left(\frac{\hat{R}}{\hat{m}} - \varepsilon \Xi_0 \hat{R} + \varepsilon \hat{c} v' + (1 + \varepsilon^2 \hat{c} \hat{d}) v \right) \quad (7.79)$$

After rearranging, (7.73) becomes

$$v'' + v = \varepsilon f(v, v', \varepsilon) \quad (7.80)$$

where

$$f(v, v', \varepsilon) = -\hat{d} v' - (1 - \varepsilon \Xi_1 \hat{m})^{-1} \left[\hat{c} v' + \hat{m} \Xi_1 v + \varepsilon \hat{c} \hat{d} v + \hat{R} (\Xi_1 - \Xi_0) \right] \quad (7.81)$$

Comparing (7.80) with (5.33), we can see that a damping term, $-\hat{d} v'$, and a higher-order term, $\varepsilon \hat{c} \hat{d} v$, are added to the system's equation. Note that (7.76) has similar Lipschitz continuity properties as (5.33) with respect to (v, v', ε) .

To transform (7.80) into the standard form, the following change of variables is used

$$v = a \cos \varphi, v' = -a \sin \varphi \quad (7.82)$$

This leads to

$$a' = -\varepsilon f(a \cos \varphi, -a \sin \varphi, \varepsilon) \sin \varphi \quad (7.83)$$

$$\varphi' = 1 - \frac{\varepsilon}{a} f(a \cos \varphi, -a \sin \varphi, \varepsilon) \cos \varphi \quad (7.84)$$

Since φ' is away from zero, dividing (7.83) by (7.84) yields

$$\frac{da}{d\varphi} = -\varepsilon \frac{f(a \cos \varphi, -a \sin \varphi, \varepsilon) \sin \varphi}{1 - \frac{\varepsilon}{a} f(a \cos \varphi, -a \sin \varphi, \varepsilon) \cos \varphi} \equiv \varepsilon g(\varphi, a, \varepsilon) \quad (7.85)$$

The system equation (7.85) is in standard form with a bounded periodic right-hand side. The averaged amplitude equation can be found as

$$\begin{aligned} a' &= \frac{\varepsilon}{2\pi} \int_0^{2\pi} g(\varphi, a, 0) d\varphi \\ &= -\frac{\varepsilon}{2\pi} \int_0^{2\pi} f(a \cos \varphi, -a \sin \varphi, 0) \sin \varphi d\varphi \end{aligned} \quad (7.86)$$

Expanding (7.86) gives

$$\begin{aligned} a' &= -\frac{\varepsilon}{2\pi} \int_0^{2\pi} \left((\hat{c} + \hat{d}) a \sin^2 \varphi + \hat{m} a \sin \varphi \cos \varphi + \hat{\mu}_0 \hat{R} \operatorname{sgn}(R\omega) \sin \varphi \right) d\varphi \\ &\quad + \frac{\varepsilon}{2\pi} \int_0^{2\pi} \left(\hat{m} a \sin \varphi \cos \varphi + \hat{R} \sin \varphi \right) \hat{\mu}_s(\varphi, a) d\varphi \end{aligned}$$

which immediately can be simplified to

$$a' = -\varepsilon \frac{(\hat{c} + \hat{d})a}{2} + \frac{\varepsilon \hat{m}}{2\pi} \int_0^{2\pi} \sin \varphi \left(a \cos \varphi + \frac{\hat{R}}{\hat{m}} \right) \hat{\mu}_s(\varphi, a) d\varphi \quad (7.87)$$

where

$$\begin{aligned} \hat{\mu}_s(\varphi, a) &= \left(\hat{\mu}_1 + \hat{\mu}_2 e^{-\tau_0 |\varpi_1 - \varpi_2 a \sin \varphi|} + \hat{\mu}_3 |\varpi_1 - \varpi_2 a \sin \varphi| \right) \left(1 - e^{-\tau_1 |\varpi_1 - \varpi_2 a \sin \varphi|} \right) \\ &\quad \times \operatorname{sgn}(\varpi_1 - \varpi_2 a \sin \varphi) \operatorname{sgn} \left(a \cos \varphi + \frac{\hat{R}}{\hat{m}} \right) \end{aligned} \quad (7.88)$$

and

$$\varpi_1 = \frac{d_1 x_{10}}{d_2 + 1} + \omega \quad (7.89)$$

$$\varpi_2 = \frac{|\omega|}{d_2 + 1} \quad (7.90)$$

Note that by setting $d_1 = d_2 = 0$, (7.88) simplifies to (5.46). In the following, the case of $\widehat{R} = O(1)$ is treated first and then the case of $\widehat{R} = O(\varepsilon)$ or $\widehat{R} = 0$ is discussed.

7.4.1.1 The Case of $\widehat{R} = O(1)$

For $\widehat{R} = O(1)$, there is $a_N = \frac{|\widehat{R}|}{\widehat{m}}$ such that $\operatorname{sgn}\left(\frac{\widehat{R}}{\widehat{m}} + a \cos \varphi\right) = \operatorname{sgn}\left(\frac{\widehat{R}}{\widehat{m}}\right) = \operatorname{sgn}(\widehat{R})$ for $0 \leq a < a_N$.

Also, since for $0 \leq a < |\varpi_1|/\varpi_2$ we have $\operatorname{sgn}(\varpi_1 - \varpi_2 a \sin \varphi) = \operatorname{sgn}(\varpi_1)$ then

$$\widehat{\mu}_s(\varphi, a) = \left(\widehat{\mu}_1 + \widehat{\mu}_2 e^{-r_0 |\varpi_1| (1 - \alpha a \sin \varphi)} + \widehat{\mu}_3 |\varpi_1| (1 - \alpha a \sin \varphi) \right) \left(1 - e^{-r_1 |\varpi_1| (1 - \alpha a \sin \varphi)} \right) \operatorname{sgn}(\varpi_1) \quad (7.91)$$

for $0 \leq a < a^*$, where $a^* = \min(a_N, |\alpha^{-1}|)$ and $\alpha = \frac{\varpi_2}{\varpi_1}$. Substituting (7.91) into (7.87) yields

$$a' = -\varepsilon \frac{(\widehat{c} + \widehat{d})a}{2} + \frac{\varepsilon}{2\pi} \widehat{R} \int_0^{2\pi} \sin \varphi \widehat{\mu}_s(\varphi, a) d\varphi, \quad 0 \leq a < a^* \quad (7.92)$$

For simplicity, here it is assumed $\varpi_1 > 0$. Simplifying (7.91), one gets

$$\widehat{\mu}_s(\varphi, a) = \left(\widehat{\mu}_1 + \widehat{\mu}_2 e^{r_0 \varpi_1 \alpha a \sin \varphi} - \widehat{\mu}_3 a \sin \varphi \right) \left(1 - r_2 e^{r_1 \varpi_1 \alpha a \sin \varphi} \right) \quad (7.93)$$

where $r_2 = e^{-r_1 \varpi_1}$ and

$$\widehat{\mu}_1 = \widehat{\mu}_1 + \widehat{\mu}_3 \varpi_1 \quad (7.94)$$

$$\widehat{\mu}_2 = \widehat{\mu}_2 e^{-r_0 \varpi_1} \quad (7.95)$$

$$\widehat{\mu}_3 = \widehat{\mu}_3 \varpi_1 \alpha \quad (7.96)$$

It is interesting to note that (7.93) is very similar to (5.49). Substituting (7.93) into (7.92) and

carrying out the integrations, one finds

$$a' = -\varepsilon \frac{\widehat{c} + \widehat{d} + \widehat{\mu}_3 \widehat{R}}{2} a + \varepsilon \widehat{\mu}_2 \widehat{R} \Lambda_{1,0}(r_0 \varpi_1 \alpha a) - \varepsilon r_2 \widehat{\mu}_1 \widehat{R} \Lambda_{1,0}(r_1 \varpi_1 \alpha a) + \varepsilon r_2 \widehat{\mu}_3 a \widehat{R} \Lambda_{2,0}(r_1 \varpi_1 \alpha a) - \varepsilon r_2 \widehat{\mu}_2 \widehat{R} \Lambda_{1,0}((r_0 + r_1) \varpi_1 \alpha a) \quad (7.97)$$

where $\Lambda_{1,0}(\cdot)$ and $\Lambda_{2,0}(\cdot)$ are defined by (5.56) and (5.57), respectively. After linearization, one finds that the origin is locally exponentially stable if (in terms of the original system parameters),

$$c + d_1 I > -r_m R \left. \frac{d\mu}{d\zeta} \right|_{\zeta=0} \quad (7.98)$$

Comparing (7.98) with (5.61), it is clear that the only difference is the addition of $d_1 I$ to the linear damping which is caused by the controller.

System (7.97) is structurally identical to (5.54)¹ and as such, results obtained in Section 5.3.4 and Appendix D apply here. Consequently, there exists $\widehat{d}_1 \geq 0$, such that selecting $\widehat{d} > \widehat{d}_1$ guarantees that the origin is an exponentially stable fixed point of the averaged equation (7.97), and no other fixed points exist over $a \in [0, a^*]$. Since the right-hand side of (7.85) is twice continuously differentiable with respect to $(a, \varepsilon) \in [0, a^*] \times [0, \varepsilon_0]$ and $g(\varphi, 0, \varepsilon) \equiv 0$, then, based on Theorem 1 of Appendix I, for sufficiently small ε , the origin of (7.85) is also exponentially stable.

For $a > a^*$, based on the arguments of Section 7.1.1 and (7.15), (7.88) is replaced by

$$\begin{aligned} \widehat{\mu}_s(\varphi, a) = & \left(\widehat{\mu}_1 + \widehat{\mu}_2 e^{-r_0 |\varpi_1 - \varpi_2 a \sin \varphi|} + \widehat{\mu}_3 \omega_{\max} \tanh \left(\frac{\varpi_1 - \varpi_2 a \sin \varphi}{\omega_{\max}} \right) \right) \left(1 - e^{-r_1 |\varpi_1 - \varpi_2 a \sin \varphi|} \right) \\ & \times \operatorname{sgn}(\varpi_1 - \varpi_2 a \sin \varphi) \operatorname{sgn} \left(a \cos \varphi + \frac{\widehat{R}}{\widehat{m}} \right) \end{aligned} \quad (7.99)$$

which is bounded and periodic with respect to φ . Substituting (7.99) into (7.87) yields the averaged amplitude equation. Due to the boundedness (7.99), the following two definite integrals are also bounded:

¹ Replace $\widehat{c} + \widehat{d}$ by \widehat{c} and $\varpi_1 \alpha$ by ω and (7.97) becomes (5.54).

$$\Psi_1(a) = \frac{1}{2\pi} \int_0^{2\pi} \sin \varphi \cos \varphi \widehat{\mu}_s(\varphi, a) d\varphi < \overline{\Psi}_1 \quad (7.100)$$

$$\Psi_2(a) = \frac{1}{2\pi} \int_0^{2\pi} \sin \varphi \widehat{\mu}_s(\varphi, a) d\varphi < \overline{\Psi}_2 \quad (7.101)$$

Using (7.100) and (7.101), from (7.87) we have

$$\begin{aligned} a' &= -\varepsilon \frac{(\widehat{c} + \widehat{d})a}{2} + \frac{\varepsilon}{2\pi} \int_0^{2\pi} (\widehat{m}a \sin \varphi \cos \varphi + \widehat{R} \sin \varphi) \widehat{\mu}_s(\varphi, a) d\varphi \\ &\leq -\varepsilon \frac{(\widehat{c} + \widehat{d})a}{2} + \varepsilon \widehat{m}a \overline{\Psi}_1 + \varepsilon \widehat{R} \overline{\Psi}_2 \end{aligned} \quad (7.102)$$

Let

$$\widehat{d}_2 = \max \left[(2\widehat{m}\overline{\Psi}_1 - \widehat{c}), \left(2\widehat{m}\overline{\Psi}_1 + \frac{2\widehat{R}}{a^*} \overline{\Psi}_2 - \widehat{c} \right), 0 \right] \quad (7.103)$$

then $a'(a) < 0$ for $\widehat{d} > \widehat{d}_2$ and $a > a^*$.

Selecting $\widehat{d} > \max(\widehat{d}_1, \widehat{d}_2)$ guarantees that the origin is an exponentially stable fixed point of the averaged system for initial condition $a(0) = a_0 \in [0, \infty)$. Since the right-hand side of (7.87) is continuously differentiable with respect to a , Theorem 2 of Appendix I states that the solutions of (7.87) and (7.85) that start from the same initial value $a_0 \in [0, \infty)$ remain $O(\varepsilon)$ close for all $\varphi \in [\varphi_0, \infty)$. Consequently, for sufficiently small ε and after a finite time, the solution of (7.85) enters $[0, a^*]$ where, as discussed above, the solution is exponentially attracted to the origin. This property naturally extends to the original system, (7.52).

7.4.1.2 The Case of $\widehat{R} = O(\varepsilon)$ or $\widehat{R} = 0$

Here it is assumed that $\widehat{R} = \varepsilon \widehat{\widehat{R}}$, where $\widehat{\widehat{R}} = O(1)$ with respect to ε . The subsequent arguments apply to the case of $\widehat{R} = 0$ by simply setting $\widehat{\widehat{R}} = 0$ and $R = 0$.

Substituting $\widehat{R} = \varepsilon \widehat{\widehat{R}}$ into (7.73) gives

$$v'' + v = \varepsilon f_1(v, v', \varepsilon) + \varepsilon^2 f_2(v, v', \varepsilon) \quad (7.104)$$

where

$$f_1(v, v', \varepsilon) = -\widehat{d}v' - (1 - \varepsilon \Xi_1 \widehat{m})^{-1} (\widehat{c}v' + \widehat{m} \Xi_1 v + \varepsilon \widehat{c} \widehat{d}v) \quad (7.105)$$

and

$$f_2(v, v', \varepsilon) = (1 - \varepsilon \Xi_1 \widehat{m})^{-1} (\Xi_0 - \Xi_1) \widehat{R} \quad (7.106)$$

where Ξ_0 and Ξ_1 are given by (7.74) and (7.75), respectively. Furthermore, the scaling $\widehat{R} = \varepsilon \widehat{\widehat{R}}$, reduces the size of x_{10} , given by (7.58), from $O(1)$ to $O(\varepsilon)$. In terms of *ordered* system parameters, (7.58) is rewritten as

$$(1 + \varepsilon^2 \widehat{d} \widehat{c}) x_{10}(\varepsilon) + \varepsilon \rho \frac{\widehat{\mu}_0 \operatorname{sgn}(R) \operatorname{sgn}(x_{20} + \omega) - 1}{1 + \widehat{\mu}_0 \operatorname{sgn}(R) \operatorname{sgn}(x_{20} + \omega)} \widehat{\widehat{R}} + \varepsilon^2 \rho \widehat{c} (d_2 + 1) \operatorname{sgn}(\omega) = 0 \quad (7.107)$$

where (7.63), (7.65), (7.66), (7.67), (7.69), (7.70), (7.71), and (7.72) were used. Assuming $d_2 = O(1)$, it is clear that $x_{10} = O(\varepsilon)$. The first order averaged equation (7.87) is reduced to

$$a' = -\varepsilon \frac{(\widehat{c} + \widehat{d})a}{2} + \frac{\varepsilon \widehat{m} a}{2\pi} \int_0^{2\pi} \sin \phi |\cos \phi| \widehat{\mu}_s(\phi, a) d\phi \quad (7.108)$$

where

$$\begin{aligned} \widehat{\mu}_s(\phi, a) = & \left(\widehat{\mu}_1 + \widehat{\mu}_2 e^{-r_0 \left| \omega - |\omega| \frac{a}{d_2+1} \sin \phi \right|} + \widehat{\mu}_3 \left| \omega - |\omega| \frac{a}{d_2+1} \sin \phi \right| \right) \left(1 - e^{-r_1 \left| \omega - |\omega| \frac{a}{d_2+1} \sin \phi \right|} \right) \\ & \times \operatorname{sgn} \left(\omega - |\omega| \frac{a}{d_2+1} \sin \phi \right) \end{aligned} \quad (7.109)$$

The following two expressions were used to reach (7.108). First, from (7.78) and after substituting the solution of (7.107), we have

$$\zeta(v, v', 0) = \frac{|\omega|}{d_2 + 1} v' + \omega$$

Second, from (7.79)

$$\begin{aligned}\operatorname{sgn}(N(v, v', \varepsilon)) &= \operatorname{sgn}\left(\frac{\varepsilon \widehat{R}}{\widehat{m}} - \varepsilon^2 \Xi_0 \widehat{R} + \varepsilon \widehat{c} v' + (1 + \varepsilon^2 \widehat{c} \widehat{d}) v\right) \\ &\rightarrow \operatorname{sgn}(N(v, v', 0)) = \operatorname{sgn}(v)\end{aligned}$$

If $0 \leq a < 1 + d_2$, then $\operatorname{sgn}\left(\omega - |\omega| \frac{a}{d_2 + 1} \sin \varphi\right) = \operatorname{sgn}(\omega)$ and consequently, (7.109) is simplified

to

$$\begin{aligned}\widehat{\mu}_s(\varphi, a) &= \left(\widehat{\mu}_1 + \widehat{\mu}_2 e^{-r_0 |\omega| \left(1 - \frac{a}{d_2 + 1} \sin \varphi\right)} + \widehat{\mu}_3 |\omega| \left(1 - \frac{a}{d_2 + 1} \sin \varphi\right) \right) \\ &\quad \times \left(1 - e^{-r_1 |\omega| \left(1 - \frac{a}{d_2 + 1} \sin \varphi\right)} \right) \operatorname{sgn}(\omega), \quad 0 \leq a < 1 + d_2\end{aligned}\quad (7.110)$$

Define

$$\psi_3(a) = \frac{1}{2\pi} \int_0^{2\pi} \sin \varphi |\cos \varphi| \widehat{\mu}_s(\varphi, a) d\varphi \quad (7.111)$$

then there exists $\overline{\psi}_3$, such that

$$\psi_3(a) < \overline{\psi}_3, \quad 0 \leq a < 1 + d_2 \quad (7.112)$$

In order to guarantee exponential stability of the origin of the averaged system for the initial conditions satisfying $a(0) \in [0, 1 + d_2]$, it suffices to select $\widehat{d} > \max(0, \widehat{d}_3)$ where

$$\widehat{d}_3 = 2\widehat{m}\overline{\psi}_3 - \widehat{c} \quad (7.113)$$

for then, (7.108) yields

$$a' = -\varepsilon \frac{(\widehat{c} + \widehat{d})a}{2} + \varepsilon \widehat{m} a \psi_3(a) < -\varepsilon \frac{(\widehat{c} + \widehat{d})a}{2} + \varepsilon \widehat{m} a \overline{\psi}_3 < -\beta a, \quad \beta > 0$$

where (7.111) was used. Moreover, since (7.110) is twice continuously differentiable with respect to a uniformly in φ , the right-hand side of (7.85) is twice continuously differentiable with respect to $(a, \varepsilon) \in [0, a^*] \times [0, \varepsilon_0]$. Also, since $g(\varphi, 0, \varepsilon) \equiv 0$, based on Theorem 1 of Appendix I, for

sufficiently small ε , the origin of (7.85) is exponentially stable.

For $a \geq 1+d_2$, based on the discussions of Section 7.1.1, (7.109) is modified to guarantee boundedness as $a \rightarrow \infty$. (7.109) is replaced by

$$\begin{aligned} \bar{\mu}_s(\varphi, a) = & \left[\hat{\mu}_1 + \hat{\mu}_2 e^{-r_0 \left| \omega - |\omega| \frac{a}{d_2+1} \sin \varphi \right|} + \hat{\mu}_3 \omega_{\max} \tanh \left(\frac{\left| \omega - |\omega| \frac{a}{d_2+1} \sin \varphi \right|}{\omega_{\max}} \right) \right] \\ & \times \left(1 - e^{-r_1 \left| \omega - |\omega| \frac{a}{d_2+1} \sin \varphi \right|} \right) \operatorname{sgn} \left(\omega - |\omega| \frac{a}{d_2+1} \sin \varphi \right) \end{aligned} \quad (7.114)$$

Due to the boundedness of (7.114), there is a $\bar{\Psi}_4$, such that

$$\Psi_3(a) < \bar{\Psi}_4, \quad \forall a \geq 1+d_2 \quad (7.115)$$

where $\Psi_3(a)$ is given by (7.111) after substituting (7.114). Once again, exponential stability of the origin of the averaged system for the initial condition $a(0) \in [1+d_2, \infty)$ is guaranteed, if we select $\hat{d} > \max(0, \hat{d}_4)$ where

$$\hat{d}_4 = 2\bar{m}\bar{\Psi}_4 - \hat{c} \quad (7.116)$$

Selecting $\hat{d} > \max(0, \hat{d}_3, \hat{d}_4)$ guarantees that the origin is an exponentially stable fixed point of the averaged system for the initial condition $a(0) = a_0 \in [0, \infty)$. Since the right-hand side of (7.108) is continuously differentiable with respect to a , Theorem 2 of Appendix I states that the solutions of (7.108) and (7.85) that start from the same initial value $a_0 \in [0, \infty)$ remain $O(\varepsilon)$ close for all $\varphi \in [\varphi_0, \infty)$. Consequently, for sufficiently small ε and after a finite time, the solution of (7.85) enters $[0, 1+d_2]$, where as discussed above, the solution is exponentially attracted to the origin. This property extends to the original system, (7.52).

7.4.1.3 Remark 1

The above arguments did not provide a closed form relationship in terms of system parameters to determine the two control parameters, d_1 and d_2 . It is, however, possible to calculate these

parameters based on the values of the system parameters, if available, or their upper and lower bounds.

7.4.1.4 Remark 2

The above proof of stability is based on the method of averaging and is applicable to systems with weak nonlinearities. In the preceding derivations, this requirement on the “size” of the nonlinear terms is quantified by the introduction of the *small* parameter ε . In particular, Theorem 1 of Appendix I states that, under the assumptions of the theorem, there exists an $\varepsilon^* > 0$, such that for $\forall \varepsilon \in [0, \varepsilon^*]$ the exponential stability of the origin of the unaveraged system can be deduced from the exponential stability of the origin of averaged system. Consequently, the upper bound on the size of the nonlinear terms is defined by ε^* . Here, it is assumed that system parameter values (or their respective upper and lower bounds) are such that the above condition is satisfied¹.

Now that it has been shown that there exists control parameters d_1 and d_2 such that the subsystem (7.52) (*i.e.* the governing equation of the sliding motion) is exponentially stable, we can proceed with the design of a control input that brings the system’s state to the sliding surface in finite time.

7.4.2 The Reaching Phase

Based on (7.51), the equation of the sliding surface is given by

$$s = 0 \tag{7.117}$$

where the variable s is defined as

$$s = x_3 - \frac{d_1}{r}x_1 + \frac{d_2}{r}x_2 \tag{7.118}$$

A controller is sought that brings s to zero in finite time. Differentiating (7.118) with respect to time, gives

¹ Considering the complexity of the system equations and the number of parameters involved, the straightforward calculation of an upper bound on ε (*i.e.* ε^*) can be very difficult. Numerical simulations may be used as an alternative to estimate this bound for a particular lead screw drive. See, for example, [100], where a similar issue is discussed in the context of the control of the underactuated manipulators.

$$\dot{s} = \dot{x}_3 - \frac{d_1}{r} \dot{x}_1 + \frac{d_2}{r} \dot{x}_2 \quad (7.119)$$

Substituting (7.49) into (7.119), yields

$$\begin{aligned} \dot{s} = & \frac{1}{J}u - \frac{1}{J}T_f \operatorname{sgn}(x_3 + r^{-1}\omega) - \frac{c_M}{Jr}\omega + \left(\frac{rk}{J} - \frac{d_2}{r} \frac{k}{\Gamma}\right)x_1 + \left(d_1 - \frac{c_M}{J}\right)x_3 \\ & - \left(\frac{d_1}{r} + \frac{d_2}{r} \frac{c}{\Gamma}\right)x_2 - \frac{1}{\Gamma} \frac{d_2}{r} (\xi R + c\omega) \end{aligned} \quad (7.120)$$

Take the Lyapunov function candidate as $V = \frac{1}{2}s^2$; its derivate along the system trajectories is found as

$$\begin{aligned} \dot{V} = & s\dot{s} \\ = & \frac{1}{J}us - \left(\frac{1}{J}T_{fM} \operatorname{sgn}(x_3 + r^{-1}\omega) + \frac{c_M}{Jr}\omega + \frac{1}{\Gamma} \frac{d_2}{r} (\xi R + c\omega)\right)s \\ & + \left[\left(\frac{rk}{J} - \frac{d_2}{r} \frac{k}{\Gamma}\right)x_1 + \left(d_1 - \frac{c_M}{J}\right)x_3 - \left(\frac{d_1}{r} + \frac{d_2}{r} \frac{c}{\Gamma}\right)x_2\right]s \\ \leq & \frac{1}{J}us + \frac{1}{J}(\rho_0 + \rho_1|x_1| + \rho_2|x_2| + \rho_3|x_3|)|s| \end{aligned} \quad (7.121)$$

where, $\rho_i, i = 0 \dots 3$ are assumed to be known constants satisfying the following relationships

$$\left|T_{fM} \operatorname{sgn}(x_3 + r^{-1}\omega) + \frac{c_M}{r}\omega + \frac{J}{\Gamma} \frac{d_2}{r} (\xi R + c\omega)\right| \leq \rho_0 \quad (7.122)$$

$$\left|rk - J \frac{d_2}{r} \frac{k}{\Gamma}\right| \leq \rho_1 \quad (7.123)$$

$$\left|J \frac{d_1}{r} + J \frac{d_2}{r} \frac{c}{\Gamma}\right| \leq \rho_2 \quad (7.124)$$

$$\left|d_1J - c_M\right| \leq \rho_3 \quad (7.125)$$

Using known upper and lower bounds of the parameters, one can find

$$\rho_0 = \bar{T}_f + \frac{\bar{c}_M}{r} \bar{\omega} + \frac{\bar{J}}{\underline{\Gamma}} \frac{d_2}{r} \left(\underline{\xi} \bar{R} + \bar{c} \bar{\omega} \right) \quad (7.126)$$

$$\rho_1 = r \bar{k} + \bar{J} \frac{d_2}{r} \frac{\bar{k}}{\underline{\Gamma}} \quad (7.127)$$

$$\rho_2 = \bar{J} \left(\frac{d_1}{r} + \frac{d_2}{r} \frac{\bar{c}}{\underline{\Gamma}} \right) \quad (7.128)$$

$$\rho_3 = d_1 \bar{J} + \bar{c}_M \quad (7.129)$$

Let

$$u = -(\beta(\mathbf{x}) + \beta_0) \text{sgn}(s) \quad (7.130)$$

where

$$\beta(\mathbf{x}) = \rho_0 + \rho_1 |x_1| + \rho_2 |x_2| + \rho_3 |x_3| \quad (7.131)$$

and $\beta_0 > 0$ is some known constant, (7.121) becomes

$$\begin{aligned} \dot{V} &\leq \frac{1}{J} us + \frac{1}{J} (\rho_0 + \rho_1 |x_1| + \rho_2 |x_2| + \rho_3 |x_3|) |s| \\ &= -\frac{1}{J} (\beta(\mathbf{x}) + \beta_0) \text{sgn}(s) s + \frac{1}{J} \beta(\mathbf{x}) |s| \\ &= -\frac{1}{J} \beta_0 |s| \end{aligned} \quad (7.132)$$

This result implies that the system trajectories reach the sliding surface $s = 0$ in finite time and, once on the surface, they cannot leave it.

The sliding mode controller consisting of a reaching phase and a sliding phase is now developed. However, a few issues remain to be addressed before signing off on this controller. These issues are:

- The steady-state error,
- Chattering, which is caused by discontinuous nature of the controller and delays in the actual switching controller implementations, and
- Initial high torque demand.

In the following three sections, several approaches are presented to modify the controller in order

to circumvent these problems without jeopardizing the stability properties of the original controller.

7.4.3 Feedforward Input

From (7.53), we saw that the origin is not an equilibrium point of the governing equation for the sliding motion. This equilibrium point was calculated by (7.58) and translated to a lead screw velocity error given by (7.59), which in turn results in a motor velocity error when considering the sliding surface equation given by (7.51). In this section, a feedforward input is considered to reduce the velocity error as much as possible, depending on the availability and the accuracy of the nominal values for the system parameters.

For the system (7.49), the constant input

$$u_0 = T_f + c_M r^{-1} \omega + r \xi_0 R + rc \omega, \omega > 0 \quad (7.133)$$

is required to have the steady state point at

$$\begin{bmatrix} x_{10} \\ x_{20} \\ x_{30} \end{bmatrix} = \begin{bmatrix} -\frac{\xi_0 R + c \omega}{k} \\ 0 \\ 0 \end{bmatrix} \quad (7.134)$$

However due to parameter uncertainty, both u_0 and x_0 are unknown values. As a compromise, it is possible to modify the controller input with

$$u = v + \hat{u}_0 \quad (7.135)$$

where \hat{u}_0 is the feedforward input obtained from (7.133) using nominal values of system parameters. Substituting (7.135) into (7.49) and setting

$$\tilde{x}_1 = x_1 - \hat{x}_{10} \quad (7.136)$$

where \hat{x}_{10} is obtained from (7.134) by using the nominal system parameters, the equations of motion become after simplification

$$\begin{aligned}
\begin{bmatrix} \dot{x}_1 \\ \dot{x}_2 \\ \dot{x}_3 \end{bmatrix} &= \begin{bmatrix} 0 & 1 & -r \\ -\Gamma^{-1}k & -\Gamma^{-1}c & 0 \\ rJ^{-1}k & 0 & -J^{-1}c_M \end{bmatrix} \begin{bmatrix} x_1 \\ x_2 \\ x_3 \end{bmatrix} \\
&+ \begin{bmatrix} 0 \\ -\frac{1}{\Gamma} \left(\xi R - \frac{k}{\hat{k}} \hat{\xi}_{\hat{R}} \right) - \frac{\omega}{\Gamma} \left(c - \frac{k}{\hat{k}} \hat{c} \right) \\ -\frac{1}{J} \left(T_f \operatorname{sgn}(x_3 + r^{-1}\omega) - \hat{T}_f \right) - \frac{\omega}{Jr} (c_M - \hat{c}_M) + \frac{r}{J} \left(\hat{\xi}_{\hat{R}} \hat{R} + \hat{c}\omega \right) \left(1 - \frac{k}{\hat{k}} \right) \end{bmatrix} + \begin{bmatrix} 0 \\ 0 \\ J^{-1} \end{bmatrix} v
\end{aligned} \tag{7.137}$$

where the tilde on x_1 was dropped to simplify the notations.

The development of the sliding mode controller follows the same steps as described above and, except for pointing out the differences, it is not repeated here. The second order differential equation governing the sliding motion, (7.53), becomes

$$\begin{aligned}
&\Gamma \ddot{x}_1 + (c + \Gamma d_1) \dot{x}_1 + ((d_2 + 1)k + cd_1)x_1 \\
&= -(d_2 + 1) \left(\left(\xi R - \frac{k}{\hat{k}} \hat{\xi}_{\hat{R}} \right) + \omega \left(c - \frac{k}{\hat{k}} \hat{c} \right) \right)
\end{aligned} \tag{7.138}$$

where the ‘‘hat’’ designates the nominal parameter values. Note that had we known the ‘‘true’’ system parameters, (7.138) would yield $x_{10} = 0$. However, one would expect that by the addition of the feedforward component, a smaller x_{10} is obtained when the nominal parameter values are reasonably close to the true values. This in turn translates to smaller steady state velocity errors for motor and lead screw.

The addition of the constant input also changes the sliding mode controller law. The equation for \dot{s} , given by (7.120) is changed to

$$\dot{s} = \frac{1}{J} v + \left(\frac{rk}{J} - \frac{d_2}{r} \frac{k}{\Gamma} \right) x_1 - \left(\frac{d_1}{r} + \frac{d_2}{r} \frac{c}{\Gamma} \right) x_2 + \left(d_1 - \frac{c_M}{J} \right) x_3 + \Delta \tag{7.139}$$

where

$$\begin{aligned} \Delta = & -\frac{1}{J} \left(T_f \operatorname{sgn}(x_3 + r^{-1}\omega) - \hat{T}_f \right) - \frac{1}{\Gamma} \frac{d_2}{r} \left(\left(\xi R - \frac{k}{\hat{k}} \hat{\xi}_0 \hat{R} \right) + \omega \left(c - \frac{k}{\hat{k}} \hat{c} \right) \right) \\ & - \frac{\omega}{Jr} (c_M - \hat{c}_M) + \frac{r}{J} \left(\hat{\xi}_0 \hat{R} + \hat{c} \omega \right) \left(1 - \frac{k}{\hat{k}} \right) \end{aligned} \quad (7.140)$$

The only difference compared with the previous controller is in ρ_0 , which is now given by

$$\begin{aligned} \rho_0 = & \max \left(\left| \bar{T}_f - \hat{T}_f \right|, \left| \hat{T}_f - \underline{T}_f \right| \right) + \frac{\bar{J}}{\Gamma} \frac{d_2}{r \hat{k}} \max \left(\left| \hat{k} \bar{\xi} R - k \hat{\xi}_0 \hat{R} \right|, \left| \hat{k} \underline{\xi} R - \bar{k} \hat{\xi}_0 \hat{R} \right| \right) \\ & + \frac{\bar{J}}{\Gamma} \frac{d_2}{r \hat{k}} \omega \max \left(\left| \bar{c} \hat{k} - k \hat{c} \right|, \left| c \hat{k} - \bar{k} \hat{c} \right| \right) + \frac{\omega}{r} \max \left(\left| \underline{c}_M - \hat{c}_M \right|, \left| \bar{c}_M - \hat{c}_M \right| \right) \\ & + \frac{r}{\hat{k}} \left(\hat{\xi}_0 \hat{R} + \hat{c} \omega \right) \max \left(\left| \hat{k} - k \right|, \left| \hat{k} - \bar{k} \right| \right) \end{aligned} \quad (7.141)$$

7.4.4 Continuous Sliding Mode Controller

The continuous version of the controller given by (7.130) can be constructed by replacing signum function with a unit saturation function

$$u = -(\beta(\mathbf{x}) + \beta_0) \operatorname{sat} \left(\frac{s}{\varepsilon_1} \right) \quad (7.142)$$

For this controller, the previous Lyapunov analysis can only show that the trajectories starting outside of the boundary layer (*i.e.* $|s| \leq \varepsilon_1$) reach it in finite time and, once inside, cannot leave it for all future time. Namely, (7.132) for the derivate of the Lyapunov function, now reads

$$\dot{V} \leq -\frac{1}{J} \beta_0 |s|, |s| \geq \varepsilon_1 \quad (7.143)$$

To ensure that the trajectories inside the boundary layer remain bounded, the boundedness of the solutions of the following system must be shown

$$\begin{aligned} \dot{x}_1 &= (d_2 + 1)x_2 - d_1 x_1 + r s \\ \dot{x}_2 &= -\frac{c}{\Gamma} x_2 - \frac{k}{\Gamma} x_1 - \frac{1}{\Gamma} \xi R - \frac{c}{\Gamma} \omega, |s| \leq \varepsilon_1 \end{aligned} \quad (7.144)$$

where (7.144) is obtained by substituting (7.118) into the first two equations of (7.49). However,

since the aim of the controller is to eliminate lead screw vibrations, proof of boundedness will not be sufficient. Instead, the analysis continues by utilizing the “high gain” behavior of the sliding mode controller inside the boundary layer to prove the asymptotic stability of the system towards its fixed point (which is not the origin). This task is accomplished by considering the system as a singularly perturbed problem. The stability property is then given by Theorem 3 of Appendix I.

To use this theorem, the control law given by (7.130) must be modified slightly to give it the required smoothness properties. Note that the partial derivatives of $\beta(\mathbf{x})$, given by (7.131), with respect to $x_i, i = 1, 2, 3$, are not continuous. Here, $\beta(\mathbf{x})$ is replaced by $\tilde{\beta}(\mathbf{x})$, which is defined similar to (7.131), except that the absolute functions are replaced by

$$\sigma_{\delta}(u) \equiv \begin{cases} |u| & , |u| \geq \delta \\ \frac{1}{2\delta}u^2 + \frac{\delta}{2} & , |u| < \delta \end{cases} \quad (7.145)$$

where $\delta > 0$ is a parameter designating the extent of the smoothed region. As illustrated in Figure 7-10, function $\sigma_{\delta}(\cdot)$ is continuously differentiable to any order and $\sigma_{\delta}(u) \geq |u|, \forall u$.

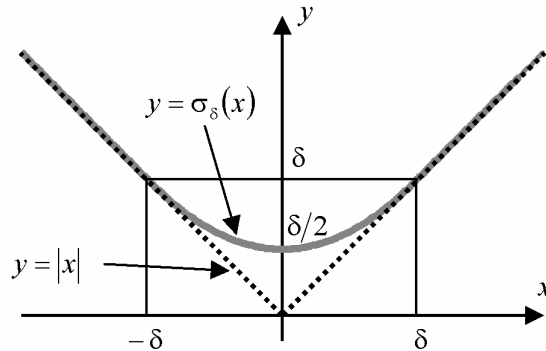


Figure 7-10: Smoothed absolute function

Now the modified controller

$$u = -(\tilde{\beta}(\mathbf{x}) + \beta_0) \frac{s}{\epsilon_1}, \quad |s| \leq \epsilon_1 \quad (7.146)$$

is continuously differentiable inside the boundary layer. For $|s| \leq \epsilon_1$, the equations of motion become

$$\begin{aligned}
\dot{x}_1 &= x_2 - rx_3 \\
\dot{x}_2 &= -\frac{c}{\Gamma}x_2 - \frac{k}{\Gamma}x_1 - \frac{\xi R}{\Gamma} - \frac{c\omega}{\Gamma} \\
\varepsilon_1 \dot{x}_3 &= -\frac{1}{J} \left(\tilde{\beta}(\mathbf{x}) + \beta_0 \right) \left(x_3 - \frac{d_1}{r}x_1 + \frac{d_2}{r}x_2 \right) + \frac{\varepsilon_1 rk}{J}x_1 - \frac{\varepsilon_1 c_M}{J}x_3 \\
&\quad - \frac{\varepsilon_1}{J} \left(T_{fM} \tanh\left(\frac{x_3 + r^{-1}\omega}{\varepsilon_2}\right) + r^{-1}c_M\omega \right)
\end{aligned} \tag{7.147}$$

where $\text{sgn}(\zeta)$ was replaced by $\tanh(\zeta/\varepsilon_2)$ for some small $\varepsilon_2 > 0$ as an approximation that has the required smoothness properties. The system described by (7.147) resembles a standard *singular perturbation* problem [84]. To convert it to the standard form, the fixed point must be transferred to the origin. Let

$$\mathbf{z} = \begin{bmatrix} z_1 \\ z_2 \\ z_3 \end{bmatrix} = \begin{bmatrix} x_1 - x_{10}(\varepsilon_1) \\ x_2 - x_{20}(\varepsilon_1) \\ x_3 - x_{30}(\varepsilon_1) \end{bmatrix} \tag{7.148}$$

where x_{20} is given by the solution of the following equation

$$\begin{aligned}
&\left(\tilde{\beta}(\mathbf{x}_0) + \beta_0 \right) \left(\frac{d_1}{k}(cx_{20} + \xi_0 R + c\omega) + (d_2 + 1)x_{20} \right) \\
&+ \varepsilon_1 r^2 (cx_{20} + \xi_0 R + c\omega) + \varepsilon_1 c_M x_{20} \\
&+ \varepsilon_1 \left(r T_{fM} \tanh\left(\frac{x_{20} + \omega}{r\varepsilon_2}\right) + c_M \omega \right) = 0
\end{aligned} \tag{7.149}$$

Also, $\mathbf{x}_0 = (x_{10}, x_{20}, x_{30})$ and $\xi_0 = \xi(x_{20})$. x_{10} is found from

$$x_{10} = -\frac{1}{k}(cx_{20} + \xi_0 R + c\omega) \tag{7.150}$$

also

$$x_{30} = x_{20} / r \tag{7.151}$$

For $\varepsilon_1 = 0$, (7.149) simplifies to

$$x_{20} = -d_1 \frac{\xi_0(x_{20})R + c\omega}{cd_1 + k(d_2 + 1)} \quad (7.152)$$

which has a unique solution, x_{20}^* . Since (7.149) is continuously differentiable with respect to x_{20} and its derivative does not vanish at $x_{20} = x_{20}^*$ and $\varepsilon_1 = 0$ (stability requirement sets $d_1 > 0$), based on the *implicit function theorem* [101] it has a solution for sufficiently small ε_1 . Substituting (7.148) into (7.147) yields

$$\begin{aligned} \dot{z}_1 &= z_2 - rz_3 \\ \dot{z}_2 &= -\frac{c}{\Gamma}(z_2 + x_{20}) - \frac{k}{\Gamma}(z_1 + x_{10}) - \frac{\xi}{\Gamma}R - \frac{c}{\Gamma}\omega \\ \varepsilon_1 \dot{z}_3 &= -\frac{1}{J}(\tilde{\beta}(\mathbf{z} + \mathbf{x}_0) + \beta_0) \left(z_3 - \frac{d_1}{r}z_1 + \frac{d_2}{r}z_2 + \frac{1}{r}((d_2 + 1)x_{20} - d_1x_{10}) \right) \\ &\quad + \frac{\varepsilon_1 rk}{J}(z_1 + x_{10}) - \frac{\varepsilon_1 c_M}{J} \left(z_3 + \frac{x_{20}}{r} \right) - \frac{\varepsilon_1}{J} \left(T_{fM} \tanh \left(\frac{z_3 + r^{-1}(x_{20} + \omega)}{\varepsilon_2} \right) + r^{-1}c_M\omega \right) \end{aligned} \quad (7.153)$$

which is in the standard singularly perturbed form for the autonomous systems [84], given by

$$\begin{aligned} \dot{x} &= f(x, y, \varepsilon) \\ \varepsilon \dot{y} &= g(x, y, \varepsilon) \end{aligned}$$

for $x = (z_1, z_2)$, $y = z_3$, and $\varepsilon = \varepsilon_1$.

First, the “reduced model” and the “boundary-layer model” are defined. Setting $\varepsilon_1 = 0$, the third differential equation degenerates to an algebraic equation. The unique solution of this equation is given by

$$z_3 = h(z_1, z_2) = \frac{d_1}{r}z_1 - \frac{d_2}{r}z_2 \quad (7.154)$$

where the fact that $(\beta(\mathbf{z}) + \beta_0) \neq 0$ is used. Also, for $\varepsilon_1 = 0$, x_{10} and x_{20} coincide with the solution of (7.58) and (7.59), which gives $(d_2 + 1)x_{20}|_{\varepsilon_1=0} - d_1x_{10}|_{\varepsilon_1=0} = 0$.

Substituting (7.154) into the first two equations of (7.153) and setting $\varepsilon_1 = 0$, the reduced model is found as

$$\begin{aligned}\dot{z}_1 &= -d_1 z_1 + (d_2 + 1)z_2 \\ \dot{z}_2 &= -\frac{c}{\Gamma} z_2 - \frac{k}{\Gamma} z_1 - \frac{\xi - \xi_0}{\Gamma} R\end{aligned}\quad (7.155)$$

which can be expressed as a single second-order differential equation, given by

$$\Gamma \ddot{z} + (c + \Gamma d_1) \dot{z} + ((d_2 + 1)k + cd_1)z = (d_2 + 1)R(\xi_0 - \xi) \quad (7.156)$$

Note that (7.156) is exactly the same as (7.61), and the analysis of Section 7.4.1 proves that the origin is an exponentially stable equilibrium point of the reduced model.

To obtain the boundary-layer model, we first apply the following change of variable

$$y = z_3 - \frac{d_1}{r} z_1 + \frac{d_2}{r} z_2 \quad (7.157)$$

Upon substituting this into the third equation of (7.153), one finds

$$\begin{aligned}\varepsilon_1 \dot{y} &= -\frac{1}{J} (\tilde{\beta}(\mathbf{z} + \mathbf{x}_0) + \beta_0) \left(y + \frac{1}{r} ((d_2 + 1)x_{20} - d_1 x_{10}) \right) + \frac{\varepsilon_1 r k}{J} (z_1 + x_{10}) \\ &\quad - \frac{\varepsilon_1 c_M}{J} \left(z_3 + \frac{x_{20}}{r} \right) - \frac{\varepsilon_1}{J} \left(T_{fM} \tanh \left(\frac{z_3 + r^{-1}(x_{20} + \omega)}{\varepsilon_2} \right) + r^{-1} c_M \omega \right) \\ &\quad - \varepsilon_1 \frac{d_1}{r} \dot{z}_1 + \varepsilon_1 \frac{d_2}{r} \dot{z}_2\end{aligned}\quad (7.158)$$

Define the *fast* time scale as $\tau = \varepsilon_1^{-1} t$, which yields $\varepsilon_1 \dot{y} = dy/d\tau$. Substituting this into (7.158) and setting ε_1 to zero, yields

$$\frac{dy}{d\tau} = -\frac{1}{J} (\tilde{\beta}(\mathbf{z}) + \beta_0) y \quad (7.159)$$

which can be shown to have an exponentially stable origin (*i.e.* $y=0$). Let $V_1 = 1/2 y^2$ be the Lyapunov function candidate. The derivative of V along the system trajectories is found as

$$\frac{d}{d\tau} V_1 = y \frac{dy}{d\tau} = -\frac{1}{J} (\tilde{\beta}(\mathbf{z}) + \beta_0) y^2 \leq -\frac{\beta_0}{J} y^2 \quad (7.160)$$

Citing Theorem 3 in Appendix I, it is concluded that the system (7.153) has an exponentially stable equilibrium point at the origin for sufficiently small ε_1 .

7.4.5 Variable Velocity Set Point

The error is inversely proportional to $d_2 + 1$ and by choosing a large enough d_2 , the position error can be limited to some allowable maximum thus reducing the lead screw and motor velocity errors. Unfortunately, this approach may increase the already large torque demand on the motor at the beginning of motion when the difference between system initial state (usually at rest, $\dot{\theta} = 0$) and the desired state ($\dot{\theta} = \omega_d$) is significant. From a practical point of view, this may not be desirable or feasible. An effective way to reduce the input torque demand is to increase the preset velocity from zero to its desired value, gradually.

If $\omega = \omega(t)$ then the change of variable (7.48) gives

$$\begin{aligned}\dot{x}_1 &= \dot{\theta} - r\dot{\theta}_M \\ \dot{x}_2 &= \ddot{\theta} - \dot{\omega} \\ \dot{x}_3 &= \ddot{\theta}_M - r^{-1}\dot{\omega}\end{aligned}\quad (7.161)$$

As a result (7.49) becomes

$$\begin{aligned}\dot{x}_1 &= x_2 - rx_3 \\ \dot{x}_2 &= -\frac{c}{\Gamma}x_2 - \frac{k}{\Gamma}x_1 - \frac{1}{\Gamma}\xi R - \frac{c}{\Gamma}\omega - \dot{\omega} \\ \dot{x}_3 &= \frac{1}{J}u - \frac{1}{J}T_f \operatorname{sgn}(x_3 + r^{-1}\omega) + \frac{rk}{J}x_1 - \frac{c_M}{J}x_3 - \frac{c_M}{J}r^{-1}\omega - r^{-1}\dot{\omega}\end{aligned}\quad (7.162)$$

From (7.162), it is easy to see that the \dot{s} equation given by (7.119) changes to

$$\begin{aligned}\dot{s} &= \frac{1}{J}u - \frac{1}{J}T_{fM} \operatorname{sgn}(x_3 + r^{-1}\omega) - \frac{c_M}{Jr}\omega + \left(\frac{rk}{J} - \frac{d_2 k}{r\Gamma}\right)x_1 + \left(d_1 - \frac{c_M}{J}\right)x_3 \\ &\quad - \left(\frac{d_1}{r} + \frac{d_2 c}{r\Gamma}\right)x_2 - \frac{1}{\Gamma} \frac{d_2}{r} (\xi R + c\omega) - \frac{d_2 + 1}{r} \dot{\omega}\end{aligned}\quad (7.163)$$

where the term $-\frac{d_2 + 1}{r} \dot{\omega}$ is the only difference compared to (7.120). To compensate for this

bounded addition, only ρ_0 in (7.126) needs to be modified. Let

$$\rho_0 = \bar{T}_{fM} + \frac{\bar{c}_M}{r} \bar{\omega} + \frac{\bar{J}}{\Gamma} \frac{d_2}{r} \left(\left| \frac{\xi}{\Xi} \right| \bar{R} + \bar{c} \bar{\omega} \right) + \frac{d_2 + 1}{r} \bar{\alpha}\quad (7.164)$$

where $\bar{\alpha}$ and $\bar{\omega}$ are chosen such that

$$\bar{\alpha} \geq \sup_{t \geq 0} \dot{\omega}(t) \text{ and } \bar{\omega} \geq \sup_{t \geq 0} \omega(t) \quad (7.165)$$

Note that since $\omega(t)$ and $\dot{\omega}(t)$ are known functions of time, $\bar{\omega}$ and $\bar{\alpha}$ can be chosen to be time-varying too.

We also need to know the effects of changing $\omega(t)$ on the stability of the sliding phase. Adopting the same sliding surface as before, the governing equations of the sliding motion become

$$\begin{aligned} \dot{x}_1 &= -d_1 x_1 + (d_2 + 1)x_2 \\ \dot{x}_2 &= -\frac{c}{\Gamma} x_2 - \frac{k}{\Gamma} x_1 - \frac{1}{\Gamma} \xi R - \frac{c}{\Gamma} \omega - \dot{\omega} \end{aligned} \quad (7.166)$$

where compared to (7.52), $\dot{\omega}$ has entered into the second equation. In the following, (7.166) is converted to a form where the variation of $\omega(t)$ appears as a *bounded* perturbation. The ultimate boundedness of the sliding motion is then follows from the global exponential stability of the unperturbed system¹.

Let

$$\omega(t) = \omega_d - \varpi(t), \quad 0 \leq \varpi(t) \leq \omega_d \quad (7.167)$$

where ω_d is the final *desired* constant angular velocity value and $\varpi(t)$ is the variable part. For the problem considered here, $\varpi(t)$ is assumed to be a decreasing function of t , with $\varpi(0) = \omega_d$ and $\varpi(t) = 0$, $\forall t \geq t_1$ for some $t_1 > 0$. Also, $\varpi(t)$ is bounded for $\forall t \geq 0$. Substituting (7.167) into (7.166) yields

$$\begin{aligned} \dot{x}_1 &= -d_1 x_1 + (d_2 + 1)x_2 \\ \dot{x}_2 &= -\frac{c}{\Gamma} x_2 - \frac{k}{\Gamma} x_1 - \frac{1}{\Gamma} \xi R - \frac{c}{\Gamma} \omega_d + \delta \end{aligned} \quad (7.168)$$

where

¹ See for example [84, Lemma 9.2].

$$\delta(t, x_2) = \frac{c}{\Gamma(x_2)} \varpi(t) + \tilde{\omega}(t) \quad (7.169)$$

is a bounded term based on the above assumptions for $\varpi(t)$ and $\tilde{\omega}(t)$ and also based on the fact that $\Gamma(x_2)$ is away from zero for $\forall x_2$.

Setting $\delta \equiv 0$, (7.168) reduces to (7.52) with constant $\omega = \omega_d$ which is globally exponentially stable. This property, together with the boundedness of $\delta(t, x_2)$, guarantees that the solutions of (7.168) remain bounded [84]. Furthermore, once $t > t_1$, the perturbation term vanishes and the exponential stability of the equations of motion of the sliding phase is restored.

7.4.6 Numerical Examples

In the numerical examples presented here, the controller law defined by (7.142) is used. The system parameters and their bounds are given by Table 7-1. In addition, the system is considered to be at rest at the start of simulations.

7.4.6.1 Example #1

In the first example, the feedforward input of Section 7.4.3 and the variable velocity set point of Section 7.4.5 are not used. The selected controller parameters are listed in Table 7-2.

Table 7-2: Controller parameters for example #1

Parameter	Value	Parameter	Value
d_1	25	ω_d	40 rad/s
d_2	0	ϵ_1	10
β_0	0		

Figure 7-11 shows the time histories of the lead screw and motor velocity errors. As can be seen, the sliding mode controller is able to dampen the lead screw vibrations in a short time. The steady state error is approximately $x_{20} \approx -2.1 \text{ rad/s}$ (about %5) for the lead screw, which is equivalent to a $x_{30} \approx -13.1 \text{ rad/s}$ error in the steady state value of the motor's angular velocity, according to (7.151).

The time history of the x_1 state is shown in Figure 7-12(a). This variable essentially represents the torsional deflection of the elements (coupling) connecting the motor to the lead screw. The steady

state deflection, x_{10} , is approximately -0.054 rad in accordance with (7.150). In Figure 7-12(b), the time history of the normal contact force of the threads is plotted. Note that, during the simulation, contact force remains greater than zero and at steady state reaches approximately, $N_{ss} \approx 98.5 \text{ N}$ which can also be found from (3.16) as

$$N_{ss} = \frac{R}{\cos \lambda + \mu_0 \operatorname{sgn}(R\omega) \sin \lambda}$$

The controlled input time history is given in Figure 7-13. As expected, at the beginning of motion, the controller demands high torque from the motor to bring the system's state from $\left(0, -40, -40 \times \frac{19}{3}\right)$ towards the boundary layer. The initial torque is about 6.23 N.m . At steady state, the torque required to maintain the system's constant velocity is $u_0 \approx 1.3 \text{ N.m}$, which agrees with (7.133).

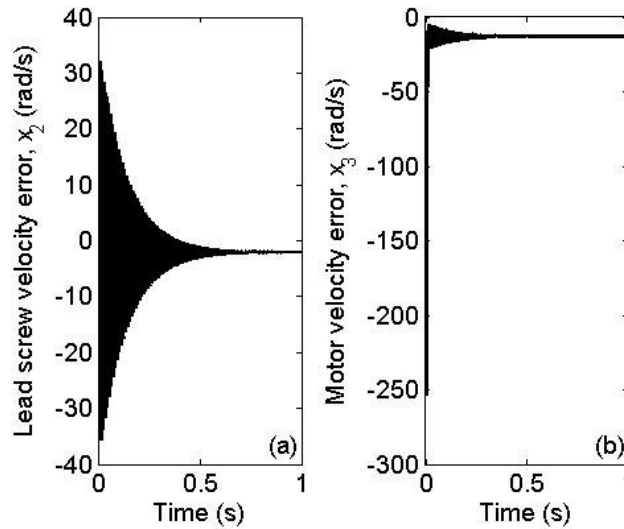


Figure 7-11: Controller performance of example #1; (a) lead screw velocity error, (b) motor velocity error

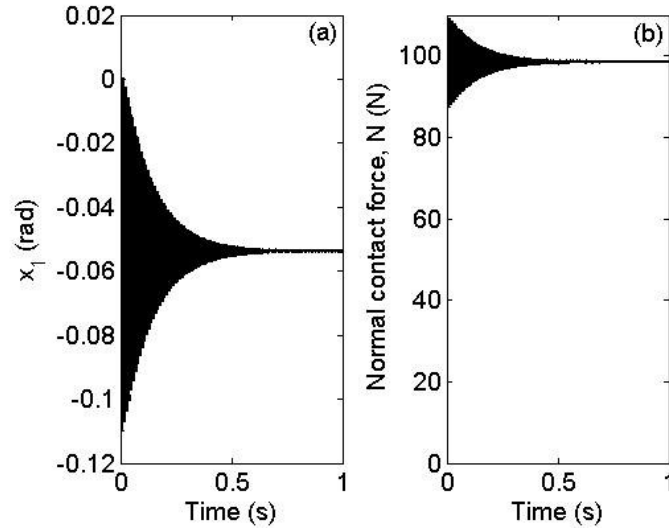


Figure 7-12: (a) Variation of the torsional deflection of the coupling, (b) variation of normal contact force

The system's trajectory is shown in Figure 7-14. The two planes in this figure are defined by $x_3 - (d_1/r)x_1 + (d_2/r)x_2 = \pm \varepsilon$ and are added to visualize the boundary layer. As can be seen, the trajectory enters the boundary layer at point "A" and, once inside, remains there for all future time.

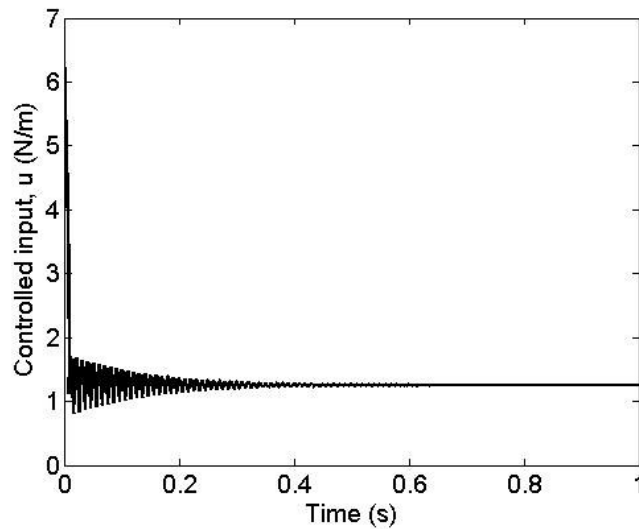


Figure 7-13: Controlled input of example #1

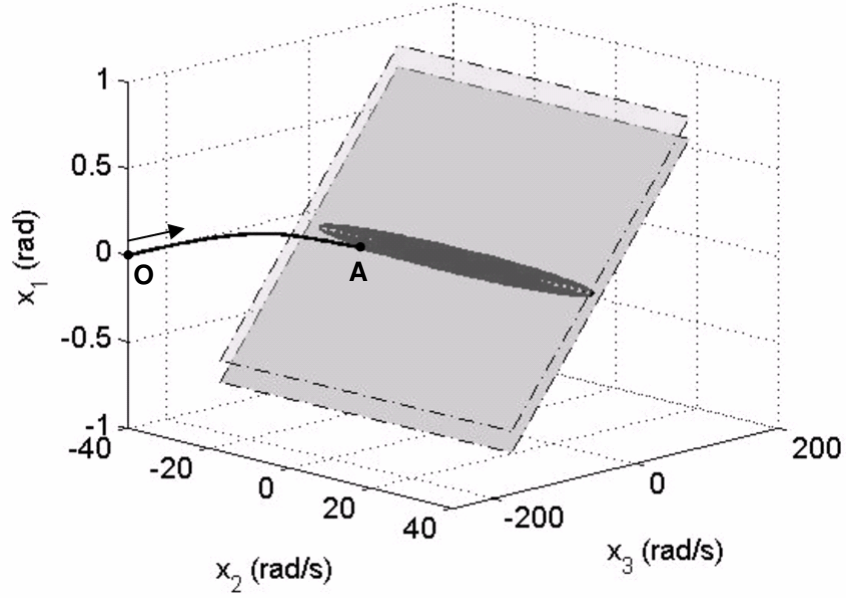


Figure 7-14: System's trajectory for example #1

7.4.6.2 Example #2

In this example, the velocity set point is gradually varied from 0 to ω_d according to

$$\omega(t) = \omega_d \left(\frac{\tanh\left(\frac{t-t_0}{\delta}\right) + \tanh\left(\frac{t_0}{\delta}\right)}{1 + \tanh\left(\frac{t_0}{\delta}\right)} \right) \quad (7.170)$$

where t_0 and δ control the onset of speed change and steepness of its ascent, respectively. Note that,

$$\text{based on (7.170), } |\dot{\omega}(t)| \leq \frac{\omega_d}{\delta \left(1 + \tanh\left(\frac{t_0}{\delta}\right) \right)}, \quad \forall t \geq 0.$$

The controller parameters are selected as the previous example. Also for this example, $t_0 = 0.25s$ and $\delta = 0.1s$. Figure 7-15 shows the lead screw and motor angular velocity time histories. The plots in this figure show successful tracking of the variable velocity set point. The controlled input for this example is shown in Figure 7-16. Compared with Figure 7-13, it is clear that by varying the velocity set point from zero to the desired final value, the initial high control torque is eliminated.

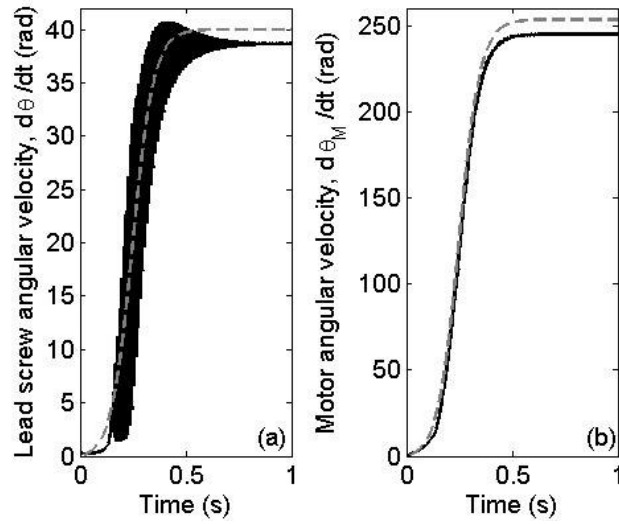


Figure 7-15: Lead screw (a) and motor (b) angular velocities of the closed loop system. Black: system response; dashed gray: velocity set point

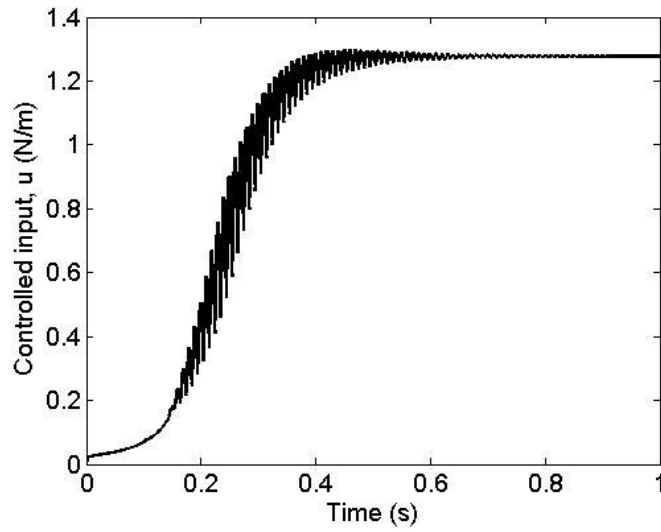


Figure 7-16: Controlled input of example #2

7.4.6.3 Example #3

In this example, the effect of the parameter d_2 on the performance of the controller is investigated. The parameter values used in this example are listed in Table 7-3.

Table 7-3: Controller parameters for example #3

Parameter	Value	Parameter	Value
d_1	40	ω_d	40 rad/s
d_2	0, 1, 10	t_0	0.25 s
β_0	0	δ	0.1 s
ϵ_1	1		

Figure 7-17 shows the lead screw and motor velocity error time histories for three different values of d_2 . It can be seen from this figure that by increasing the value of d_2 , the steady state velocity error decreases, as was shown by (7.152).

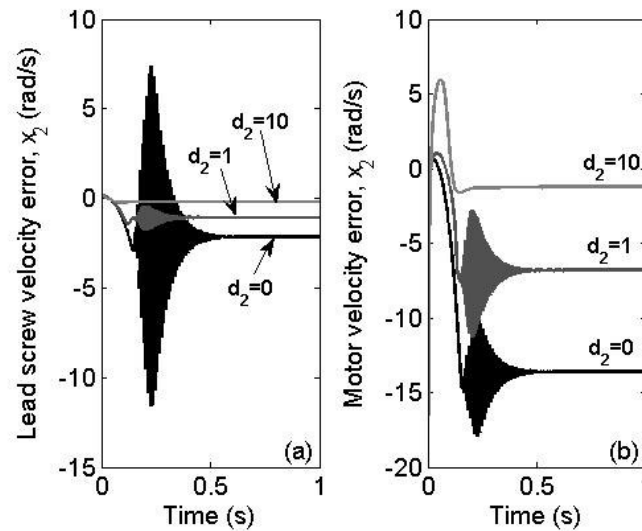


Figure 7-17: Effect of d_2 on the performance of the controller.

In Section 7.4.1, it was shown that d_2 has a stiffness-like effect on the reduced order model of sliding phase. It is interesting to note that the simulation results of Figure 7-17 show this effect; by increasing d_2 , the amplitude of the transient vibrations of the lead screw is reduced.

7.4.6.4 Example #4

In this example, the feedforward input of Section 7.4.3 is added to the controller. To implement the feedforward input together with the variable velocity sliding mode controller of Section 7.4.5, the

feedforward input defined by (7.133) is changed to

$$u_0 = \hat{T}_{fM} + \hat{c}_M r^{-1} \omega(t) + r \hat{\xi}_0 \hat{R} + r \hat{c} \omega(t) \quad (7.171)$$

Also, the term ρ_0 given by (7.141) for the feedforward input of Section 7.4.3, and the term ρ_0 given by (7.164) for the variable velocity method of Section 7.4.5, are combined to give

$$\begin{aligned} \rho_0 = & \max\left(\left|\bar{T}_f - \hat{T}_f\right|, \left|\hat{T}_f - \underline{T}_f\right|\right) + \frac{\bar{J}}{\underline{\Gamma}} \frac{d_2}{r \hat{k}} \max\left(\left|\hat{k} \bar{\xi}_0 \bar{R} - \underline{k} \hat{\xi}_0 \hat{R}\right|, \left|\hat{k} \underline{\xi}_0 \underline{R} - \bar{k} \hat{\xi}_0 \hat{R}\right|\right) \\ & + \frac{\bar{J}}{\underline{\Gamma}} \frac{d_2}{r \hat{k}} \bar{\omega} \max\left(\left|\bar{c} \hat{k} - \underline{k} \hat{c}\right|, \left|\underline{c} \hat{k} - \bar{k} \hat{c}\right|\right) + \frac{\bar{\omega}}{r} \max\left(\left|\underline{c}_M - \hat{c}_M\right|, \left|\bar{c}_M - \hat{c}_M\right|\right) \\ & + \frac{r}{\hat{k}} \left(\hat{\xi}_0 \hat{R} + \hat{c} \bar{\omega}\right) \max\left(\left|\hat{k} - \underline{k}\right|, \left|\hat{k} - \bar{k}\right|\right) + \frac{d_2 + 1}{r} \bar{\alpha} \end{aligned} \quad (7.172)$$

Finally, the sliding mode control law given by (7.142) is changed to

$$u = -(\beta(\tilde{\mathbf{x}}) + \beta_0) \text{sat}\left(\frac{s}{\epsilon_1}\right) \quad (7.173)$$

where $\tilde{\mathbf{x}} = [x_1 + \hat{x}_{10} \quad x_2 \quad x_3]$ and \hat{x}_{10} is calculated by substituting nominal values into (7.134).

The controller variables for this numerical example are given in Table 7-4. Figure 7-18 shows the performance of the sliding mode controller with and without the feedforward input. The addition of the feedforward component clearly improved the steady state results. It must be noted that, this improvement is highly dependent on the accuracy of the nominal values of the system parameters.

Table 7-4: Controller parameters for example #4

Parameter	Value	Parameter	Value
d_1	25	ω_d	40 rad/s
d_2	0	t_0	0.25 s
β_0	0	δ	0.1 s
ϵ_1	1		

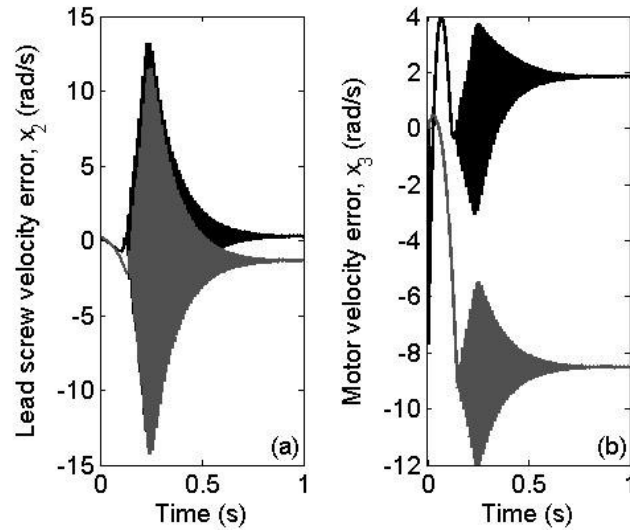


Figure 7-18: Effect of feedforward part on the performance of the controller.
Gray: without feedforward; black: with feedforward

The controller effort is shown in Figure 7-19 for the two cases considered in this example. It can be seen that the addition of feedforward input only slightly increased the input. The reduction of the sliding mode controller gain (comparing (7.172) with (7.164)) is compensated by the nominal input (7.171), resulting in reduced steady-state errors.

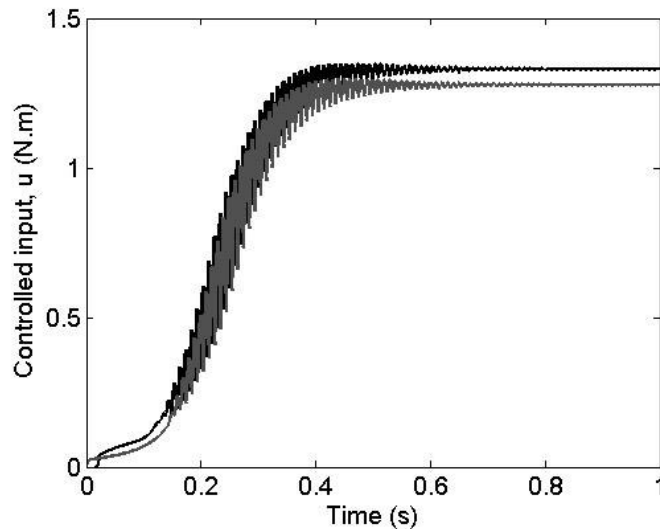


Figure 7-19: Controlled inputs of example #4.
Black: with feedforward input; gray: without feedforward input.

For comparison, Figure 7-20 shows simulations results when *only* the feedforward input was applied (open-loop system). The system is unstable and the lead screw DOF exhibits stick-slip behavior. The vibration amplitude of the motor, on the other hand, is significantly smaller which is due to the high gear ratio, r , between motor and lead screw¹. The error in the steady state value of motor velocity error is attributed the difference between nominal values and true values of the system parameters.

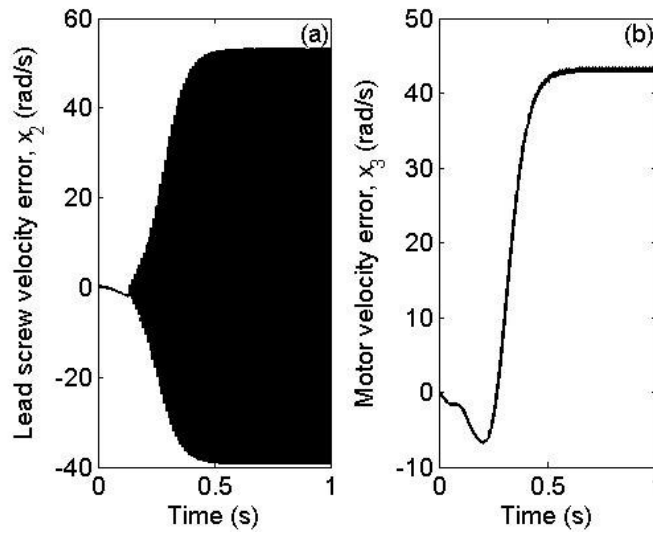


Figure 7-20: Performance under the action of feedforward input alone

7.4.6.5 Example #5

In the development of the sliding mode controller of this chapter, the velocity-dependent coefficient of friction was smoothed to satisfy the smoothness requirement for the averaging process of Section 7.4.1 and the singular perturbation analysis of Section 7.4.4. However, there is no limit on the size of r_1 parameter, since this parameter does not appear in the control law. The only difference is that a somewhat larger d_1 value may be needed to guarantee stability due to the increased negative slope of the friction curve at the lower relative velocities. This, however, does not affect the stability of the

¹ Similar behavior was observed in the open-loop test results of Chapter 4. See Figure 4-15(a).

system once the variable reference velocity reaches its desired final value. This feature can be used to effectively recover the cases where the coefficient of friction does not vanish near zero relative velocity by selecting very large values for r_1 .

In this example, the actual value for r_1 is set to 10000 (compared with the previous examples, where $r_1 = 2$). The resulting coefficient of friction is shown in Figure 7-21. Controller parameters used in this example are given in Table 7-5.

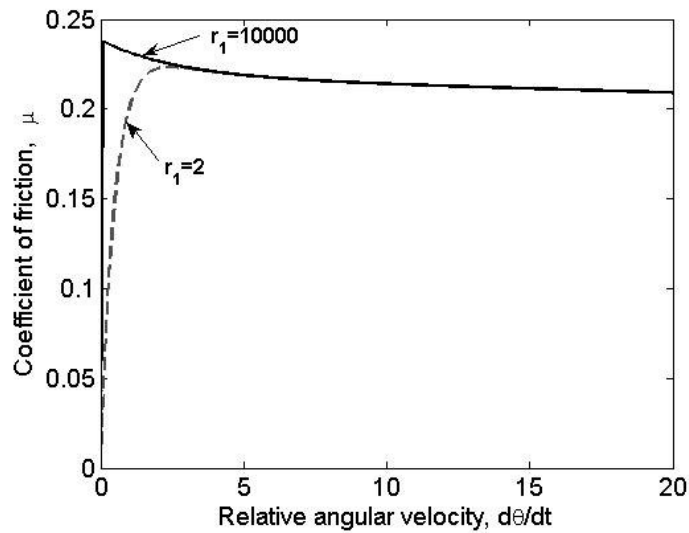


Figure 7-21: Smoothed coefficient of friction

Table 7-5: Controller parameters for example #5

Parameter	Value	Parameter	Value
d_1	40	ω_d	40 rad/s
d_2	0	t_0	0.25 s
β_0	0	δ	0.1 s
ε_1	1	r_1	10000

The performance of the controller is shown by the error time histories plotted in Figure 7-22. The stick-slip transient vibration in the lead screw angular velocity is clearly visible in the close-up view of Figure 7-23. The controlled input for this example is shown in Figure 7-24.

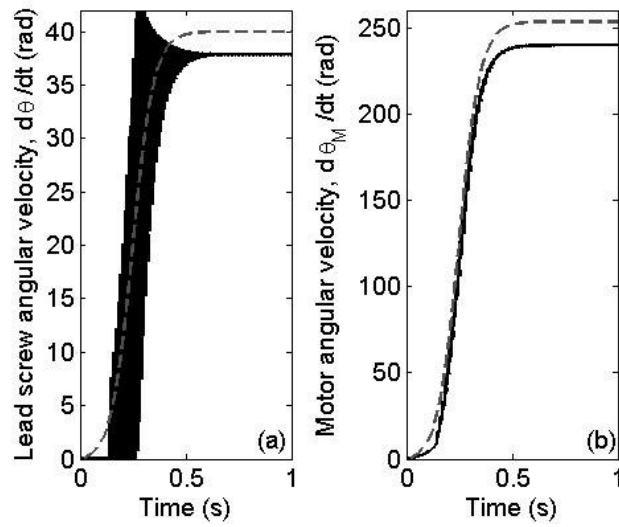


Figure 7-22: Lead screw (a) and motor (b) angular velocities of the closed loop system. Black: system response; dashed gray: velocity set point

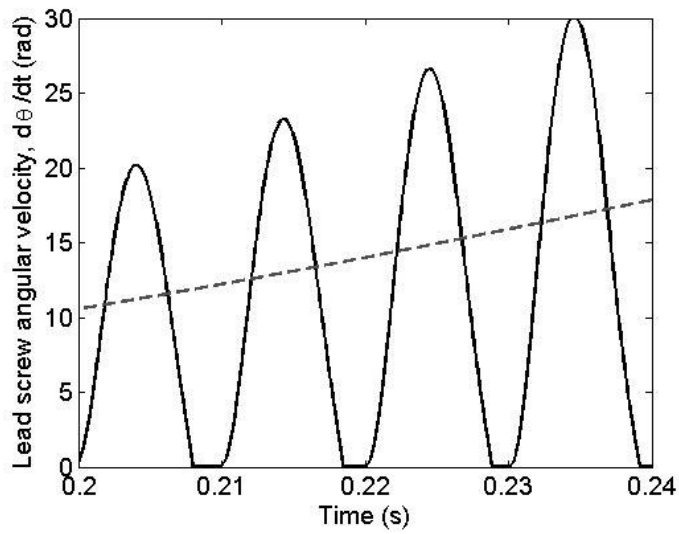


Figure 7-23: Close-up view of the transient vibrations of the lead screw

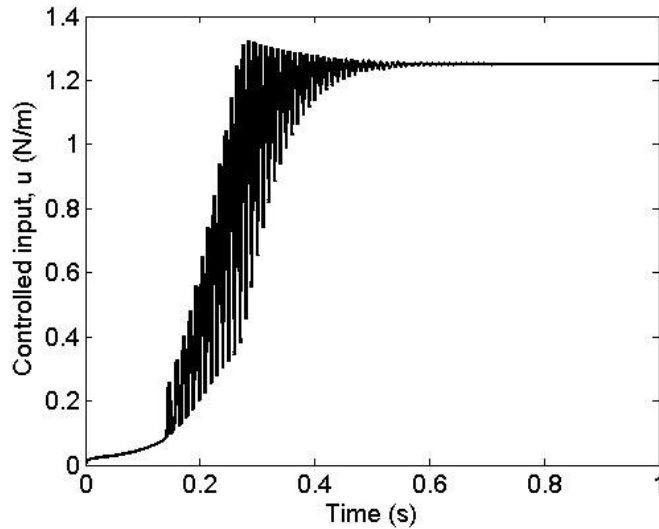


Figure 7-24: Controlled input for example #5

7.5 Conclusions

Active vibration control for lead screw systems was studied in this chapter. Based on the sliding mode control method, two robust regulators were designed that are capable of stabilizing the steady sliding fixed point of the system to a predefined set point. These controllers actively diminish the vibrations caused by the negative damping mechanism that is assumed to be present in the system. To implement these controllers, no knowledge of any of the system parameters is needed and only the bounds of the parameters are assumed to be available.

In Section 7.3, the model of the lead screw drive was simplified under the assumption that all of the rotating parts, from motor to lead screw, are rigidly connected. The problem of chattering, which is an inherent consequence of all discontinuous (switching) controllers such as the sliding mode, was addressed, and a continuous version of the controller was developed to avoid chattering. Stability of this controller was proven using an appropriate Lyapunov function. Numerical simulation results also confirmed the applicability of the controller.

This assumption of rigidity was relaxed in Section 7.4. In this section, a more realistic 2-DOF lead screw drive system was analyzed. First, a basic sliding mode controller was developed that addressed the presence of unmatched uncertainties in the system. The process of the proof of stability of this controller involved the analysis of the governing equations of sliding motion as a weakly nonlinear

system. Drawing heavily on the results of Section 5.2, it was proven that for a suitable choice of sliding surface, the sliding motion is globally exponentially stable.

Three areas of deficiency were identified regarding the performance of the basic sliding mode controller. Each of these issues was addressed through an appropriate modification to the basic controller that retained its stability properties:

1. Chatter – This problem stems from the discontinuous nature of the controller. Similar to the case of Section 7.3, boundary layer approximate control law was introduced. The asymptotic stability of the system inside the boundary layer was proven by recasting the equations of motion into a standard singular perturbation problem
2. Steady state error – The origin (*i.e.* zero steady sliding error state) is not the fixed point of the sliding phase. As a result, the stable system exhibits a steady state difference between the attained velocity and the desired set point. To reduce this error, an additional feedforward input was added to the controller that utilizes the available knowledge of the system parameters (*i.e.* nominal values).
3. High initial torque demand – For initial conditions that are away from the sliding surface, the controller requires high torque at the start of the motion. It was proven that the developed sliding mode control is capable of stabilizing the system while the velocity set point is varied. The proof of stability only requires bounded variations velocity set point with bounded rate of change. By gradually varying the velocity set point from zero (system at rest) to the desired value, the initial high torque was eliminated.

The numerical simulation results showed the effectiveness of the modified sliding mode controller in dampening the vibrations caused by the negative damping instability mechanism and regulating the angular velocity of the lead screw to the desired set point.

Chapter 8

Results Summary and Future Work

In this chapter, a summary of the results obtained in this thesis is presented and possible areas for future work are discussed.

8.1 Results Summary

This thesis covers a wide range of topics regarding the dynamics of lead screw drives with friction. Mathematical modeling, model/friction parameters identification, mechanisms of friction-induced instability, and robust vibration control are the four areas that make up this research. The results obtained in this work aim to fill a substantial gap in the literature regarding the dynamics of lead screw systems with friction.

A lead screw drive consists of a meshing lead screw and nut pair and converts rotary motion to translation. Depending on the configuration of the system, the driver (*e.g.* electric motor) may rotate either the lead screw or the nut. In both cases, the load may be translated by either translating the lead screw or translating the nut. Clearly, vibratory behavior in any mechanical system requires some degree of flexibility in that system. In lead screw drives, numerous compliant elements may contribute to the overall flexibility of the system and affect the number of degrees of freedom required for modeling the system accurately. In this work, a unified mathematical framework is presented for modeling the lead screw drives. Depending on the complexity of the drives under study and the elements (flexible or rigid) included in the power transmission chain, the mathematical models developed in this work are capable of representing the system's dynamics while incorporating the handedness of the screw, direction of motion, and the direction of applied force. All models presented in this thesis are based on the basic 1-DOF lead screw drive model.

A mathematical model by itself is an abstract object suitable only for qualitative studies. In order to convert such a model to a design tool, a (quantitative) validation process is needed. In this thesis, the

lead screw drive mechanism of a powered seat adjuster is investigated. The preliminary test results show that the friction-induced vibration of the two lead screws in the horizontal motion mechanism of this seat adjuster is the cause of unacceptable levels of audible noise. Based on the developed mathematical model of the lead screw drive of this seat adjuster, a novel parameter identification technique is introduced, which consists of an identification step and a fine-tuning step. Using the measurement data collected from the drive, system parameters such as velocity-dependent friction parameters, damping, and coupling stiffness are identified. Comparison between the measurements and simulation results confirms the accuracy of the identified parameters and validates the mathematical model of the lead screw drive. This model is then used to perform parameter studies, which results in the discovery of possible simple design modification to eliminate audible noise problem.

Three distinct frictional instability mechanisms can affect a lead screw system. These mechanisms are: 1. Negative damping, 2. Kinematic constraint, and 3. Mode coupling. In this thesis, all of these mechanisms are studied in detail. Negative damping instability, which is a consequence of decreasing friction with increasing sliding velocity, is studied first. This mechanism is responsible for the instabilities observed in the lead screw drive of the seat adjuster mentioned above. The negative damping instability mechanism is studied using the 1-DOF basic lead screw model. After linearization, local stability of the steady-sliding fixed point is investigated by evaluating the eigenvalues of the Jacobian matrix of the system, which resulted in a parametric condition for stability in terms of the coefficient of friction (more precisely, the rate of decay of friction with sliding velocity) and rotational damping of the lead screw supports. This analysis is expanded by the application of the method of averaging. It is shown that, depending on the value of the parameters and because of the assumption of exponentially decaying coefficient of friction, one of the following three scenarios define the steady state solutions of the averaged system: 1. The origin (steady-sliding state) is stable and no other periodic solutions (limit cycles) exist; 2. The origin is unstable and it is surrounded by a stable limit cycle, or; 3. The origin is stable and it is surrounded by an unstable limit cycle (which defines the region of attraction of the stable trivial fixed point). The unstable limit cycle is inside a stable limit cycle.

The kinematic constraint and mode coupling stability mechanisms can destabilize a mechanical system even with a constant (velocity-independent) coefficient of friction. The kinematic constraint instability can occur in 1-DOF systems, whereas mode coupling instability is exclusive to multi-DOF systems.

Parametric conditions for the onset of the kinematic constraint instability are found by analyzing the eigenvalues of the linearized version of the basic 1-DOF model. This analysis gives three conditions that together define the sufficient conditions for the steady sliding state to become unstable. The first condition states that the lead screw must be self-locking. The second condition requires that the force applied to the nut be in same direction as the nut translation. The third condition defines a limit ratio between the mass of the translating part and the inertia of the rotating part. In other words, there is limiting value for the mass of the translating part (depending on the lead screw inertia, coefficient of friction, and geometry of lead screw), below which instability does not occur.

The mode coupling is by far the most complex instability mechanism of the three mechanisms studied in this thesis. In an undamped system with two or more DOFs mode coupling (flutter), instability occurs whenever two of the system modes merge. The necessary condition for the mode coupling instability is the presence of forces that are not conservative. In lead screw systems, friction provides the necessary condition for the mode coupling instability to occur. In this work, two 2-DOF models and a 3-DOF model of lead screw drives are studied. By evaluating the eigenvalues of the Jacobian matrix of the linearized equations, parametric stability conditions are derived in each case. These conditions, especially in the case of damped systems, are very complex, and numerical analysis is necessary to evaluate the effects of each system parameter on stability. The two 2-DOF models studied differ from each other in the source of additional compliance. One model incorporates compliance in the threads (contact of the lead screw and the nut threads are modeled with linear springs and dampers) and the other incorporates axial flexibility in the lead screw support. It is found that self-locking is a necessary condition for instability in both of these models. Another necessary condition for instability (similar to the kinematic constraint instability) is the application of external force in the direction of motion. It is also shown that introducing damping to only one of the two DOFs of the system (either translational or rotational), destabilizes the steady sliding fixed point.

Design constraints, properties of the available materials, or variations in the operating conditions may hinder efforts to design a lead screw drive that operates without friction-induced vibrations. In such cases, active vibration control may be applied to guarantee vibration free operation. In this thesis, two speed regulators are designed based on the sliding mode control method. The most important feature of these controllers is their robustness to parameter uncertainties. It is assumed that the actual values of the system parameters are not available and only their upper and lower bounds are known.

The first controller applies to a simplified 1-DOF model, where it is assumed that all of the rotating parts are rigid and rigidly connected. Necessary modifications are made to this controller to eliminate the chattering problem, which is an inherent drawback of the discontinuous (switching) sliding mode control law. Stability properties of the modified controller are proven based on Lyapunov's direct method.

The second controller is developed for a more realistic model that incorporates a flexible torsional element between motor and lead screw. The presence of unmatched uncertainties (*i.e.* uncertain terms and inputs do not enter the equations at the same point) makes this model much more complicated compared to the 1-DOF case. Three modifications are applied to this sliding mode controller to improve its performance. First, to eliminate chattering, an approximate continuous version of the controller is developed. Second, a feedforward input is added to improve the steady state error. Third, the velocity set point is set to vary with time from zero to the final desired value, thus eliminating the high torque demand at the start of motion. Using Lyapunov's direct method, the method first order averaging, and the singular perturbation approach, stability the controller is proven for each of these modifications. The presented numerical simulation results show the effectiveness of the two sliding mode controllers.

8.2 Future Work

Based on the results obtained in this thesis, some areas for further research are identified. These topics are listed here.

1. The models presented in Chapter 3 do not include lateral, torsional, or axial flexibility of the lead screw. In applications where long and slender lead screws are used, it may be necessary to incorporate flexibility of the lead screw in to the model.
2. Although backlash can be included in the models developed in Chapter 3, the dynamic effects of backlash on the friction-induced vibrations or active vibration control are not considered here. The study of the effects of backlash is important in positioning lead screws.
3. The micro-pump system presented in Section 1.2 uses stepper motor, and the additional nonlinearities introduced by this driver to the system warrant a further focused study.
4. In this thesis, the method of averaging was used to study the negative damping mechanism. This method or other perturbation techniques can be applied to systems with mode-coupling or kinematic constraint mechanisms. Such analyses may provide a more

complete picture of the nonlinear system as well as approximate and efficient methods to predict steady-state amplitude of vibrations for parameter studies.

5. The controller presented in Section 7.4 assumes that all of the states are measured. Further research may be directed towards the development of output feedback versions of this controller that do not require measurement of all of the states.

Appendices

Appendix A

Test Setups

A.1 Complete Seat Adjuster Experimental Setup

As mentioned in Section 4.1, the preliminary phase of the experiments on the powered seat adjuster was limited to the analysis of the audible noise generated under different operational conditions. Figure A-1 shows the test setup developed for these experiments.



Figure A-1: Experimental setup for preliminary tests on the complete powered seat adjuster

The instruments used, shown in Figure 4-1, were as follows:

- Force measurements: OMEGA¹ pancake style LCHD 1000lb capacity
- Sound level (dBA): TES 1350A Sound Level Meter²

¹ www.omega.com

² www.tes.com.tw

- Audible noise (sound wave): A general purpose PC microphone
- Seat displacement: CELESCO¹ position transducer SP1-12

Signals from load cell, position transducer, and sound level meter were collected using a PC equipped with a Measurement Computing² data acquisition card model PCI-DAS1602/16. A small Matlab/Simulink program was written to record signals received by the data acquisition card. A screenshot of the data acquisition program during one test is shown in Figure A-2. The sampling frequency was set to 1000Hz.

The signal from the microphone was recorded by Windows[®] standard sound recorder accessory software. The sound sampling frequency was 22050Hz.

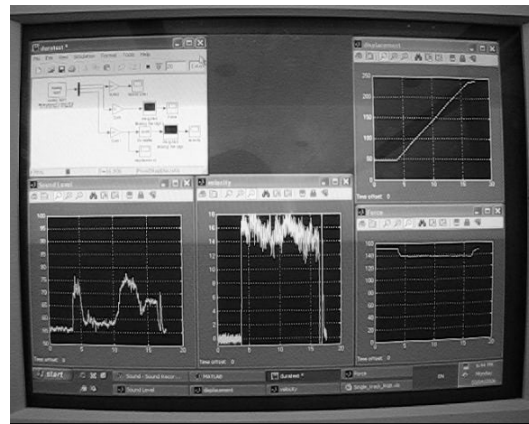


Figure A-2: Data acquisition in Matlab/Simulink environment

A.2 Single Slider Experimental Setup

The experiments performed on the complete seat adjuster were repeated for a single slider. Figure 4-4 shows the test setup developed for these tests. To simplify the test setup, the lead screw slider mechanism was installed upside-down compared to its configuration in the complete seat adjuster. In this setup, the DC motor rotates a single lead screw, which is horizontally fixed. As in the case of the complete seat experiments, a pneumatic cylinder applies the required axial force to the system. As shown in Figure 4-4, force is applied directly to the nut parallel to the lead screw axis.

¹ www.celesco.com

² www.measurementcomputing.com

Instrumentations used in these tests were those listed in the previous section.

A.3 Lead Screw Experimental Setup

The test setup used in the friction identification experiments of Chapter 4 is shown in Figures A-3 and A-4. See Table A-1 for a list of instruments and components of this test setup. Two separate sets of experiments were performed using this setup: a) closed-loop tests of Section 4.2. and open-loop tests of Section 4.4.

In closed-loop tests, the DC motor is driven through a servo amplifier operating in the “current mode” (see Figure A-4). In this mode, the current output of the amplifier is proportional to the input voltage control signal. Consequently, the motor torque is proportional to the control signal. The amplifier gain and the DC motor torque constant are 1.0 (A/V) and 0.0266 (N.m/A), respectively.

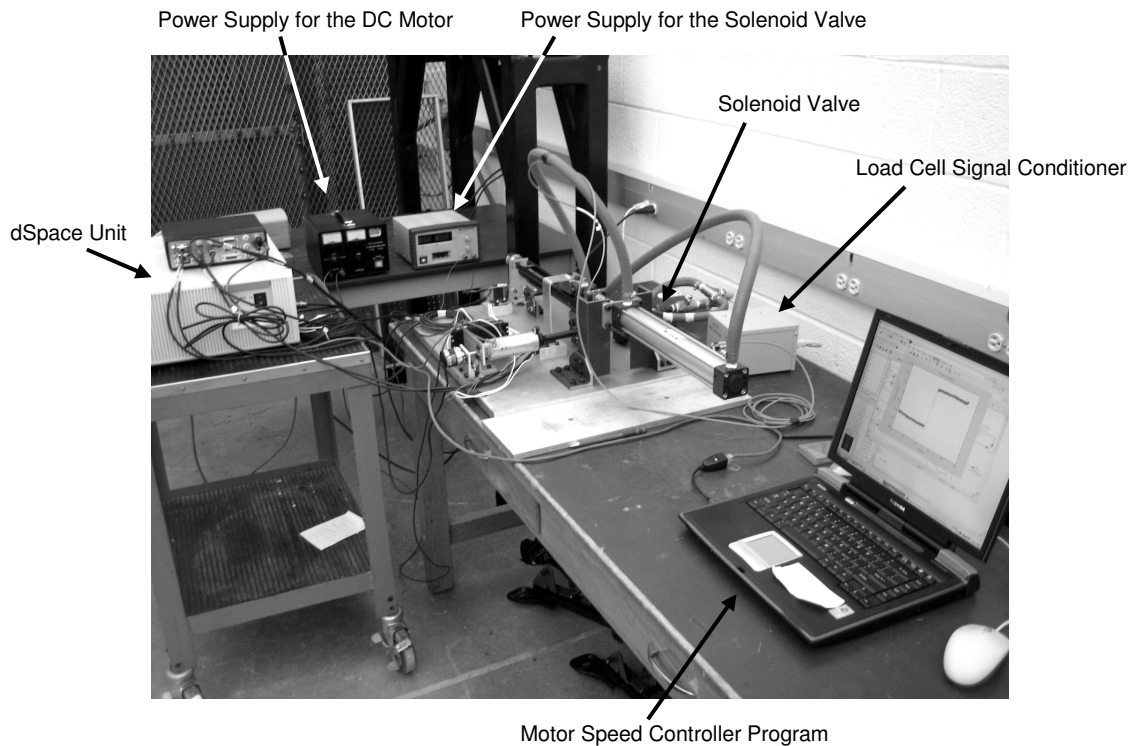


Figure A-3: Experimental setup for the lead screw friction identification tests

The control signal for the closed-loop tests is generated by the dSpace¹ controller, which is programmed in Matlab. The pneumatic cylinder is activated by a solenoid valve which is also commanded by the controller. Two identical analog rotary encoders (sinusoidal signal, 1V_{pp}) are used to measure the angular displacement of the lead screw and the DC motor. These encoders have a resolution of 3600 counts per revolution, which is interpolated up to 4000 times by the dSpace controller and recorded. Other measured signals in these tests are the load cell signal (applied axial force) and the motor current, which are also acquired by the dSpace system.

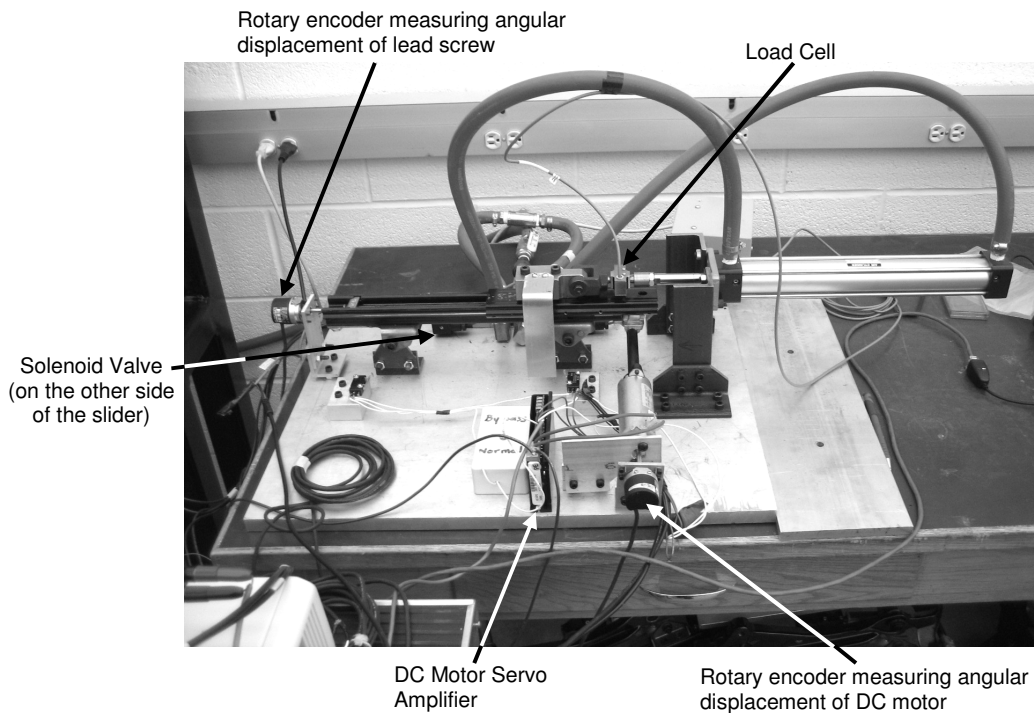


Figure A-4: Instrumentation used in the friction identification test setup

Figure A-5 shows a sample of measured angular displacement and calculated angular velocity (by numerical differentiation) of the lead screw. The measurement data corresponding to the accelerating (start of motion) and decelerating (end of motion) portions of each test is discarded and the resulting near steady-state measurements is averaged and recorded as one data point. See Figure A-6 for a sample of near steady-state measurement results.

¹ www.dspaceinc.com

Table A-1: Partial list of components of the lead screw test setup

NO.	ITEM	SPECIFICATION	MODEL	MANUFACTURER
1	Rotary Encoders	3600 lines per revolution, sinusoidal incremental signal (1Vpp)	ERN 1080	Heidenhain
				www.heidenhain.com
2	Load Cell	200 lbf Mini Universal Link Load Cell	LC703-200	Omega
				www.omega.com
3	Load Cell Signal Conditioner	Strain Gage Amplifier	DMD-465	Omega
				www.omega.com
4	Motor Servo Amplifier	Pulse width modulation amplifier	12A8M	Advance Motion Control
				www.a-m-c.com
5	Power Supply	DC Regulated Power Supply	-	BK Precision
				www.bkprecision.com
6	Solenoid Valve	4 way, 2 solenoids valve with center exhaust	MVSC 300 4E2R	Mindman Pneumatics
				www.mindman.com.tw
7	Pneumatic Cylinder	Double acting with 11¼" stroke	MCQNF 11-1.5-1175	Mindman Pneumatics
				www.mindman.com.tw

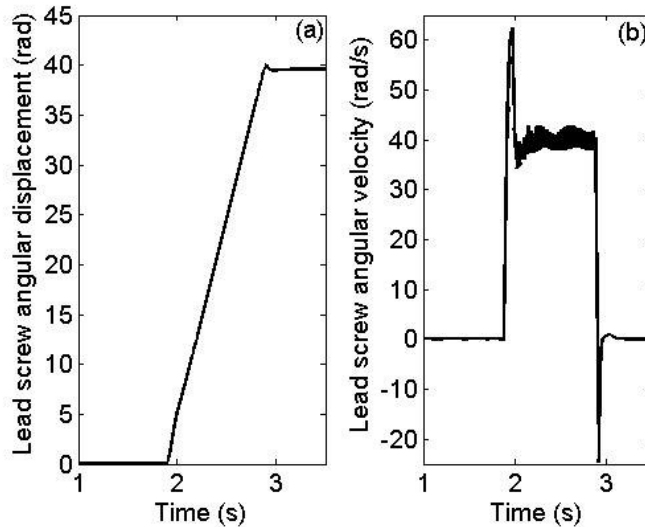


Figure A-5: Sample test results. (a) Lead screw angular displacement, (b) Lead screw angular velocity.

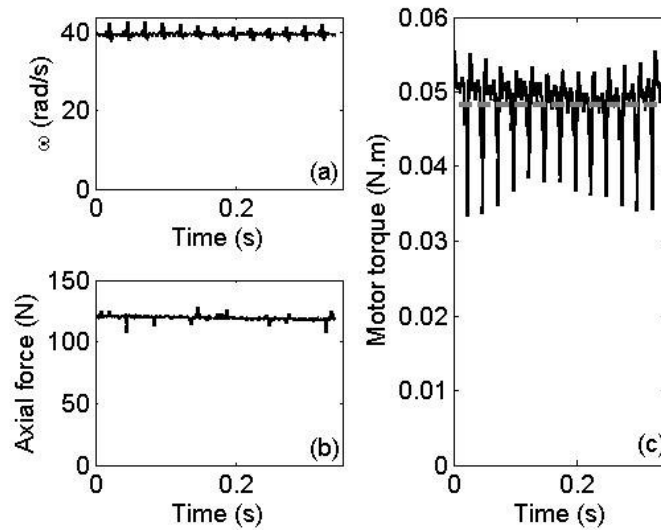


Figure A-6: Near steady-state portion of a sample test results.
(a) Lead screw angular velocity, (b) Axial load, and (c) Motor torque.

In the second part of the experiments with this test setup, the same configuration was used but without the motor speed controller. The motor servo amplifier was switched to “voltage mode” and the dSpace system was only used to collect data. A sample of the open-loop experimental results is shown in Figure 4-14(b).

Appendix B

First Order Averaging Theorem – Periodic

Case

In this appendix, based on theorems and proofs given in [35,44], a version of the first order averaging for the periodic systems is stated and proven that is used in Chapter 5.

Theorem

Consider the following system in *standard form*

$$\dot{\mathbf{x}} = \varepsilon \mathbf{f}(t, \mathbf{x}, \varepsilon), \quad \mathbf{x}(0) = \mathbf{x}_0 \quad (\text{B.1})$$

Suppose

- The function $\mathbf{f} : R_+ \times D \times [0, \varepsilon_0] \rightarrow R^n$ is a T -periodic with respect to t for $x \in D$.
 $D \subset R^n$ is an open bounded set and $\varepsilon_0 > 0$ is some number.
- There exists a constant $M > 0$ such that $\|\mathbf{f}(t, \mathbf{x}, \varepsilon)\| \leq M$.
- $\mathbf{f}(t, \mathbf{x}, \varepsilon)$ is Lipschitz continuous with respect to \mathbf{x} and ε with Lipschitz constants λ_x and λ_ε , respectively.
- The average, $\bar{\mathbf{f}}(\mathbf{x}) = \frac{1}{T} \int_0^T \mathbf{f}(\tau, \mathbf{x}, 0) d\tau$ exists uniformly with respect to \mathbf{x} .
- Considered the *averaged* system;

$$\dot{\mathbf{z}} = \varepsilon \bar{\mathbf{f}}(\mathbf{z}), \quad \mathbf{z}(0) = \mathbf{x}_0 \quad (\text{B.2})$$

- The solution of (B.2), $\mathbf{z}(t; 0, \mathbf{x}_0)$, belongs to interior subset of D on time scale $1/\varepsilon$.

Then

There exists $c > 0$, $\varepsilon_0 > 0$, and $L > 0$, such that the following holds for the solutions of (B.1) and (B.2)

$$\|\mathbf{x}(t, \varepsilon) - \mathbf{z}(t, \varepsilon)\| \leq c\varepsilon \quad (\text{B.3})$$

For $0 \leq \varepsilon \leq \varepsilon_0$ and $0 \leq t \leq L/\varepsilon$. Also, c is independent of ε .

Proof:

Let

$$\mathbf{E}(t, \varepsilon) = \mathbf{x}(t, \varepsilon) - \mathbf{z}(t, \varepsilon) \quad (\text{B.4})$$

denote the error. From the two differential equations, (B.4) is found as

$$\mathbf{E}(t, \varepsilon) = \varepsilon \int_0^t [\mathbf{f}(\tau, \mathbf{x}(\tau, \varepsilon), \varepsilon) - \bar{\mathbf{f}}(\mathbf{z}(\tau, \varepsilon))] d\tau \quad (\text{B.5})$$

The integrand in (B.5) can be written as

$$[\mathbf{f}(\tau, \mathbf{x}, \varepsilon) - \mathbf{f}(\tau, \mathbf{z}, \varepsilon)] + [\mathbf{f}(\tau, \mathbf{z}, \varepsilon) - \mathbf{f}(\tau, \mathbf{z}, 0)] + [\mathbf{f}(\tau, \mathbf{z}, 0) - \bar{\mathbf{f}}(\mathbf{z})]$$

where argument of \mathbf{E} , \mathbf{x} , and \mathbf{z} are omitted for brevity. As a result, from (B.5) we have

$$\|\mathbf{E}\| \leq \varepsilon \int_0^t \|\mathbf{f}(\tau, \mathbf{x}, \varepsilon) - \mathbf{f}(\tau, \mathbf{z}, \varepsilon)\| d\tau + \varepsilon \int_0^t \|\mathbf{f}(\tau, \mathbf{z}, \varepsilon) - \mathbf{f}(\tau, \mathbf{z}, 0)\| d\tau + \varepsilon \left\| \int_0^t [\mathbf{f}(\tau, \mathbf{z}, 0) - \bar{\mathbf{f}}(\mathbf{z})] d\tau \right\| \quad (\text{B.6})$$

The first and second terms on the right-hand side of (B.6) can be estimated using the Lipschitz constant λ_x and λ_ε

$$\|\mathbf{E}\| \leq \varepsilon \lambda_x \int_0^t \|\mathbf{E}\| d\tau + \varepsilon^2 \lambda_\varepsilon t + \varepsilon \left\| \int_0^t [\mathbf{f}(\tau, \mathbf{z}, 0) - \bar{\mathbf{f}}(\mathbf{z})] d\tau \right\| \quad (\text{B.7})$$

The third term in (B.6) or (B.7) is estimated as follows:

$$\left\| \int_0^t [\mathbf{f}(\tau, \mathbf{z}, 0) - \bar{\mathbf{f}}(\mathbf{z})] d\tau \right\| \leq \sum_{i=1}^N \left\| \int_{(i-1)T}^{iT} [\mathbf{f}(\tau, \mathbf{z}, 0) - \bar{\mathbf{f}}(\mathbf{z})] d\tau \right\| + \left\| \int_{NT}^t [\mathbf{f}(\tau, \mathbf{z}, 0) - \bar{\mathbf{f}}(\mathbf{z})] d\tau \right\| \quad (\text{B.8})$$

where N is chosen such that, $NT \leq t \leq (N+1)T$. We have

$$\begin{aligned}
& \int_{(i-1)T}^{iT} [\mathbf{f}(\tau, \mathbf{z}(\tau, \varepsilon), 0) - \bar{\mathbf{f}}(\mathbf{z}(\tau, \varepsilon))] d\tau \\
&= \int_{(i-1)T}^{iT} [\mathbf{f}(\tau, \mathbf{z}(\tau, \varepsilon), 0) - \bar{\mathbf{f}}(\mathbf{z}(\tau, \varepsilon)) - \mathbf{f}((i-1)T, \mathbf{z}((i-1)T, \varepsilon), 0) + \bar{\mathbf{f}}(\mathbf{z}((i-1)T, \varepsilon))] d\tau
\end{aligned}$$

which holds since

$$\int_{(i-1)T}^{iT} [\mathbf{f}(\tau, \mathbf{z}((i-1)T, \varepsilon), 0) - \bar{\mathbf{f}}(\mathbf{z}((i-1)T, \varepsilon))] d\tau = 0$$

As a result

$$\begin{aligned}
& \sum_{i=1}^N \left\| \int_{(i-1)T}^{iT} [\mathbf{f}(\tau, \mathbf{z}, 0) - \bar{\mathbf{f}}(\mathbf{z})] d\tau \right\| \\
&= \sum_{i=1}^N \left\| \int_{(i-1)T}^{iT} [\mathbf{f}(\tau, \mathbf{z}(\tau, \varepsilon), 0) - \bar{\mathbf{f}}(\mathbf{z}(\tau, \varepsilon)) - \mathbf{f}(\tau, \mathbf{z}((i-1)T, \varepsilon), 0) + \bar{\mathbf{f}}(\mathbf{z}((i-1)T, \varepsilon))] d\tau \right\| \\
&\leq \sum_{i=1}^N \left\| \int_{(i-1)T}^{iT} [\mathbf{f}(\tau, \mathbf{z}(\tau, \varepsilon), 0) - \mathbf{f}(\tau, \mathbf{z}((i-1)T, \varepsilon), 0)] d\tau \right\| + \sum_{i=1}^N \left\| \int_{(i-1)T}^{iT} [\bar{\mathbf{f}}(\mathbf{z}((i-1)T, \varepsilon)) - \bar{\mathbf{f}}(\mathbf{z}(\tau, \varepsilon))] d\tau \right\| \quad (\text{B.9}) \\
&\leq 2\lambda_x \sum_{i=1}^N \left\| \int_{(i-1)T}^{iT} [\mathbf{z}(\tau, \varepsilon) - \mathbf{z}((i-1)T, \varepsilon)] d\tau \right\| \\
&\leq 2\varepsilon\lambda_x T^2 MN
\end{aligned}$$

The first inequality in (B.9) holds since $\bar{\mathbf{f}}(\mathbf{x})$ has the same Lipschitz constant as $\mathbf{f}(t, \mathbf{x}, \varepsilon)$ with respect to \mathbf{x}

$$\begin{aligned}
\|\bar{\mathbf{f}}(\mathbf{x}_1) - \bar{\mathbf{f}}(\mathbf{x}_2)\| &= \frac{1}{T} \left\| \int_0^T [\mathbf{f}(\tau, \mathbf{x}_1, 0) - \mathbf{f}(\tau, \mathbf{x}_2, 0)] d\tau \right\| \leq \frac{1}{T} \int_0^T \|\mathbf{f}(\tau, \mathbf{x}_1, 0) - \mathbf{f}(\tau, \mathbf{x}_2, 0)\| d\tau \\
&\leq \frac{\lambda_x}{T} \int_0^T \|\mathbf{x}_1 - \mathbf{x}_2\| d\tau = \lambda_x \|\mathbf{x}_1 - \mathbf{x}_2\|
\end{aligned}$$

The second inequality in (B.9) holds since $\mathbf{z}(\tau, \varepsilon)$ is the solution of (B.2) and as such is slowly varying:

$$\|\mathbf{z}(\tau, \varepsilon) - \mathbf{z}((i-1)T, \varepsilon)\| \leq \varepsilon TM$$

Also note that

$$\left\| \int_{NT}^t [\mathbf{f}(\tau, \mathbf{z}, 0) - \bar{\mathbf{f}}(\mathbf{z})] d\tau \right\| \leq 2TM \quad (\text{B.10})$$

Using (B.9) and (B.10), (B.8) becomes

$$\left\| \int_0^t [\mathbf{f}(\tau, \mathbf{z}, 0) - \bar{\mathbf{f}}(\mathbf{z})] d\tau \right\| \leq 2\varepsilon T^2 M \lambda_x N + 2TM \leq 2TM (\lambda_x L + 1) \quad (\text{B.11})$$

Note that in (B.11), the inequality $NT \leq t \leq L/\varepsilon$ was used. Finally, using (B.11) the error estimate (B.7) becomes

$$\|\mathbf{E}\| \leq \varepsilon \lambda_x \int_0^t \|\mathbf{E}\| d\tau + \varepsilon \lambda_\varepsilon L + 2\varepsilon TM (\lambda_x L + 1) \quad (\text{B.12})$$

Applying the Gronwall's lemma [35,44] to (B.12) yields

$$\begin{aligned} \|\mathbf{x}(t, \varepsilon) - \mathbf{z}(t, \varepsilon)\| &\leq \varepsilon [\lambda_\varepsilon L + 2TM (\lambda_x L + 1)] e^{\varepsilon \lambda_x t} \\ &\leq \varepsilon [\lambda_\varepsilon L + 2TM (\lambda_x L + 1)] e^{\lambda_x L} \end{aligned} \quad (\text{B.13})$$

Taking $c = [\lambda_\varepsilon L + 2TM (\lambda_x L + 1)] e^{\lambda_x L}$ completes the proof. \square

Appendix C

A Definite Integral Used in Averaging

As seen in Section 5.3.3, the averaging equations lead to the following integral

$$\Lambda_{n,m}(\xi) = \frac{1}{2\pi} \int_0^{2\pi} \sin^n \phi \cos^m \phi e^{\xi \sin \phi} d\phi \quad (\text{C.1})$$

Using the power series expansion for the exponential function

$$e^x = \sum_{n=0}^{\infty} \frac{x^n}{n!} \quad (\text{C.2})$$

(C.1) can be written as

$$\Lambda_{n,m}(\xi) = \frac{1}{2\pi} \sum_{k=0}^{\infty} \frac{1}{k!} \xi^k \int_0^{2\pi} \sin^{n+k} \phi \cos^m \phi d\phi \quad (\text{C.3})$$

Noting that,

$$\int_0^{2\pi} \sin^p \phi \cos^q \phi d\phi = 0 \text{ if } p \text{ or } q \text{ is odd.}$$

The following derivations are due to Moll [102]. The following two cases are identified:

Case 1: n and m are both even numbers.

Replacing n and m in (C.3) by $2n$ and $2m$, yields

$$\begin{aligned}
\Lambda_{2n,2m}(\xi) &= \frac{1}{2\pi} \int_0^{2\pi} \sin^{2n} \phi \cos^{2m} \phi \left(\sum_{k=0}^{\infty} \frac{1}{k!} \xi^k \sin^k \phi \right) d\phi \\
&= \frac{1}{2\pi} \sum_{k=0}^{\infty} \frac{1}{k!} \xi^k \int_0^{2\pi} \sin^{2n+k} \phi \cos^{2m} \phi d\phi \\
&= \frac{1}{2\pi} \sum_{k=0}^{\infty} \frac{1}{(2k)!} \xi^{2k} \int_0^{2\pi} \sin^{2(n+k)} \phi \cos^{2m} \phi d\phi
\end{aligned} \tag{C.4}$$

It can be shown that

$$\int_0^{2\pi} \sin^{2p} x \cdot \cos^{2q} x \cdot dx = 4 \int_0^{\pi/2} \sin^{2p} x \cdot \cos^{2q} x \cdot dx = 2B\left(p + \frac{1}{2}, q + \frac{1}{2}\right) \tag{C.5}$$

where B represents the *Beta* function and is given by

$$B(p, q) = \frac{\Gamma(p)\Gamma(q)}{\Gamma(p+q)} \tag{C.6}$$

which is defined using the *Gamma* function and is given for $p, q \in \mathbf{Z}^+$ as

$$B(p, q) = \frac{(p-1)!(q-1)!}{(p+q-1)!} \tag{C.7}$$

and in the special case

$$B\left(p + \frac{1}{2}, q + \frac{1}{2}\right) = \frac{\pi}{2^{2(p+q)}} \frac{(2p)!(2q)!}{p!q!(p+q)!} \tag{C.8}$$

Substituting (C.5) into (C.4) and using (C.8) yields

$$\Lambda_{2n,2m}(\xi) = \sum_{k=0}^{\infty} \frac{1}{2^{2(n+k+m)}} \frac{(2n+2k)!(2m)!}{(2k)!(n+k)!m!(n+k+m)!} \xi^{2k}, \quad n, m = 1, 2, \dots \tag{C.9}$$

Case 2: n is an odd number and m is an even number.

Replacing n and m in (C.3) by $2n-1$ and $2m$, yields

$$\begin{aligned}
\Lambda_{2n-1,2m}(\xi) &= \frac{1}{2\pi} \int_0^{2\pi} \sin^{2n-1} \phi \cos^{2m} \phi \left(\sum_{k=0}^{\infty} \frac{1}{k!} \xi^k \sin^k \phi \right) d\phi \\
&= \frac{1}{2\pi} \sum_{k=0}^{\infty} \frac{1}{k!} \xi^k \int_0^{2\pi} \sin^{2n+k-1} \phi \cos^{2m} \phi d\phi \\
&= \frac{1}{2\pi} \sum_{k=1}^{\infty} \frac{1}{(2k-1)!} \xi^{2k-1} \int_0^{2\pi} \sin^{2(n+k-1)} \phi \cos^{2m} \phi d\phi
\end{aligned} \tag{C.10}$$

Once again substituting (C.5) into (C.10) and using (C.8) yields

$$\Lambda_{2n-1,2m}(\xi) = \sum_{k=1}^{\infty} \frac{4}{2^{2(n+k+m)}} \frac{(2n+2k-2)!(2m)!}{(2k-1)!(n+k-1)!m!(n+k+m-1)!} \xi^{2k-1}, \quad n, m = 1, 2, \dots \tag{C.11}$$

Here are some special cases:

$$\Lambda_{0,0}(\xi) = \sum_{k=0}^{\infty} \frac{1}{2^{2k}} \frac{1}{k!} \xi^{2k} \tag{C.12}$$

$$\Lambda_{1,0}(\xi) = \sum_{k=1}^{\infty} \frac{1}{2^{2k-1}} \frac{k}{k!} \xi^{2k-1} \tag{C.13}$$

$$\Lambda_{2,0}(\xi) = \sum_{k=0}^{\infty} \frac{1}{2^{2(1+k)}} \frac{(2+2k)!}{(2k)!(1+k)!} \xi^{2k} = \sum_{k=1}^{\infty} \frac{1}{2^{2k-1}} \frac{k(2k-1)}{k!} \xi^{2k-2} \tag{C.14}$$

Appendix D

Steady-state Solutions of the Averaged 1-DOF Lead Screw Model

In this appendix, the averaged amplitude equation derived for the 1-DOF lead screw model in Chapter 5 is examined. It will be shown that, depending on the system parameters, the averaged equation can have 1, 2, or 3 fixed points. The dynamic behavior of the system is described by one of the following scenarios:

1. The trivial solution is stable and no other solution exists.
2. The trivial solution is stable and is surrounded by an unstable limit cycle, which defines the region of attraction of the trivial solution. The unstable limit cycle is inside a stable limit cycle.
3. The trivial solution is unstable and is surrounded by a stable limit cycle.

Before continuing, it is important to take a closer look at the velocity-dependent coefficient of friction given by (5.20). The coefficient of friction as a function velocity, $\omega > 0$, can be written as;

$$\mu(\omega) = (\mu_1 + \mu_2 e^{-r_0 \omega} + \mu_3 \omega)(1 - e^{-r_1 \omega}) \quad (\text{D.1})$$

where $r_1 > r_0 > 0$.

As shown in Figure D-1, depending on the value of μ_2 and μ_3 , four cases can be identified for the variation of the coefficient of friction with velocity¹. These cases are:

- Case I: $\mu_2 = 0 \wedge \mu_3 \geq 0$. In this case, for the entire range of applicable velocities we have

¹ Cases where $\mu_2 < 0$ are not considered since the term $\mu_2 e^{-r_0 \omega}$ is added to the friction model only to emulate the Stribeck effect (*i.e.* decreasing of the coefficient of friction with increasing relative velocity at low velocities).

$$\frac{\partial \mu}{\partial \omega} > 0.$$

- Case II: $\mu_2 = 0 \wedge \mu_3 < 0$. In this case, $\frac{\partial \mu}{\partial \omega} \geq 0$ when $0 \leq \omega < \omega_b$ and $\frac{\partial \mu}{\partial \omega} < 0$ when $\omega > \omega_b$. ω_b designates the local maximum of the friction curve and defines the boundary of the “smoothed” neighborhood of zero velocity. Note that $\omega_b \rightarrow 0$ as $r_1 \rightarrow \infty$.

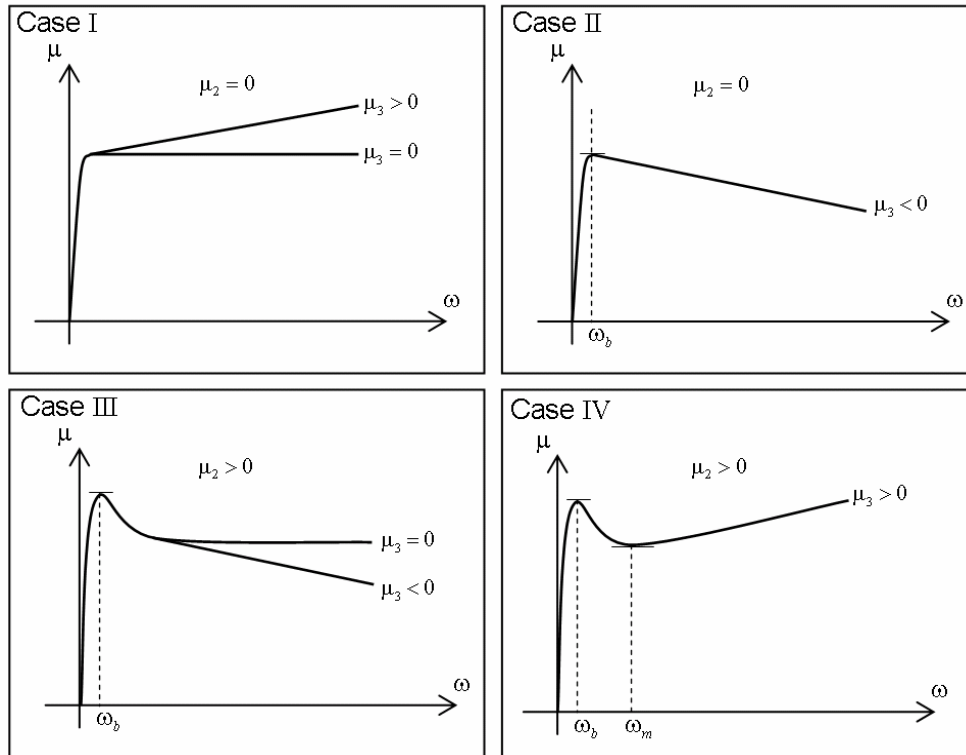


Figure D-1: The velocity-dependent coefficient of friction.

- Case III: $\mu_2 > 0 \wedge \mu_3 \leq 0$. This case is similar to Case II. However, a distinction is made due to the possibility of additional periodic solutions, as shown later in this section.
- Case IV: $\mu_2 > 0 \wedge \mu_3 > 0$. In this case, similar to the Cases II and III, $\frac{\partial \mu}{\partial \omega} \geq 0$ when $0 \leq \omega < \omega_b$. Also $\frac{\partial \mu}{\partial \omega} < 0$ when $\omega_b < \omega < \omega_m$ and $\frac{\partial \mu}{\partial \omega} \geq 0$ when $\omega \geq \omega_m$. Here ω_b is

defined as before and ω_m designates the local minimum of the friction curve.

It must be noted that for the cases where $\mu_3 \neq 0$ and particularly when $\mu_3 < 0$, the assumed model of friction implies a limiting value for the coefficient of friction at high velocities. Beyond a certain value of the velocity, which is typically well outside the range of interest, the friction-velocity curve is assumed to be constant¹.

In Sections D.1 to D.4, each of the above cases is studied separately and the existence of limit cycles is investigated. The stability of each solution (trivial and non-trivial) is also evaluated. The study in this section, for simplicity, is limited to the cases where $R > 0$, $N > 0$, $\omega > 0$, and $\dot{\theta} = \dot{u} + \omega = \omega(v' + 1) \geq 0^2$. The last inequality, limits the averaged amplitude equation to $0 \leq a \leq 1$. Some numerical examples are presented in Section D.5.

Assuming $a \neq 0$ (for non-trivial solutions) and dividing (5.58) by a , an equating the right-hand side of the resulting equation to zero, the following polynomial equation in a^2 is reached

$$\frac{a'}{a} \equiv y = b_0 + \sum_{n=1}^{\infty} b_n a^{2n} = 0 \quad (\text{D.2})$$

where

$$b_0 = -\frac{\hat{c}}{2} + \frac{\hat{R}}{2} ((r_2 - 1)\hat{\mu}_3 + \hat{\mu}_2 \omega r_0 - r_2 \hat{\mu}_1 \omega r_1 - r_2 \hat{\mu}_2 \omega (r_0 + r_1)) \quad (\text{D.3})$$

$$b_n = \frac{\omega^{2n} \hat{R}}{2^{2n+1} n! (n+1)!} (r_2 \hat{\mu}_3 (2n+1) r_1^{2n} + \hat{\mu}_2 \omega r_0^{2n+1} - r_2 \hat{\mu}_1 \omega r_1^{2n+1} - r_2 \hat{\mu}_2 \omega (r_0 + r_1)^{2n+1}) \quad (\text{D.4})$$

where $r_2 = e^{-r_1 \omega}$.

D.1 Case I: $\mu_2 = 0 \wedge \mu_3 \geq 0$

As mentioned earlier, in this case, $\frac{\partial \mu}{\partial \omega} > 0$ for the entire range of applicable velocities. As a result,

¹ See Section 7.1.1.

² See change of variables (5.25) and (5.32).

(5.61) is satisfied for any $c \geq 0$ and the trivial solution is stable in $D = \{a | 0 \leq a \leq 1\}$. To investigate the possibility of non-trivial solutions, (5.53) is examined. Setting $\mu_2 = 0$ in (5.53) and rearranging gives

$$a' = -\varepsilon \frac{\widehat{c}a}{2} - \varepsilon \frac{\widehat{\mu}_3 \widehat{R}a}{2} \left(1 - \frac{r_2}{\pi} \int_0^{2\pi} \sin^2 \phi e^{r_1 \omega a \sin \phi} d\phi \right) - \frac{\varepsilon}{2\pi} r_2 \widehat{\mu}_1 \widehat{R} \int_0^{2\pi} \sin \phi e^{r_1 \omega a \sin \phi} d\phi \quad (\text{D.5})$$

From (5.56) and (5.57), we know that the two definite integrals in (D.5) are non-negative and also,

$$\begin{aligned} 0 \leq a \leq 1 &\rightarrow e^{-r_1 \omega (1-a \sin \phi)} \leq 1 \\ \rightarrow \frac{r_2}{\pi} \int_0^{2\pi} \sin^2 \phi e^{r_1 \omega a \sin \phi} d\phi &= \frac{1}{\pi} \int_0^{2\pi} \sin^2 \phi e^{-r_1 \omega (1-a \sin \phi)} d\phi \leq \frac{1}{\pi} \int_0^{2\pi} \sin^2 \phi d\phi = 1 \end{aligned}$$

which means that the second term in (D.5) is less than or equal to zero for $\mu_3 \geq 0$. Since the first and third terms are also non-positive, one concludes that $a'(a) < 0$ for $0 \leq a \leq 1$, and there are no other non-trivial fixed points in D . A typical plot of amplitude equation, (D.5), is shown in Figure D-2.

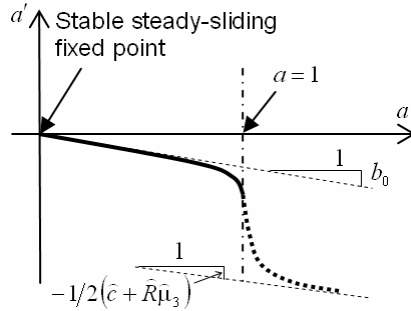


Figure D-2: Schematic plot of amplitude equation for Case I.

D.2 Case II: $\mu_2 = 0 \wedge \mu_3 < 0$

First, we notice that for small velocities satisfying

$$0 \leq \omega < \omega_b \quad (\text{D.6})$$

where ω_b is the solution of $(r_2 - 1)\widehat{\mu}_3 - r_2 \widehat{\mu}_1 \omega r_1 = 0$, (5.61) is satisfied for any $c \geq 0$. Thus, the trivial solution is stable. Moreover, since all of the coefficients of (D.2) are non-positive, no other

solution exists. When $\omega > \omega_b$, the trivial solution is stable if

$$\hat{c} > \hat{R}((r_2 - 1)\hat{\mu}_3 - r_2\hat{\mu}_1\omega r_1) > 0 \quad (\text{D.7})$$

and it is unstable otherwise. In the case of stable trivial fixed point, once again all of the coefficients of equation (D.2) are non-positive, which implies that no other solutions are possible. However, if (D.7) is not satisfied, b_0 (given by (D.3)) is positive while the rest of the coefficients, b_n , (given by (D.4)) remain less than or equal to zero. According to Descartes' Rule of Signs [103], (D.2) has a positive solution which corresponds to a stable periodic solution of the original system. Going back to (D.5) with $\mu_3 < 0$ the condition for the positive solution, say a^* , to be inside the region of validity of the approximation is $a'(1) \leq 0$. In terms of the system's parameters, this condition can be written as

$$\mu_3 < -\frac{\frac{\mu_1 B}{\omega} + \frac{c}{2r_m R}}{1/2 - A + B} < 0 \quad (\text{D.8})$$

where, $A = \frac{1}{2\pi} \int_0^{2\pi} \sin^2 \phi e^{r_1 \omega(-1+\sin \phi)} d\phi$ and $B = \frac{1}{2\pi} \int_0^{2\pi} \sin \phi e^{r_1 \omega(-1+\sin \phi)} d\phi$. Also $0 < A < 1/2$. If this

condition is violated the above first averaging results loses its $O(\epsilon)$ accuracy. To obtain solutions with $O(\epsilon)$ accuracy, (5.45) or (5.48) must be used in the averaging process to obtain results with $O(\epsilon)$ accuracy. Typical plots of amplitude equation, (D.5), for these two cases are shown in Figure D-3.

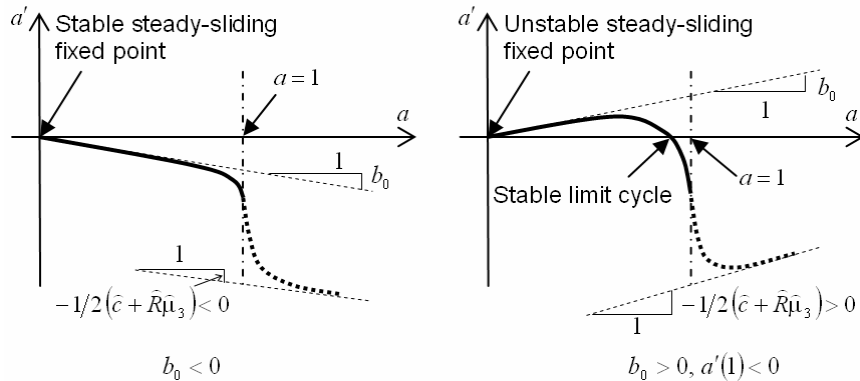


Figure D-3: Schematic plots of amplitude equation for Case II.

C.3 Case III: $\mu_2 > 0 \wedge \mu_3 \leq 0$

Similar to the previous case, for low velocities satisfying

$$0 \leq \omega < \omega_b \quad (\text{D.9})$$

where ω_b is the solution of $(r_2 - 1)\widehat{\mu}_3 + \widehat{\mu}_2\omega r_0 - r_2\widehat{\mu}_1\omega r_1 - r_2\widehat{\mu}_2\omega(r_0 + r_1) = 0$, (5.61) is satisfied for any $c \geq 0$. Thus, the trivial solution is stable. From (D.9), we have

$$(r_2 - 1)\widehat{\mu}_3 + r_0\widehat{\mu}_2\omega - r_1r_2\widehat{\mu}_1\omega - (r_0 + r_1)r_2\widehat{\mu}_2\omega < 0 \quad (\text{D.10})$$

which yields, $b_0 < 0$. Multiplying (D.10) by r_0^{2n} yields,

$$r_0^{2n}(r_2 - 1)\widehat{\mu}_3 - r_0^{2n}r_1r_2\widehat{\mu}_1\omega - r_0^{2n}(r_0 + r_1)r_2\widehat{\mu}_2\omega + r_0^{2n+1}\widehat{\mu}_2\omega < 0$$

Since $r_0^{2n} < (r_0 + r_1)^{2n}$, $r_0^{2n} < r_1^{2n}$, $(r_2 - 1)r_0^{2n} - r_2(2n + 1)r_1^{2n} < 0$, and $\widehat{\mu}_3 < 0$, from the above inequality one finds

$$r_2\widehat{\mu}_3(2n + 1)r_1^{2n} - r_2r_1^{2n+1}\widehat{\mu}_1\omega - (r_0 + r_1)^{2n+1}r_2\widehat{\mu}_2\omega + \widehat{\mu}_2r_0^{2n+1}\omega < 0$$

Consequently, from (D.4) it is obvious that $b_n < 0$. Thus (D.2) has no other solutions.

When $\omega > \omega_b$, the trivial solution is stable if

$$\widehat{c} > \widehat{R}((r_2 - 1)\widehat{\mu}_3 + \widehat{\mu}_2\omega r_0 - r_2\widehat{\mu}_1\omega r_1 - r_2\widehat{\mu}_2\omega(r_0 + r_1)) \quad (\text{D.11})$$

If (D.11) holds $b_0 < 0$ otherwise $b_0 > 0$. Note that $r_2 = e^{-r\omega}$ is small for $\omega > \omega_b$. For sufficiently large $\widehat{\mu}_2$, say $\widehat{\mu}_2 > \widehat{\mu}_2^*$, there exists $N > 1$ such that for $1 < n \leq N$,

$$\widehat{\mu}_2r_0^{2n+1} > -r_2\widehat{\mu}_3(2n + 1)r_1^{2n} + r_2\widehat{\mu}_1r_1^{2n+1} + r_2\widehat{\mu}_2(r_0 + r_1)^{2n+1}$$

and

$$\widehat{\mu}_2r_0^{2n+1} < -r_2\widehat{\mu}_3(2n + 1)r_1^{2n} + r_2\widehat{\mu}_1r_1^{2n+1} + r_2\widehat{\mu}_2(r_0 + r_1)^{2n+1}$$

for $n > N$. As a result, the first few b_n 's are dominated by $\frac{\omega^{2n}\widehat{R}\widehat{\mu}_2\omega r_0^{2n+1}}{2^{2n+1}n!(n+1)!}$ and are positive. As n

grows, the other terms (all negative) will dominate the positive term and change the sign of b_k to

negative. Hence, depending on the parameters values, one the following three scenarios may occur;

Scenario 1: If (D.11) holds and $\hat{\mu}_2 > \hat{\mu}_2^*$, then the polynomial equation given by (D.2) has two sign changes in its coefficients. According to Descartes' Rule of Signs, for the first case, (D.2) can have either two or zero positive roots. Typical plots of a' as a function of a are shown in Figure D-4. Note that similar to the previous case, for parameter values such that $a'(1) > 0$, the amplitude of the stable limit cycle can be greater than 1.

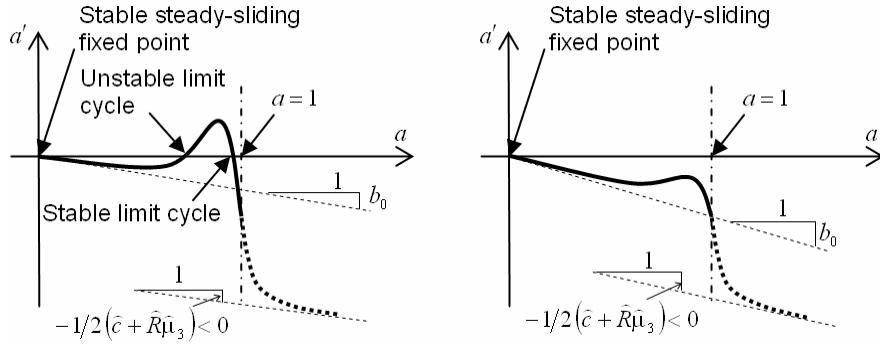


Figure D-4: Schematic plots of amplitude equation for Case III - Scenario 1.

The lead screw damping may act as the deciding factor between the above situations. A typical plot of (D.2) is shown in Figure D-5 for the case where two positive roots exist. Since the polynomial equation for y (*i.e.* (D.2)) is continuous, according to the mean-value theorem there is a maximum between the two roots and if this value for $b_0 = 0$ is y_{\max} (which is a finite number), the condition for non-existence of non-trivial solutions (*i.e.* no limit cycles) is

$$b_0 < -y_{\max}$$

or

$$\hat{c} > \hat{c}_2 = \hat{c}_1 + 2y_{\max} > \hat{c}_1 > 0 \quad (\text{D.12})$$

where $\hat{c}_1 = \Omega \hat{R} [(r_2 - 1)\hat{\mu}_3 + \hat{\mu}_2 r_0 - r_2 \hat{\mu}_1 r_1 - r_2 \hat{\mu}_2 (r_0 + r_1)]$.

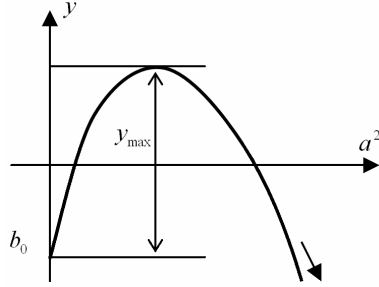


Figure D-5: The case of two positive zeros of (D.2)

Scenario 2: If (D.11) holds and $\bar{\mu}_2 < \bar{\mu}_2^*$, then the polynomial equation given by (D.2) has no sign changes. As a result, the trivial solution is stable and there are no non-trivial solutions. A typical plot of a' as a function of a are similar to the one shown in Figure D-2.

Scenario 3: If (D.11) does not hold, then the polynomial equation given by (D.2) has only one sign change. As a result, there is a non-trivial solution. In this case, the trivial solution is unstable and there is a stable limit cycle. A typical plot of a' as a function of a is shown in Figure D-6.

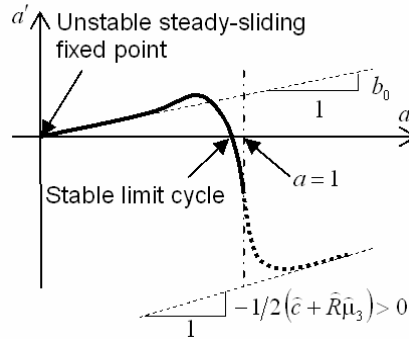


Figure D-6: Schematic plot of amplitude equation for Case III - Scenario 3.

C.4 Case IV: $\mu_2 > 0 \wedge \mu_3 > 0$

Similar to the previous case for velocities satisfying (D.9), the trivial fixed point is stable and there are no other solutions. In addition to the above condition, if

$$\omega > \omega_m \approx -\frac{1}{r_0} \ln\left(\frac{\mu_3}{r_0 \mu_2}\right) \quad (\text{D.13})$$

then (5.61) is satisfied for any $c \geq 0$, which implies that the trivial solution is stable.

For $\omega > \omega_b$ and for sufficiently large $\widehat{\mu}_2$, $\exists N_1, N_2$, $N_2 > N_1 \geq 1$ such that

$$1 \leq n \leq N_1 \rightarrow r_2 \widehat{\mu}_3 (2n+1) r_1^{2n} + \widehat{\mu}_2 r_0^{2n+1} > r_2 \widehat{\mu}_1 r_1^{2n+1} + r_2 \widehat{\mu}_2 (r_0 + r_1)^{2n+1} \rightarrow b_n > 0$$

$$N_1 < n \leq N_2 \rightarrow r_2 \widehat{\mu}_3 (2n+1) r_1^{2n} + \widehat{\mu}_2 r_0^{2n+1} < r_2 \widehat{\mu}_1 r_1^{2n+1} + r_2 \widehat{\mu}_2 (r_0 + r_1)^{2n+1} \rightarrow b_n < 0$$

For the first few terms, b_n 's are dominated by $\frac{\omega^{2n} \widehat{R} \widehat{\mu}_2 \omega r_0^{2n+1}}{2^{2n+1} n! (n+1)!}$ term which is positive. As n grows,

the negative terms grow faster and change the sign of b_n 's to negative. For even higher values of n more sign changes are possible; however, the polynomial coefficients become exceedingly small for large n and the associated roots will be well outside the applicable region of the approximations.

Based on the above argument, for $\omega > \omega_m$ or for $\omega_b < \omega < \omega_m$ when c is large enough to satisfy (5.61), the equation given by (D.2) has at least two sign changes in its coefficients, resulting in either two or zero *valid* non-trivial solutions. Similar to the argument in Section C.3, the damping value may act as a deciding factor between these two cases. In other words, for sufficiently large damping, no non-trivial solution exists. A typical plot of a' as a function of a is shown in Figure D-4. Finally for $\omega_b < \omega < \omega_m$, if c does not satisfy (5.61), the equation given by (D.2) has at least one sign change in its coefficients, resulting in one non-trivial solution. A typical plot of a' as a function of a is shown in Figure D-6.

C.5 Numerical Examples

In Chapter 5, numerical examples were presented that focus on the accuracy of the vibration amplitude prediction from averaging as well as the effect of friction parameters. The parameter values used were taken from the experimental case study of Chapter 4 and correspond to the cases II and III in Figure D-1 and Sections D.2 and D.3 of this appendix. Here, numerical examples are presented that also cover case IV. In the bifurcation plots presented, input constant angular velocity, ω , is taken as the control parameter. Instead of a , $\alpha = (\omega/\Omega)a$ is plotted versus the control parameter to better demonstrate the evolution of non-trivial solution in terms the original system vibration amplitudes. Parameter values not given in the examples are taken from Table 5-2 and are listed Table C-1 for ease of reference.

Table C-1: Parameter values used in the simulations

Parameter	Value	Parameter	Value
d_m	10.37 mm	μ_1	0.2
λ	5.57°	r_0	0.25 rad/s
I	$3.12 \times 10^{-6} \text{ kg.m}^2$	r_1	2 rad/s
k	1 N.m/rad	ω	0-40 rad/s
m	1kg	R	100 N

Results of the first example are shown in Figure D-7. In this example $\mu_3 = 0$ and three different values are considered for μ_2 . The lead screw support damping is chosen as $c = 1 \times 10^{-4} \text{ (N.m.rad/s)}$. For each value of μ_2 , the coefficient of friction as a function of relative angular velocity is plotted in Figure D-7(left). As shown in the steady-state vibration amplitude plots in Figure D-7(right), for the selected damping value, as friction reaches its maximum the gradient becomes negative ($\omega > \omega_b$) the trivial solution loses its stability and a stable limit cycle emerges.

For the three values of μ_2 selected, 0.01, 0.05, and 0.1, ω_b is found to be 2.92, 2.08, and 1.76 (rad/s), respectively. These values are in agreement with (D.9). For smaller values of μ_2 , the region of instability of the trivial solution is smaller. As shown in the close-up view, larger values of μ_2 result in stable amplitude of vibration closer to the limiting value (for the validity of approximations) of $a_{\max} = 1$ (or $\alpha_{\max} = \omega/\Omega$), where Ω is the natural frequency of the unperturbed system given by (5.24). For even larger values of μ_2 (not shown), the non-trivial solution of the amplitude equation (corresponding to the stable limit cycle), (5.58), becomes greater than 1 and is inadmissible due to violation of the approximating assumptions. In these cases, $O(\epsilon)$ accurate averaging results can be found by using (5.45) or (5.48) and carrying on the integrations numerically.

It is interesting to note that in this example as well as the two examples that follow, as ω is gradually increased, the trivial fixed point first goes through a supercritical pitchfork bifurcation and then a subcritical pitchfork bifurcation at a higher velocity. These bifurcations in the amplitude equation correspond to Hopf-bifurcations of the original equation. Figure D-8 shows results for $\mu_2 = 0.1$ and $\mu_3 = -4 \times 10^{-4}$ for three different values of lead screw damping.

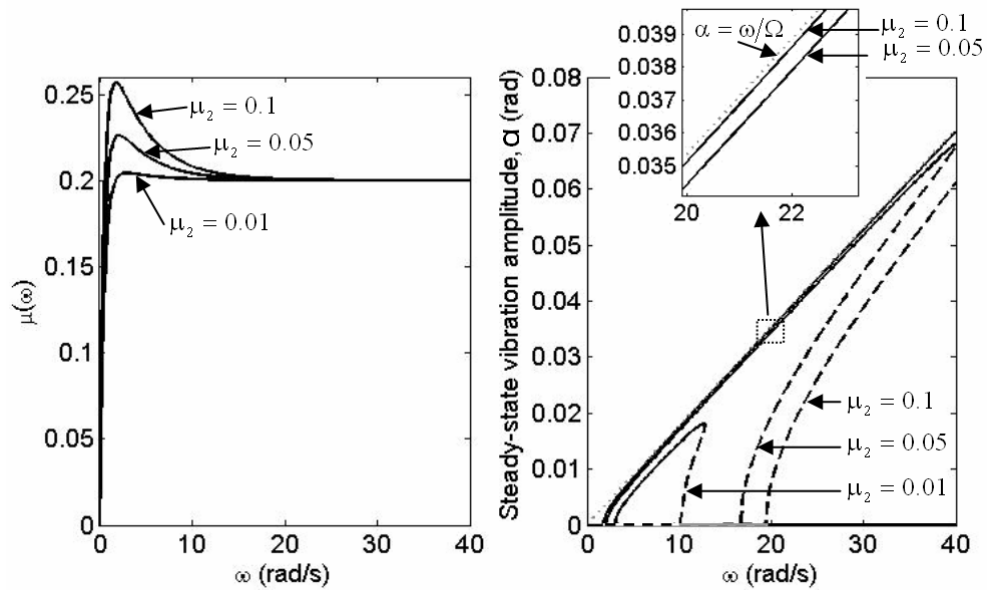


Figure D-7: First example, $\mu_3 = 0$, $c = 10^{-4}$.
 Left - variation of the coefficient of friction with velocity;
 Right - variation of steady-state vibration amplitude with input angular velocity

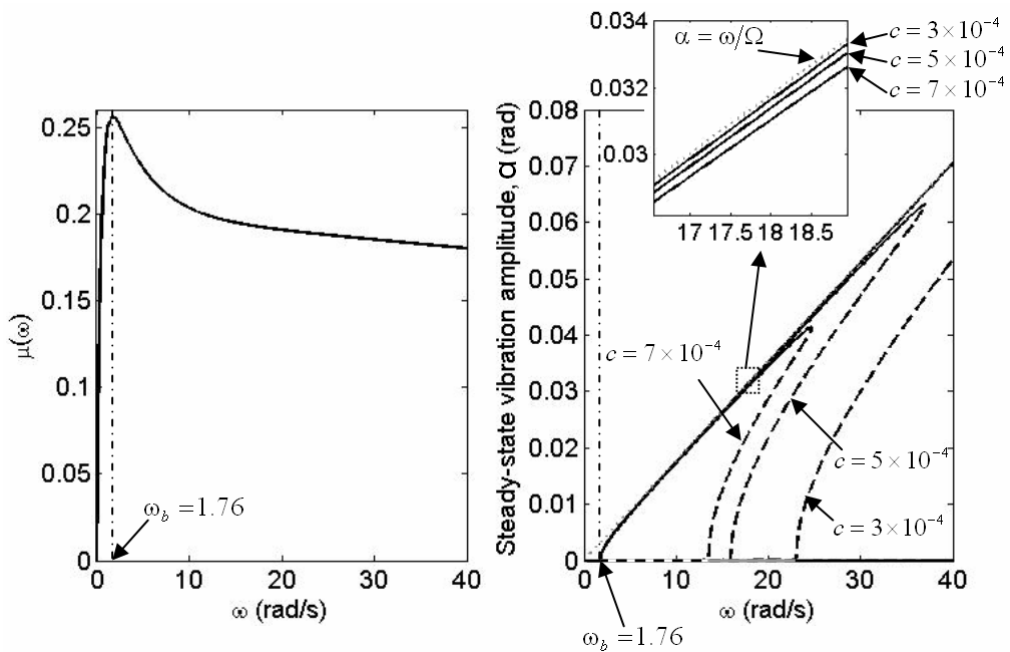


Figure D-8: Second example, $\mu_2 = 0.1$, $\mu_3 = -5 \times 10^{-4}$.
 Left - variation of the coefficient of friction with velocity;
 Right - variation of steady-state vibration amplitude with input angular velocity

As expected, the trivial solution becomes unstable as ω becomes greater than $\omega_b = 1.76$. As shown, increasing the damping decreases the region of instability of the origin.

Figure D-9 shows results for $\mu_2 = 0.1$ and $\mu_3 = 4 \times 10^{-4}$ for three different values of lead screw damping. As expected, the trivial solution becomes unstable as ω becomes greater than $\omega_b = 1.76$. Moreover, for $c = 0$ the trivial solution becomes stable again when $\omega > \omega_m = 15.68$. Note that from (D.13), one finds $\omega_m \approx 15.65$. At higher values of c , the trivial solution becomes stable at lower velocities. As shown, increasing the damping decreases the region of instability of the origin and decreases the amplitude of stable periodic vibration.

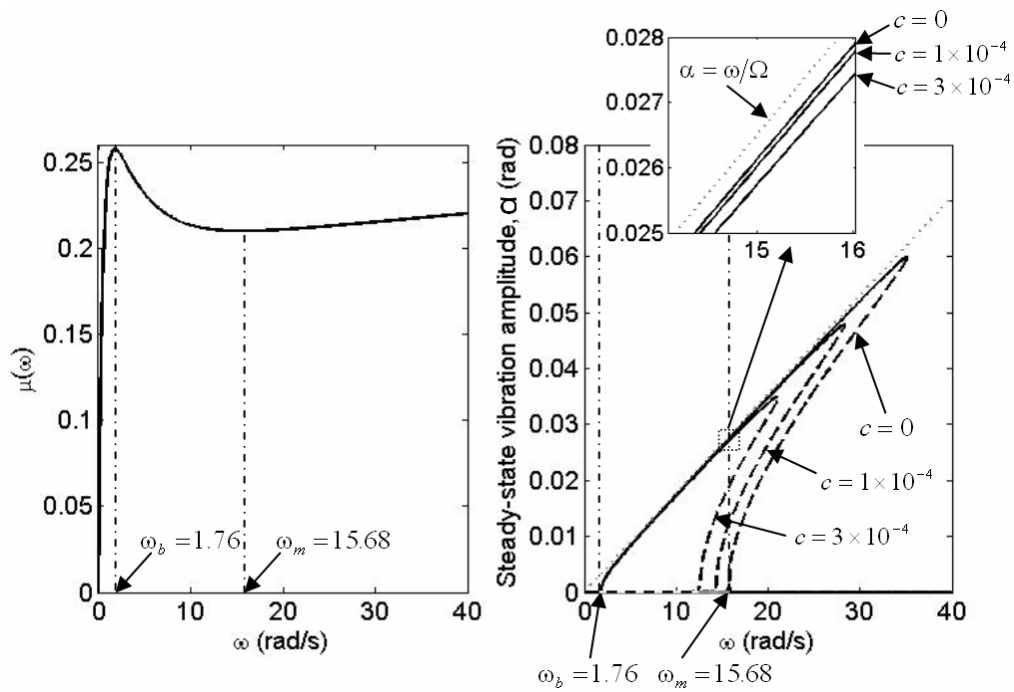


Figure D-9: Third example, $\mu_2 = 0.1$, $\mu_3 = 5 \times 10^{-4}$.
Left - variation of the coefficient of friction with velocity;
Right - variation of steady-state vibration amplitude with input angular velocity

Appendix E

Higher-order Averaging

The accuracy of the results obtained in Section 5.3 depends heavily on the “size” of the system parameters. In practical applications, such as the experimental example of Chapter 4, the $O(\varepsilon)$ error of the first order averaging may not be sufficiently accurate for the entire range of parameters in the domain of interest. A possible way to improve the accuracy of the amplitude and frequency estimates is to extend the averaging to higher orders.

A slightly different approach to finding the equation of motion in standard form is used here. In Section E.1, the approximate system’s equation accurate to $O(\varepsilon^4)$ is derived. The steps needed to carry out the averaging process up to the third order are presented in Section E.2. In Section E.3, a numerical example is presented that compares averaging results with numerical simulation results and actual measurements.

E.1 Equation of Motion in Standard Form

Two simplifying assumptions made in Chapter 5 to reach the averaged equation (5.54) – namely, the contact force does not change sign and lead screw velocity does not change sign. These assumptions are made here from the start to ensure the equations have the required smoothness properties. For simplicity here the analysis is limited to the case of $R > 0$ (thus $N > 0$) and $\omega > 0$ (thus $\dot{\theta} > 0$). Starting from (5.33)

$$\begin{aligned} v'' + \varepsilon[1 - \varepsilon\Xi_1(v, v', \varepsilon)\widehat{m}]^{-1}\widehat{c}v' + [1 - \varepsilon\Xi_1(v, v', \varepsilon)\widehat{m}]^{-1}v \\ = \varepsilon\widehat{R}[1 - \varepsilon\Xi_1(v, v', \varepsilon)\widehat{m}]^{-1}[\Xi_0(\varepsilon) - \Xi_1(v, v', \varepsilon)] \end{aligned} \quad (\text{E.1})$$

where $\Xi_0(\varepsilon)$ and $\Xi_1(v, v', \varepsilon)$ are given by (5.34) and (5.35), respectively. The above assumptions simplify these functions to

$$\Xi_0(\varepsilon) = \frac{\widehat{\mu}_0 - 1}{1 + \varepsilon^2 \widehat{\mu}_0} \quad (\text{E.2})$$

$$\Xi_1(v', \varepsilon) = \frac{\widehat{\mu}(v') - 1}{1 + \varepsilon^2 \widehat{\mu}(v')} \quad (\text{E.3})$$

where $\widehat{\mu}(v')$ is obtained from (5.36)

$$\widehat{\mu}(v') = (\widehat{\mu}_1 + \widehat{\mu}_2 e^{-r_0 \omega(v'+1)} + \widehat{\mu}_3 \omega(v'+1)) (1 - e^{-r_1 \omega(v'+1)}) \quad (\text{E.4})$$

$\Xi_0(\varepsilon)$ and $\Xi_1(v', \varepsilon)$ can be expanded in powers of ε as

$$\Xi_0(\varepsilon) = (\widehat{\mu}_0 - 1)(1 - \varepsilon^2 \widehat{\mu}_0^2) + O(\varepsilon^4) \quad (\text{E.5})$$

$$\Xi_1(v', \varepsilon) = (\widehat{\mu} - 1)(1 - \varepsilon^2 \widehat{\mu}^2) + O(\varepsilon^4) \quad (\text{E.6})$$

Also

$$\begin{aligned} \left(1 - \varepsilon \frac{\widehat{\mu} - 1}{1 + \varepsilon^2 \widehat{\mu}} \widehat{m}\right)^{-1} &= 1 + \varepsilon(\widehat{\mu} - 1)\widehat{m} + \varepsilon^2(\widehat{\mu} - 1)^2 \widehat{m}^2 + \varepsilon^3(\widehat{\mu} - 1)^3 \widehat{m}^3 \\ &\quad - \varepsilon^3 \widehat{\mu}(\widehat{\mu} - 1)\widehat{m} + O(\varepsilon^4) \end{aligned} \quad (\text{E.7})$$

Substituting (E.5), (E.6), and (E.7) into (E.1) and keeping terms up to $O(\varepsilon^3)$ gives

$$v'' + v = \varepsilon f_1(v, v') + \varepsilon^2 f_2(v, v') + \varepsilon^3 f_3(v, v') \quad (\text{E.8})$$

where

$$f_1(v, v') = -\widehat{c}v' - (\widehat{\mu} - 1)\widehat{m}v + \widehat{R}(\widehat{\mu}_0 - \widehat{\mu}) \quad (\text{E.9})$$

$$f_2(v, v') = -(\widehat{\mu} - 1)\widehat{m}\widehat{c}v' - (\widehat{\mu} - 1)^2 \widehat{m}^2 v + \widehat{R}(\widehat{\mu} - 1)(\widehat{\mu}_0 - \widehat{\mu})\widehat{m} \quad (\text{E.10})$$

$$\begin{aligned} f_3(v, v') &= -(\widehat{\mu} - 1)^2 \widehat{m}^2 \widehat{c}v' - (\widehat{\mu} - 1)^3 \widehat{m}^3 v + \widehat{R}(\widehat{\mu} - 1)^2 (\widehat{\mu}_0 - \widehat{\mu})\widehat{m}^2 \\ &\quad + \widehat{\mu}(\widehat{\mu} - 1)\widehat{m}v - \widehat{R}[\widehat{\mu}_0^2 (\widehat{\mu}_0 - 1) - \widehat{\mu}^2 (\widehat{\mu} - 1)] \end{aligned} \quad (\text{E.11})$$

Unfortunately, the expressions involved become too cumbersome to be of any practical use in closed-form. However, if approached numerically, these higher order approximations can be used to

estimate the amplitude of the steady-state vibrations, efficiently.

E.2 Higher-order Averaging Formulation

In this appendix, following [104] the general formulations of first, second, and third order averaging are derived for a system of differential equations in standard form

$$\dot{\mathbf{x}} = \varepsilon \mathbf{X}_1(t, \mathbf{x}) + \varepsilon^2 \mathbf{X}_2(t, \mathbf{x}) + \varepsilon^3 \mathbf{X}_3(t, \mathbf{x}) \quad (\text{E.12})$$

where

$$\mathbf{x} = \begin{Bmatrix} a \\ \beta \end{Bmatrix} \quad (\text{E.13})$$

$$\mathbf{X}_i = \begin{Bmatrix} X_{i1} \\ X_{i2} \end{Bmatrix} \quad (\text{E.14})$$

To clarify the notations, the following expressions are given here

$$\nabla \mathbf{X}_i(t, \xi) = \nabla_{\xi} \mathbf{X}_i(t, \xi) = \begin{bmatrix} \frac{\partial X_{i1}}{\partial a} & \frac{\partial X_{i1}}{\partial \beta} \\ \frac{\partial X_{i2}}{\partial a} & \frac{\partial X_{i2}}{\partial \beta} \end{bmatrix} \quad (\text{E.15})$$

and

$$\nabla^2 X_{ij}(t, \xi) = \begin{bmatrix} \frac{\partial^2 X_{ij}}{\partial a^2} & \frac{\partial^2 X_{ij}}{\partial a \partial \beta} \\ \frac{\partial^2 X_{ij}}{\partial \beta \partial a} & \frac{\partial^2 X_{ij}}{\partial \beta^2} \end{bmatrix} \quad (\text{E.16})$$

E.2.1 First Order Averaging

Introducing the following *near-identity transform*

$$\mathbf{x} = \xi + \varepsilon \mathbf{F}_1(t, \xi) \quad (\text{E.17})$$

where ξ is the solution of

$$\dot{\xi} = \varepsilon \mathbf{P}_1(\xi) \quad (\text{E.18})$$

where \mathbf{F}_1 and \mathbf{P}_1 are unknown functions to be determined. Substituting (E.17) into (E.12) (neglecting ε^2 and ε^3 terms)

$$\frac{d}{dt}(\xi + \varepsilon \mathbf{F}_1(t, \xi)) = \varepsilon \mathbf{X}_1(t, \xi + \varepsilon \mathbf{F}_1(t, \xi))$$

expanding RHS using Taylor series expansion and substituting (E.18) gives

$$\varepsilon \mathbf{P}_1 + \varepsilon \frac{\partial \mathbf{F}_1}{\partial t} + \varepsilon^2 \nabla \mathbf{F}_1 \cdot \mathbf{P}_1 = \varepsilon \mathbf{X}_1 + \varepsilon^2 \nabla \mathbf{X}_1 \cdot \mathbf{F}_1$$

Neglecting ε^2 terms

$$\frac{\partial \mathbf{F}_1(t, \xi)}{\partial t} = \mathbf{X}_1(t, \xi) - \mathbf{P}_1(\xi) \quad (\text{E.19})$$

The solution to this equation can be written as

$$\mathbf{P}_1(\xi) = \frac{1}{T} \int_0^T \mathbf{X}_1(t, \xi) dt \quad (\text{E.20})$$

Substituting (E.20) into (E.19) and integrating

$$\mathbf{F}_1(t, \xi) = \int_0^t [\mathbf{X}_1(\tau, \xi) - \mathbf{P}_1(\xi)] d\tau + \mathbf{a}_1(\xi) \quad (\text{E.21})$$

where following [35], $\mathbf{a}_1(\xi)$ is chosen such that $\mathbf{F}_1(t, \xi)$ has a zero mean

$$\mathbf{a}_1(\xi) = \frac{1}{T} \int_0^T \int_0^t [\mathbf{X}_1(\tau, \xi) - \mathbf{P}_1(\xi)] d\tau dt \quad (\text{E.22})$$

It can be shown that the solution of (E.18) remains $O(\varepsilon)$ close to the solution of the original differential equation (E.12) on a time scale of $O(1/\varepsilon)$, *i.e.*

$$\|\mathbf{x}(t) - \xi(t)\| \leq k\varepsilon, \quad \forall 0 \leq t \leq \frac{L}{\varepsilon} \quad (\text{E.23})$$

for some $k > 0$ and $L > 0$.

E.2.2 Second Order Averaging

The near-identity transform is modified to

$$\mathbf{x} = \boldsymbol{\xi} + \varepsilon \mathbf{F}_1(t, \boldsymbol{\xi}) + \varepsilon^2 \mathbf{F}_2(t, \boldsymbol{\xi}) \quad (\text{E.24})$$

where $\boldsymbol{\xi}$ is the solution of

$$\dot{\boldsymbol{\xi}} = \varepsilon \mathbf{P}_1(\boldsymbol{\xi}) + \varepsilon^2 \mathbf{P}_2(\boldsymbol{\xi}) \quad (\text{E.25})$$

where \mathbf{F}_1 and \mathbf{P}_1 are defined as before, and \mathbf{F}_2 and \mathbf{P}_2 are unknown functions to be determined.

Substituting (E.24) into (E.12) (neglecting ε^3 terms)

$$\begin{aligned} \frac{d}{dt}(\boldsymbol{\xi} + \varepsilon \mathbf{F}_1(t, \boldsymbol{\xi}) + \varepsilon^2 \mathbf{F}_2(t, \boldsymbol{\xi})) &= \varepsilon \mathbf{X}_1(t, \boldsymbol{\xi} + \varepsilon \mathbf{F}_1(t, \boldsymbol{\xi}) + \varepsilon^2 \mathbf{F}_2(t, \boldsymbol{\xi})) \\ &\quad + \varepsilon^2 \mathbf{X}_2(t, \boldsymbol{\xi} + \varepsilon \mathbf{F}_1(t, \boldsymbol{\xi}) + \varepsilon^2 \mathbf{F}_2(t, \boldsymbol{\xi})) \end{aligned}$$

Expanding the RHS using Taylor series expansion

$$\begin{aligned} \dot{\boldsymbol{\xi}} + \varepsilon \frac{\partial \mathbf{F}_1}{\partial t} + \varepsilon \nabla \mathbf{F}_1 \cdot \dot{\boldsymbol{\xi}} + \varepsilon^2 \frac{\partial \mathbf{F}_2}{\partial t} + \varepsilon^2 \nabla \mathbf{F}_2 \cdot \dot{\boldsymbol{\xi}} &= \varepsilon \mathbf{X}_1 + \varepsilon^2 \nabla \mathbf{X}_1 \cdot \mathbf{F}_1 + \varepsilon^3 \nabla \mathbf{X}_1 \cdot \mathbf{F}_2 \\ &\quad + \varepsilon^3 \left[\begin{aligned} &[\mathbf{F}_1 + \varepsilon \mathbf{F}_2]^T \nabla^2 X_{11} [\mathbf{F}_1 + \varepsilon \mathbf{F}_2] \\ &[\mathbf{F}_1 + \varepsilon \mathbf{F}_2]^T \nabla^2 X_{12} [\mathbf{F}_1 + \varepsilon \mathbf{F}_2] \end{aligned} \right] \\ &\quad + \varepsilon^2 \mathbf{X}_2 + \varepsilon^3 \nabla \mathbf{X}_2 \cdot \mathbf{F}_1 \end{aligned}$$

Substituting (E.25) and neglecting ε^3 terms

$$\mathbf{P}_2 + \nabla \mathbf{F}_1 \cdot \mathbf{P}_1 + \frac{\partial \mathbf{F}_2}{\partial t} = \nabla \mathbf{X}_1 \cdot \mathbf{F}_1 + \mathbf{X}_2 \quad (\text{E.26})$$

The solution to (E.26) can be written as

$$\mathbf{P}_2(\boldsymbol{\xi}) = \frac{1}{T} \int_0^T [\nabla \mathbf{X}_1(t, \boldsymbol{\xi}) \cdot \mathbf{F}_1(t, \boldsymbol{\xi}) - \nabla \mathbf{F}_1(t, \boldsymbol{\xi}) \cdot \mathbf{P}_1(\boldsymbol{\xi}) + \mathbf{X}_2(t, \boldsymbol{\xi})] dt$$

or since $\nabla \mathbf{F}_1(t, \boldsymbol{\xi}) \cdot \mathbf{P}_1(\boldsymbol{\xi})$ has a zero mean

$$\mathbf{P}_2 = \frac{1}{T} \int_0^T [\nabla \mathbf{X}_1(t, \xi) \cdot \mathbf{F}_1(t, \xi) + \mathbf{X}_2(t, \xi)] dt \quad (\text{E.27})$$

where $\mathbf{F}_1(t, \xi)$ is given by (E.21). Subsequently, integrating (E.26) gives

$$\mathbf{F}_2(t, \xi) = \int_0^t [\nabla \mathbf{X}_1(\tau, \xi) \cdot \mathbf{F}_1(\tau, \xi) - \nabla \mathbf{F}_1(\tau, \xi) \cdot \mathbf{P}_1(\xi) + \mathbf{X}_2(\tau, \xi) - \mathbf{P}_2(\xi)] d\tau + \mathbf{a}_2(\xi) \quad (\text{E.28})$$

where $\mathbf{a}_2(\xi)$ is chosen such that $\mathbf{F}_2(t, \xi)$ has zero mean

$$\mathbf{a}_2(\xi) = \frac{1}{T} \int_0^T \int_0^t [\nabla \mathbf{X}_1(\tau, \xi) \cdot \mathbf{F}_1(\tau, \xi) - \nabla \mathbf{F}_1(\tau, \xi) \cdot \mathbf{P}_1(\xi) + \mathbf{X}_2(\tau, \xi) - \mathbf{P}_2(\xi)] d\tau dt \quad (\text{E.29})$$

It can be shown that given $\xi(t)$ to be the solution of (E.25)

$$\|\mathbf{x}(t) - \xi(t) - \varepsilon \mathbf{F}_1(t, \xi(t))\| = O(\varepsilon^2) \quad (\text{E.30})$$

for time $O(1/\varepsilon)$.

E.2.3 Third Order Averaging

Similar to the previous section, the near-identity transform is now defined as

$$\mathbf{x} = \xi + \varepsilon \mathbf{F}_1(t, \xi) + \varepsilon^2 \mathbf{F}_2(t, \xi) + \varepsilon^3 \mathbf{F}_3(t, \xi) \quad (\text{E.31})$$

where ξ is the solution of

$$\dot{\xi} = \varepsilon \mathbf{P}_1(\xi) + \varepsilon^2 \mathbf{P}_2(\xi) + \varepsilon^3 \mathbf{P}_3(\xi) \quad (\text{E.32})$$

where \mathbf{F}_1 , \mathbf{F}_2 and \mathbf{P}_1 , \mathbf{P}_2 are defined as Section E.2 and \mathbf{F}_3 and \mathbf{P}_3 are unknown functions to be determined. Substituting (E.31) into (E.12)

$$\begin{aligned} \frac{d}{dt} (\xi + \varepsilon \mathbf{F}_1(t, \xi) + \varepsilon^2 \mathbf{F}_2(t, \xi) + \varepsilon^3 \mathbf{F}_3(t, \xi)) &= \varepsilon \mathbf{X}_1(t, \xi + \varepsilon \mathbf{F}_1(t, \xi) + \varepsilon^2 \mathbf{F}_2(t, \xi) + \varepsilon^3 \mathbf{F}_3(t, \xi)) \\ &\quad + \varepsilon^2 \mathbf{X}_2(t, \xi + \varepsilon \mathbf{F}_1(t, \xi) + \varepsilon^2 \mathbf{F}_2(t, \xi) + \varepsilon^3 \mathbf{F}_3(t, \xi)) \\ &\quad + \varepsilon^3 \mathbf{X}_3(t, \xi + \varepsilon \mathbf{F}_1(t, \xi) + \varepsilon^2 \mathbf{F}_2(t, \xi) + \varepsilon^3 \mathbf{F}_3(t, \xi)) \end{aligned}$$

Expanding the RHS using Taylor series expansion

$$\begin{aligned}
& \dot{\xi} + \varepsilon \frac{\partial \mathbf{F}_1}{\partial t} + \varepsilon \nabla \mathbf{F}_1 \cdot \dot{\xi} + \varepsilon^2 \frac{\partial \mathbf{F}_2}{\partial t} + \varepsilon^2 \nabla \mathbf{F}_2 \cdot \dot{\xi} + \varepsilon^3 \frac{\partial \mathbf{F}_3}{\partial t} + \varepsilon^3 \nabla \mathbf{F}_3 \cdot \dot{\xi} \\
&= \varepsilon \mathbf{X}_1 + \varepsilon^2 \nabla \mathbf{X}_1 \cdot \mathbf{F}_1 + \varepsilon^3 \nabla \mathbf{X}_1 \cdot \mathbf{F}_2 \\
&+ \varepsilon^4 \nabla \mathbf{X}_1 \cdot \mathbf{F}_3 \\
&+ \frac{1}{2} \varepsilon^3 \left[\begin{array}{l} \left[\mathbf{F}_1 + \varepsilon \mathbf{F}_2 + \varepsilon^2 \mathbf{F}_3 \right]^T \nabla^2 X_{11} \left[\mathbf{F}_1 + \varepsilon \mathbf{F}_2 + \varepsilon^2 \mathbf{F}_3 \right] \\ \left[\mathbf{F}_1 + \varepsilon \mathbf{F}_2 + \varepsilon^2 \mathbf{F}_3 \right]^T \nabla^2 X_{12} \left[\mathbf{F}_1 + \varepsilon \mathbf{F}_2 + \varepsilon^2 \mathbf{F}_3 \right] \end{array} \right] \\
&+ \varepsilon^2 \mathbf{X}_2 + \varepsilon^3 \nabla \mathbf{X}_2 \cdot \mathbf{F}_1 + \varepsilon^4 \nabla \mathbf{X}_2 \cdot \mathbf{F}_2 + \varepsilon^5 \nabla \mathbf{X}_2 \cdot \mathbf{F}_3 \\
&+ \frac{1}{2} \varepsilon^4 \left[\begin{array}{l} \left[\mathbf{F}_1 + \varepsilon \mathbf{F}_2 + \varepsilon^2 \mathbf{F}_3 \right]^T \nabla^2 X_{21} \left[\mathbf{F}_1 + \varepsilon \mathbf{F}_2 + \varepsilon^2 \mathbf{F}_3 \right] \\ \left[\mathbf{F}_1 + \varepsilon \mathbf{F}_2 + \varepsilon^2 \mathbf{F}_3 \right]^T \nabla^2 X_{22} \left[\mathbf{F}_1 + \varepsilon \mathbf{F}_2 + \varepsilon^2 \mathbf{F}_3 \right] \end{array} \right] \\
&+ \varepsilon^3 \mathbf{X}_3 + \varepsilon^4 \nabla \mathbf{X}_3 \cdot \mathbf{F}_1 + \varepsilon^5 \nabla \mathbf{X}_3 \cdot \mathbf{F}_2 + \varepsilon^6 \nabla \mathbf{X}_3 \cdot \mathbf{F}_3
\end{aligned}$$

Substituting known functions \mathbf{F}_1 , \mathbf{F}_2 , \mathbf{P}_1 , and \mathbf{P}_2 and neglecting higher order terms, yields

$$\frac{\partial \mathbf{F}_3}{\partial t} = \nabla \mathbf{X}_1 \cdot \mathbf{F}_2 - \nabla \mathbf{F}_2 \cdot \mathbf{P}_1 + \nabla \mathbf{X}_2 \cdot \mathbf{F}_1 - \nabla \mathbf{F}_1 \cdot \mathbf{P}_2 + \mathbf{X}_3 - \mathbf{P}_3 + \frac{1}{2} \left[\begin{array}{l} \mathbf{F}_1^T \nabla^2 X_{11} \mathbf{F}_1 \\ \mathbf{F}_1^T \nabla^2 X_{12} \mathbf{F}_1 \end{array} \right] \quad (\text{E.33})$$

\mathbf{P}_3 is found to be

$$\mathbf{P}_3 = \frac{1}{T} \int_0^T \left\{ \nabla \mathbf{X}_1 \cdot \mathbf{F}_2 - \nabla \mathbf{F}_2 \cdot \mathbf{P}_1 + \nabla \mathbf{X}_2 \cdot \mathbf{F}_1 - \nabla \mathbf{F}_1 \cdot \mathbf{P}_2 + \mathbf{X}_3 + \frac{1}{2} \left[\begin{array}{l} \mathbf{F}_1^T \nabla^2 X_{11} \mathbf{F}_1 \\ \mathbf{F}_1^T \nabla^2 X_{12} \mathbf{F}_1 \end{array} \right] \right\} dt \quad (\text{E.34})$$

It can be shown that given $\xi(t)$ to be the solution of (E.32)

$$\| \mathbf{x}(t) - \xi(t) - \varepsilon \mathbf{F}_1(t, \xi(t)) - \varepsilon^2 \mathbf{F}_2(t, \xi(t)) \| = O(\varepsilon^3) \quad (\text{E.35})$$

for time $O(1/\varepsilon)$.

E.3 A Numerical Example

Here a numerical example is presented that is taken from the test results of Chapter 4. The parameter values are selected according to the sample simulation results/measurements depicted in Figure 4-16. The identified coupling stiffness, damping coefficient, and all of the friction parameters are given, for reference, in Table E-1. The applied axial force and input angular velocity values are also listed in this table.

Table E-1: Parameter values used in the higher order averaging example

Parameter	Value	Friction Parameter	Value
k	1.18 N.m/rad	μ_1	0.218
c	$19 \times 10^{-5} \text{ Nms/rad}$	μ_2	0.0203
		μ_3	$-4.47 \times 10^{-4} \text{ s/rad}$
Inputs	Value	r_0	0.38 <i>rad/s</i>
ω	35.6 <i>rad/s</i>	r_1	0.41 <i>rad/s</i>
R	153 <i>N</i>	s_μ	0.97

The results from the numerical averaging method are presented in Figure E-1. In Figure E-1(b), the measurements are compared with simulation results showing the accuracy of modeling and the identified parameters similar to Figure 4-16. In Figure E-1(a), the same simulation results are compared with the first, second, and third order averaging.

It can be seen that for the selected parameter values, the first order averaging has considerable error in predicting the steady-state amplitude of vibrations (a relative error of approximately 22%). The second order averaging results, on the other hand, show significant improvement in both predicting the steady-state vibration amplitude (relative error is approximately 5%) and conforming to the shape of the observed limit-cycle. The accuracy of the approximation is further improved, though only slightly, by the third order averaging which has approximately 4% relative error in predicting the amplitude of vibration.

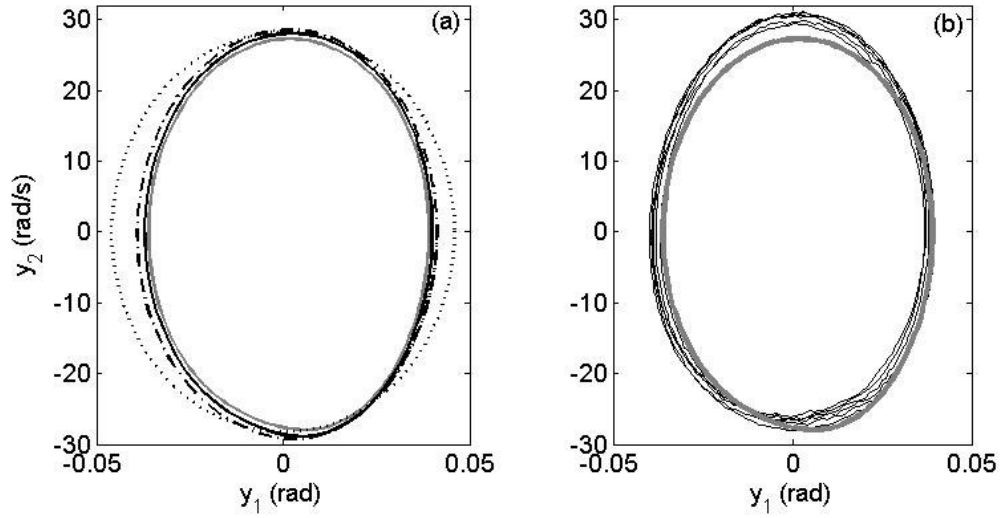


Figure E-1: First, second, and third order averaging results.
(a) Numerical averaging results; gray solid: nonlinear system equation; dotted black: first order averaging; dashed-dot: second order averaging; solid black: third order averaging,
(b) black: measurements; gray: simulation results

Appendix F

First-order Averaging Applied to the 2-DOF Lead Screw Model with Axially Compliant Supports

In this appendix, the method of first-order averaging is used to analyze the 2-DOF model of Section 3.6. The equations of motion are given by (3.29) and (3.30). Neglecting F_0 and T_0 for simplicity and repeating the transfer of coordinates done in Section 6.3;

$$\begin{aligned}\theta &= v_1 + \theta_i + u_{10} \\ x_1 &= r_m \tan \lambda v_2 + u_{20}\end{aligned}\tag{F.1}$$

where u_{10} and u_{20} are given by (6.53) and (6.54), respectively. After this change of variables, equations of motion in matrix form become

$$\mathbf{M}(\dot{v}_1)\ddot{v} + \mathbf{C}(\dot{v}_1)\dot{v} + \mathbf{K}(\dot{v}_1)v = \mathbf{f}(\dot{v}_1)\tag{F.2}$$

where

$$\mathbf{M} = \begin{bmatrix} I - \xi m r_m \tan \lambda & -\xi m r_m \tan \lambda \\ m & m + m_1 \end{bmatrix}\tag{F.3}$$

$$\mathbf{C} = \begin{bmatrix} c & 0 \\ 0 & c_1 \end{bmatrix}\tag{F.4}$$

$$\mathbf{K} = \begin{bmatrix} k & 0 \\ 0 & k_1 \end{bmatrix}\tag{F.5}$$

and

$$\mathbf{f} = \begin{bmatrix} (\xi_0 - \xi)R \\ 0 \end{bmatrix} \quad (\text{F.6})$$

Also

$$\xi(\mathbf{v}, \dot{\mathbf{v}}) = r_m \frac{\mu_s(\mathbf{v}, \dot{\mathbf{v}}) - \tan \lambda}{1 + \mu_s(\mathbf{v}, \dot{\mathbf{v}}) \tan \lambda} \quad (\text{F.7})$$

and

$$\mu_s(\mathbf{v}, \dot{\mathbf{v}}) = \mu(\dot{v}_1) \operatorname{sgn}(N(\mathbf{v}, \dot{\mathbf{v}})) \operatorname{sgn}(\dot{v}_1 + \omega) \quad (\text{F.8})$$

where the contact normal force is given by

$$N = \frac{\left(\frac{I}{m} + \frac{I}{m_1} - r_m \tan \lambda \xi_0 \right) R + r_m \tan \lambda \left(\frac{Ik_1}{m_1} v_2 + \frac{Ic_1}{m_1} \dot{v}_2 + kv_1 + c\dot{v}_1 \right)}{(\cos \lambda + \mu_s \sin \lambda) \left(\frac{I}{m} + \frac{I}{m_1} - r_m \tan \lambda \xi \right)} \quad (\text{F.9})$$

Assuming \mathbf{M} to be non-singular

$$\mathbf{M}^{-1} = \frac{1}{1 - r_m \tan \lambda \xi \frac{mm_1}{I(m+m_1)}} \begin{bmatrix} \frac{1}{I} & \frac{\xi mr_m \tan \lambda}{I(m+m_1)} \\ -\frac{m}{I(m+m_1)} & \frac{I - \xi mr_m \tan \lambda}{I(m+m_1)} \end{bmatrix} \quad (\text{F.10})$$

Multiplying both sides of (F.2) by \mathbf{M}^{-1} , one finds

$$\left(1 + r_m \tan \lambda \xi(\dot{v}_1) \frac{mm_1}{I(m+m_1)} \right) \ddot{\mathbf{v}} + \hat{\mathbf{C}}(\dot{v}_1) \dot{\mathbf{v}} + \hat{\mathbf{K}}(\dot{v}_1) \mathbf{v} = \hat{\mathbf{f}}(\dot{v}_1) \quad (\text{F.11})$$

where

$$\hat{\mathbf{C}} = \begin{bmatrix} \frac{c}{I} & \frac{c_1 \xi mr_m \tan \lambda}{I(m+m_1)} \\ -\frac{cm}{I(m+m_1)} & \frac{c_1(I - \xi mr_m \tan \lambda)}{I(m+m_1)} \end{bmatrix} \quad (\text{F.12})$$

$$\hat{\mathbf{K}} = \begin{bmatrix} \frac{k}{I} & \frac{k_1 \xi m r_m \tan \lambda}{I(m+m_1)} \\ -\frac{km}{I(m+m_1)} & \frac{k_1(I - \xi m r_m \tan \lambda)}{I(m+m_1)} \end{bmatrix} \quad (\text{F.13})$$

$$\hat{\mathbf{f}} = \begin{bmatrix} 1 \\ m \\ (m+m_1) \end{bmatrix} \frac{R}{I} (\xi - \xi_0) \quad (\text{F.14})$$

The two natural frequencies of the undamped unperturbed system are

$$\Omega_1 = \sqrt{\frac{k}{I}}, \Omega_2 = \sqrt{\frac{k_1}{m+m_1}} \quad (\text{F.15})$$

Let

$$\hat{m} = r_m^2 \tan \lambda \frac{m}{I} \quad (\text{F.16})$$

$$\hat{\mu}_s = \frac{\mu_s}{\tan \lambda} \quad (\text{F.17})$$

Taking $\varepsilon \equiv \tan \lambda$ as the *small* parameter, it is assumed that \hat{m} and $\hat{\mu}_s$ are $O(1)$ with respect to ε .

We can write the following asymptotic expansion for ξ

$$\xi = \varepsilon r_m (\hat{\mu}_s - 1) - \varepsilon^3 r_m \hat{\mu}_s (\hat{\mu}_s - 1) + \dots \quad (\text{F.18})$$

Also

$$\left(1 - \varepsilon \frac{\hat{m} m_1}{m+m_1} \frac{\hat{\mu}_s - 1}{1 + \varepsilon^2 \hat{\mu}_s} \right)^{-1} = 1 + \varepsilon \frac{\hat{m} m_1}{m+m_1} (\hat{\mu}_s - 1) + O(\varepsilon^3) \quad (\text{F.19})$$

Define the non-dimensionalized time as $\tau = \Omega_1 t$. Derivative with respect to τ is given by

$$\frac{d(\cdot)}{dt} = \Omega_1 \frac{d(\cdot)}{d\tau}, \quad (\cdot)' \equiv \frac{d(\cdot)}{d\tau} \quad (\text{F.20})$$

Also, limiting the analysis to weakly damped systems, take

$$\varepsilon \hat{c} = \frac{c}{I\Omega_1}, \quad \varepsilon \hat{c}_1 = \frac{c_1}{\Omega_1(m+m_1)} \quad (\text{F.21})$$

Assume $|\omega|/\Omega_1 = \rho\varepsilon$ where ρ is $O(1)$ with respect to ε . Let,

$$\mathbf{v} = \varepsilon \rho \mathbf{z} \quad (\text{F.22})$$

Substituting (F.15), (F.16), (F.17), (F.21), and (F.22) into (F.23) and using (F.18), (F.19), and (F.20) and truncating $O(\varepsilon^2)$ terms, yields

$$\mathbf{z}'' + \tilde{\mathbf{K}}_0 \mathbf{z} = -\varepsilon \tilde{\mathbf{C}}_1 \mathbf{z}' + \varepsilon \tilde{m}(1-\alpha)(1-\hat{\mu}_s) \tilde{\mathbf{K}}_0 \mathbf{z} - \varepsilon \tilde{\mathbf{K}}_1 \mathbf{z} + \varepsilon \tilde{\mathbf{f}}_0 \quad (\text{F.23})$$

where

$$\alpha = \frac{m}{m+m_1} \quad (\text{F.24})$$

$$\tilde{\mathbf{K}}_0 = \begin{bmatrix} 1 & 0 \\ -\alpha & \eta^2 \end{bmatrix} \quad (\text{F.25})$$

$$\tilde{\mathbf{K}}_1 = \eta^2(1-\hat{\mu}_s) \tilde{m} \begin{bmatrix} 0 & -1 \\ 0 & 1 \end{bmatrix} \quad (\text{F.26})$$

$$\tilde{\mathbf{C}}_1 = \begin{bmatrix} \hat{c} & 0 \\ -\alpha \hat{c} & \hat{c}_1 \end{bmatrix} \quad (\text{F.27})$$

$$\tilde{\mathbf{f}}_0 = \hat{R}(\hat{\mu}_0 \operatorname{sgn}(R\omega) - \hat{\mu}_s) \begin{bmatrix} 1 \\ -\alpha \end{bmatrix} \quad (\text{F.28})$$

where

$$\hat{R} = \frac{\Omega_1}{|\omega|} \frac{r_m R}{k} \quad (\text{F.29})$$

is considered to be $O(1)$ with respect to ε . Also, η is the ratio of the two natural frequencies

$$\eta = \frac{\Omega_2}{\Omega_1} \quad (\text{F.30})$$

Assuming the two natural frequencies of the unperturbed system are widely apart, let

$$\mathbf{T} = \begin{bmatrix} 1 & 0 \\ \alpha \frac{1}{\eta^2 - 1} & 1 \end{bmatrix} \quad (\text{F.31})$$

then

$$\mathbf{\Omega}^2 = \mathbf{T}^{-1} \hat{\mathbf{K}}_0 \mathbf{T} = \begin{bmatrix} 1 & 0 \\ 0 & \eta^2 \end{bmatrix} \quad (\text{F.32})$$

Let $\mathbf{z} = \mathbf{T}\mathbf{w}$, systems' equations (F.23) are transformed to

$$\mathbf{w}'' + \mathbf{\Omega}^2 \mathbf{w} = -\varepsilon \mathbf{T}^{-1} \tilde{\mathbf{C}}_1 \mathbf{T} \mathbf{w}' + \varepsilon \hat{m} (1 - \alpha) (1 - \hat{\mu}_s) \mathbf{\Omega}^2 \mathbf{w} - \varepsilon \mathbf{T}^{-1} \tilde{\mathbf{K}}_1 \mathbf{T} \mathbf{w} + \varepsilon \mathbf{T}^{-1} \tilde{\mathbf{f}}_0 \quad (\text{F.33})$$

Finally, let¹

$$\mathbf{w} = \begin{bmatrix} y_1 \cos \tau - y_2 \sin \tau \\ y_3 \cos \eta \tau - \eta^{-1} y_4 \sin \eta \tau \end{bmatrix}, \quad \mathbf{w}' = \begin{bmatrix} -y_1 \sin \tau - y_2 \cos \tau \\ -\eta y_3 \sin \eta \tau - y_4 \cos \eta \tau \end{bmatrix} \quad (\text{F.34})$$

Substituting (F.34) into (F.33) and expanding, after some algebra the following four first order differential equations in *standard form* are reached

$$\begin{aligned} y_1' &= -\varepsilon \hat{c} (y_1 \sin \tau + y_2 \cos \tau) \sin \tau \\ &\quad - \varepsilon \hat{m} \left(1 + \frac{\alpha}{\eta^2 - 1} \right) (1 - \hat{\mu}_s) (y_1 \cos \tau - y_2 \sin \tau) \sin \tau \\ &\quad - \varepsilon \hat{m} \eta^2 (1 - \hat{\mu}_s) (y_3 \cos \eta \tau - \eta^{-1} y_4 \sin \eta \tau) \sin \tau \\ &\quad - \varepsilon \hat{R} (\hat{\mu}_0 \operatorname{sgn}(R\omega) - \hat{\mu}_s) \sin \tau \end{aligned} \quad (\text{F.35})$$

¹ Note that the more convenient choice of “amplitude/phase” transform (see Section 5.3.2) is not used here since the resulting differential equations would have been singular at the origin.

$$\begin{aligned}
y_2' &= -\varepsilon \widehat{c} (y_1 \sin \tau + y_2 \cos \tau) \cos \tau \\
&\quad - \varepsilon \widehat{m} \left(1 + \frac{\alpha}{\eta^2 - 1} \right) (1 - \widehat{\mu}_s) (y_1 \cos \tau - y_2 \sin \tau) \cos \tau \\
&\quad - \varepsilon \widehat{m} \eta^2 (1 - \widehat{\mu}_s) (y_3 \cos \eta \tau - \eta^{-1} y_4 \sin \eta \tau) \cos \tau \\
&\quad - \varepsilon \widehat{R} (\widehat{\mu}_0 \operatorname{sgn}(R\omega) - \widehat{\mu}_s) \cos \tau
\end{aligned} \tag{F.36}$$

$$\begin{aligned}
y_3' &= -\varepsilon \frac{\alpha(\widehat{c}_1 - \eta^2 \widehat{c})}{\eta(\eta^2 - 1)} (y_1 \sin \tau + y_2 \cos \tau) \sin \eta \tau - \varepsilon \frac{\widehat{c}_1}{\eta} (\eta y_3 \sin \eta \tau + y_4 \cos \eta \tau) \sin \eta \tau \\
&\quad - \varepsilon \eta \widehat{m} (1 - \alpha) (1 - \widehat{\mu}_s) (y_3 \cos \eta \tau - \eta^{-1} y_4 \sin \eta \tau) \sin \eta \tau \\
&\quad + \varepsilon \eta (1 - \widehat{\mu}_s) \widehat{m} \alpha \frac{1}{\eta^2 - 1} \left(\alpha \frac{1}{\eta^2 - 1} + 1 \right) (y_1 \cos \tau - y_2 \sin \tau) \sin \eta \tau \\
&\quad + \varepsilon \eta (1 - \widehat{\mu}_s) \widehat{m} \left(\alpha \frac{1}{\eta^2 - 1} + 1 \right) (y_3 \cos \eta \tau - \eta^{-1} y_4 \sin \eta \tau) \sin \eta \tau \\
&\quad + \varepsilon \alpha \frac{\eta}{\eta^2 - 1} \widehat{R} (\widehat{\mu}_0 \operatorname{sgn}(R\omega) - \widehat{\mu}_s) \sin \eta \tau
\end{aligned} \tag{F.37}$$

$$\begin{aligned}
y_4' &= -\varepsilon \frac{\alpha(\widehat{c}_1 - \eta^2 \widehat{c})}{(\eta^2 - 1)} (y_1 \sin \tau + y_2 \cos \tau) \sin \eta \tau - \varepsilon \widehat{c}_1 (\eta y_3 \sin \eta \tau + y_4 \cos \eta \tau) \cos \eta \tau \\
&\quad - \varepsilon \eta \widehat{m} (1 - \alpha) (1 - \widehat{\mu}_s) (\eta y_3 \cos \eta \tau - y_4 \sin \eta \tau) \cos \eta \tau \\
&\quad + \varepsilon \eta^2 (1 - \widehat{\mu}_s) \widehat{m} \alpha \frac{1}{\eta^2 - 1} \left(\alpha \frac{1}{\eta^2 - 1} + 1 \right) (y_1 \cos \tau - y_2 \sin \tau) \cos \eta \tau \\
&\quad + \varepsilon \eta (1 - \widehat{\mu}_s) \widehat{m} \left(\alpha \frac{1}{\eta^2 - 1} + 1 \right) (\eta y_3 \cos \eta \tau - y_4 \sin \eta \tau) \cos \eta \tau \\
&\quad + \varepsilon \alpha \frac{\eta^2}{\eta^2 - 1} \widehat{R} (\widehat{\mu}_0 \operatorname{sgn}(R\omega) - \widehat{\mu}_s) \cos \eta \tau
\end{aligned} \tag{F.38}$$

where $O(\varepsilon^2)$ terms were neglected. From this point on, for simplicity, we assume that $N(\mathbf{y}, \mathbf{y}') > 0$.

Also note that argument of $\widehat{\mu}_s(\dot{\theta})$ (lead screw angular velocity) is given by

$$\dot{\theta} = \omega - |\omega| (y_1 \sin \tau + y_2 \cos \tau) \tag{F.39}$$

It is more convenient to express the above system of first-order differential equations as

$$\begin{aligned}
\mathbf{y}' &= \varepsilon \mathbf{g}(\mathbf{y}, \boldsymbol{\psi}, \varepsilon) \\
\boldsymbol{\psi}'_1 &= 1 \\
\boldsymbol{\psi}'_2 &= \eta
\end{aligned} \tag{F.40}$$

where $\mathbf{y} = [y_1 \ y_2 \ y_3 \ y_4]^T$. The right-hand-side of (F.40) is quasi-periodic in τ (*i.e.* it is 2π periodic with respect to both $\boldsymbol{\psi}_1$ and $\boldsymbol{\psi}_2$). Hence, the first order averaged equations can be derived from [35]

$$\bar{\mathbf{y}}' = \frac{\varepsilon}{4\pi^2} \int_0^{2\pi} \int_0^{2\pi} \mathbf{g}(\bar{\mathbf{y}}, \boldsymbol{\psi}, 0) d\boldsymbol{\psi}_1 d\boldsymbol{\psi}_2 \tag{F.41}$$

After some simplifications, carrying out the integration for (F.35), (F.36), (F.37), and (F.38) yields (dropping the bars)

$$\begin{aligned}
\dot{y}_1 &= -\varepsilon \frac{\hat{c}}{2} y_1 + \varepsilon \hat{R} \frac{1}{2\pi} \int_0^{2\pi} \hat{\mu}_s \sin \boldsymbol{\psi}_1 d\boldsymbol{\psi}_1 \\
&\quad - \varepsilon \hat{m} \left(1 + \frac{\alpha}{\eta^2 - 1} \right) \frac{1}{2\pi} \int_0^{2\pi} (1 - \hat{\mu}_s) \left(y_1 \sin \boldsymbol{\psi}_1 \cos \boldsymbol{\psi}_1 - \frac{y_2}{\omega_1} \sin^2 \boldsymbol{\psi}_1 \right) d\boldsymbol{\psi}_1
\end{aligned} \tag{F.42}$$

$$\begin{aligned}
\dot{y}_2 &= -\varepsilon \frac{\hat{c}}{2} y_2 + \varepsilon \hat{R} \frac{1}{2\pi} \int_0^{2\pi} \hat{\mu}_s \cos \boldsymbol{\psi}_1 d\boldsymbol{\psi}_1 \\
&\quad - \varepsilon \hat{m} \left(1 + \frac{\alpha}{\eta^2 - 1} \right) \frac{1}{2\pi} \int_0^{2\pi} (1 - \hat{\mu}_s) \left(y_1 \cos^2 \boldsymbol{\psi}_1 - \frac{y_2}{\omega_1} \sin \boldsymbol{\psi}_1 \cos \boldsymbol{\psi}_1 \right) d\boldsymbol{\psi}_1
\end{aligned} \tag{F.43}$$

$$\begin{aligned}
\dot{y}_3 &= -\varepsilon \frac{\hat{c}_1}{2} y_3 + \varepsilon \hat{m} (1 - \alpha) y_4 \frac{1}{4\pi} \int_0^{2\pi} (1 - \hat{\mu}_s) d\boldsymbol{\psi}_1 \\
&\quad - \varepsilon \hat{m} \left(\alpha \frac{1}{\eta^2 - 1} + 1 \right) y_4 \frac{1}{4\pi} \int_0^{2\pi} (1 - \hat{\mu}_s) d\boldsymbol{\psi}_1
\end{aligned} \tag{F.44}$$

$$\begin{aligned}
\dot{y}_4 &= -\varepsilon \frac{\hat{c}_1}{2} y_4 - \varepsilon \eta^2 \hat{m} (1 - \alpha) y_3 \frac{1}{4\pi} \int_0^{2\pi} (1 - \hat{\mu}_s) d\boldsymbol{\psi}_1 \\
&\quad + \varepsilon \eta^2 \hat{m} \left(\alpha \frac{1}{\eta^2 - 1} + 1 \right) y_3 \frac{1}{4\pi} \int_0^{2\pi} (1 - \hat{\mu}_s) d\boldsymbol{\psi}_1
\end{aligned} \tag{F.45}$$

where $\widehat{\mu}_s = \widehat{\mu}_s(\omega - |\omega|)(y_1 \sin \psi_1 + y_2 \cos \psi_1)$. Introducing the polar coordinates

$$\begin{aligned} y_1 &= a_1 \cos \beta_1 \\ y_2 &= a_1 \sin \beta_1 \\ y_3 &= a_2 \cos \beta_2 \\ y_4 &= a_2 \eta \sin \beta_2 \end{aligned} \quad (\text{F.46})$$

the amplitude equations are found as

$$\begin{aligned} a'_1 &= -\varepsilon \frac{\widehat{c}}{2} a_1 + \varepsilon \frac{\widehat{R}}{2\pi} \int_0^{2\pi} \widehat{\mu}_s \sin(\psi_1 + \beta_1) d\psi_1 \\ &\quad - \varepsilon \widehat{m} \left(1 + \frac{\alpha}{\eta^2 - 1} \right) \frac{a_1}{2\pi} \int_0^{2\pi} (1 - \widehat{\mu}_s) \cos(\psi_1 + \beta_1) \sin(\psi_1 + \beta_1) d\psi_1 \end{aligned} \quad (\text{F.47})$$

$$a'_2 = -\varepsilon \frac{\widehat{c}_1}{2} a_2 \quad (\text{F.48})$$

This equation is similar to the 1-DOF case studied in Section 5.3.3. In fact, if the same limitations are considered as in Section 5.3.1 (*i.e.* $\text{sgn}(\dot{\theta}) = \text{sgn}(N) = 1$), it further simplifies to

$$a'_1 = -\varepsilon \frac{\widehat{c}}{2} a_1 + \varepsilon \frac{\widehat{R}}{2\pi} \int_0^{2\pi} \widehat{\mu} \sin \psi_1 d\psi_1 \quad (\text{F.49})$$

where $\widehat{\mu} = \widehat{\mu}(\omega(1 - a_1 \sin \psi_1))$ and is defined similar to (5.49) by

$$\widehat{\mu} = \left(\widehat{\mu}_1 + \widehat{\mu}_2 e^{r_0 \omega a_1 \sin \psi_1} - \widehat{\mu}_3 a_1 \sin \psi_1 \right) \left(1 - r_2 e^{r_1 \omega a_1 \sin \psi_1} \right) \quad (\text{F.50})$$

and $\widehat{\mu}_1$, $\widehat{\mu}_2$, and $\widehat{\mu}_3$ are given by (5.50), (5.51), and (5.52), respectively.

Notice that (F.49) is exactly the same as (5.48) if a_1 is replaced by a . The first order averaged equations for a_1 , (F.49), and a_2 , (F.48), are decoupled. Furthermore, (F.48) shows that, to this order of approximations, the vibration component with the frequency ω_2 dies out exponentially independent of a_1 .

Appendix G

Similarities in the Conditions for Local Stability of the Steady-sliding Fixed Point Between the 2-DOF Model of Section 3.5 and the 2-DOF model of Section 3.6

The Routh-Hurwitz stability conditions for the 2-DOF models of Section 3.5 and 3.6, with constant coefficient of friction, are given in Chapter 6. These conditions were obtained from the characteristic equations of the linearized system models. For the 2-DOF model with compliant threads, the characteristic equation given by (6.43) is expanded as

$$a_4\eta^4 + a_3\eta^3 + a_2\eta^2 + a_1\eta + a_0 = 0 \quad (\text{G.1})$$

where

$$a_4 = I\hat{m} \quad (\text{G.2})$$

$$a_3 = \hat{c}_c [(1 + \mu \operatorname{sgn}(R\omega) \tan \lambda)(I - r_m \tan \lambda \xi_0 m)] + c\hat{m} \quad (\text{G.3})$$

$$a_2 = \hat{k}_c [(1 + \mu \operatorname{sgn}(R\omega) \tan \lambda)(I - r_m \tan \lambda \xi_0 m)] + k\hat{m} + c\hat{c}_c (1 + \mu \operatorname{sgn}(R\omega) \tan \lambda) \quad (\text{G.4})$$

$$a_1 = (c\hat{k}_c + \hat{c}_c k)(1 + \mu \operatorname{sgn}(R\omega) \tan \lambda) \quad (\text{G.5})$$

$$a_0 = k\hat{k}_c (1 + \mu \operatorname{sgn}(R\omega) \tan \lambda) \quad (\text{G.6})$$

where \hat{k}_c , \hat{c}_c , and \hat{m} are given by (6.24), (6.25), and (6.26), respectively. For the 2-DOF model

with axially compliant lead screw supports, the characteristic equation given by (6.80) is expanded as

$$b_4\eta^4 + b_3\eta^3 + b_2\eta^2 + b_1\eta + b_0 = 0 \quad (\text{G.7})$$

where

$$b_4 = I(m + m_1) - mm_1\xi_0 r_m \tan \lambda \quad (\text{G.8})$$

$$b_3 = c(m + m_1) + c_1(I - \xi_0 r_m \tan \lambda m) \quad (\text{G.9})$$

$$b_2 = k(m + m_1) + cc_1 + k_1(I - \xi_0 m r_m \tan \lambda) \quad (\text{G.10})$$

$$b_1 = kc_1 + ck_1 \quad (\text{G.11})$$

$$b_0 = kk_1 \quad (\text{G.12})$$

To see the similarities between (G.1) and (G.7), we divide (G.1) by the strictly positive quantity $r_m^2 \sin^2 \lambda (1 + \mu \operatorname{sgn}(R\omega) \tan \lambda)^1$. Also using (6.24), (6.25), and (6.26), (G.1) becomes

$$a'_4\eta^4 + a'_3\eta^3 + a'_2\eta^2 + a'_1\eta + a'_0 = 0 \quad (\text{G.13})$$

where

$$a'_4 = I(m + m_8) \quad (\text{G.14})$$

$$a'_3 = c(m + m_8) + c_c(I - \xi_0 r_m \tan \lambda m) \quad (\text{G.15})$$

$$a'_2 = k_c(I - \xi_0 r_m \tan \lambda m) + k(m + m_8) + cc_c + k_c(I - \xi_0 r_m \tan \lambda m) \quad (\text{G.16})$$

$$a'_1 = ck_c + c_c k \quad (\text{G.17})$$

$$a'_0 = kk_c \quad (\text{G.18})$$

where m_8 is defined as

¹ See footnote on page 97.

$$m_{\delta} = \left(\frac{1}{\cos^2 \lambda (1 + \mu \operatorname{sgn}(R\omega) \tan \lambda)} - 1 \right) m \quad (\text{G.19})$$

Note that for $\mu > \tan \lambda$ and $R\omega > 0$, m_{δ} is a small negative quantity. For example, for $\mu = 0.218$ and $\lambda = 5.57^\circ$, $m_{\delta}/m \approx -0.012$.

The coefficients given by (G.9), (G.10), (G.11), and (G.12) are structurally identical to (G.15), (G.16), (G.17), and (G.18), respectively. In the two models, k_1 and c_1 have the same effect on the eigenvalues as k_c and c_c . The major difference between the two characteristic equations is in (G.8) and (G.14). However, for small lead screw mass (m_1), the difference is small. As an example, compare Figure 6-12 with Figure 6-24. The difference between the stability conditions of the two models becomes significant for sufficiently large m and m_1 , since b_4 can become negative, leading to kinematic constraint instability (see Section 6.3.2), while a'_4 is always positive.

Appendix H

Further Observations on the Mode Coupling

Instability in Lead Screw Drives

Although the linear complex eigenvalue analysis method is useful in establishing the local stability boundaries of the fixed points of a system, it does not reveal any information regarding the dynamic behavior of the original nonlinear system. Since the focus of this work is on the lead screw vibration and the possibility of generation of undesirable noise, there is a great deal of interest in the actual behavior of the system. Even when the steady-sliding fixed point is unstable, there could be situations where the resulting amplitude of steady-state vibrations is very small and consequently no audible noise is generated from the system.

In this appendix, through numerical simulation, the effects of various system parameters on the dynamic behavior of the lead screw drive under the mode coupling instability condition are investigated. First, in Section H.1, variations in the steady-state vibration amplitude of the lead screw is studied as the two damping coefficients in the 2-DOF model of Section 3.5 are varied. The effects of coupling stiffness and contact stiffness of the same model are investigated in Section H.2 through five different numerical simulations. In the last simulation, the possibility of chaos is also briefly mentioned.

Unless otherwise specified, numerical values of the system parameters are those listed in Table 6-1.

H.1 Effects of Damping on Mode Coupling Instability in a 2-DOF System with Constant Coefficient of Friction

In Section 6.2.2, it was proven that in the extreme cases where damping is present in only one of the two system DOFs, the steady-sliding fixed point is unstable. In addition, the complex effect of damping in expanding *or* reducing the parameter regions of stability was shown by the examples in Figure 6-12 and Figure 6-14. The actual variations in the steady-state amplitude of vibrations can

have an even more complex behavior.

Figure H-1 shows a map of averaged amplitude of vibrations of the lead screw for $k_c = 2 \times 10^7$, as lead screw support damping and contact damping coefficients are varied. The two natural frequencies of the undamped system are approximately 148.2 and 194.6 Hz. The initial conditions were chosen close to the fixed point; $u_1(0) = u_2(0) = 0$ and $\dot{u}_1(0) = \dot{u}_2(0) = -\%$. For each pair of damping coefficients, the numerical simulations were carried out for four seconds. The results for the first second were discarded to exclude the transients. As can be seen, the steady-state amplitude of vibrations varies considerably with the changes of the two damping coefficients.

For the numerical value of the parameters chosen here, the system exhibits chaotic or multi-period behavior for many of the selected values of the two damping coefficients. Figure H-2(a) and Figure H-2(b) show the bifurcation diagrams of Poincare sections ($\dot{u}_1 = 0$), as the damping parameter is changed along the horizontal dotted line and the vertical dotted line in Figure H-1, respectively. Further examples of this phenomenon are presented in Section H.2 below.

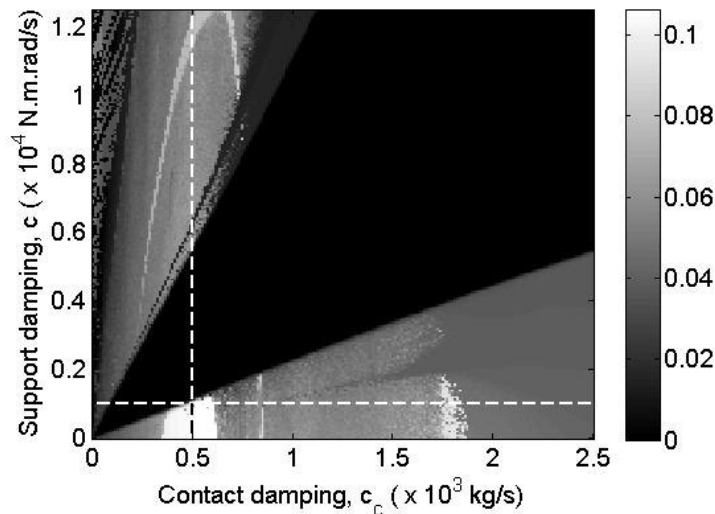


Figure H-1: Averaged amplitude of vibration, y_1 (rad), as lead screw support damping, c , and contact damping c_c are varied

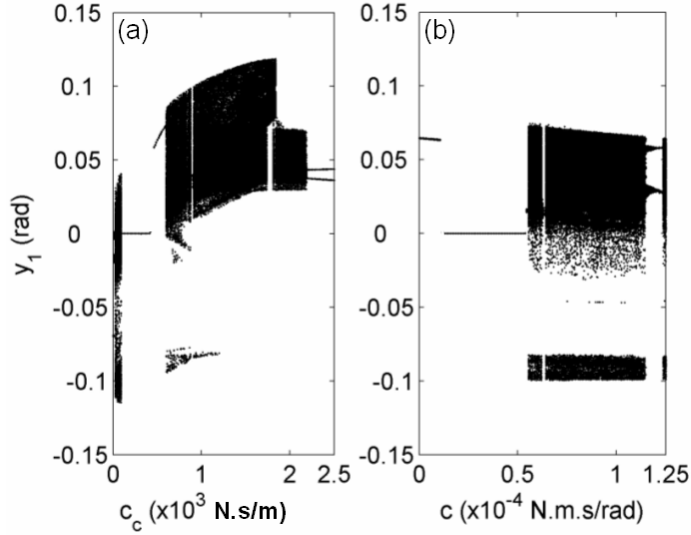


Figure H-2: Bifurcation of Poincare sections. a) Along the horizontal dashed line in Figure H-1
b) Along the vertical dashed line in Figure H-1.

H.2 Effects of Stiffness on Mode Coupling Instability in a 2-DOF System with Velocity-dependent Coefficient of Friction

In this section, results from five series of numerical simulations are presented that show the effect of stiffness (coupling, k , and contact, k_c) on the stability of the 2-DOF model of Section 3.5. These numerical studies also include the amplitude and frequency of the steady-state vibration of the lead screw.

Here the friction coefficient is assumed according to (3.10) with parameters taken from Table 4-3. Other system parameters, not specified in the examples, are selected as before.

H.2.1 Example #1

For this first example, the following parameters are considered;

$$m = 1, c = 40 \times 10^{-5}, c_c = 10^2$$

and the contact stiffness, k_c , is varied between 10^4 to 10^6 (N/m). Figure H-3(b) shows the variation of the real parts of the eigenvalues of the system's Jacobian matrix as the contact stiffness is varied. The steady-sliding fixed points becomes unstable between $k_c = 1.91 \times 10^5$ and $k_c = 6.35 \times 10^5$. As

shown in Figure H-3(a) by the two-sided Poincare sections, the amplitude of lead screw vibrations varies considerably in this range and reaches a maximum of approximately 0.1 (*rad*).

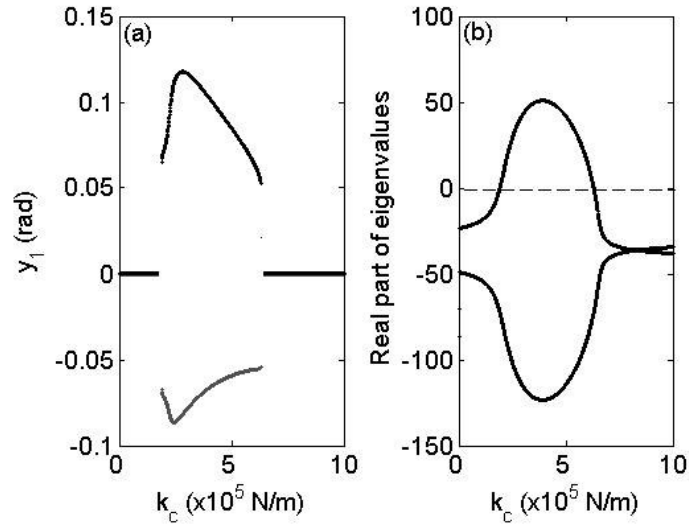


Figure H-3: Effect of contact stiffness
(a) Two-sided Poincare bifurcation diagram, (b) Real part of the eigenvalues

During this range, the two natural frequencies are close to each other as shown by the dashed lines in Figure H-4. It can be seen in this figure that the dominant frequency of vibrations follows the higher linear mode at the beginning of the unstable range and moves towards the lower linear mode at the end of it.

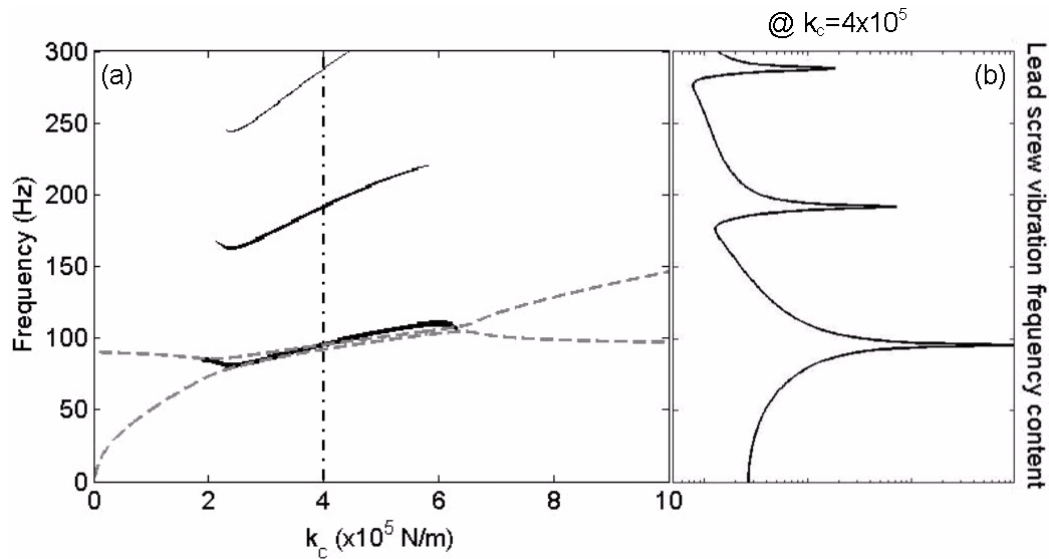


Figure H-4: (a) Black lines: Evolution of peak lead screw vibration frequencies, dashed grey lines: eigenfrequencies; (b) Frequency content of steady-state lead screw vibration at $k_c = 4 \times 10^5$

H.2.2 Example #2

In this example, parameter values are chosen the same as the previous example except for the lead screw support damping, which is lowered to $c = 5 \times 10^{-5}$. As shown in Figure H-5(b), by lowering the lead screw damping, the system is unstable throughout the simulated range of k_c . The amplitude of vibrations, as shown in Figure H-5(a), hits a maximum of approximately 0.12 (rad) which is slightly higher than the previous case.

It is interesting to note that at approximately $k_c = 8.7 \times 10^5$, the system undergoes a *period-doubling bifurcation* [36] which lasts until $k_c = 9.5 \times 10^5$. The evolution of peak vibration frequencies are shown in Figure H-6(a). The dominant vibration frequency follows the higher linear mode and then shifts to the lower mode as the two linear frequencies move closer to each other. The dominant frequency of vibration continues to follow the lower mode as the two linear frequencies grow apart. The period-doubling bifurcation is also visible in this frequency plot and in the section shown in Figure H-6(b). At the instant plotted, the dominant frequency is 94Hz and the two peaks at either side of it, caused by the bifurcation, are at $94 \pm \frac{94}{2}$ Hz.

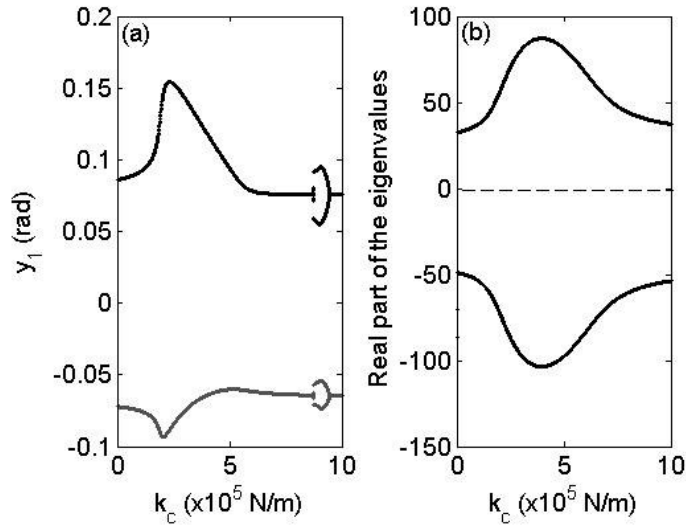


Figure H-5: Effect of contact stiffness
 (a) Two-sided Poincaré bifurcation diagram, (b) Real part of the eigenvalues

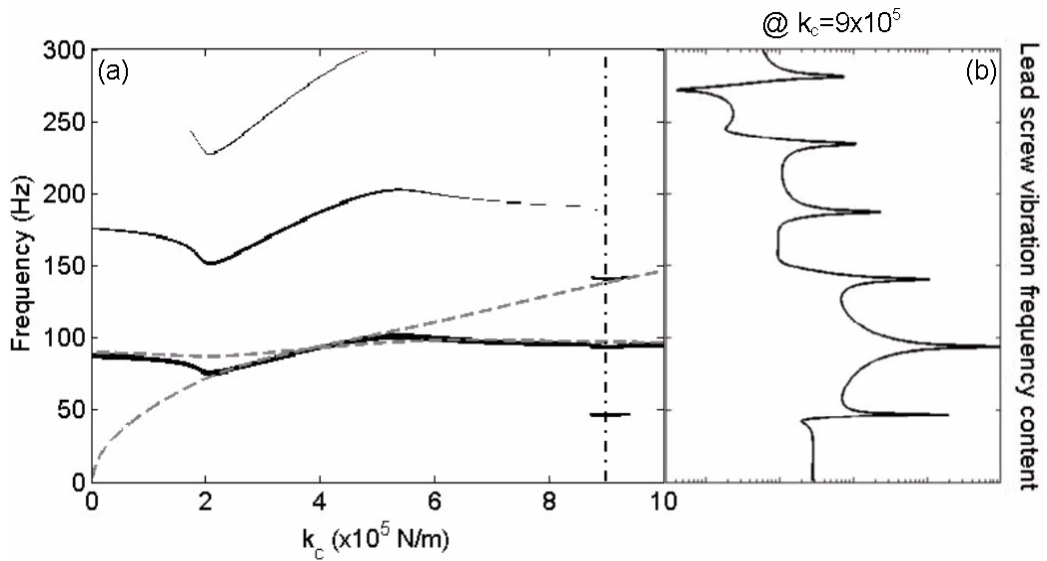


Figure H-6: (a) Black lines: Evolution of peak lead screw vibration frequencies, dashed grey lines: eigenfrequencies; (b) Frequency content of steady-state lead screw vibration at $k_c = 9 \times 10^5$

H.2.3 Example #3

In this example the contact stiffness is fixed at $k_c = 10^6$, and in its place the coupling stiffness, k , is varied between 0.1 and 8 ($N.m/rad$). The other parameters are selected as;

$$m = 1, c = 40 \times 10^{-5}, c_c = 10^2$$

Similar to example #1 above, Figure H-7(b) shows that the steady-sliding fixed point is unstable in a portion of the parameter range (*i.e.* approximately between 1.58 and 5.57). The Poincare sections in Figure H-7(a) show that during the unstable parameter range, the amplitude of steady-state varies considerably. There is also a discontinuity at about 5.05 ($N.m/rad$). The amplitude of vibrations remains around 0.046 (rad) before the discontinuity but afterwards starts to diminish.

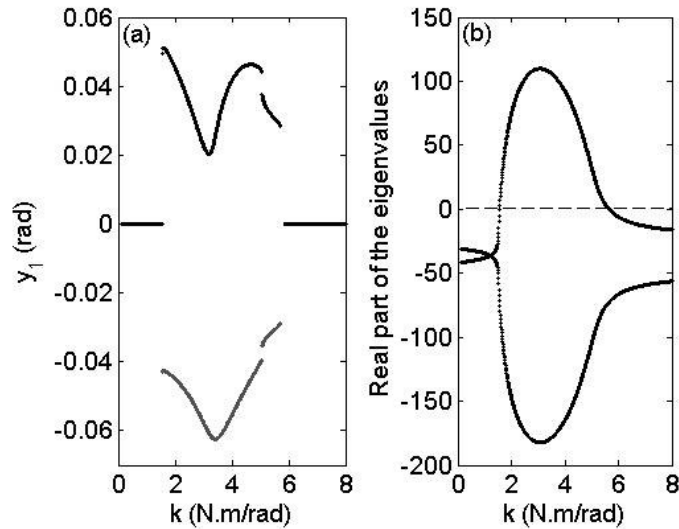


Figure H-7: Effect of coupling stiffness
(a) Two-sided Poincare bifurcation diagram, (b) Real part of the eigenvalues

Parallel to the jump in the amplitude, a distinguishable jump in the dominant frequency of lead screw vibrations is discernable in Figure H-8(a). At this point, the two linear frequencies start to move away from each other and the frequency of vibration jumps toward the higher mode and follows it on. A section of this figure is shown in Figure H-8(b) for $k = 4$.

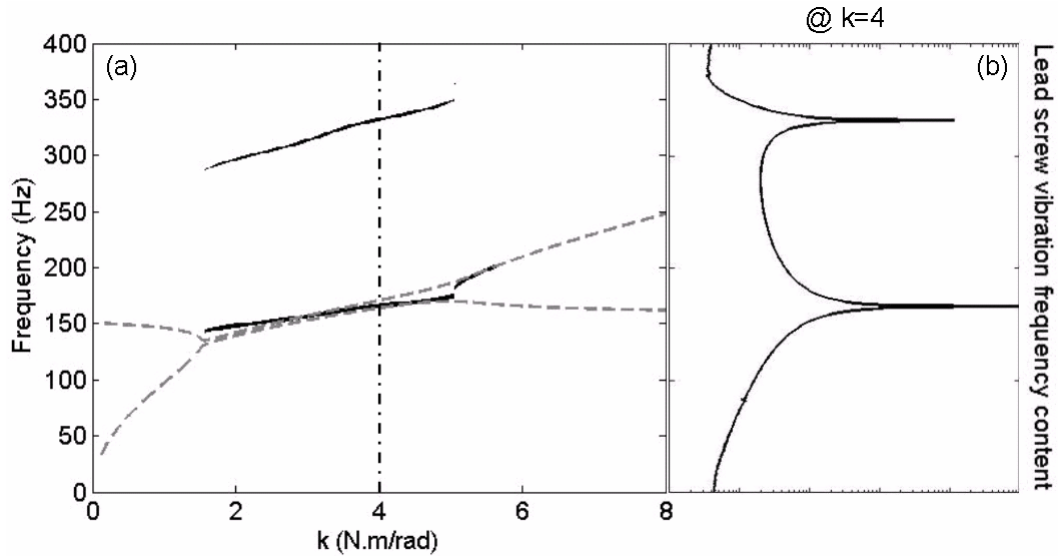


Figure H-8: (a) Black lines: Evolution of peak lead screw vibration frequencies, dashed grey lines: eigenfrequencies; (b) Frequency content of steady-state lead screw vibration at $k=4$

H.2.4 Example #4

The parameters chosen for this example are exactly the same as the previous example except for the two damping coefficients which are reduced to $c = 4 \times 10^{-5}$ and $c_c = 10$. As can be seen from Figure H-9(b), the system's fixed point is stable throughout the considered parameter range. Figure H-9(a) shows the bifurcation plot of two-sided Poincaré sections. As expected, the vibration amplitude grows as the coupling stiffness is reduced. Also, it can be seen that the system exhibits chaotic behavior for the selected value of the parameters.

Figure H-10 shows the evolution of dominant frequencies of the lead screw vibration as the coupling stiffness is varied. For $k = 4$, $k = 7$, and $k = 1$, various simulation results are plotted in Figures H-11, H-12, and H-13, respectively.

At $k = 4$, the spectrum plot in Figure H-11(a) shows well separated peaks (those peaks which are visible in Figure H-10 are at 28.6, 157.6, 186.2, and 315.2 (Hz)). The y_1 - y_2 projection of the system trajectory in Figure H-11(b) shows a periodic orbit (limit-cycle). The Poincaré section shown in Figure H-11(c), confirms the presence of a 15-period periodic solution at $k = 4$.

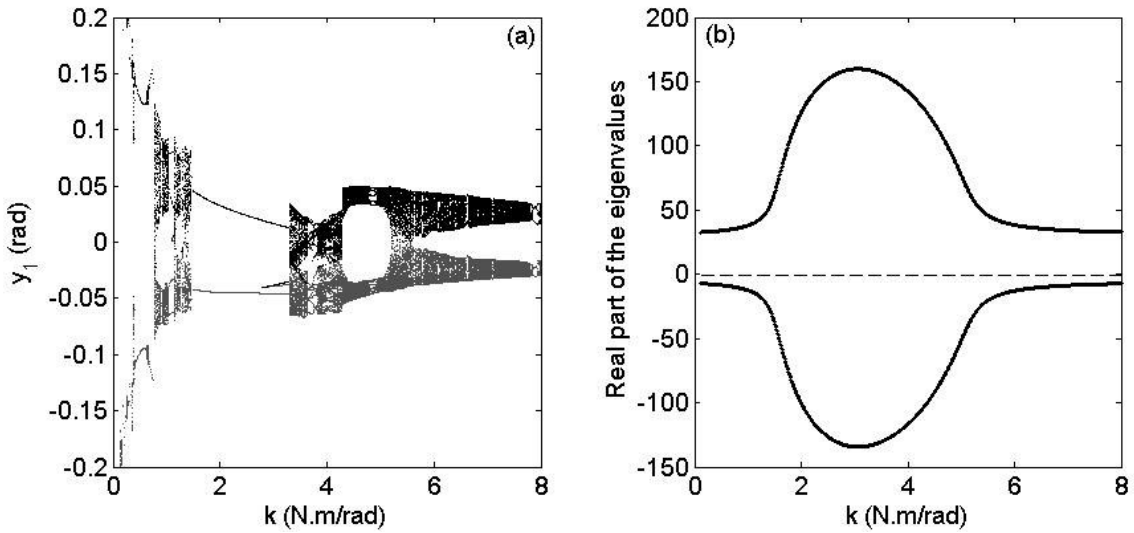


Figure H-9: Effect of coupling stiffness
(a) Two-sided Poincare bifurcation diagram, (b) Real part of the eigenvalues

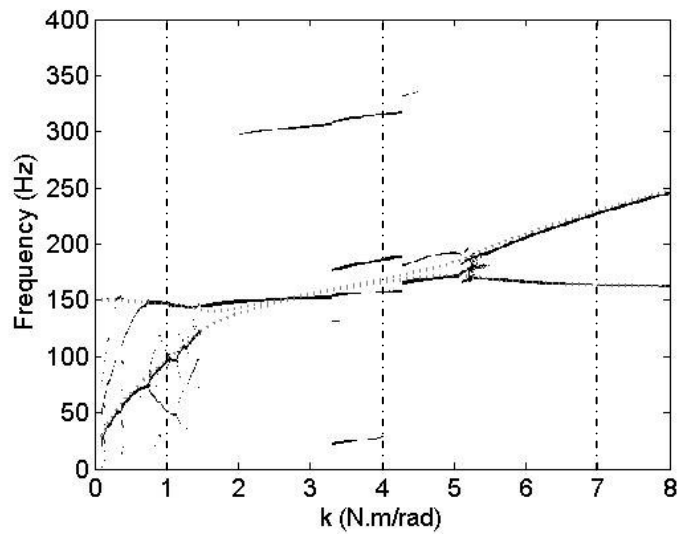


Figure H-10: Black lines: Evolution of peak lead screw vibration frequencies, dotted grey lines: eigenfrequencies

The spectrum plot of lead screw vibration at $k = 7$ is shown in Figure H-12(a). The two incommensurable dominant frequencies are 163.8 and 227.2. The resulting quasi-periodic orbit is shown in Figure H-12(b), by the filled out region of the phase plane, and in Figure H-12(c), by the closed-curve Poincaré section.

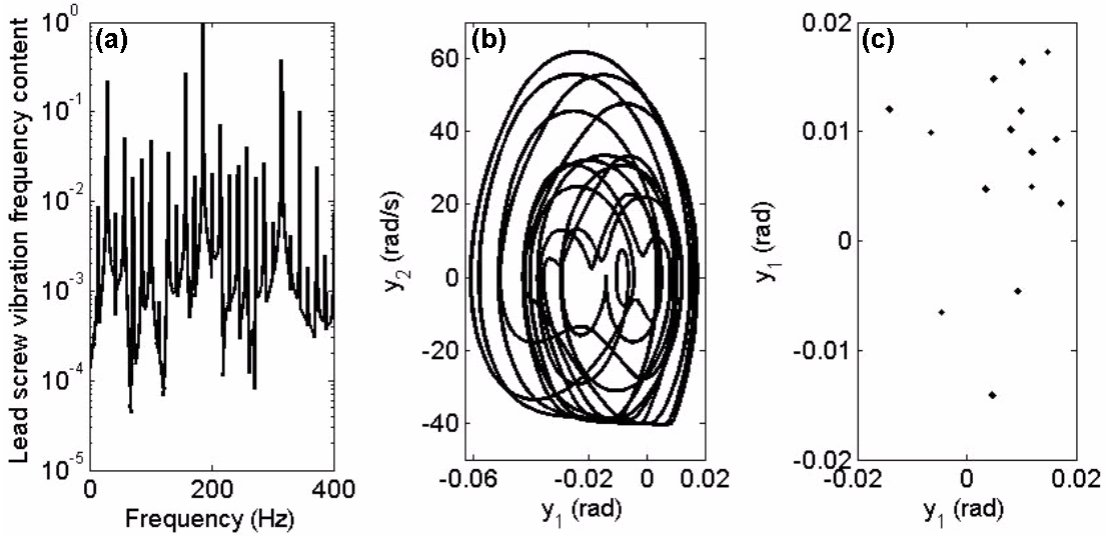


Figure H-11: Simulation results for lead screw at $k=4$; (a) Vibration frequency content, (b) y_1 - y_2 projection of the trajectories, (c) Poincare section

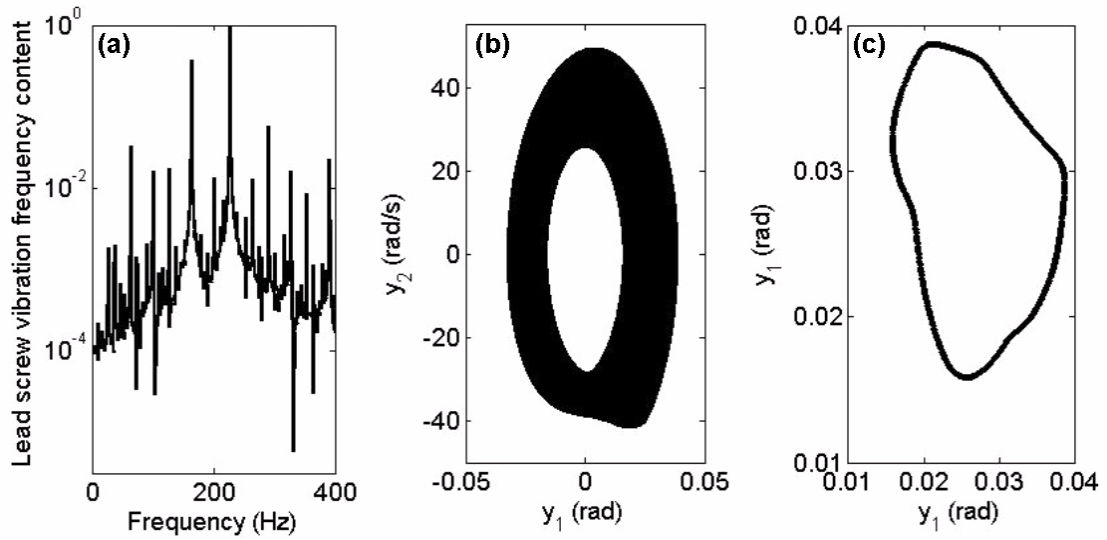


Figure H-12: Simulation results for lead screw at $k=7$; (a) Vibration frequency content, (b) y_1 - y_2 projection of the trajectories, (c) Poincare section

The spectrum plot of lead screw vibration at $k = 1$ is shown in Figure H-13(a). Here, in contrast to the two previous cases, the spectrum has a broadband character. The two dominant peaks are located at 95.2 and 147.3Hz. The y_1 - y_2 projection of the system trajectory in Figure H-13(b) is similar to Figure H-12(b) and fills out a portion of the phase plane; however, the possibility of chaotic behavior is shown by Poincare section in Figure H-13(c). Further investigation is needed to confirm that this

attractor is indeed chaotic¹, which is outside the scope of this work.

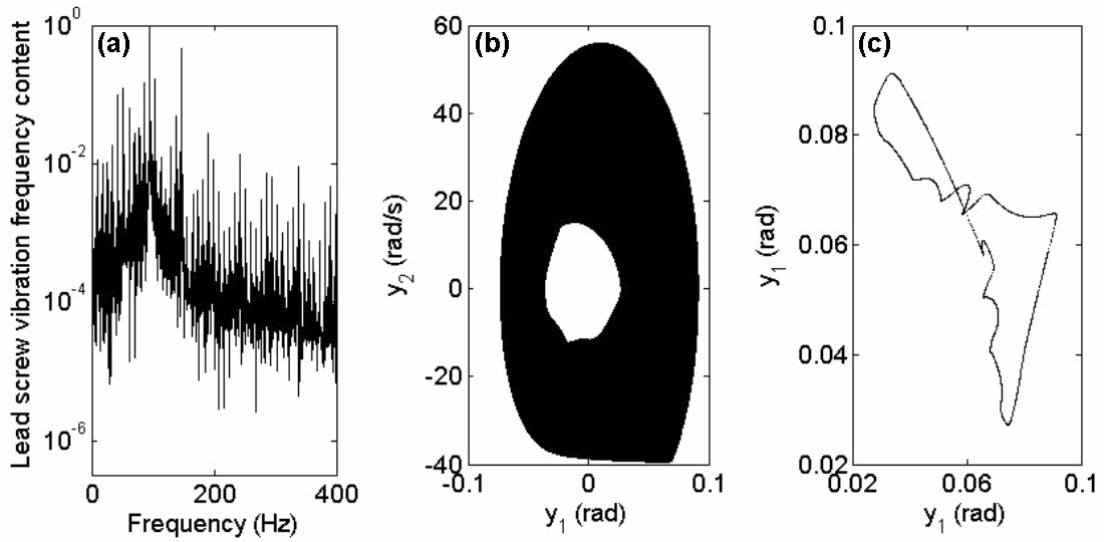


Figure H-13: Simulation results for lead screw at $k=1$; (a) Vibration frequency content, (b) y_1 - y_2 projection of the trajectories, (c) Poincare section

¹ To verify that the attractor is chaotic, the sensitivity to the initial conditions must be shown [36].

Appendix I

Theorems Cited in Chapter 7

In this appendix, three theorems used in Section 7.4 are stated without proof. Theorems 1 and 3 are taken from [84], and Theorem 2 is taken from [44]. The proof for these theorems is given in their respective references.

I.1 Theorem 1 [84]

Consider the following system

$$\dot{\mathbf{x}} = \varepsilon \mathbf{f}(t, \mathbf{x}, \varepsilon), \quad \mathbf{x}(0, \varepsilon) = \mathbf{x}_0 \quad (\text{I.1})$$

Let $\mathbf{f}(t, \mathbf{x}, \varepsilon)$ and its partial derivatives with respect to $(\mathbf{x}, \varepsilon)$ up to the second order be continuous and bounded for $(t, \mathbf{x}, \varepsilon) \in [0, \infty) \times D_0 \times [0, \varepsilon_0]$, for every compact set $D_0 \subset D$, where $D \subset \mathfrak{R}^n$ is a domain. Suppose that \mathbf{f} is T -periodic in t for some $T > 0$ and ε is a positive parameter. Let $\mathbf{x}(t, \varepsilon)$ be the solution of (I.1) and $\mathbf{z}(\varepsilon t)$ be the solution of the average system

$$\dot{\mathbf{z}} = \varepsilon \bar{\mathbf{f}}(\mathbf{z}), \quad \mathbf{z}(0) = \mathbf{z}_0 \quad (\text{I.2})$$

Then

- If $\mathbf{z}(\varepsilon t) \in D \quad \forall t \in [0, L/\varepsilon]$ and $\mathbf{x}(0, \varepsilon) - \mathbf{z}(0) = O(\varepsilon)$, then there exists $\varepsilon^* > 0$ such that for all $0 < \varepsilon < \varepsilon^*$, $\mathbf{x}(t, \varepsilon)$ is defined and $\mathbf{x}(t, \varepsilon) - \mathbf{z}(\varepsilon t) = O(\varepsilon)$ on $[0, L/\varepsilon]$.
- If the origin $\mathbf{z} = 0 \in D$ is an exponentially stable equilibrium point of the average system, $\Omega \subset D$ is a compact subset of its region of attraction, $\mathbf{z}(0) \in \Omega$, and $\mathbf{x}(0, \varepsilon) - \mathbf{z}(0) = O(\varepsilon)$, then there exists $\varepsilon^* > 0$ such that for all $0 < \varepsilon < \varepsilon^*$, $\mathbf{x}(t, \varepsilon)$ is defined and $\mathbf{x}(t, \varepsilon) - \mathbf{z}(\varepsilon t) = O(\varepsilon)$ for all $t \in [0, \infty)$.
- If the origin $\mathbf{z} = 0 \in D$ is an exponentially stable equilibrium point of the average system,

then there exist positive constants ε^* and c such that, for all $0 < \varepsilon < \varepsilon^*$, (I.1) has a unique, exponentially stable, T -periodic solution $\bar{\mathbf{x}}(t, \varepsilon)$ with the property $\|\bar{\mathbf{x}}(t, \varepsilon)\| \leq c\varepsilon$.

- If the origin $\mathbf{z} = 0 \in D$ is an exponentially stable equilibrium point of the average system, and if $\mathbf{f}(t, 0, \varepsilon) = 0$ for all $(t, \varepsilon) \in [0, \infty) \times [0, \varepsilon_0]$, then $\mathbf{x} = 0$ is an exponentially stable equilibrium point of (I.1).

Proof:

The proof is given in [84, Theorem 10.4].

I.2 Theorem 2 [44]

Consider the following system in *standard form*

$$\dot{\mathbf{x}} = \varepsilon \mathbf{f}(t, \mathbf{x}, \varepsilon), \quad \mathbf{x}(0) = \mathbf{x}_0 \quad (\text{I.3})$$

where $\mathbf{x}, \mathbf{x}_0 \in D \subset \mathfrak{R}^n$. Also consider the averaged system

$$\dot{\mathbf{z}} = \varepsilon \bar{\mathbf{f}}(\mathbf{z}), \quad \mathbf{z}(0) = \mathbf{x}_0 \quad (\text{I.4})$$

where $\bar{\mathbf{f}}(\mathbf{x}) = \frac{1}{T} \int_0^T \mathbf{f}(\tau, \mathbf{x}, 0) d\tau$.

Suppose that all of the conditions of the first order averaging theorem of Appendix B are satisfied. Assume further that:

- The averaged system has an exponentially stable equilibrium point $\mathbf{z} = 0$.
- The function $\bar{\mathbf{f}}(\mathbf{z})$ is continuously differentiable with respect to \mathbf{z} in D .
- The stable equilibrium point $\mathbf{z} = 0$ has a domain of attraction $D_0 \subset D$.

Then, if $\mathbf{x}_0 \in D_0$, then

$$\|\mathbf{x}(t, \varepsilon) - \mathbf{z}(t, \varepsilon)\| \leq c\varepsilon \quad (\text{I.5})$$

for some $c > 0$ independent of ε and $0 \leq t < \infty$.

Proof:

The proof is given in [44, Appendix II].

Remark:

This theorem is similar to part 2 of theorem 1 given in Section I.1. However, the assumptions made are much weaker here than those of theorem 1.

I.3 Theorem 3 [84]

Consider the singularly perturbed system

$$\begin{aligned}\dot{\mathbf{x}} &= \mathbf{f}(t, \mathbf{x}, \mathbf{z}, \varepsilon) \\ \varepsilon \dot{\mathbf{z}} &= \mathbf{g}(t, \mathbf{x}, \mathbf{z}, \varepsilon)\end{aligned}\tag{I.6}$$

Assume that the following assumptions are satisfied for all $(t, \mathbf{x}, \varepsilon) \in [0, \infty) \times B_r \times [0, \varepsilon_0]$, where $B_r = \{\mathbf{x} \in \mathfrak{R}^n \mid \|\mathbf{x}\| \leq r\}$.

- $\mathbf{f}(t, 0, 0, \varepsilon) = 0$ and $\mathbf{g}(t, 0, 0, \varepsilon) = 0$.
- The equation $0 = \mathbf{g}(t, \mathbf{x}, \mathbf{z}, 0)$ has an isolated root $\mathbf{z} = \mathbf{h}(t, \mathbf{x})$ such that $\mathbf{h}(t, 0) = 0$.
- The functions \mathbf{f} , \mathbf{g} , \mathbf{h} , and their partial derivatives up to the second order are bounded for $\mathbf{z} - \mathbf{h}(t, \mathbf{x}) \in B_\rho$.
- The origin of the reduced system $\dot{\mathbf{x}} = \mathbf{f}(t, \mathbf{x}, \mathbf{h}(t, \mathbf{x}), 0)$ is exponentially stable.
- The origin of the boundary-layer system $\frac{d\mathbf{y}}{d\tau} = \mathbf{g}(t, \mathbf{x}, \mathbf{y} + \mathbf{h}(t, \mathbf{x}), 0)$ is exponentially stable, uniformly in (t, \mathbf{x}) .

Then, there exists $\varepsilon^* > 0$ such that for all $\varepsilon < \varepsilon^*$, the origin of (I.6) is exponentially stable.

Proof:

The proof is given in [84, theorem 11.4].

Bibliography

- [1] P. Gallina and M. Giovagnoni, “Design of screw jack mechanism to avoid self-excited vibrations”, *Journal of Dynamic Systems, Measurement, and Control*, Vol. 124, 2002, pp. 477-480.
- [2] K. W. Hollander, T. G. Sugar, “Design of Lightweight Lead Screw Actuators for Wearable Robotic Applications”, *Transactions of the ASME Journal of Mechanical Design*, Vol. 128, 2006, pp. 644-648.
- [3] R. Buck, “A Few Pointers for Selecting Pumps”, *Medical Design*, November 2006.
- [4] R. V. MacKenzie, *Screw Threads - Design, Selection, and Specification*, The Industrial Press, 1961.
- [5] J. E. Shigley and C. R. Mischke, *Mechanical Engineering Design*, 5th ed., McGraw-Hill, 1989.
- [6] M. F. Spotts, *Design of Machine Elements*, 4th ed., Printice-Hall, 1971.
- [7] –, “High Precision Ballscrew and Leadscrew Driven Tables”, Parker Products Catalog 8092/USA Section B, URL: <http://www.parker.com/literature/Literature%20Files/emn/SectionB.pdf> accessed 11/30/08.
- [8] –, “Miniature Precision Stages”, Parker Products Catalog 8092/USA Section C, URL: <http://www.parker.com/literature/Literature%20Files/emn/SectionC.pdf>, accessed 11/30/08.
- [9] –, “Lead and Ball Screw Catalog”, Thomson BSA, <http://www.thomsonbsa.com/pdf/ThomsonBSA-Lead-and-Ball-Screw-Catalog.pdf>, accessed 11/30/08.
- [10] –, “Precision Rolled Lead Screws – Metric Series”, Thomson BSA, URL: <http://www.thomsonbsa.com/pdf/ThomsonBSA-Precision-Rolled-Lead-Screws-Metric-Series.pdf>, accessed 11/30/08.
- [11] –, “PowerAc™ Precision Lead Screw Assemblies”, Nook Industries, URL: <http://www.nookindustries.com/pdf/NookAcmeScrew.pdf>, accessed 11/30/08.
- [12] –, “Which Screw? Picking the Right Technology”, Tolomatic, Inc., URL: http://mail.tolomatic.com/archives/pdfs/9900-4644_00_WhichScrew.pdf, accessed 11/30/08.
- [13] –, “Ballscrews vs. lead screws”, *Motion System Design*, 1/1/2008.

- [14] Tom Solon, "Taking the Lead", *Motion System Design*, Vol. 48, No. 1, pp. 20-26, 2006.
- [15] T. Solon, "Leadscrews roll over ball screws", *Machine Design*, Vol. 75, No. 23, 2003, pp. 94-98.
- [16] –, "Kerk Motion Products Catalog", Kerk Motion Products, Inc., URL:
<http://www.kerkmotion.com/pdf/kerk-catalog-2008.pdf>, accessed 11/30/08.
- [17] –, "Lead Screw Nut: General Catalog – (A) Technical Descriptions of Products", THK, URL:
http://thk.com/documents/us_pdf/products/generalA/en_A_1_general.pdf, accessed 11/30/08.
- [18] B. Feeny, A. Guran, N. Hinrichs, and K. Popp, "Historical review on dry friction and stick-slip phenomena", *Applied Mechanics Reviews*, Vol. 51, No. 5, pp. 321-341, 1998.
- [19] B. Armstrong-Helouvry, P. Dupont, and C. Canudas de Wit, "A Survey of Models, Analysis Tools and Compensation Methods for the Control of Machines with Friction", *Automatica*, Vol. 30, No. 7, pp. 1083-1138, 1994.
- [20] R. A. Ibrahim, "Friction-induced vibration, chatter, squeal, and chaos. Part I: Mechanics of contact and friction", *Applied Mechanics Reviews*, Vol. 47, No. 7, pp. 209-226, 1994.
- [21] J. Awrejcewicz and P. Olejnik, "Analysis of Dynamic Systems with Various Friction Laws", *Applied Mechanics Reviews*, Vol. 58, pp. 389-411, 2005.
- [22] E. J. Berger, "Friction modeling for dynamic system simulation", *Applied Mechanical Reviews*, Vol. 55, No. 6, pp. 535-577, 2002.
- [23] C. Canudas de Wit, H. Olsson, K. J. Åström, and P. Lischinsky, "A New Model for Control of Systems with Friction", *IEEE Transactions on Automatic Control*, Vol. 40, No. 3, pp. 419-425, 1995.
- [24] B. Armstrong- Helouvry, "Stick-Slip Arising from Stribeck Friction", *Proceedings of the IEEE International Conference on Robotics and Automation*, Cincinnati, OH, USA, pp. 1377-1382, 1990.
- [25] B. Armstrong- Helouvry, *Control Machines with Friction*, Kluwer Academic Publishers, 1991.
- [26] L. Marton and B. Lantos, "Modeling, Identification, and Compensation of Stick-Slip Friction", *IEEE Transactions on Industrial Electronics*, Vol. 54, No. 1, pp. 511-521, 2007.
- [27] R. I. Leine, D. H. van Campen, and A. de Kraker, "Stick-Slip Vibrations Induced by Alternate Friction Models", *Nonlinear Dynamics*, Vol. 16, pp. 41-54, 1998.

- [28] R. A. Ibrahim, "Friction-induced vibration, chatter, squeal, and chaos. Part II: Dynamics and modeling", *Applied Mechanics Reviews*, Vol. 47, No. 7, pp. 227-253, 1994.
- [29] N. M. Kinkaid, O. M. O'Reilly, and P. Papadopoulos, "Review: Automotive disc brake squeal", *Journal of Sound and Vibration*, Vol. 267, pp. 105-166, 2003.
- [30] A. F. D'Souza and A. H. Dweib, "Self-excited Vibrations Induced by Dry Friction, part 2: Stability and Limit-cycle Analysis", *Journal of Sound and Vibration*, Vol. 137, No. 2, pp. 177-190, 1990.
- [31] K. Popp, "Modelling and control of friction-induced vibrations", *Mathematical and Computer Modelling of Dynamical Systems*, Vol. 11, No. 3, pp. 345 – 369, 2005
- [32] B. F. Feeny, "The Nonlinear Dynamics of Oscillators with stick-slip friction", *Dynamics with Friction*, In A. Guran, F. Pfeiffer, and K. Popp, Eds., World Scientific, River Edge, pp. 36-92, 1996.
- [33] K. Popp and M. Rudolph, "Vibration control to avoid stick-slip motion", *Journal of Vibration and Control*, Vol. 10, No. 11, pp. 1585-1600, 2004.
- [34] H. Hetzler, D. Schwarzer, and W. Seemann, "Analytical investigation of steady-state stability and Hopf-bifurcations occurring in sliding friction oscillators with application to low-frequency disc brake noise", *Communications in Nonlinear Science and Numerical Simulation*, Vol. 12, pp. 83–99, 2007.
- [35] J. Sanders, F. Verhulst, J. Murdock, *Averaging Methods in Nonlinear Dynamical Systems*, 2nd ed., Springer, 2007.
- [36] A. H. Nayfeh and B. Balachandran, *Applied Nonlinear Dynamics*, John Wiley & Sons, Inc., 1995.
- [37] J. J. Thomsen and A. Fidlin, "Analytical Approximations for Stick–slip Vibration Amplitudes", *International Journal of Non-Linear Mechanics*, Vol. 38, pp. 389–403, 2003.
- [38] C. A. Brockley and P. L. Ko, "Investigation of rail corrugation using friction-induced vibration theory", *Wear*, Vol. 128, No. 1, pp. 99 -106, 1988.
- [39] F. J. Elmer, "Nonlinear dynamics of dry friction", *Journal of Physics A: Mathematical and General*, Vol. 30, pp. 6057-6063, 1997.

- [40] P. E. Dupont and S. P. Yamajako, “Jamming and Wedging in Constrained Rigid-body Dynamics”, *Proceedings of the 1994 IEEE International Conference on Robotics and Automation*, No. 3, pp. 2349 -2354, 1994.
- [41] P. E. Dupont, “The Effect of Coulomb Friction on the Existence and Uniqueness of the Dynamics Problem”, *Proceedings of the 1992 IEEE International Conference on Robotics and Automation*, Nice, France, pp. 1442-1447, 1992.
- [42] N. Hoffmann and L. Gaul, “A sufficient criterion for the onset of sprag-slip oscillations”, *Archive of Applied Mechanics*, Vol. 73, pp. 650–660, 2004.
- [43] K. Huseyin, *Vibrations and stability of multiple parameter systems*, Noordhoff International Publishing, 1978.
- [44] A. Fidlin, *Nonlinear Oscillations in Mechanical Engineering*, Springer-Verlag, 2006.
- [45] K. Ono, J. S. Chen, and D. B. Bogy, “Stability analysis of the head-disk interface in a flexible disc drive”, *ASME Journal of Applied Mechanics*, Vol. 58, pp. 1005-1014, 1991.
- [46] J. E. Mottershead and S. N. Chan, “Flutter instability of circular discs with frictional followers loads”, *Journal of Vibration and Acoustics*, Vol. 117, pp. 161-163, 1995.
- [47] N. Hoffmann and L. Gaul, “Effects of damping on mode-coupling instability in friction induced oscillations”, *ZAMM*, Vol. 83, No. 8, pp. 524 – 534, 2003.
- [48] N. Hoffmann, S. Bieser, and L. Gaul, “Harmonic Balance and Averaging Techniques for Stick-Slip Limit-Cycle Determination in Mode-Coupling Friction Self-Excited Systems”, *Technische Mechanik*, Vol. 24, No. 3-4, pp. 185-197, 2004.
- [49] N. Hoffmann, M. Fischer, R. Allgaier, and L. Gaul, “A minimal model for studying properties of the mode-coupling type instability in friction induced oscillations”, *Mechanics Research Communications*, Vol. 29, pp. 197–205, 2002.
- [50] N. Hoffmann, “Transient Growth and Stick-Slip in Sliding Friction”, *Journal of Applied Mechanics*, Vol. 73, No. 4, pp. 642-647, 2006.
- [51] N. P. Hoffmann, “Linear stability of steady sliding in point contacts with velocity dependent and LuGre type friction”, *Journal of Sound and Vibration*, Vol. 301, pp. 1023–1034, 2007.

- [52] G. Fritz, J.-J. Sinou, J.-M. Duffala, and L. Jézéquel, “Investigation of the relationship between damping and mode-coupling patterns in case of brake squeal”, *Journal of Sound and Vibration*, Vol. 307, pp. 591–609, 2007.
- [53] J.-J. Sinou and L. Jézéquel, “Mode coupling instability in friction-induced vibrations and its dependency on system parameters including damping”, *European Journal of Mechanics A/Solids*, Vol. 26, pp. 106–122, 2007.
- [54] J.-J. Sinou and L. Jézéquel, “The influence of damping on the limit cycles for a self-exciting mechanism” *Journal of Sound and Vibration*, Vol. 304, No. 3-5, pp. 875-893, 2007.
- [55] G. Fritz, J.-J. Sinou, J.-M. Duffal, and L. Jézéquel, “Effects of damping on brake squeal coalescence patterns – application on a finite element model”, *Mechanics Research Communications*. Vol. 34, pp.181–190, 2007.
- [56] J.-J. Sinou, G. Fritz, and L. Jézéquel, “The Role of Damping and Definition of the Robust Damping Factor for a Self-Exciting Mechanism with Constant Friction”, *Journal of Vibration and Acoustics*, Vol. 129, No. 3, pp. 297-306, 2007.
- [57] B. Hervé, J.-J. Sinou, H. Mahéa, and L. Jézéquel, “Analysis of squeal noise and mode coupling instabilities including damping and gyroscopic effects”, *European Journal of Mechanics A/Solids*, Vol. 27, pp. 141–160, 2008.
- [58] J.-J. Sinou and L. Jézéquel, “On the stabilizing and destabilizing effects of damping in a non-conservative pin-disc system”, *Acta Mechanica*, Vol. 199, pp. 43–52, 2008.
- [59] F. Chevillot, J.-J. Sinou, G.-B. Mazet, N. Hardouin, and L. Jézéquel, “The destabilization paradox applied to friction-induced vibrations in an aircraft braking system”, *Archive of Applied Mechanics*, Vol. 78, pp. 949–963, 2008.
- [60] M. Rusli and M. Okuma, “Effect of surface topography on mode-coupling model of dry contact sliding systems”, *Journal of Sound and Vibration*, Vol. 308, pp. 721–734, 2007
- [61] U. von Wagner, D. Hochlenert, and P. Hagedorn, “Minimal models for disk brake squeal”, *Journal of Sound and Vibration*, Vol. 302, pp. 527–539, 2007.
- [62] J. Huang, C. M. Krousgrill, and A. K. Bajaj, “An efficient approach to estimate critical value of friction coefficient in brake squeal analysis”, *Journal of Applied Mechanics*, Vol. 74, No. 3, pp. 534-541, 2007.

- [63] S. Chatterjee, "On the Design Criteria of Dynamic Vibration Absorbers for Controlling Friction-Induced Oscillations", *Journal of Vibration and Control*, Vol. 14, No. 3, pp. 397-415, 2008.
- [64] J. Kang, "Parametric study on friction-induced coupled oscillator", *Proceedings of the Institution of Mechanical Engineers, Part C: Journal of Mechanical Engineering Science*, Vol. 222, No. 8, pp. 1381-1387, 2008.
- [65] U. Olofsson and L. Ekerfors, "Friction-induced noise in screw-nut transmissions", *Wear*, Vol. 148, 1991, pp. 25-37.
- [66] P. Gallina, "Vibration in screw jack mechanisms: experimental results", *Journal of Sound and Vibration*, Vol. 282, 2005, pp. 1025-1041.
- [67] A. A. Oledzki, "Modeling and simulation of self-locking drives", *Mechanism and Machine Theory*, Vol. 30, No. 6, pp. 929-942, 1995.
- [68] P. Scott, "Ball-screw basics: Debunking the myths", *Machine Design*, Vol. 76, No. 13, 2004, pp. 88-92.
- [69] J. Otsuka, "Nanometer level positioning using three kinds of lead screws", *Nanotechnology*, Vol. 3, 1992, pp. 29-36.
- [70] A. Shimokohbe, "The state of the art of nano-meter motion control in Japan", *Proceedings of the International Conference on Trends in Industrial Measurements Automation*, 1996, pp. 2-8.
- [71] A. Shimokohbe, "The Development of nano-meter positioning technology in Japan", *Proceedings of the International Conference on Advanced Manufacturing Technology*, 1999, pp. 83-87.
- [72] B. A. Awabdy, W.-C. Shih, and D. M. Auslander, "Nanometer positioning of a linear Motion stage under static loads", *IEEE/ASME Transactions on Mechatronics*, Vol. 3, No. 2, 1998, pp. 113-119.
- [73] K. Erkorkmaz and Y. Altintas, "High speed CNC system design. Part II: modeling and identification of feed drives", *International Journal of Machine Tools & Manufacture*, Vol. 41, 2001, 1487-1509.
- [74] K. K. Varanasi and S. A. Nayfeh, "The dynamics of lead-screw drives: Low-order modeling and experiments", *Journal of Dynamic Systems, Measurement, and Control*, Vol. 126, 2004, pp. 388-396.

- [75] C. L. Chen, M. J. Jang, and K. C. Lin, “Modeling and high-precision control of a ball-screw-driven stage”, *Precision Engineering*, Vol. 28, 2004, pp. 483–495.
- [76] R. Whalley, M. Ebrahimi, and A.A. Abdul-Ameer, “Hybrid modelling of machine tool axis drives”, *International Journal of Machine Tools & Manufacture*, Vol. 45, 2005, pp. 1560–1576.
- [77] K. Sato, H. Fujimoto, H. Osada, and A. Shimokohbe, “Dynamic behavior of lead screw mechanism with backlash”, *Japan Society of Mechanical Engineers, Part C*, Vol. 61, No. 584, 1995, pp. 1423-1430.
- [78] K. Sato, Y. Murayama, S. Imada, and A. Shimokohbe, “Control and elimination of lead screw backlash for ultra-precision positioning”, *JSME International Journal, Series C*, Vol. 38, No. 1, 1995, pp. 36-41.
- [79] T. A. Stolarski, *Tribology in Machine Design*, Butterworth-Heinemann, 1990.
- [80] K. Erkorkmaz and A. Kamalzadeh, “High bandwidth control of ball screw drives”, *Annals of CIRP*, Vol. 55, No. 1, 2006.
- [81] A. Kamalzadeh and K. Erkorkmaz, “Accurate Tracking Controller Design for High-speed Drives”, *International Journal of Machine Tools & Manufacture*, Vol. 47, 2007, pp. 1393-1400.
- [82] J. T. Oden and J. A. C. Martins, “Models and computational methods for dynamic friction phenomena”, *Computer Methods in Applied Mechanics and Engineering*, Vol. 52, pp. 527–634, 1985.
- [83] S. Chatterjee, “Non-linear control of friction-induced self-excited vibration”, *International Journal of Non-Linear Mechanics*, Vol. 42, pp. 459 – 469, 2007.
- [84] H. K. Khalil, *Nonlinear Systems*, 3rd ed.,
- [85] P. E. Dupont, “The Use of Compliance to Resolve the Existence and Uniqueness of the Forward Dynamics Solution with Coulomb Friction”, *Proceedings CSME Forum 1992*, Montreal, Canada, 1992.
- [86] P. E. Dupont and S. P. Yamajako, “Stability of Frictional Contact in Constrained Rigid-body Dynamics”, *IEEE transactions on robotics*, Vol. 13, No. 2, pp. 230 -236, 1997.
- [87] K. Shin, M. J. Brennan, J.-E. Oh, and C. J. Harris, “Analysis of disc brake noise using a two-degree-of-freedom model”, *Journal of Sound Vibration*, Vol. 254, No. 5, pp. 837-848, 2002.

- [88] J.-J. Sinou and L. Jézéquel, "Mode coupling instability in friction-induced vibrations and its dependency on system parameters including damping", *European Journal of Mechanics A/Solids*, Vol. 26, pp. 106–122, 2007.
- [89] J.-J. Sinou and L. Jézéquel, "The influence of damping on the limit cycles for a self-exciting mechanism", *Journal of Sound and Vibration*, Vol. 304, pp. 875-893, 2007.
- [90] J.-J. Sinou, G. Fritz, and L. Jézéquel, "The role of damping and definition of the robust damping factor for a self-exciting mechanism with constant friction", *Journal of Vibration and Acoustics*, Vol. 129, pp. 297-306, 2007.
- [91] V. I. Utkin, "Variable Structure Systems with Sliding Modes", *IEEE Transactions on Automatic Control*, Vol. AC-22, No. 2, pp. 212-222, 1977.
- [92] J. -J. E. Slotine and W. Li, *Applied Nonlinear Control*, Prentice-Hall, 1991.
- [93] J. Y. Hung, W. Gao, and J. C. Hung, "Variable Structure Control: A Survey", *IEEE Transactions on Industrial Electronics*, Vol. 40, No. 1, pp. 2-22, 1993.
- [94] K. D. Young, V. I. Utkin, and U. Özgüner, "A Control Engineer's Guide to Sliding Mode Control" *IEEE Transactions on Control Systems Technology*, Vol. 7, No. 3, pp. 328-342, 1999.
- [95] J. -J. E. Slotine and S. S. Sastry, "Tracking Control of Non-linear Systems Using Sliding Surface, with Application to Robot Manipulators", *International Journal of Control*, Vol. 38, No. 2, pp. 465-492, 1983.
- [96] P. Kachroo and M. Tomizuka, "Chattering Reduction and Error Convergence in the Sliding-mode Control of a Class of Nonlinear Systems", *IEEE Transactions on Automatic Control*, Vol. 41, No. 7, pp. 1063-1068, 1996.
- [97] H. Lee and V. I. Utkin, "Chattering Suppression Methods in Sliding Mode Control Systems", *Annual Reviews in Control*, Vol. 31, pp. 179–188, 2007.
- [98] G. Bartolini, A. Pisano, E. Punta, and E. Usai, "A Survey of Applications of Second-order Sliding Mode Control to Mechanical Systems", *International journal of control*, Vol. 76, No. 9, pp. 875-892, 2003.
- [99] S. Seshagiri and H. K. Khalil, "On Introducing Integral Action in Sliding Mode Control", Proceedings of the 41st IEE Conference on Decision and Control, Las Vegas, Nevada USA, December 2002, 1473-1478.

- [100] K.-S. Hong, "An Open-Loop Control for Underactuated Manipulators Using Oscillatory Inputs: Steering Capability of an Unactuated Joint", *IEEE Transactions on Control Systems Technology*, Vol. 10, No. 3, pp. 469-480, 2002.
- [101] J. Mardsen and A. Tromba, *Vector Calculus*, 4th ed., W. H. Freeman, New York, 1996.
- [102] V. H. Moll, "The Integrals in Gradshteyn and Ryzik. Part 21: Trigonometric Functions", http://www.math.tulane.edu/~vhm/web_html/trigoweb.pdf, 2006.
- [103] P. Henrici, *Applied and Computational Complex Analysis*, Volume I, John Wiley & Sons, Inc., 1974.
- [104] N. N. Bogoliubov and Y. A. Mitropolsky, *Asymptotic methods in the theory of non-linear oscillations*, 2nd ed., (Translated from Russian), Hindustan Publishing Corporation, Delhi, India 1961.